Mineral solubility measurements at high pressures:
Redesigning the hydrothermal diamond anvil cell,
crystal volume computations and birefringence mapping.

Dissertation

zur Erlangung des akademischen Grades eines

Doktors der Naturwissenschaften

der

Fakultät für Geowissenschaften der Ruhr-Universität Bochum

von

Juliane Groß

- Bochum 2009 –

Erstgutachter: Prof. W.V. Maresch

Zweitgutachter: Prof. S. Chakraborty

Tag der mündlichen Prüfung: 06.07.2009

"Happy are those who dream dreams and are ready to pay the price to make them come true"

L.J. Cardinal Suenens

Abstract

Abstract

The role of fluids in the reequilibration of minerals and rocks is fundamental to understanding the mechanisms and kinetics of metamorphic and metasomatic processes. Data for the solubility of minerals in aqueous solutions at high pressures are essential for our understanding of fluid properties, mass transport and growth/dissolution processes of minerals in Earth's crust and upper mantle.

Although a fairly extensive dataset is now available on the solubility of minerals in aqueous fluids at high pressures and high temperatures, most of the data above 0.5 GPa have been obtained by *ex situ* quench methods in piston-cylinder presses. A few comparative studies between such indirect weight-loss techniques and direct disappearance-of-phase, *in situ* methods are available, but only for trace elements. The results show huge differences, which so far have not been satisfactorily explained.

In the present study new *in situ* mass-loss approaches for determining solubilities of dissolved components have been developed, using a specially designed and reconstructed hydrothermal diamond anvil cell (HDAC). This construction allows to achieve fluid-pressures up to 4.0 GPa.

In the first method the tendency of crystals to approach an idiomorphic habit during HDAC runs is exploited, as observed in our HDAC studies. By defining the habit of a crystal before the run, its changing geometry can be modeled at various stages of the experiment and solubilities can be calculated.

The second method is based on measuring, mapping and analyzing mineral birefringence to quantify the thickness of a crystal. Changes in crystal volume can be directly obtained. With this method crystal masses less then a few μg can be determined.

Both approaches and the reconstructed HDAC have been successfully tested on the basis of the voluminous published data on SiO_2 solubility. Both methods show that the derived solubility data are compatible down to the ppm-level.

The results derived in this study contribute to our technical arsenal of high-pressure, high-temperature equipment as well as to our overall understanding of the chemical properties of fluids in high-pressure environments, such as in subduction zones.

1 Introduction

1.1 The critical importance of mineral solubility data

Understanding the physical and geochemical processes occurring in the Earth's mantle and crust is one of the fundamental tasks of experimental research in the Earth Sciences community. Earth is a planet that, due to its internal structure and temperature field, is subject to permanent change (e.g. Jamtveit and Yardley, 1997; Manning, 2007a; Manning, 2007b; Marshak, 2008). Convection in the mantle is the motor that drives the lithosphere plates, whereas their deformation is mostly concentrated along plate boundaries. In subduction zones, which can extend from trenches to beneath volcanic arcs, Earth's lithosphere returns to the deep mantle. Here profound chemical changes are located. While the subducting plate descends it drives off volatiles (most importantly water) from the hydrated oceanic crust. These fluids play a major role in virtually all crustal processes. They have an effect on redistributing material and are responsible for mass and energy transport in the Earth's interior, controlling for example hydrothermal ore deposits. The mechanical processes that control rock deformation in subduction zones are strongly influenced by the volume of fluid and the pore-fluid pressure. Numerous geological processes such as spectacular explosive volcanic eruptions, the planet's greatest earthquakes, the development of sedimentary basins and mid-ocean ridges are the result (e.g. Vrolijk and Myers, 1990; Todd and Evans, 1993; Manning, 2004b; Manning, 2007a). Metasomatic alteration in the upper mantle and deep crust resulting from the infiltration of silicate-saturated aqueous fluid may result in compositional changes in these regions (e.g. Mysen and Acton, 1999; Gross *et al.*, 2008). The accurate understanding of the mechanical behavior of rocks under different boundary conditions such as porosity, permeability, and reactive surface area is thus essential for quantifying chemical mass transport in natural systems (Evans and Kohlstedt, 1995; Colón *et al.*, 2004).

Most of the "reactive flows" are understood quite well and can be modeled with success for relative low depth (e.g. Bjørlykke, 1997; Cartwright, 1997). In contrast, we know little about the fluids in subduction zones that begin the process of material transfer, primarily because we lack basic information on fluid composition and how it is controlled (Manning, 2004b; Manning, 2007c).

The present study was carried out under the auspices of the SFB 526 "Rheology of the Earth - from the upper crust to the subduction zone", where the rheology of rocks

in subduction zones represents the central theme. Accordingly, the focus of this thesis lies in the importance of solubility data for understanding the role of silicate-rich aqueous fluids in deforming rock systems at high pressures.

Fluids ranging from hydrous melts to dense aqueous solutions play a major role in the ductile behavior of rocks in the deeper levels of the crust of crustal rocks subducted into the mantle (Maresch *et al.*, 2002). Although the basic atomistic mechanisms governing phenomenological rate laws for the chemical and rheological behavior of complex deforming rock-water systems at high pressures and temperatures, such as those typical for subduction zones, have been largely identified, the quantification of characteristic rate-law parameters at high pressures and temperatures remains problematic.

For example, Ranalli (1995) offers the following proportionality between strain rate $\dot{\varepsilon}$, and stress η for a quasi-static system in which the solid phases predominate volumetrically and take up most of the stress imposed on the system:

$$\dot{\varepsilon} \sim \frac{c_0 F D_F \upsilon \Omega}{kT\tau^2}\left(\frac{\eta}{\upsilon}\right)$$

where $\dot{\varepsilon}$, Ω, υ, τ, F, c_0, D_F, η, T, k (strain rate, atomic volume, shear modulus, average grain diameter, proportion by volume of the fluid, solubility, diffusion coefficient, stress rate, temperature, Boltzmann constant, respectively) are characteristic parameters of the system. The quantification of the solubilities c_0 and diffusion coefficients D_F of the coexisting fluid phase at elevated pressure and temperature is still critical (e.g. Evans and Kohlsted, 1995; Watson and Wark, 1997; Fockenberg *et al.*, 2008). Legend and abbreviations can be found in the Appendix I and II. In addition, as the relative proportion of fluid increases in the system, its physical properties will begin to dominate the system, and derivative properties such as density and viscosity will become of central concern (e.g. Gerya *et al.*, 2001; Willner *et al.*, 2002; Gerya *et al.*, 2007). Above all, there is at present no internally consistent theory that allows either a thermodynamic, macroscopic description of aqueous fluids with dissolved silicate components at high pressures or a microscopic approach to describe the atomistic structure of the fluid itself (e.g. Helgeson *et al.*, 1981; Connolly, 1997a and 1997b; Gerya *et al.* 2004a and 2004b; Doltsinis *et al.*, 2004). Progress on both aspects is required in order to allow prediction of the structure and properties of high-pressure aqueous fluids from general principles. Consequently, experimental approaches are

needed which are able to simulate the conditions of the deep Earth and allow direct measurement of critical parameters such as c_o.

1.2 Methodology for determining mineral solubilities in aqueous fluids
1.2.1 *Ex situ* approaches

Commonly, mineral solubilities are obtained by weight-loss techniques. Thereby the weight of a starting crystal is compared with the undissolved remnant quenched from experimental runs in high-pressure apparatus at pressure and temperature of interest. At present there is an increasingly comprehensive data set becoming available on mineral solubility in aqueous fluids at high pressures using this technique (e.g. Manning, 1994; Newton and Manning, 2002a and 2002b; Gerya *et al.*, 2005; Newton and Manning, 2006; Burchard *et al.*, 2006; Fockenberg *et al.*, 2006). However, the uncertainties are generally large and often difficult to quantify, because the resulting phase assemblages and product textures are characterized 'post-mortem', that is at post-experimental conditions.

This can be problematic for an interpretation of the results if temperature gradients within the reaction vessel are present. Such a gradient can affect weight-loss results by initiating dissolution at the hotter end of the run capsule and re-precipitation at the cooler end (e.g. Manning and Boettcher, 1994). If phase transitions during heating and cooling as well as incongruent dissolution are involved, the interpretation of the 'post-mortem' product can also be critical (Manning and Boettcher, 1994; Fockenberg *et al.*, 2008). Problems can also arise from the possibility of uncontrolled mechanical fragmentation due to good cleavage of a mineral phase. In addition it is known that phases and micro-fabrics can change dramatically during quenching (Bureau & Burchard, 2006). The quench process also carries with it the possibility of reaction between the undissolved solid phase and the solution as the system is cooled (Manning, 1994; Verlaguet *et al.*, 2006; Verlaguet and Brunet, 2007; Fockenberg *et al.*, 2008). Any such loss of sample cannot be determined accurately, nor is it possible to decide with certainty whether the reprecipitated material is a quench product or not (e.g. Manning, 1994; Manning and Boettcher, 1994; Fockenberg *et al.*, 2008). These difficulties remain despite improvements in quench technique that reduce quench times from a scale of minutes to seconds (Manning, 1994).

Nevertheless, such experiments rely on high-pressure techniques that are now routine, and they are relatively rapid and easy to carry out. For this reason, most solubility data have been obtained in such studies.

1.2.2 *In situ* approaches

One of the most important properties of *in situ* experimental techniques is the fact that the reaction path can be observed directly, and continuous visual monitoring during changing P-T conditions is possible, thus avoiding the quench problems of *ex situ* experiments. In addition the accessibility of the parameter time, allowing the observation of process rates such as dissolution, chemical exchanges between phases, bubble growth, crystal growth and others is a major advantage. Hydrothermal diamond anvil cells (HDAC) possess a unique design which allows *in situ* observation of the sample during an experiment (Bassett *et al.*, 1993) and therefore play an increasingly important role in experimental investigations within the Earth Sciences and especially in Mineral Physics. The HDAC is a small, compact instrument holding two diamonds. The transparency of the diamonds to light allows direct observation of the sample and aqueous medium which are held inside a gasket between the two diamond faces.

Nevertheless, *in situ* experiments to determine mineral solubility in HDACs can be problematic as well. Published *in situ* studies have concentrated on the "disappearance-of-phase" method, meaning that the sample chamber is heated until the observed crystal fragment vanishes (e.g. Bureau and Keppler, 1999; Zotov and Keppler, 2002; Audétat and Keppler, 2005). In addition, a few comparative studies between *ex situ* weight-loss techniques and direct disappearance-of-phase, *in situ* methods are available, but only for trace elements (Ayers and Watson, 1993; Audétat and Keppler, 2005; Tropper and Manning, 2005). The results show huge differences, which so far have not been satisfactorily explained. At present, however, little is known about the kinetics of mineral dissolution, so that an overstepping of solubility isopleths can be a problem. The results reported in the literature to date were not carried out reversibly, so that the actual extent of possible overstepping is unclear.

2 Motivation of the present study

Due to the known difficulties and discrepancies with *ex situ* experiments and the problems involved with *in situ* experiments as described above, the motivation for this study was to develop totally new *in situ* mass-loss approaches in conjunction with the hydrothermal diamond anvil cell, in order to combine the advantages of *in situ* and *ex situ* experiments, while circumventing their obvious disadvantages. These new techniques were then to be tested and assessed on the basis of the voluminous published data on SiO_2 solubility at hand, most of which have been obtained by *ex situ* methods. These new methods were then to be used to determine solubilities of additional rock-forming minerals at high pressures and temperatures. The two new approaches developed during this study were based on a new type of HDAC, which was developed earlier at the Ruhr-University of Bochum (RUB). However, routine use of this HDAC demonstrated the existence of a number of constructional problems that had to be overcome. Therefore it became necessary first to optimize the available experimental equipment, especially with respect to developing technical solutions for the heaters, the adjustment of the diamond anvils and the pressurizing system of the HDAC.

Thus the goal of this study was to contribute to our technical arsenal of high-pressure, high-temperature equipment as well as to our overall understanding of the chemical properties of fluids in high-pressure environments, such as in subduction zones.

3 Diamond anvil cell techniques

3.1 The significance of the diamond anvil cell (DAC)

The diamond anvil cell (DAC) has revolutionized high-pressure research, both in terms of the range of static pressure that can be reached and the variety of techniques that can be employed to study the behavior of matter at high pressure (Jayaraman, 1986). DACs are used in many fields of research, such as geosciences, physics, and material sciences, as well as organic, inorganic, physical chemistry, and biochemistry. The primary interest in DACs stems from the fact that great varieties of different materials can be studied with *in situ* methods under great varieties of pressure and temperature conditions and gas/fluid environments (Burchard *et al.*, 2003).

The basic principle of the DAC is very simple. A metal gasket, usually filled with a pressure-transmitting medium and/or the sample itself, is subjected to pressure when placed between the plane-parallel culets of two opposed, brilliant-cut, gem-quality diamond anvils (see Fig. 3.1). An external force pushes the two opposed anvils together. For successful operation of the DAC, the two anvil flats must be accurately centered and set parallel to each other.
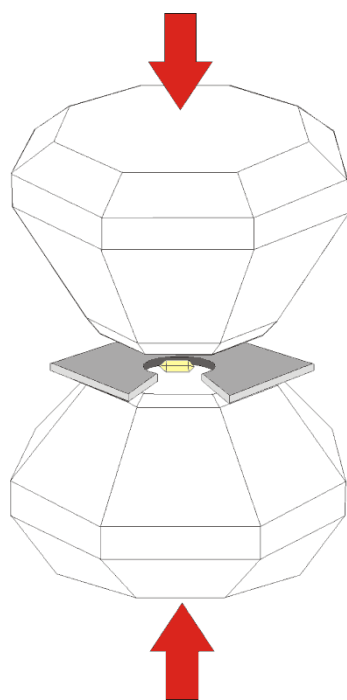

Fig. 3.1: Simplified schematic sketch of the basic principle of DACs. A metal gasket usually filled with a pressure medium and/or the sample (yellow) itself is placed between the plane-parallel culets of two opposed brilliant-cut diamond anvils. An external force (indicated by the two red arrows) pushes the two opposed anvils together, initiating pressure.

Three broad areas of DAC application can be recognized. The first involves experiments at room temperature and below, down to several Kelvins and high pressures (e.g. Webb *et al.*, 1976; Mao and Bell, 1979; Diatschenko and Chu, 1981). The second is concerned with the attainment of extremely high pressures extending into the megabar range (e.g. LeToullec *et al.*, 1988), which can be reached by using extremely small micrometer-sized culets at the diamond anvil tips. If high temperatures are necessary, such experiments can be laser heated. Several types of pressure medium have been used for such applications, such as methanol-ethanol mixtures (e.g. Piermarini *et al.*, 1973), helium, neon, argon (Bell and Mao, 1981), xenon (Liebenberg, 1979) and others.

The third main area of application is the use of diamond anvil cells with a hydrothermal pressurizing system using aqueous fluids (e.g. pure water, or an electrolyte with NaCl) as the pressure medium. These are commonly called hydrothermal diamond anvil cells (HDACs) (e.g. Burchard *et al.*, 2003).

3.2 Types of diamond anvil cells

Variations in DACs arise from different ways in which the force-generating and the anvil-aligning mechanisms are designed (Jayaraman, 1983) and the needs and ingenuity of the designer (Yousuf, 1998). Accordingly, six major types of DACs have evolved: NBS-Cell, Bassett-Takahashi-Stook Cell, Mao-Bell Cell, Merrill-Bassett Cell, Huber-Syassen-Holzapfel Cell, LeToullec-Pinceaux-Loubyre Cell. These types are described briefly in the following sections.

3.2.1 NBS Cell

The NBS cell was invented by Piermarini and Block in 1975. The main body of the cell consists of a rectangular plate made of steel, with provision for holding the stationary and moving pistons (Yousuf, 1998). The stationary diamond mount can be translated for centering and locking. The diamond anvil mounted in the hemisphere can be tilted to obtain parallel anvil culets. Force is generated through a lever arm (Fig. 3.2) and controlled by Belleville spring washers. Generated pressures of ~ 50 GPa are reported (Piermarini and Block, 1975).
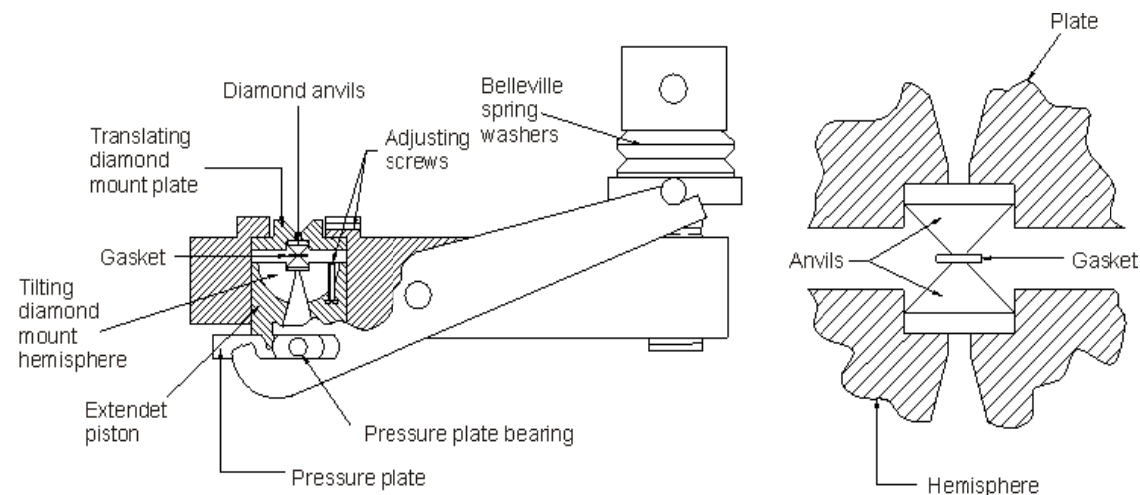
Fig. 3.2: NBS Cell (modified from Yousuf, 1998).

3.2.2 Mao-Bell Cell

Mao *et al.* (1978) developed this cell to exceed pressures of 100 GPa. Like the NBS Cell it has a Belleville spring-washer, lever-arm mechanism for generating the force. Modifications include a long detachable piston-cylinder assembly to ensure proper alignment of the diamonds (Fig. 3.3). For anvil centering and alignment two tungsten carbide half-cylinders can be tilted and translated. The axes of these cylinders are set perpendicular to each other. Mao *et al.* (1978) report pressures of ~ 100GPa and Mao (1989) reports pressures in excess of 500 GPa by using beveled diamond anvils.
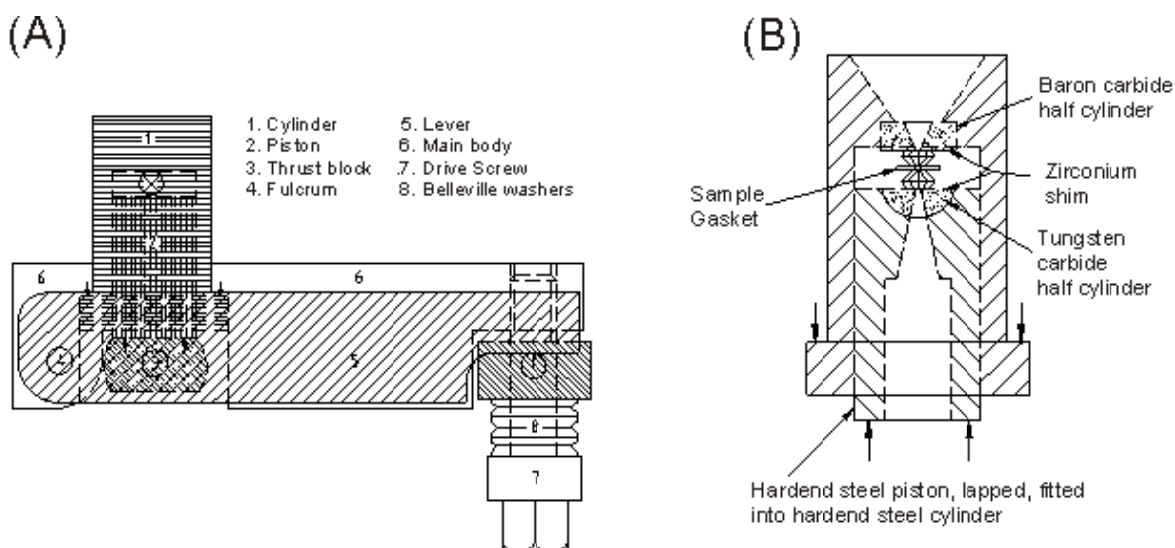
Fig. 3.3: (A) Mao-Bell Cell; **(B)** Detail of Mao-Bell Cell piston-cylinder (modified from Yousuf, 1998).

3.2.3 Huber-Syassen-Holzapfel Cell

This cell uses a lever arm system (Fig. 3.4), driven by a thread-and-nut mechanism for applying the force. A hemispherical mount on the upper piston is used for parallel alignment of the diamonds. The special geometry of the brackets, levers and threads results in a large force multiplication. This device has very good alignment stability because of the thrusts acting strictly parallel to the axis of the instrument. Huber *et al.* (1977) reported pressures of 50 GPa using this type of cell.
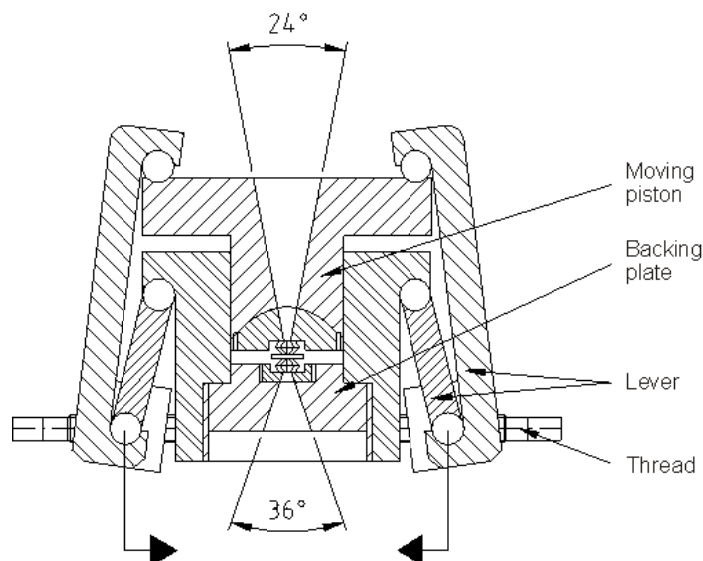
Fig. 3.4: Huber-Syassen-Holzapfel Cell (modified from Jayaraman, 1986)

3.2.4 Bassett-Takahashi-Stook Cell

Figure 3.5 shows the compact cell based on the design of Bassett *et al.* (1967). The movable piston is pushed by driving the nut. To prevent rotation, the former is arrested by a key in a slot. Hardened steel half-cylinders enable centering and parallel alignment of the two diamond anvils. Pressures of 40 GPa (Jayaraman, 1986) have been reached in a configuration without gasket using 0.3 mm culets.
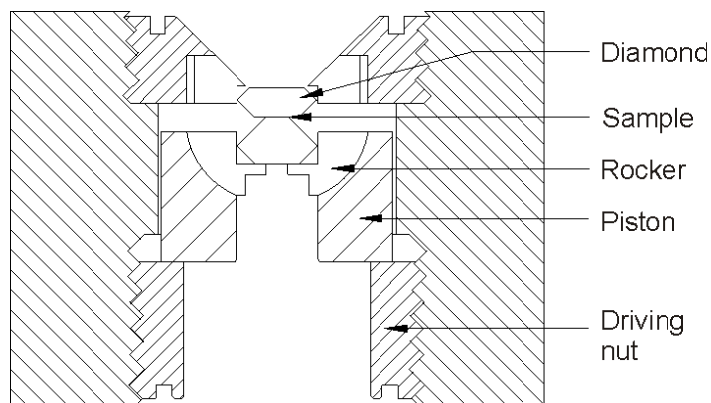
Fig. 3.5: Bassett-Takahashi-Stook Cell (modified from Yousuf, 1998).

3.2.5 Merrill-Bassett Cell

Merrill and Bassett (1974) developed a cell that consists of two triangular-shaped platens, which are pulled together by three spring-loaded Belleville-spring washer screws (Fig. 3.6A). For proper alignment the upper platen slides on three guiding pins anchored to the lower platen. This cell is very compact and because of its miniature size can be placed inside a helium cryostat for low-temperature studies (Yousuf, 1998).

3.2.6 LeToullec-Pinceaux-Loubeyre Cell

This DAC uses a membrane system driven by gas and allows the force to be varied very smoothly (LeToullec *et al.*, 1988). With beveled anvils, the cell can be operated at multi-megabar pressure (Fig. 3.6B).
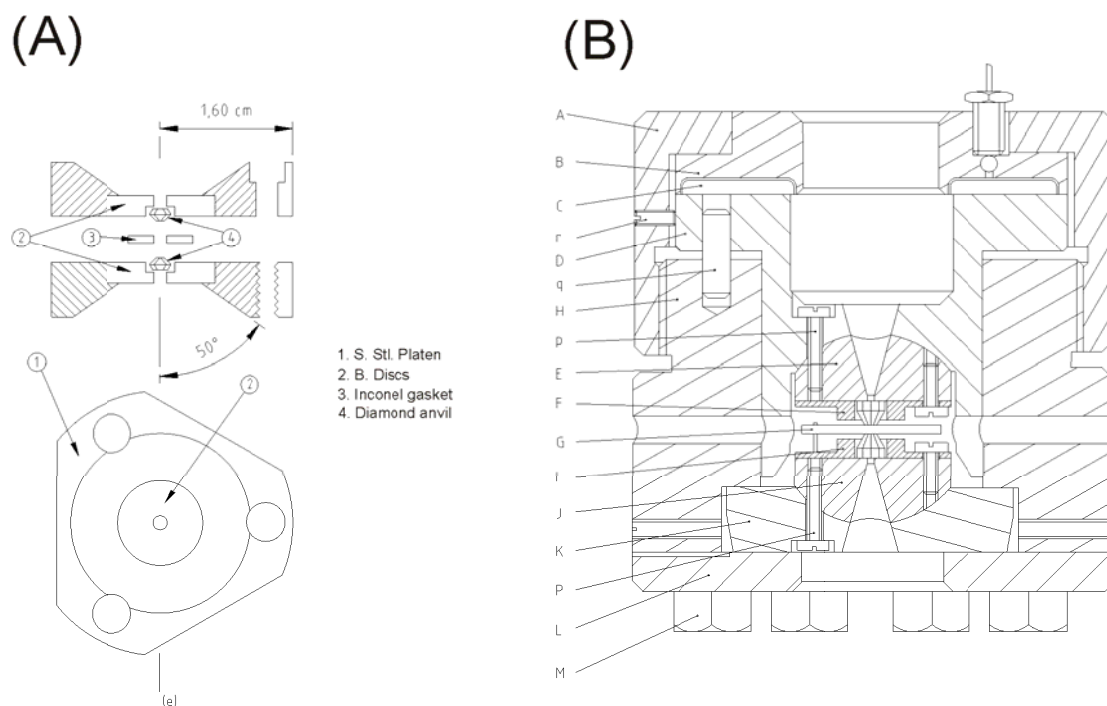
Fig. 3.6: (A) Merrill-Bassett Cell (modified from Jayaraman, 1986); **(B)** LeToullec-Pinceaux-Loubeyre Cell, A: retaining nut; B: the support onto which the membrane is soldered; C: push-piece to transmit the force to piston D; E and J: half-sphere seats of the diamonds; G: gasket; H: cell body; I and F: copper pieces in which the diamond anvils are inserted; K and L: supports of the fixed anvil seat; M, p and r: screws.

3.3 Types of hydrothermal diamond anvil cells (HDACs)

In HDACs the required pressures are achieved by first sealing and pressurizing the fluid-filled sample volume, followed by isochoric heating. The heaters are usually resistance heaters, with the wire coils made of materials such as molybdenum. The functional principle of HDACs is perfectly suited for high-pressure/high-temperature studies in solid–fluid or fluid–fluid systems that often involve sluggish reactions and represent a predominant research thrust in the geosciences (Burchard *et al.*, 2003).

3.3.1 Bassett Cell

The most widely used HDAC at present is described by Bassett *et al.* (1993) and therefore is often called the ''Bassett Cell''. This type of HDAC consists of two platens with diamond anvils and heaters mounted at their centers (Fig. 3.7).
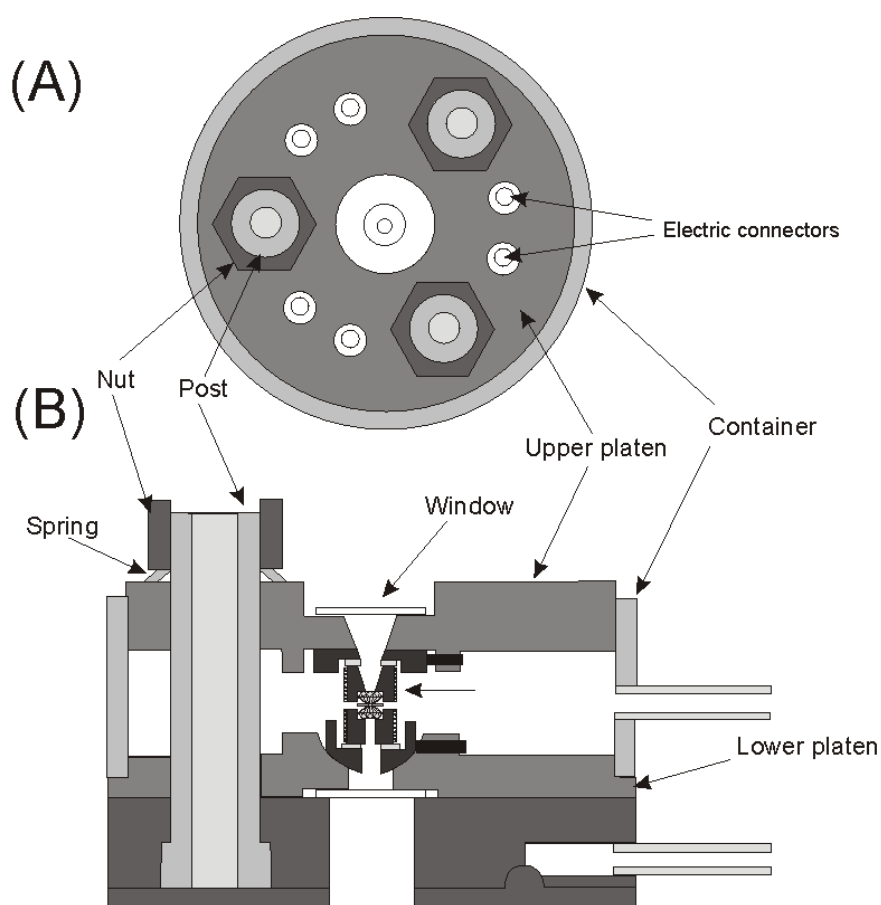
Fig. 3.7: Schematic top view (A) and cross-section (B) of a Bassett-type HDAC (modified after Bassett *et al.*, 1993)

Force is applied by the two platens that are drawn together by tightening nuts on the threaded ends of the three posts. Hence pressure is applied to the sample which is held between the diamond anvils inside a metal gasket. Holes through the centers of the platens allow visual observation of the sample along the compression axis. Molybdenum wires wrapped around the tungsten carbide seats, which support the diamond anvils, serve as resistance heaters (Fig. 3.8).
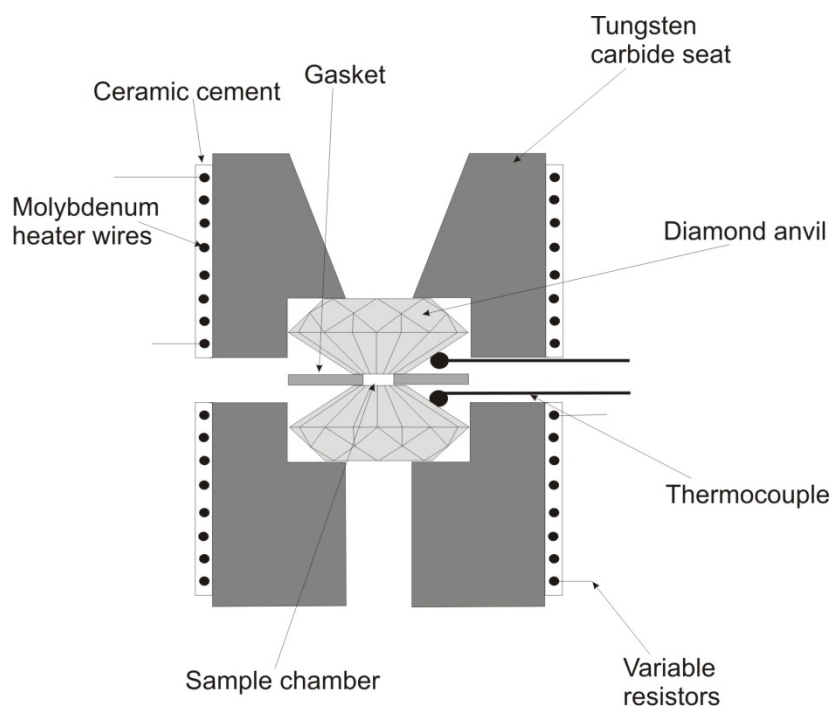
Fig. 3.8: Schematic diagram of the heating system of a Bassett-type HDAC (modified after Bassett *et al.*, 1993)

The volume containing the heaters, the anvils, and the sample can be enclosed by a gas mixture made of Argon with 1% H_2 which can be introduced to prevent oxidation. Bassett *et al.* (1993) report attainable pressures and temperatures of 2.5 GPa and 1200°C for this cell design.

3.3.2 Burchard-Zaitsev Cell

The Burchard-Zaitsev HDAC is quite different from the classical Bassett type of HDAC (Fig. 3.9). It is characterized by a hollow screw structure and spring-mounted anvils (Burchard *et al.*, 2003). The essential features of the Burchard-Zaitsev Cell are:
(1) The pressurizing mechanism that is reported to guarantee an absolutely parallel alignment and precludes accidental collision of the anvils;

(2) The mechanical anvil holders that provide both robust fixation of the anvils without any glue and reliable electrical contacts with the anvil facets;

(3) An integrated cooling system. Hence the diamond anvils can be heated while the anvil backing plates and the holders remain comparatively cool.
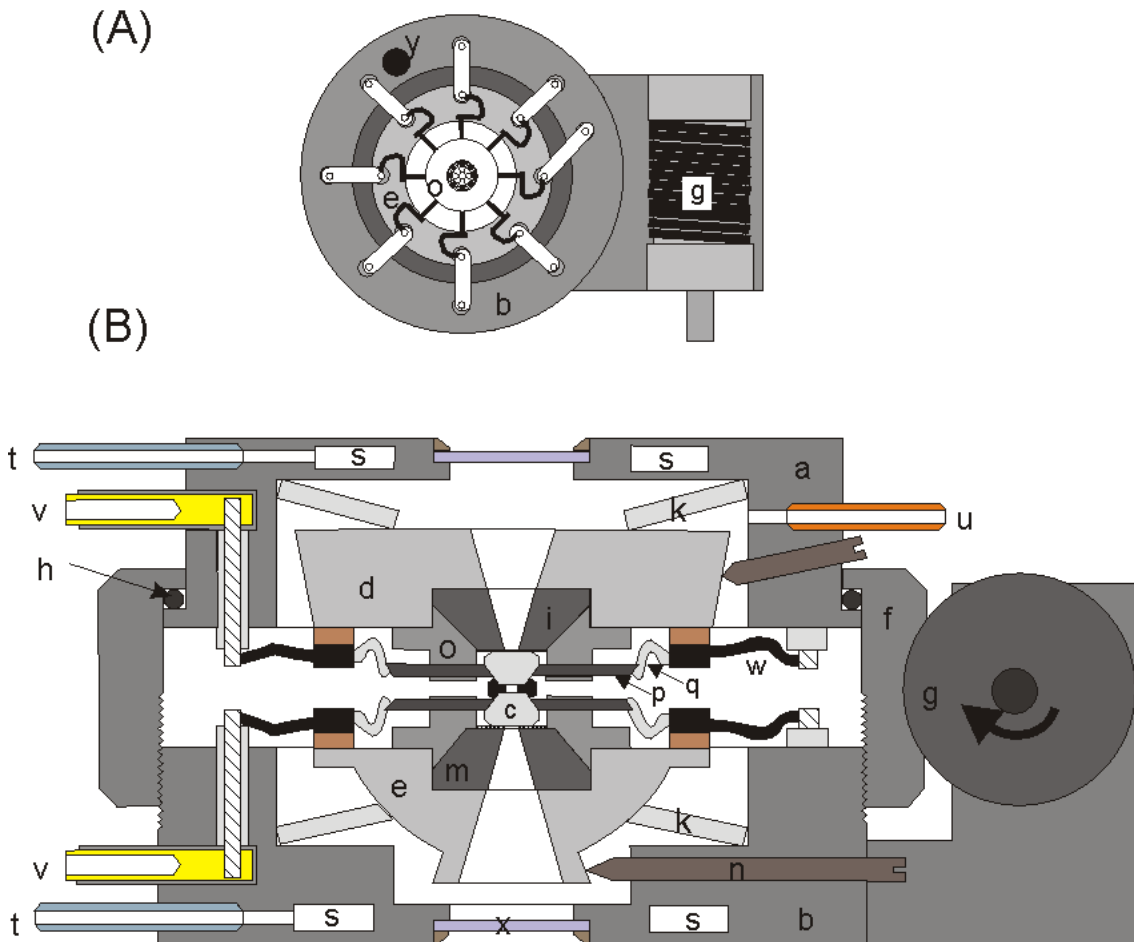
Fig. 3.9: View of the lower segment **(A)** as well as cross-section **(B)** of a Burchard-Zaitsev HDAC. (a) upper platen, (b) lower platen, (c) diamond anvils, (d) upper adjustable seat, (e) lower adjustable seat, (f) pressurizing nut with sprocket, (g) worm drive, (h) ball-bearing, (k) Belleville spring washers, (i) upper anvil holder, (m) lower anvil holder, (n) adjusting screws, (o) ceramic plate guiding the electrodes (p) tungsten carbide electrodes, (q) steel wire springs, (s) cooling conduits, (t) inlets of the cooling system, (u) protective gas inlet, (v) electrical connectors, (w) electric wire, (x) windows, (y) polished guiding pin. (modified after Burchard *et al.,* 2003).

Two threaded opposing platens enclose the diamond anvils on adjustable seats between them. After the usual adjustment and loading of the sample volume, the cell is pressurized by screwing the nut and lower platen together with the help of a worm

drive. A ball-bearing between the nut and the upper platen of the hollow cell body decouples both elements from each other and enables rotation of the nut even under high load, ensuring precisely uniaxial pressures and avoiding inhomogeneous gasket flow. The upper platen is guided by a polished pin to ensure accurate alignment of the platen movement towards each other (Burchard *et al.*, 2003).

Burchard *et al.* (2003) suggest that hydrothermal working conditions to at least 4.5 GPa and 1000°C are attainable.

3.4 Heating devices and temperature control

Various modes of sample heating in the diamond anvil cell have been designed. As described below, these can be roughly classified into direct and indirect alternative types.

3.4.1 Direct heating

With the simplest type of design, the sample is heated in a direct manner, without an actual heating element in the diamond anvil cell itself. For instance, a laser beam can be used to irradiate the sample through the diamond (Ming and Bassett, 1974; Jeanloz and Heinz, 1984), or an electric current can be supplied to the sample itself (Boehler *et al.*, 1986). This direct-heating design is applicable to any type of diamond anvil cell without special modifications. However, with this design it is difficult to accurately measure the true temperature of the sample, because an extremely large thermal gradient is usually present across the sample. In addition, the heating efficiency strongly depends on the optical or electrical properties of sample materials (Kikegawa, 1987).

3.4.2 Indirect heating

With an alternative type of design, the sample is heated indirectly by using a heating device integrated into the diamond anvil cell. There are various ways in which a heater can be placed in the cell. In one design a metal gasket that encloses the sample materials serves as the heater (Moore *et al.*, 1970), while in a more elaborate design a resistance wire that is wound around the diamond anvil seats serves as the heater (e.g. Ming *et al.*, 1983; Bassett, 1985). Alternatively, a heating element can be placed outside of the cylinder containing the diamond anvils, mounting plate, and extended piston

(Weir *et al.*, 1965; Barnett *et al.*, 1973), or the heating element can be placed outside the whole cell body (Asaumi *et al.*, 1980). Recently, new types of diamond anvils have been designed with heating structures consisting of implanted boron. In this case the diamond anvils themselves serve as resistance heaters (Zaitsev *et al.*, 2001). In all these cases the sample is heated uniformly and the heating efficiency is independent of the sample properties (Kikegawa, 1987).

3.4.3 Temperature measurement

Temperature measurement inside an indirectly heated diamond anvil cell is usually done via two thermocouples attached to the diamonds. These are not subject to any pressure-induced error because they are external and therefore not pressurized. The thermocouples are calibrated using the melting points of well-known substances such as S_2, NaCl, $NaNO_3$, CsCl at ambient pressure. However, when DACs are heated directly, the temperature is measured by optical pyrometry. This technique is better suited for very high temperatures (e.g. 3000 K), where the black-body radiation maximum is within the range of the photodiode detectors than for lower temperatures (Besson, 1997).

3.5 Pressure determination

The difficulty of determining the pressure precisely and accurately is a critical limitation for diamond anvil cells. A direct calculation of pressure from measurements of the applied force is not possible, because the distribution of the force over the anvil is unknown and losses due to internal friction cannot be quantified exactly. Several different approaches have been developed in the past. The most important techniques are described in the following sections.

3.5.1 Fluorescence

The ruby fluorescence emission consists of two well-defined, quite intense peaks at wavelengths of 6942Å (R_1 line) and 6927Å (R_2 line). These lines shift to higher wavelengths with increasing pressure. The R_1 shift has been calibrated against standard substances to construct a pressure-scale (e.g. Barnett *et al.*, 1973; Piermarini and Block, 1975). In 1975 Piermarini and Block showed that the shift is linear up to 2.91 GPa. Mao and Bell (1976a and 1976b) extended the ruby scale to 100 GPa. Later Mao *et al.*

(1978) calibrated ruby against copper, molybdenum, lead and silver as standards (Fig. 3.10). They showed that at pressures above 3 GPa the slope of the shift with pressure deviates from linearity (see Fig. 9). Mao *et al.* (1986) proposed that under quasi-hydrostatic pressure P (MPa) is

$$P(MPa) = \frac{A}{B}\left[\left(1 + \frac{\Delta\lambda}{\lambda_0}\right)^B - 1\right]$$

where A = 19.04 MPa; B = 7.665; $\Delta\lambda$ is the ruby R_1 line wavelength shift in Å, and λ_0 is the ruby R_1 line wavelength measured at 1 bar. This scale is widely used at the present time.
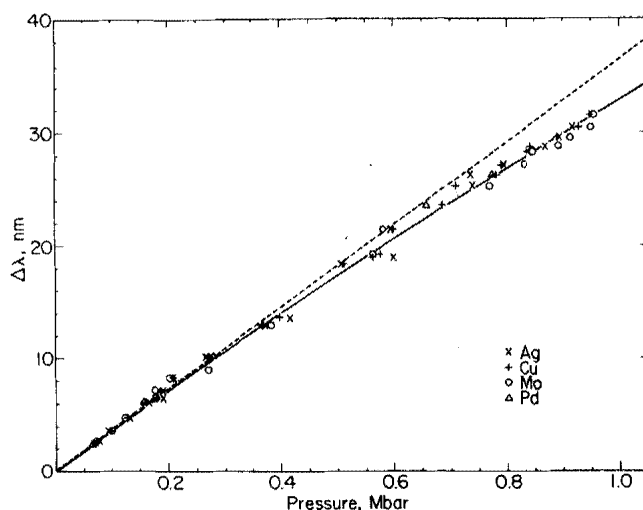
Fig. 3.10: Wavelength shift ($\Delta\lambda$) of the ruby R1 fluorescence line with pressure. The dashed line is a linear extrapolation; the solid line is the least-squares curve fitted to the data points (from Mao *et al.*, 1978).

The critical limitation of this technique is the reduction of the intensity of the ruby fluorescence at high pressures (Xu *et al.*, 1986). At about 100 GPa the intensity of the R_{1+2} lines decreases to such an extent that they become comparable to that of the R'_3 line (see Fig. 3.11) (Mao *et al.*, 1992). In addition, the fluorescence of the diamonds increases between 110-210 GPa and seriously interferes with the ruby fluorescence. However, above 200 GPa this interference from the diamond fluorescence apparently vanishes (Bell *et al.*, 1984; Xu *et al.*, 1986). Another problem arises in the very strong temperature dependence of the ruby fluorescence emission. The signal degrades as the temperature increases (Shen *et al.*, 1992).

16
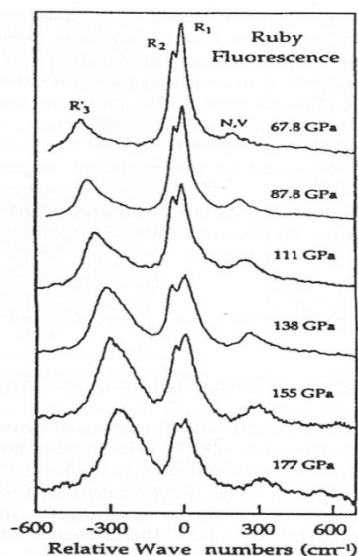
Fig. 3.11: Fluorescence spectra of ruby R lines in hydrogen from 68 to 177 GPa at 298 K (from Mao *et al.*, 1992)

3.5.2 Equations of state of standard materials

Pressure measurements can also be based on a pressure scale derived from a combination of theoretically calculated equations of state (EOS) of various materials, and multiple comparisons with the results from shock-wave methods (Holzapfel and Isaacs, 1997). Au, Ag, Pt, Cu and MgO have been suggested as internal standards (Ming *et al.*, 1983; Heinz and Jeanloz, 1984a; Jayaraman, 1986). One of these materials is placed in the cell together with the sample. Its lattice parameter is determined from its x-ray diffraction pattern, and with this information its unit cell volume can be calculated. The pressure is then determined using the EOS of this material from shock wave data (Jayaraman, 1986). Kikegawa (1987) effectively used NaCl as internal standard and Decker's EOS (Decker, 1971) for a pressure range of 0-30 GPa and 0-800 °C. However, for high-pressure, high-temperature calibrations shock wave data are again the basis for generating high-temperature EOS for the internal standards. In this connection Au has been suggested as the best internal standard (Jayaraman, 1986).

3.5.3 Equation of state of water

Shen *et al.* (1992) demonstrated a technique for determining pressure using the EOS of H_2O, which has been thoroughly studied. There are several versions available throughout the literature in geology, chemistry, and chemical engineering (e.g. Kerrick

and Jacobs, 1981; Halbach and Chatterjee, 1982; Haar *et al.*, 1984; Brown and Lamb, 1989; Saul and Wagner, 1989; Wagner and Pruß, 2002).

Shen *et al.* (1992) recognized that the EOS of water could be a valuable means of determining pressure if the sample volume can be held constant, temperature can be measured accurately, and phase relations can be observed visually. If the liquid H_2O and its vapor bubble are sealed in a container (e.g. the sample chamber), the P-T relationship in the system is defined by the univariant liquid-vapor coexistence curve (Fig. 3.12).
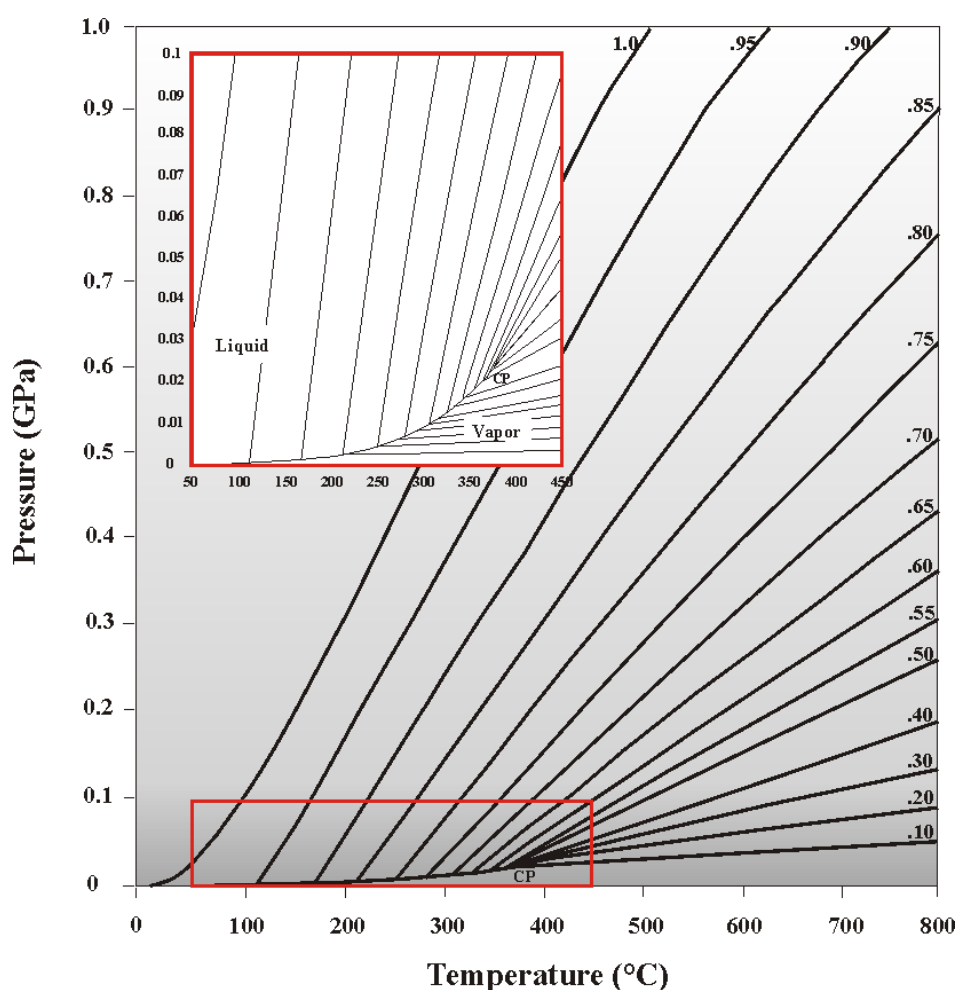
Fig. 3.12: Pressure-temperature plot of the equation of state of H_2O. The isochors are labeled as densities in g/cm^3. The two-phase liquid-vapor coexistence curve emanates from the critical point (CP) towards lower temperatures. The rectangle in the lower left corner is shown enhanced in the upper left corner. (modified after Shen *et al.*, 1992).

When heating the sample chamber, the bubble becomes smaller due to the thermal expansion of the liquid. However, the P-T relationship of the system is still fixed along the univariant curve. At a particular temperature, the bubble disappears

when the system becomes homogenized. This temperature is called the homogenization temperature (T_H) and determines the bulk density of the water in the chamber (Bassett, 2003). If the volume inside the chamber is constant, then the system behaves as an isochoric system, and the pressure-temperature dependence is still univariant, as it is constrained to one of the density isochores. By measuring T_H, the isochore the system will follow can be determined. Therefore the pressure can be calculated at any temperature from the equation of state of water with density and temperature as known variables (Shen *et al.*, 1992).

3.5.4 Phase transformations

Another possibility to determine the pressure inside a HDAC is to use the occurrence of phase transformations. If the univariant phase transformation curve is accurately known, pressure can be calculated at any temperature. Burchard *et al.* (2003) were able to study the reversible phase transition of wollastonite I to wollastonite II (Fig. 3.13B), and of quartz to coesite (Fig. 3.13A), and determined the pressure from measured temperatures
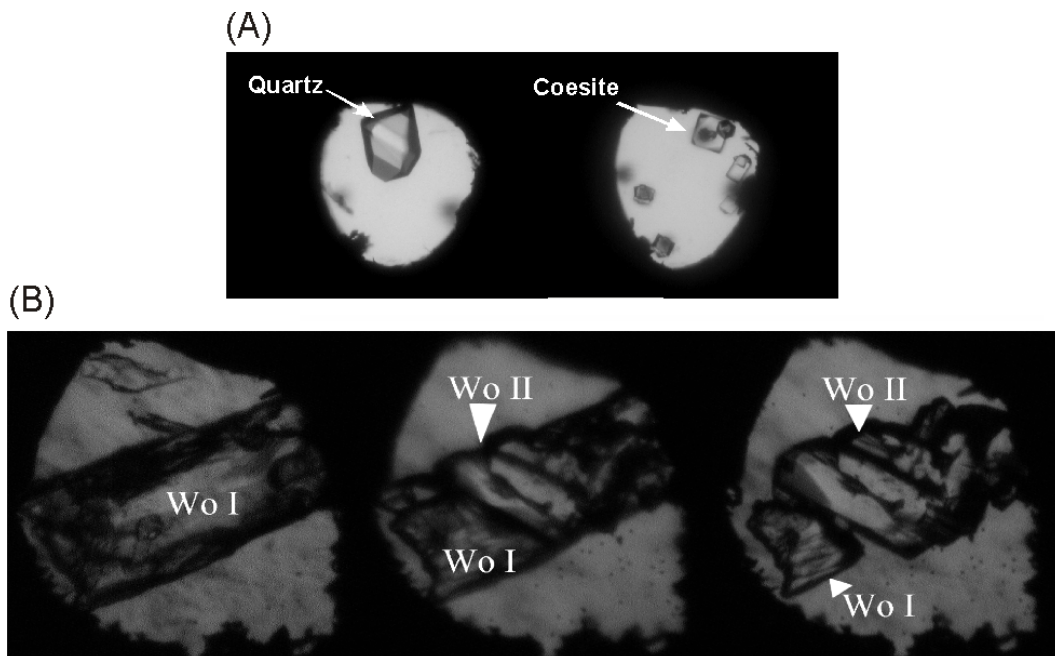
Fig. 3.13: **(A)** Phase transition of quartz to coesite at 2.9 GPa and 700°C; **(B)** Phase transition of wollastonite I to wollastonite II at 3.5 GPa and 700°C (modified after Burchard, personal communication, 2007).

19

For H_2O densities >1.0 g/cm^3 Haselton *et al.* (1995) established a technique for determining pressure using the identification of ice polymorphs. They recognized that the univariant solid-liquid phase transition in H_2O provides an excellent means of determining the densities of an isochor (Fig. 3.14A). By inducing pressures of about 1 GPa at room temperature onto the sample chamber, the ice polymorph VI can be produced (Fig. 3.14B). The melting temperature (T_M) of ice then determines the density of water in the sample chamber, and again the pressure can be calculated at any temperature from the EOS.
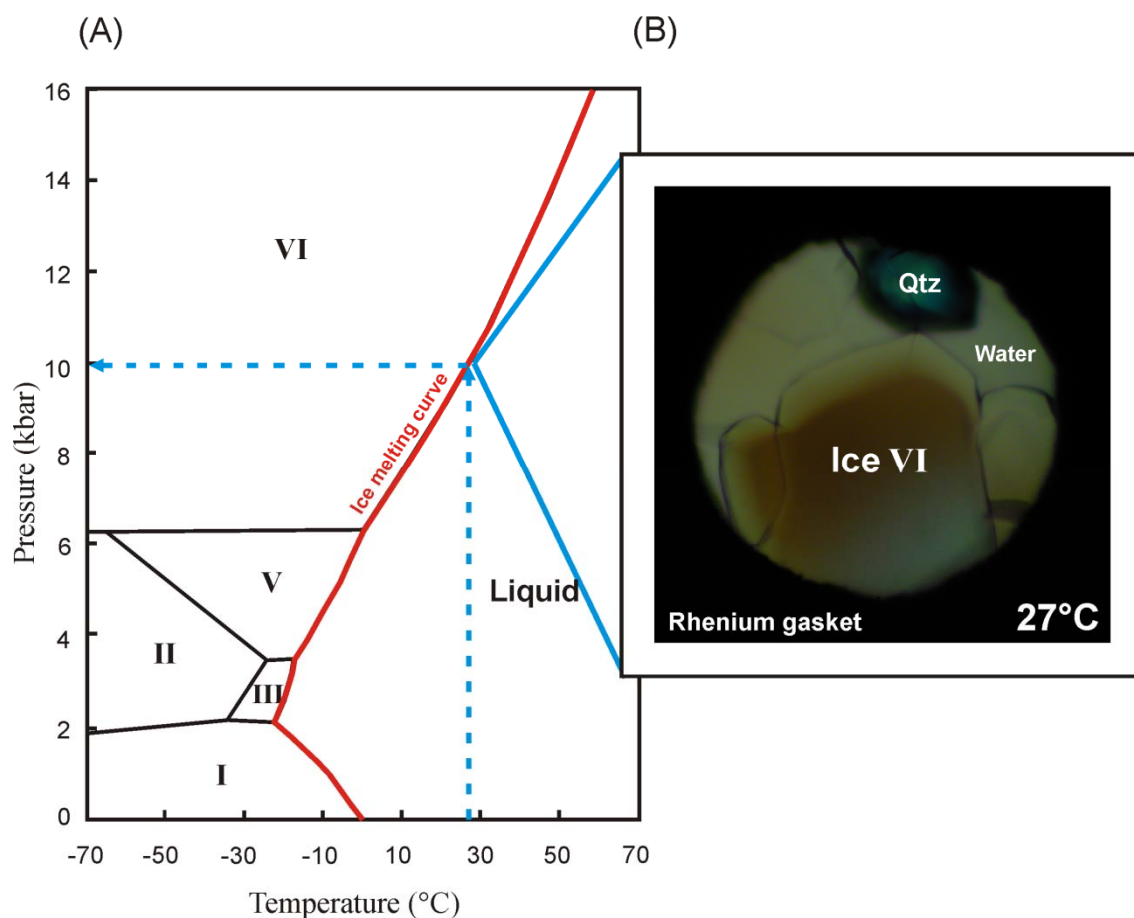
Fig. 3.14: **(A)** Pressure-temperature phase diagram for H_2O (modified after Haselton *et al.*, 1995). **(B)** Ice VI polymorphs of an experimental quartz run with crossed polarizers. Pressure: 1GPa, Temperature 27°C, as indicated by the blue arrows in (A). The diameter of the sample chamber is 300 μm.

3.5.5 i-Anvils

Recently, it has been proposed that pressure measurements in DACs can also be performed employing the anvils themselves, by imbedding pressure sensors into the anvils as electronic structures (Bureau *et al.*, 2006). These structures are implanted into the diamond lattice below the diamond surface by high-energy implantation of boron

(Zaitsev *et al.*, 2001). The implanted sensors are ideally located in the diamond culet a few μm below the sample chamber, being chemically isolated from the sample (Bureau *et al.*, 2006). This new generation of anvils is called "intelligent anvils" (i-Anvils) (Kubsky *et al.*, 2005). These i-Anvils are still in development. First test runs indicated that pressure measurements express the stress on the anvil surface (Simon *et al.*, 2009, in prep.).

3.5.6 Raman spectroscopy

Pressure determinations using the EOS of H_2O are based upon a system with a constant volume chamber and behavior as an isochoric system. This method fails as soon as this condition is no longer met. Figure 3.15A shows a sample chamber at the beginning of an experimental run. The sample chamber dimensions are well defined. Figure 3.15B shows the same sample chamber at 450°C. It did not remain constant and pressure can not be calculated from the EOS of H_2O.
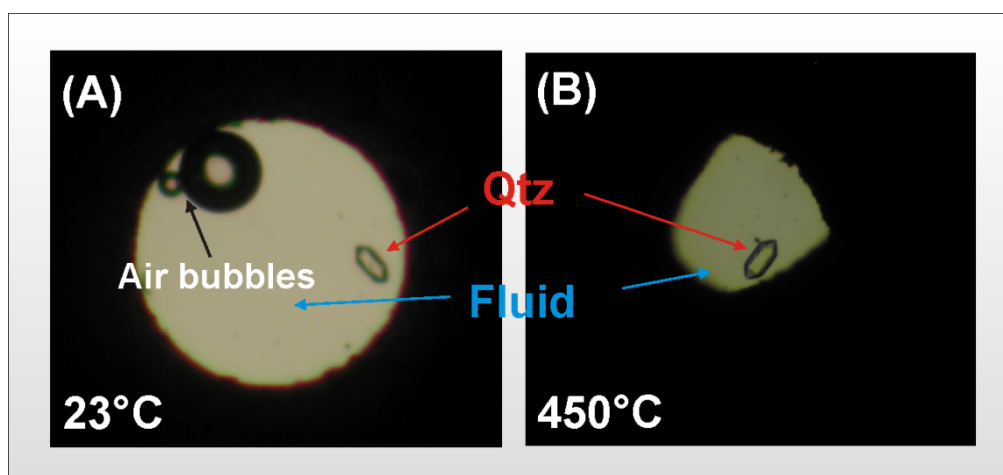
Fig. 3.15: Sample chamber of a HDAC run with a quartz crystal as sample. **(A)** Sample chamber at 23°C with air bubbles, fluid and the quartz sample; **(B)** same sample chamber at 450°C with fluid and quartz sample. The volume of the sample chamber obviously did not remain constant.

A possibility to overcome this critical requirement is micro-Raman spectroscopy. Schiferl *et al.* (1997) developed Raman spectroscopy of ^{13}C diamond as a new method for measuring pressure at high temperatures in diamond anvil cells. Schmidt and Ziemann (2000) determined the frequency shifts of the 464 cm^{-1} Raman line of quartz as a function of pressure. Figure 3.16 shows this frequency shift versus

pressure and temperature as measured during the present study at the GeoForschungsZentrum (GFZ) in Potsdam.

Raman spectroscopy is based on electromagnetic radiation (e.g. photons) that excites molecules. The energy can be transmitted, absorbed, or scattered. Most photons are elastically scattered, a process which is called Rayleigh scattering. The emitted photon has the same wavelength as the absorbing photon. Raman spectroscopy is based on the Raman effect, which is the inelastic scattering of photons by molecules. The energies of the scattered photons either increased or decreased relative to the exciting photons which is related to the vibrational energy spacing in the ground electronic state of the molecule. The resulting wavelengths are longer (called Stokes lines) or shorter (called anti-Stokes lines). Therefore the wave-number of the Stokes and anti-Stokes lines are a direct measurement of the vibrational energies of the molecule (Colthup *et al.*, 1964).
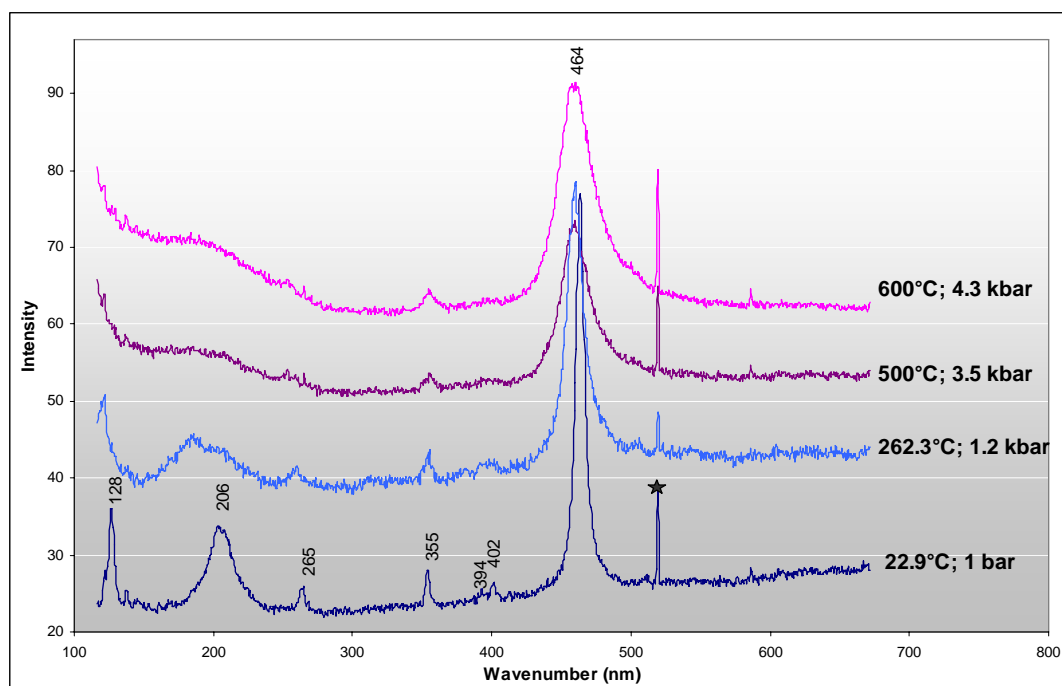
Fig. 3.16: Frequency shift of the 464 cm^{-1} Raman line of quartz with pressure and temperature measured in the present study at the GFZ in Potsdam. The star indicates the reference plasma line of the laser. Pressures are calculated after Schmidt and Ziemann (2000).

A 514.53 nm Argon laser was used; the excitation line was 251 mW at the source and about 4.5 mW at the sample in the HDAC. Therefore, heating of the quartz sample from the laser was insignificant. The CCD spectrum covered a wave number range between 115 and 672 cm^{-1} at the spectrometer position of 400 cm^{-1}. Collection times for Raman spectra were 10 accumulations of 20 s each.

3.6 Limitations imposed by the properties of diamond anvils

Diamond anvils owe their usefulness to the extreme hardness (10 on the Mohs scale), optical transparency, chemical inertness (Seal, 1987) and excellent thermal conductivity (at 25°C ca 1 $Wcm^{-1}°C^{-1}$) of this extraordinary material (Seal, 1990). The great strength of diamond allows very high static pressures to be created and sustained. Diamond is transparent from ultraviolet to radio frequencies (apart from a region of two-phonon absorption near 2000 cm^{-1}), and thus it is compatible with many kinds of optical and spectroscopic work. Its low atomic number similarly makes diamond suitable for x-ray studies of materials at high pressures (Adams and Shaw, 1982).

However, diamond is crystalline and therefore has anisotropic mechanical properties. It can also "burn" or transform to softer forms outside of its P-T stability field. These factors set the main limits to the range of conditions attainable in the DACs. In addition diamond anvils seem to fail in a variety of ways such as under shear beneath the culets (Seal, 1987). The effects of stress in diamond, particularly in relation to modes of failure, have also been intensively investigated (e.g. Adams and Shaw, 1982). Hence the ultimate strength of diamonds at very high pressures has become a major design consideration. Based on the results of Adams and Shaw (1982), the design called "Drukker standard" (Fig. 3.17) is believed to perform most satisfactorily.
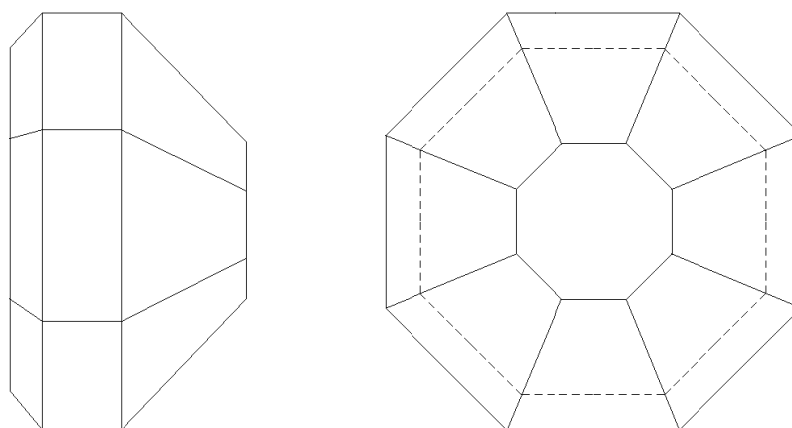
Fig. 3.17: Optimum shape of diamond anvil: Drukker standard design (modified from Seal, 1987)

Results of finite-element stress analyses of diamond anvils (Moss *et al.*, 1986) have also made it possible to optimize designs. Bevels that are ground on diamond anvils are designed to avoid sharp stress gradients at high pressures.

The effect of chemical impurities on the performance of the diamond material has been reviewed by Seal (1990). The main impurity in natural diamond is nitrogen. Two types of diamonds are classified: type I contain significantly more nitrogen then type II diamonds. As a result of this dispersed nitrogen impurity, type I diamond is stronger. Since the type II diamond is purer then type I, it is as transparent as possible throughout the infrared region, but also tends to cleave rather easily and hence does not sustain ultra-high pressure (Yousuf, 1998). The two types I and II are further subdivided into A and B according to their nitrogen concentration and the form in which nitrogen occurs within the diamond (Seal, 1987).

The diamond anvils used in this study are of the Drukker design with beveled culets. The anvils are a set of two type IA, 8-sided, gem-quality diamonds with the following design parameters (Fig. 3.18): C=1.0 mm; H=2.0 mm; X=3.6 mm; BC=15° and B=1.24 mm with C=culet diameter; H=height; X=girdle diameter; BC=bevel angle; *b*=bevel diameter
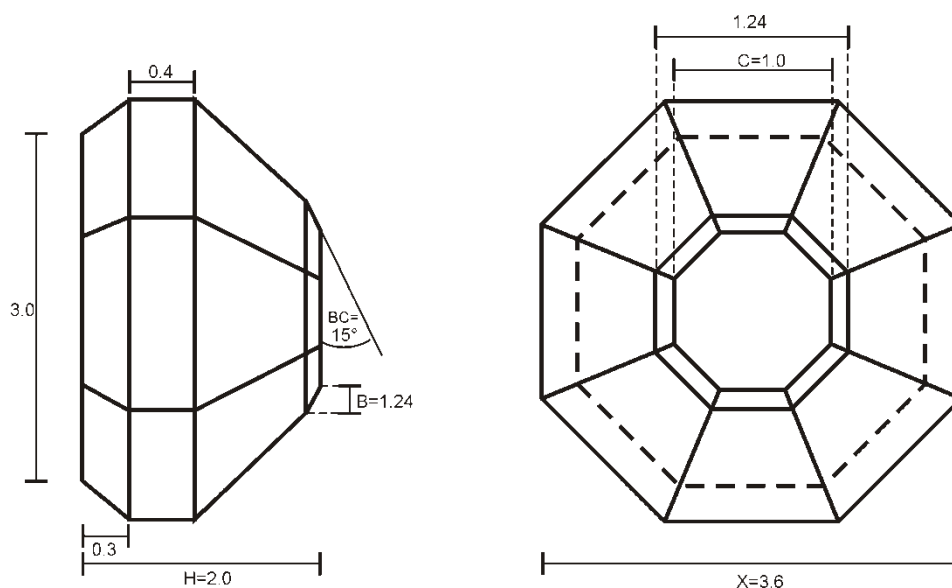
Fig. 3.18: Diamond anvil design used in this study. All specifications stated in mm.

3.7 Required specifications for gaskets

In earlier studies, experiments with the DAC were limited to solids which were squeezed between the anvils to apply the pressure. Large pressure gradients within the sample were the consequence. Van Valkenburg (1962) introduced a metal gasket to encapsulate liquids and other materials under pressure between the diamond anvils. Functionally, the gasket reduces the magnitude of pressure gradients and confines the

sample, pressure standard and pressure-transmitting medium such as fluids like water or methanol-ethanol solutions. Through the opposing force of the diamond anvils the gasket lying between them is deformed ductile and elastic in such a way that the central sample chamber is reduced in its size (Fig. 3.19). Hence the volume is reduced and coincidentally the fluid is compressed leading to an increase of the hydrostatic pressure (Miletich, 1998). Therefore using a gasket ensures hydrostatic pressure as long as the fluid does not solidify in the pressure range considered (Piermarini *et al.*, 1973). Beyond these functions, the gasket provides an additional support to the diamond anvils, thereby enhancing their pressure-sustaining capability (Yousuf, 1998).
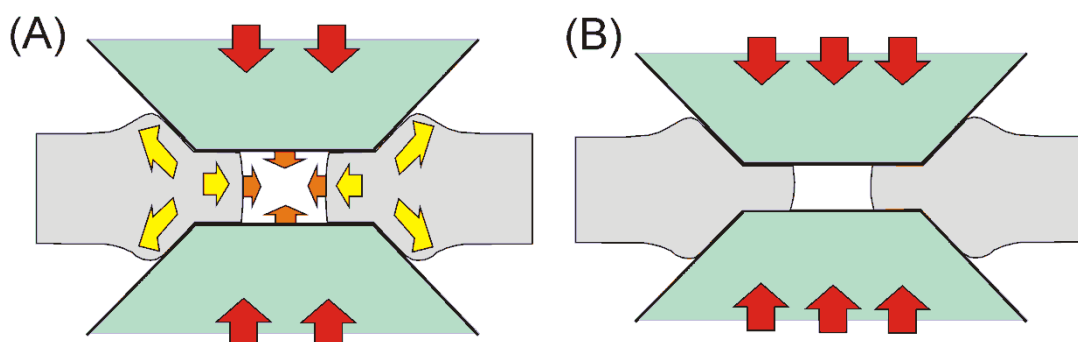
Fig. 3.19: (A) Schematic description of deformation within the gasket material **(B)** accompanied with volume reduction of the sample chamber (modified from Miletich, 1998).

For high-pressure and high-temperature experiments, rhenium or iridium is used as gasket material. These are inert and do not react with the sample. The optimum thickness of a gasket depends on the culet size, gasket hole diameter, the maximum intended pressure and the type of the sample to be investigated. Usually the gasket is pre-indented to harden the material and to minimize and reduce cracks and micro-fractures within the gasket material.

4 Optimization and reconstruction of experimental equipment

The available technical and experimental equipment for this study had to be modified, optimized and reconstructed to attain routine and good quality experimental runs. The following sections summarize the critical requirements demanded of the components of the HDAC, as well as the technical solutions and structural modifications that have been realized in the course of this study.

4.1 Critical appraisal of available HDACs for the present study

The Bassett Cell is the most popular HDAC design presently in use (see section 3.3.1) because of the relatively simple handling involved. However, a number of critical aspects in its constructional design make this cell type unsuitable for the purpose of this study.

Thermal expansion within the cell due to heating can become a problem during experimental runs. The resulting progressively higher pressures exerted by the diamond anvils on the gasket material lead to compression and flattening of the gasket. Burchard *et al.* (2003) measured local pressures of up to 10 GPa with increasing temperature. Hence the diameter of the sample chamber decreases and the assumption of constant sample volume during the experimental run becomes invalid. Constant sample volume is necessary if pressure is to be calculated with the EOS of water. During heating the whole cell body becomes very hot, reaching several 100°C (Schmidt, personal communication, 2008). As a result the objective of the microscope, which is located above the HDAC, also becomes very hot, and the image from inside the cell runs out of the focus constantly (Schmidt, personal communication, 2008). Constant focus is important for the later development of the *in situ* mass-loss approaches that are the goal of this study. In addition, the lenses of the objective are also subject to cracking due to the heat development of the cell body.

Another problem that can arise with this type of cell is the critical misalignment of the diamond anvils. The three pressurizing screws are tightened independently, and exact parallel alignment of the anvils with respect to each other is difficult to achieve. The lack of parallel alignment of the culets leads to the initiation of shear forces between the gaskets and the anvils. Lateral movement of the gasket will be induced.

26

The Burchard-Zaitsev HDAC provides some technical solutions for ensuring proper alignment of the diamond anvils on the one hand and for minimizing internal build-up of pressure due to differential thermal expansion on the other. Mechanical compensation for absolute and differential thermal expansion within the cell upon heating is provided by two stiff Belleville springs directly supporting both anvil seats (see section 3.3.2, Fig. 3.9). A cooling structure is also provided to minimize thermal expansion and other resulting mechanical problems due to heating. A water flow as low as 10 liters/h is sufficient to maintain the cell body at room temperature (Burchard *et al.*, 2003). Therefore the optical image from inside of the HDAC remains in focus at all times, and the danger of cracking the microscope objective is minimized. Finally, the nut-and-worm drive of the Burchard-Zaitsev Cell (Fig. 3.9, section 3.3.2) provides a mean of pressurizing the sample volume and the gasket homogeneously with the diamond culets remaining absolutely parallel.

For the above reasons, and also because this cell type was available at the Ruhr-University of Bochum, the Burchard-Zaitsev Cell provided a good alternative HDAC device that is used in this study. Unfortunately, the intensive use of the Burchard-Zaisev HDAC in the present study showed that it was not yet well-engineered and tested for routine experimental usage. In this study critical constructional problems were found and routine experimentation was not possible without further changes in design and construction. In conjunction with the faulty machining of the available cell, it was found necessary to redesign and reconstruct most parts of the HDAC entirely. In certain cases it was necessary to use a classical Bassett-type of HDAC in other laboratories in order to test the approaches developed here, and to obtain experimental data while the Burchard-Zaitsev Cell was being remachined. Visits to mineralogical departments in Germany and France were necessary.

4.2 Redesigning and reconstruction the Burchard-Zaitsev Cell

4.2.1 Operation and design of the original Burchard-Zaitsev Cell

4.2.1.1 General assembly

The original Burchard-Zaitsev Cell was designed for even pressure distribution and especially for the use of i-Anvils (see section 3.3.2). The i-Anvils are placed inside the heating devices, attached to the electrical connections, and the culet faces are

27

carefully cleaned. Then the cell is manually closed by slowly lowering the upper anvil down onto the lower anvil. Care has to be taken that the two opposing anvils do not touch, otherwise they might damage each other. As soon as the anvils are close enough, they are positioned and aligned with respect to X-Y position and parallelism of the culet faces, in order to avoid a non uniform deformation between the anvil culets. After the alignment procedure the cell is re-opened, and a pre-indented gasket is placed on the top and in the middle of the lower i-Anvil. The hole inside the gasket serves as the sample chamber. It is then loaded with the pressurizing material and the sample to be investigated. The cell is now manually closed quickly until the anvils touch the gasket very tightly. Now the worm gear is applied to the cell body. By turning the gear, the pressurizing nut screws both platens together and thus force is induced onto the i-Anvils. Further details of the operating systems are given below as they appear within the original Burchard-Zaitsev Cell.

4.2.1.2 The original systems

4.2.1.2.1 Heating system

The heating system within the Burchard-Zaitsev Cell is designed for i-Anvil use. The diamond anvils are implanted with boron to produce internal resistance heaters directly in the anvils next to the sample volume (Burchard *et al.*, 2001). Figure 4.1 shows such a diamond anvil with implanted heating structures that was produced during this study.
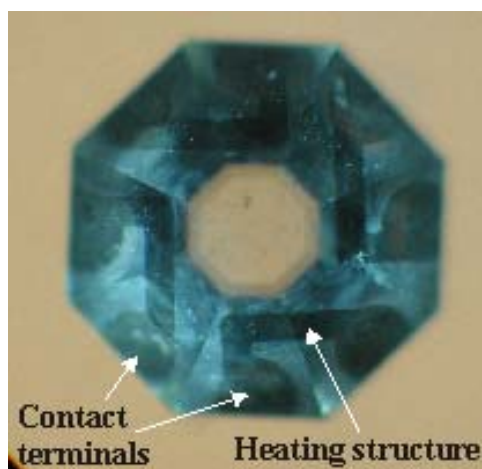
Fig. 4.1: Diamond anvil with four boron-implanted heating devices and contact terminals.

The diamond anvils are seated in holders (Fig. 4.2). These holders provide robust electrical connections, an indispensable feature for the reliable electronic operation of such anvils (Burchard *et al.*, 2003). They consist of disk-shaped hardened steel holders (c) with eight radially disposed openings (Fig. 4.2). Tungsten-carbide rod electrodes with beveled and polished ends (b) are inserted into these openings. Steel wire springs (d) are used to force the electrodes towards the centre of the hardened steel plate, where the i-Anvil (a) is positioned. The hardened steel plate itself is mounted on the adjustable seat (g) also made of hardened steel. The working surface of the backing plate (e) holding the anvil is covered with mica sheets (f) (for more details see Burchard *et al.*, 2003).
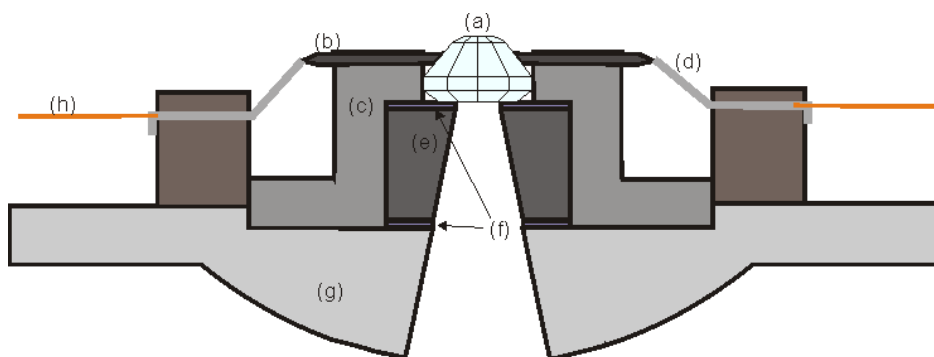
Fig. 4.2: Schematic diagram of the heating system for i-Anvil use within the Burchard-Zaitsev Cell. (a) diamond anvil; (b) tungsten-carbide rod electrodes; (c) disk-shaped hardened steel holder; (d) steel wire springs; (e) backing plate; (f) mica sheet; (g) adjustable seat; (h) electric connecting wires.

Burchard *et al.* (2003) reported that temperatures of 1200°C can be reached with this device.

4.2.1.2.2 Gasket

The gasket material used is generally rhenium for high temperatures and high pressures. For low-pressure and low-temperature experiments, hardened steel or stainless steel is used as gasket material. The hole in the middle of the gasket that serves as the actual sample chamber is drilled or spark eroded into the gasket.

4.2.1.2.3 Adjustment system

In order to achieve a proper function of the HDAC it is necessary to position and align the diamonds with respect to (a) X-Y position and (b) parallelism of the culet

faces, in order to avoid non-uniform deformation between the diamond anvil culets. The lack of parallel alignment of the culets leads to the initiation of shear forces between the gasket and the diamond anvil, as well as in the gasket itself. Lateral movement of the gasket will be induced, and loss of the fluid and possibly the sample will result (Burchard *et al.*, 2003). However, misalignment or rough treatment can also easily result in damage to the diamonds.

Alignment is be achieved by loosen and/or tighten six adjusting screws constraining the two adjustable seats, three screws on every seat (Fig. 4.3). The upper seat (Fig. 4.3A) is designed with a flat bottom to allow in-plane tuning (axial or X-Y positioning). The lower seat (Fig. 4.3B) is provided with a spherical bottom to allow rocking movements (parallel alignment).
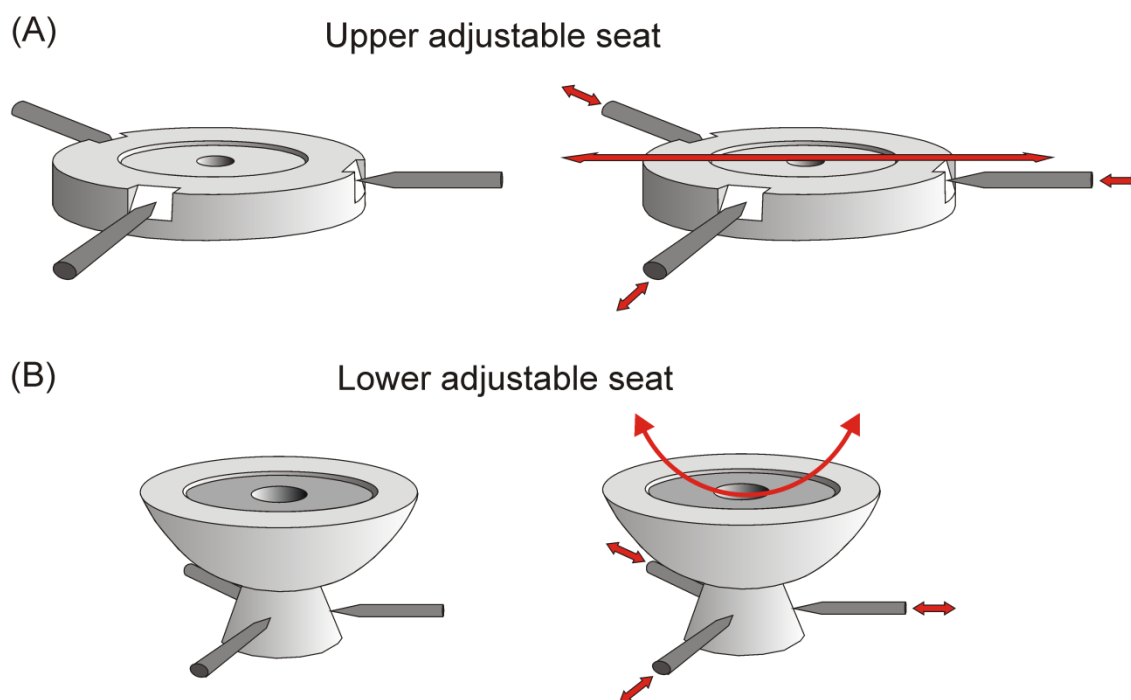
Fig. 4.3: (A) Upper adjustable seat with its adjusting screws. The seat is designed to allow in-plane tuning. **(B)** Lower adjustable seat with its screws. It is designed with a spherical bottom to allow rocking movements.

The first adjustment is axial and undertaken by turning (*e.g.* backing out (loosening) and/or advancing (tightening)) the adjustable screws on the upper seat. The upper anvil axis is then positioned directly onto the lower anvil axis. This is carried out

with direct observation of the culet faces by illumination through the diamond anvils under a binocular (Fig. 4.4).
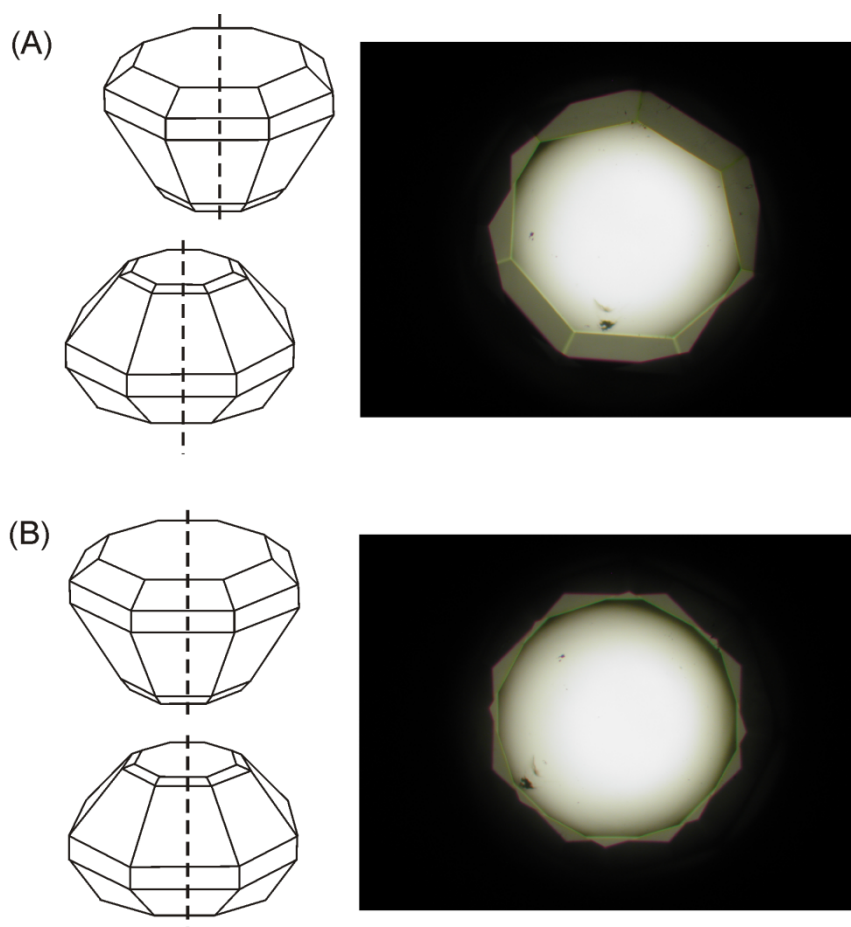
Fig. 4.4: **(A)** Axial misalignment of the two diamond anvils in a 3-dimensional view, and observed misalignment under a binocular. **(B)** Axial aligned diamond anvils in a 3-dimensional view and observed alignment under a binocular.

Final alignment for parallelism is then carried out by turning (*e.g.* backing out (loosening) and/or advancing (tightening)) the adjustable screws on the lower seat. The lower anvil culet has to be brought into absolute parallelism with the upper anvil culet. By using optical interference fringes in transmitted white light (Newton's rings), this alignment can be directly controlled (Fig. 4.5). With no sample between the anvils and with the upper anvil gently touching the lower one, the interference fringes appear (Fig. 4.5A). By backing out some screws and advancing others, the contact of the two anvils is spread over the entire anvil area. One fringe or one color will then cover the entire anvil area (Fig. 4.5B). Subsequently the three set screws are gently tightend to hold the lower rocker in place.
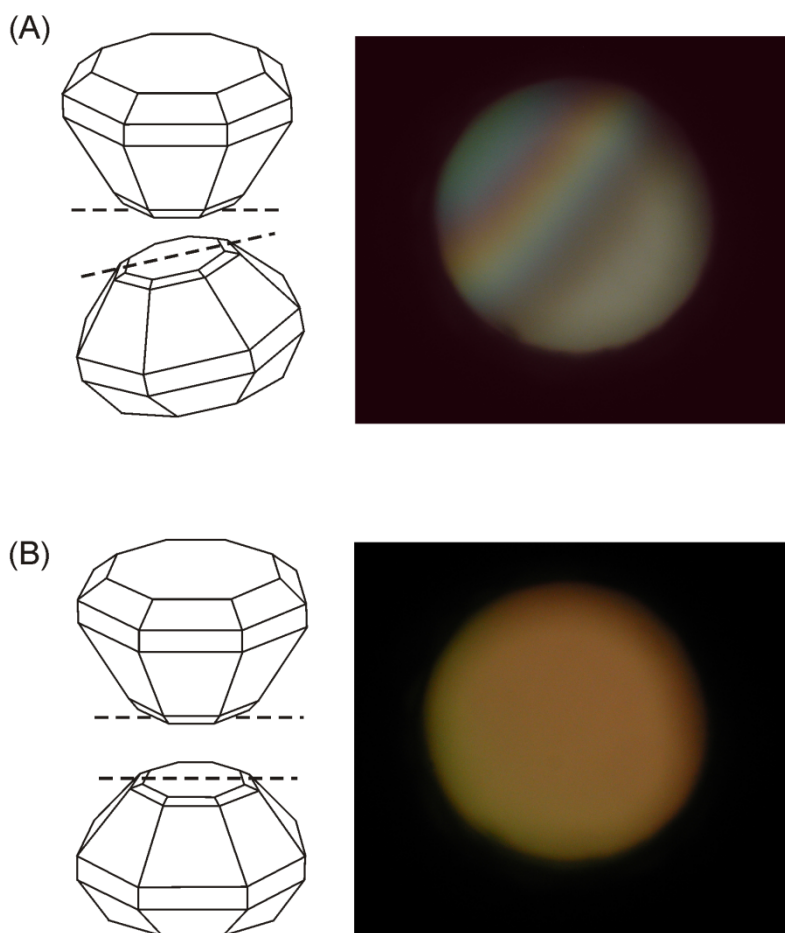
Fig. 4.5: (A) Non-parallelism of the culets with respect to each other in a 3-Dimensional view, and observed interference fringes due to misalignment under a binocular; **(B)** parallel alignment of the culets in a 3-Dimensional view and observed parallel alignment (just one interference fringe) under a binocular.

4.2.1.2.4 Guiding system

To ensure accurate alignment of the platen movement towards each other, the upper platen is guided by one polished pin (Fig. 3.9(y), section 3.3.2).

4.2.1.2.5 Pressurizing mechanism

After the usual adjustment and loading of the sample volume, the cell is pressurized by screwing the nut and lower platen together with the help of a worm gear (Fig. 3.9 (g, f, h), section 3.3.2). A ball-bearing between the nut and the upper platen of the hollow cell body decouples both elements from each other and enables rotation of the nut even under high load, ensuring precisely uniaxial pressures and avoiding inhomogeneous gasket flow. The polished pin that guides the upper platen is also supposed to prevent any possible rotation of the upper platen imposed by friction in the

ball-bearing. A buffering mechanism (Fig. 4.6) provided by two stiff Belleville springs, which directly support both anvil seats and compensate for thermal expansion of the anvil–sample–anvil assembly at the core of the cell, avoids rapid build-up of effective pressure on the gaskets at high temperatures (Burchard *et al.*, 2003).
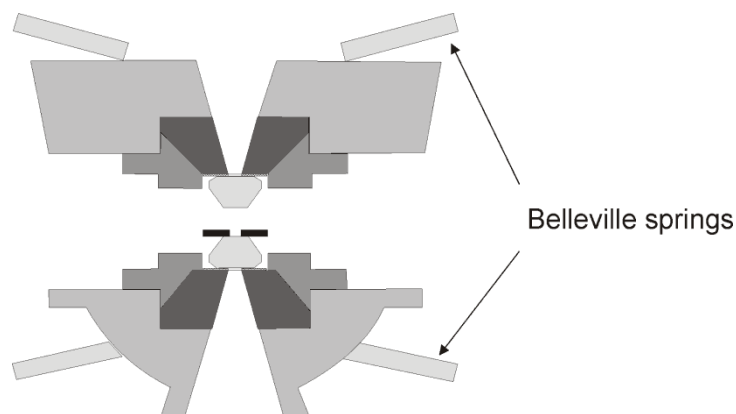
Fig. 4.6: Schematic sketch of the inner part of a Burchard-Zaitsev HDAC.

4.2.2 Inadequacies of the Burchard-Zaitsev Cell for the present study

In the course of this study it became clear that significant systems of the construction of the Burchard-Zaitsev Cell are not adequate for the routine experimental use required here. These are the adjustment system, the guiding system and the pressurizing system. These systems have several constructional problems themselves, six all together. The heating system will be described in a later chapter since it is strictly speaking not a constructional aspect of the Burchard-Zaitsev Cell.

The combination of all these constructional problems (see below) leads to the initiation of significant relative movement of the diamond anvils and shearing of the sample chamber even under high pressure. This was first noticed from inspection of the gasket imprints and the axial alignment of the anvils after the experimental runs. Four different types of culet face imprints on the gaskets were identified. These imprints indicated that the anvil culets must have been misaligned and moved with respect to each other during experimental runs even under high pressure.

The first kind of imprint, type I, shows half of the culet faces on the gasket after the experiments which indicate critical misalignment of both anvils during the experiment. Figure 4.7 shows imprinted gaskets type I.

33
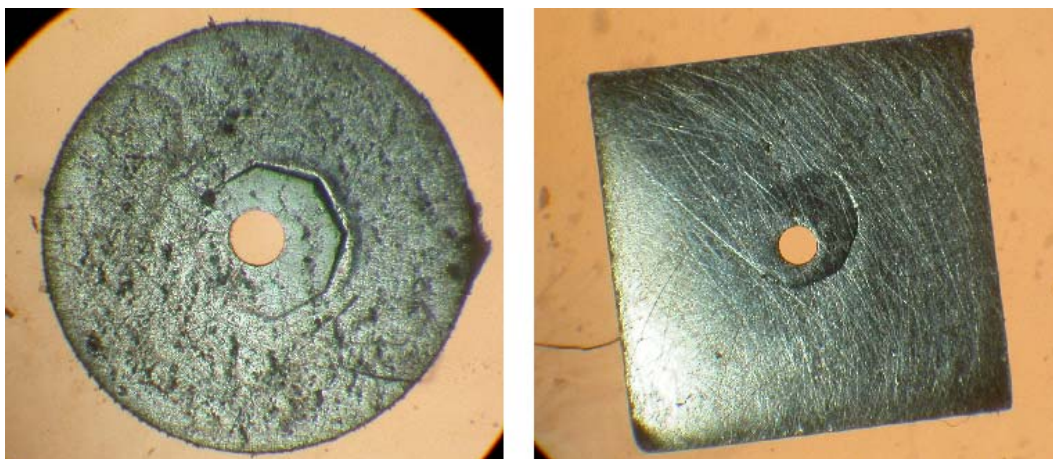
Fig. 4.7: Non-uniform imprints of the culet faces on rhenium gaskets. Only half of the culet face is imprinted.

The second kind of imprint, type II (Fig 4.8A, 4.8B), shows half of the culet face of the lower anvil and an entire culet imprint of the upper anvil with one side imprinted deeper than the other side, indicating misalignment of at least the lower anvil.
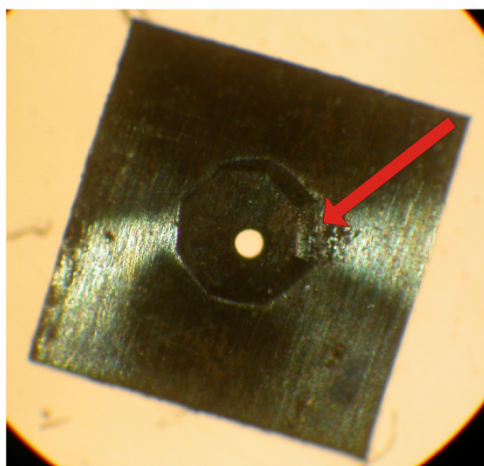
(A) (B)
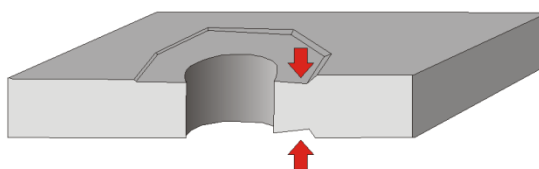
Fig. 4.8: (A) Observed upper imprint on a gasket that is imprinted deeper on one side (indicated through the red arrow). **(B)** Schematic sketch of the cross section of the observed gasket. The deeper imprinted culet faces are indicated through the red arrows. The lower culet face is only imprinted half on the gasket.

Type III of imprint (Fig. 4.9) educes that the culet faces have been parallel to each other during experimental runs but have not been perpendicular to the pressure axis. Figure 4.9 shows a schematic sketch of a cross section of the imprint type III. Slight deformation of the sample chamber can occur within this type of imprint.
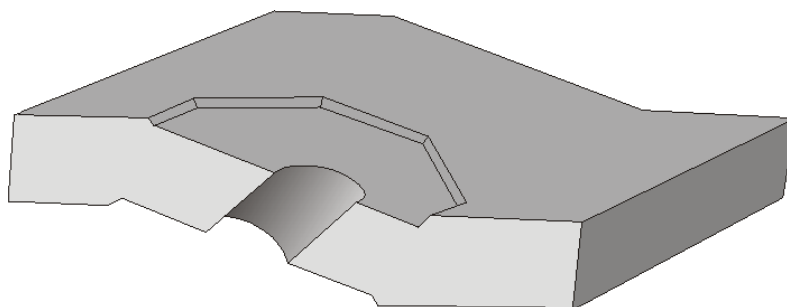
Fig. 4.9: Schematic sketch of the imprint of culet faces on a gasket. The culet faces are parallel to each other but not perpendicular to the pressure axis.

Type IV of imprint onto a gasket, in conjunction with a strongly sheared sample chamber, concludes movement of the anvils with respect to each other even under high pressure. These gaskets (Fig. 4.10 and Fig. 4.11) show imprints of a shifted culet on the gasket during an experimental run. The initial imprint in figure 4.10A can easily be observed and is indicated by the red lines. The final culet imprint is indicated by the yellow lines. The relative movement of the diamond anvil was 0.21 mm which is considerable. Movement structures can be clearly observed on the detailed picture of Fig. 4.10B. The orange arrow indicates the direction of movement.
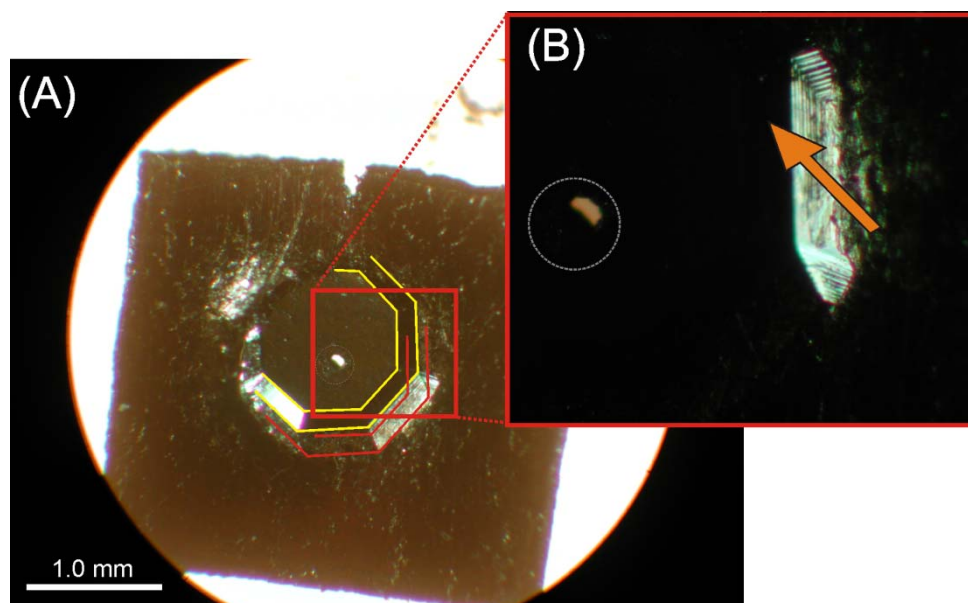
Fig. 4.10: **(A)** Evidence for movement of diamond anvil culets from imprints on a rhenium gasket. The red stripes outline the initial position and the yellow stripes indicate the final position of the anvil culet and bevels during a test run. The diamond anvil moved 0.21 mm. **(B)** The enhanced detail of the gasket shows imprinted structures caused by the movement of the diamond anvils. The orange arrow indicates the direction of movement. Grey dashed circle indicates the original sample chamber dimensions.
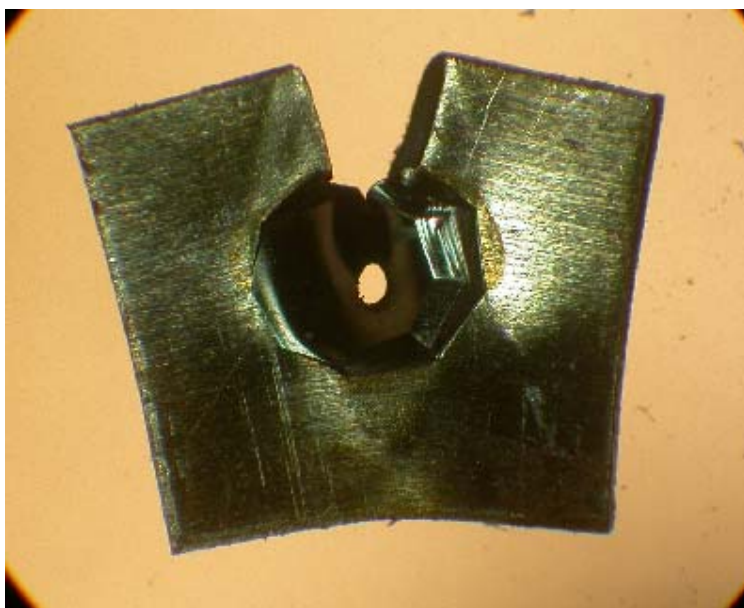
Fig. 4.11: Movement signs of imprinted diamond anvil culets on a rhenium gasket. Because of the movement the gasket was ruptured on the upper half.

Movement on the gasket (Figs. 4.10, 4.11) may also result in rupture of the gasket and in shearing of the sample chamber in the middle of the gasket (see Fig. 4.10; the original sample chamber dimensions are indicated by the dashed grey circle) observed by several gaskets.

The axial alignment of the anvils controlled before and after the experiments approves the assumption that the diamond anvils move with respect to each other even under high pressure. Figure 4.12 shows the axial alignment of the diamond anvils before and after a test run. It can be clearly noticed that the anvils after the experiments are not aligned any more. At least one anvil must have moved during the run.
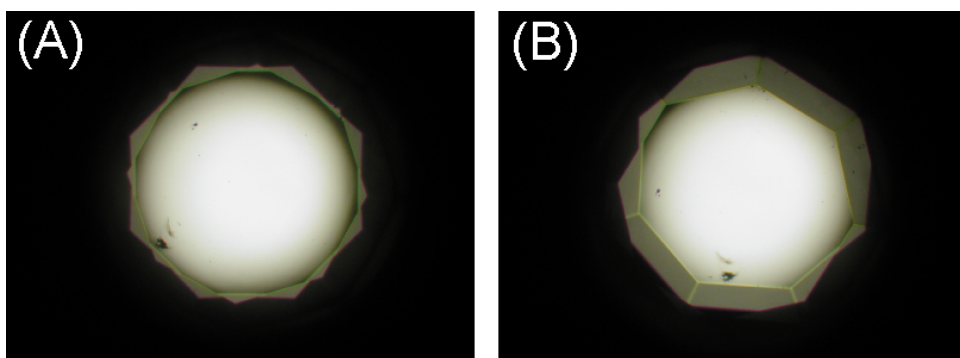
Fig. 4.12: Axial movement of the diamond anvils in relation to each other made obvious by comparison of the alignment before (**A**) and after an experimental run (**B**).

A consequence of the movements and misalignments of the anvils can be rupturing of the gasket or deformation of the sample chamber (as in Fig. 4.10, 4.11). Loss of fluid and possible the sample itself are the result. The ultimate consequence can be the cracking of the diamond anvils. Neither case is an acceptable option and certainly not useful for routine experimental runs.

In the following sections the correlations of the observed gasket imprints with the constructional problems of each system of the Burchard-Zaitsev Cell are outlined in detail.

4.2.3 Reconstructed and optimized systems

4.2.3.1 Gasket

The gasket is strictly speaking not a constructional part of the Buchard-Zaitsev cell but it also poses some requirements that need to be considered.

4.2.3.1.1 Critical requirements

Mechanical failure during experiments can be induced by defects in the gasket material itself or by propagation of scratches and grooves from the gasket surface. This results in the loss of the pressurizing fluid. Overpressure induced by the expansion of the fluid in the sample volume with increasing temperature can induce abrupt mechanical failure of the gasket material (Fig. 4.13). Alternatively, the anvil may be separated from the gasket, leading to leakage (Burchard *et al.*, 2003). In either case, loss of the contents of the sample volume will usually result, and the experiment will fail.
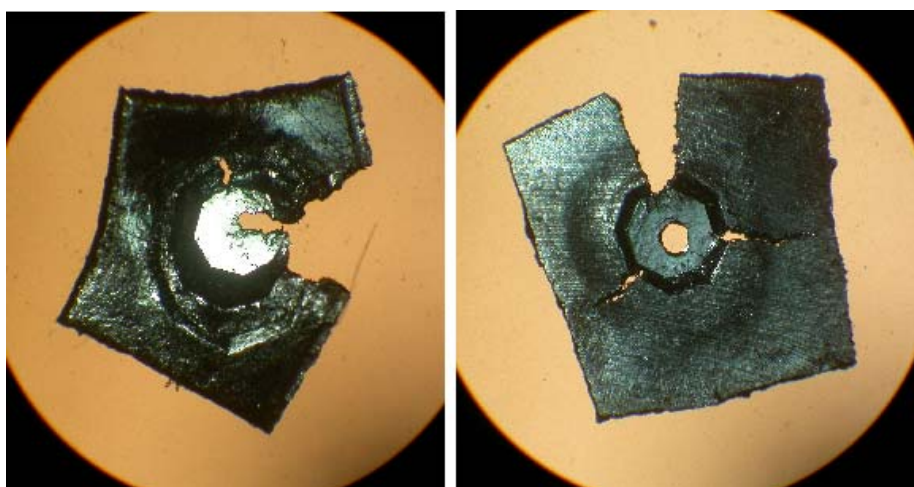
Fig. 4.13: Mechanical failure of the gasket material caused by overpressure induced by the expansion of the fluid in the sample chamber and by overpressure applied to the gasket.

The flow strength of the gasket may be exceeded by the build-up of pressure between the anvils and compression and flattening of the gasket will result. As the inner diameter of the experimental sample volume of the gasket decreases, the assumption of constant sample volume during the run becomes invalid. The flow strength of the gaskets depends on the thickness, material properties, and sample volume dimension (Burchard *et al.*, 2003).

For low-pressure and low-temperature experiments, hardened steel or stainless steel is generally used as gasket material. It is easy to machine and inexpensive. However, the iron from the steel may react with the sample. Figure 4.14 shows a reaction of the steel gasket with a SiO_2 sample. The reaction started at about 290°C and 1.2 kbar.
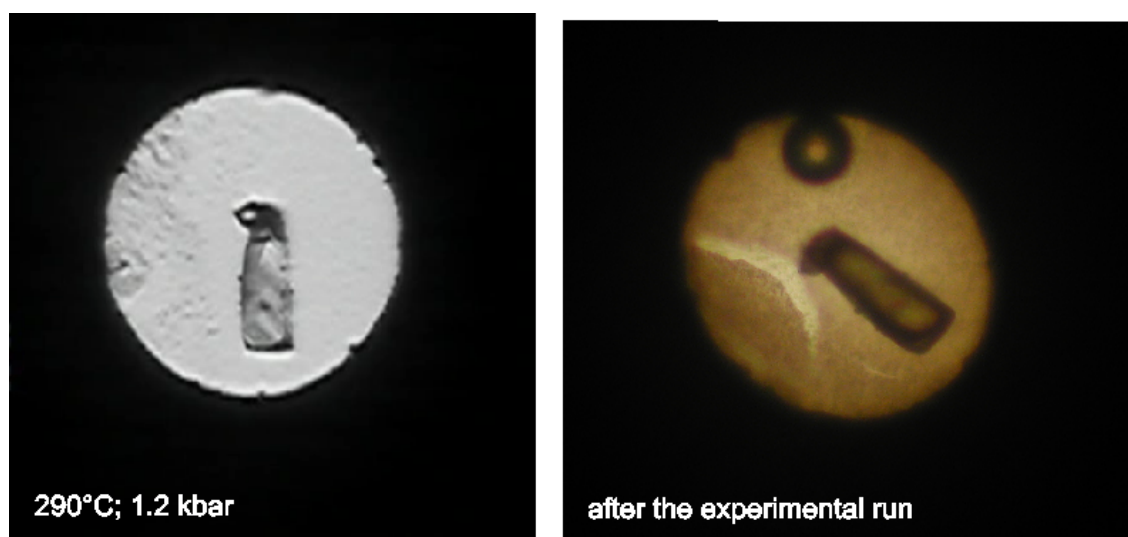
Fig. 4.14: (A) Quartz sample within a steel gasket at 290°C and 1.2 kbar, where SiO_2 began to react with the iron from the gasket (black and white image). (B) Observed sample chamber after the experimental run, true colors. A layer of reddish-brown products from the reaction of SiO_2 with the steel gasket has precipitated on both anvils. The gasket diameter in both images is 400μm.

The experimental run was terminated at 362°C and 2.4 kbar. Scanning electron microprobe analyses revealed crusts of an iron-bearing silicate (Fig. 4.15) that grew both on the diamond anvils and the quartz crystal.

Analysis 1		
Element	Mass%	Atom%
O K	40.94	63.48
Si K	23.45	20.71
Fe K	35.61	15.82
Sum	100.00	

Analysis 2		
Element	Mass%	Atom%
O K	41.94	64.93
Si K	21.28	18.77
Fe K	36.78	16.31
Sum	100.00	
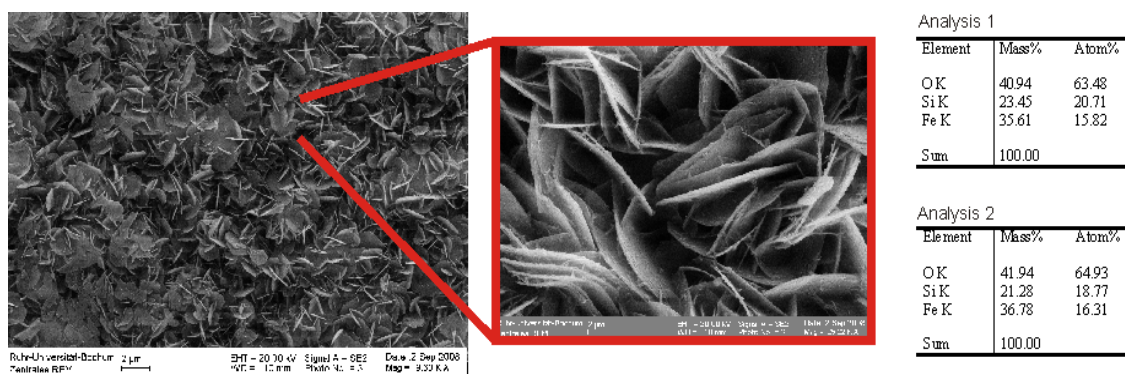
Fig. 4.15: SEM image and enlarged SEM image of the iron silicate crust which grew on the diamond anvils. Analyses from the SEM.

4.2.3.1.2 Technical solutions and results

The gaskets were polished to eliminate scratches and grooves from the surface and then pre-indented to harden the material. Afterwards they were sputtered with a thin gold layer. This layer is only a few nm thick, just enough to produce a golden color. This "gold-procedure" has two advantages: (1) the gold seals possible micro-defects on the gasket surface, and (2) it is soft. Hence it serves as a sealing ring around the diamond anvils additional to the gasket material. This minimizes fluid loss.

To pre-indent the gasket new technical solutions had to be found. Pre-indentation with the 1.0 mm culet diamond anvils from the HDAC itself turned out to be insufficient, because the diamonds were moving on the scale of μm relative to each other. Therefore exact repositioning of the gasket after pre-indentation was not possible. The gaskets were then pre-indented by using tungsten carbide anvils and a large anvil press. Unfortunately, it turned out that rhenium is much harder than tungsten carbide, and the anvils broke (see Fig. 4.16) while the gaskets remained essentially un-indented. Another problem that evolved from this method was that the gaskets started to develop cracks within them. During experimental runs the gaskets cracked open from the inside towards the outside at these weakened locations (Fig. 4.16B), and the complete loss of the fluid was the result.
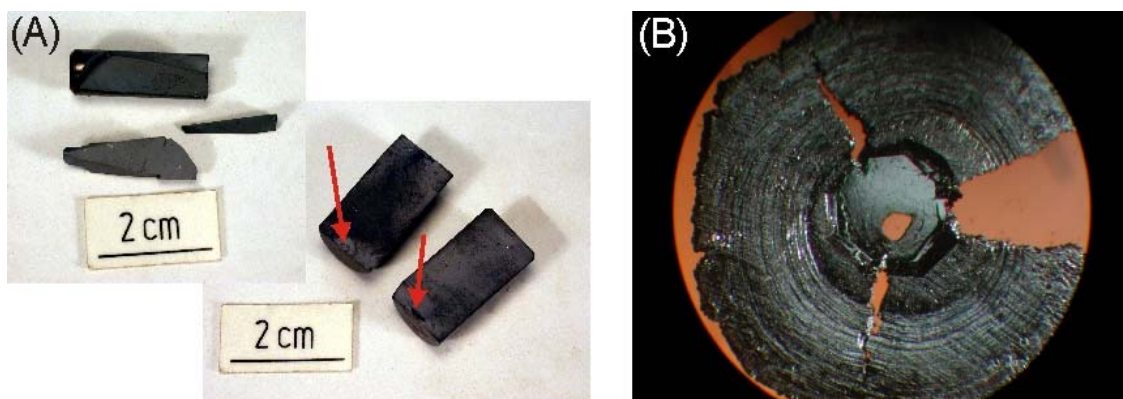
Fig. 4.16: (A) Broken tungsten carbide anvils, red arrows indicate material compression due to the hardness of the rhenium gaskets; **(B)** cracks opened during experimental runs from to weakening points due to pre-intention with tungsten carbide anvils from the inner part of the gasket towards the outer part.

Therefore the gaskets were pre-indented using diamond anvils with larger culets of 1.5mm. Exact positioning was now possible and no cracks developed during experimental runs. The results were very good sealing gaskets for routine experimental runs, and loss of the fluid phase due to the gaskets themselves did not occur in any experiment.

4.2.3.2 Adjustment system

4.2.3.2.1 Critical requirements

Through the observed imprints on the gaskets it became clear that the adjustment system of the Burchard-Zaitsev Cell is critical and represents a constructional problem of this cell type.

During test and experimental runs with the HDAC it was noticed that the sample chamber was sheared more or less strongly both during heating (Fig. 4.17A) and pressure application to the anvils at the beginning of the experiment (Fig. 4.17B-1). In addition the sample chamber wandered from the middle of the flat diamond culets to the inclined culet edges, thus resulting in complete loss of the contents of the sample volume. Imprints on the gasket of type II and IV were noticed after the experiments.
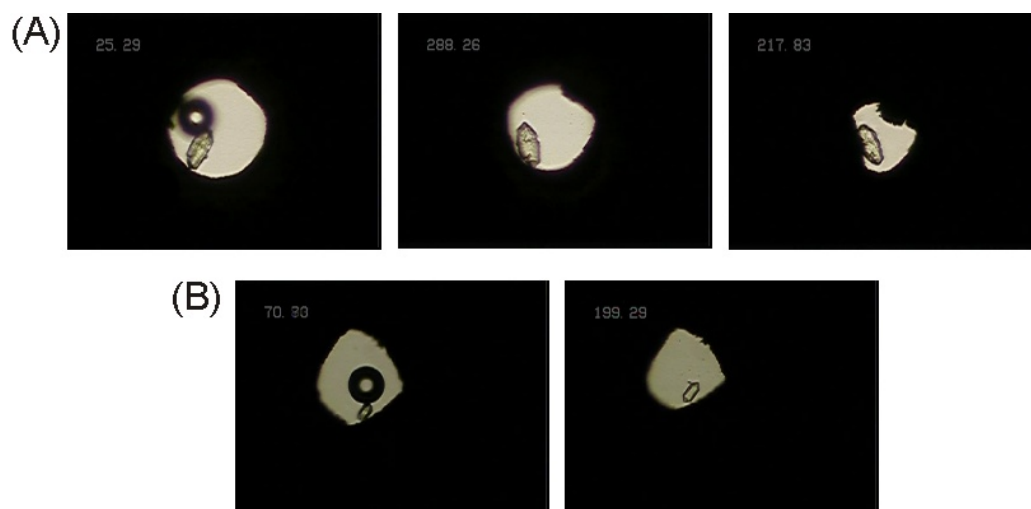
Fig. 4.17: Shearing of the sample chamber during two experimental runs. **(A)** Shearing during heating; **(B)** shearing of the sample chamber started during initial pressure application to the anvils and continued further during heating.

4.2.3.2.2 Error analysis

The sheared and wandered sample chamber and the observed culet imprints can be related to non-uniform deformation of the gasket between the diamond anvil culets, pointing to critical misalignment of parallelism of the anvils (Burchard *et al.*, 2003). Lateral movement of the gasket will be induced. It is pointed out again that the anvils had to be aligned and positioned before the experiments were started.

Closer inspection of the design of adjustment system of the Burchard-Zaitsev Cell revealed that the first constructional problem is to be found in the adjusting screws. These are located diagonal to the adjustable seats and keep these in place (Fig. 4.18). Here, the axial adjustment of the upper anvil is particularly problematic. If the screws are loosened, even only one of them, by the alignment procedure of the upper seat in x, y direction, the whole seat will move slightly in the z-direction and the seat as well as the diamond anvil will no longer be parallel to the cell body.
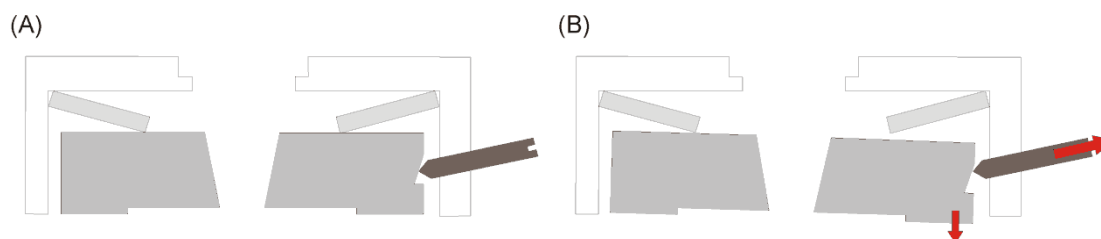
Fig. 4.18: Schematic sketch of the upper platen. **(A)** Initial position of the upper adjustable seat with its adjusting screws; **(B)** by loosening the screws the seat will loose its halt and will move in z-direction.

41

Next the lower anvil will be adjusted parallel to the culet face of the upper anvil. Hence the culet faces are parallel with respect to each other (Fig. 4.19A), but are tilted with respect to the pressure axis. If pressure is applied in this position (Fig. 4.19B), a strong shear force will be induced on the gasket indicated through the small red arrows in figure 4.19B and C. Slight deformation of the sample chamber may occur.
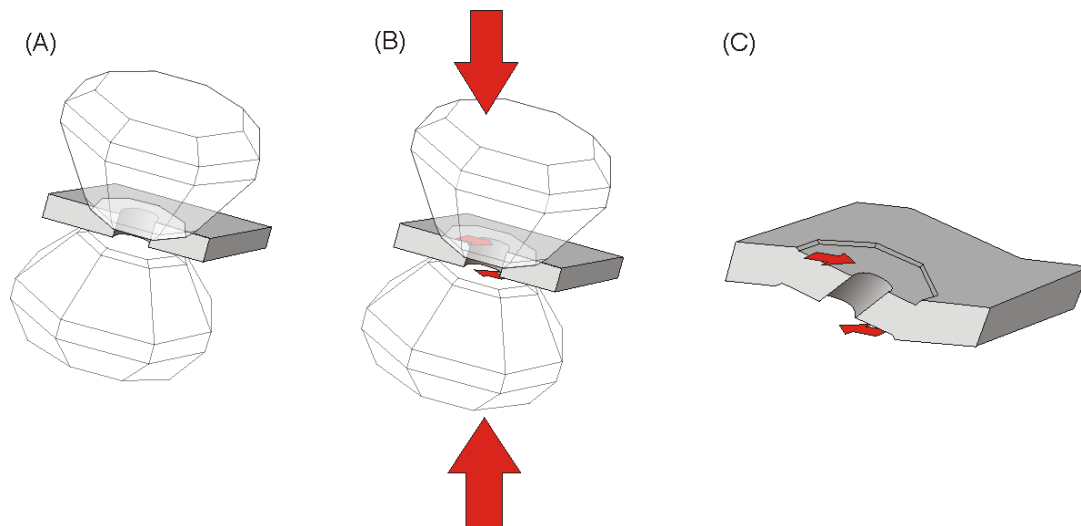
Fig. 4.19: Schematic sketch of the analysis of the second type of gasket imprints in conjunction with the constructional problem of the adjustment system. **(A)** Parallel culet faces are achieved, but the anvils are tilted in respect to the pressure axis. **(B)** Pressure is applied (indicated through the large red arrows) and a shear force is induced onto the gasket indicated through the small red arrows. **(C)** Resulting gasket as it is observed after experiments. Slight deformation of the sample chamber may occur.

The strong deformation of the sample chamber (Fig. 4.10B) that was noticed and the observed imprint of type IV can also be explained with this critical flaw in design. If the force upon the parallel aligned but tilted culet faces (see Fig. 4.19B) becomes too strong (Fig. 4.20A) the anvils will slide in the direction of the tilt (indicated by the blue arrows in figure 4.20A). This results in movement structures on the gaskets (Fig. 4.20B) as observed in type IV imprints and a strongly sheared sample chamber.
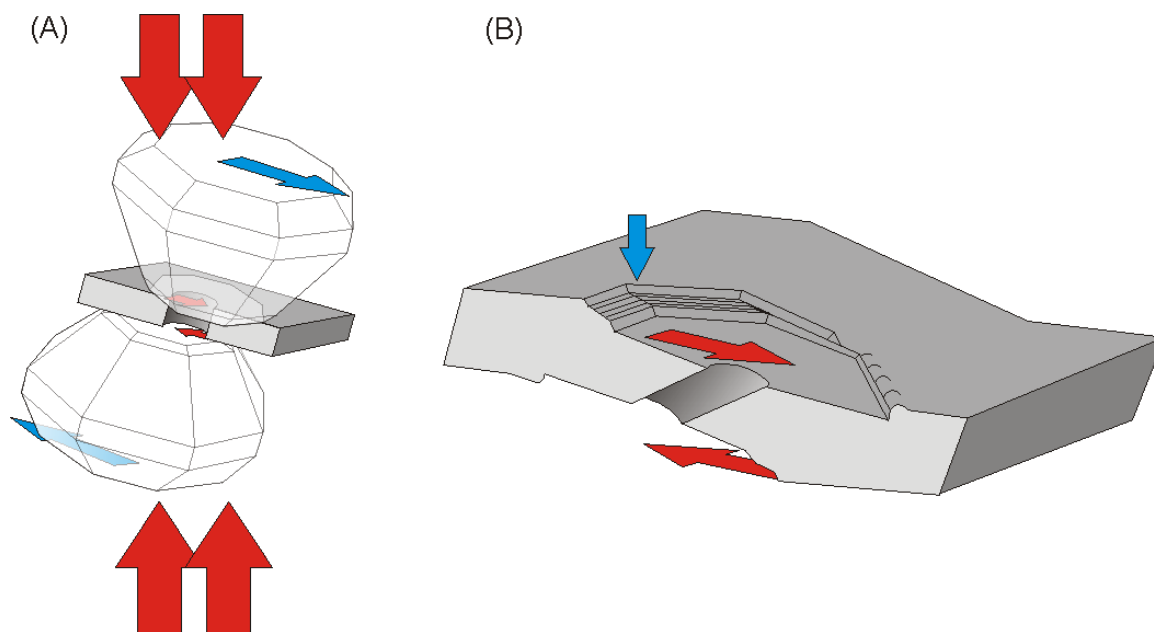
Fig. 4.20: Schematic sketch of the analysis of type IV of imprints on gasket in conjunction with the constructional problem of the adjustment system. Position of the anvils is based on the anvil end-position of figure 4.19B **(A)** Pressure is increased (indicated through the large red arrows) and a shear force is induced onto the gasket indicated through the small red arrows. If the pressure becomes too strong the anvils will slide in the direction of tilt, indicated by the blue arrows. **(B)** Resulting sheared gasket as it is observed after experiments with the observed movement structures and sheared sample chamber.

Type II of gasket imprints can be explained by a second constructional problem that results from the use of Belleville springs in conjunction with the adjusting screws. The springs are placed directly underneath the adjustable seats (see Fig. 3.9, section 3.3.2) to compensate for thermal expansion of the anvil–sample–anvil assembly at the core of the cell, and to avoid rapid build-up of effective pressure on the gaskets at high temperatures (Burchard *et al.*, 2003). While lowering the upper anvil during the assembling procedure, pressure is built up on the Belleville springs leading to their compression. As a result, the adjusting screws will lose their hold on the adjusting seats (Fig. 4.21), not keeping them in place anymore.
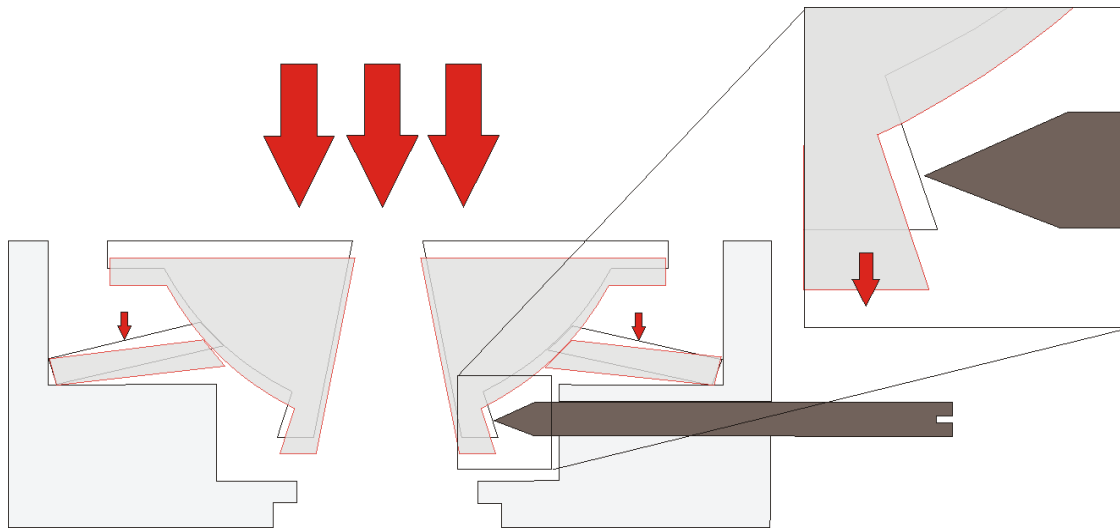
Fig. 4.21: Schematic sketch of the adjustable seat in its initial position (black solid line) exemplary shown on the lower seat. By inducing pressure the Belleville spring will be compressed, the seat is lowered (red dotted line) and the screws are loosened. If one screw is tightened a bit stronger than the others it will loosen later and pushes the seat in its alignment direction.

Now, if just one of the screws was tightened a bit more strongly than the others, it will loosen slightly later and give the adjustable seat a push in its particular alignment direction. Unacceptable, critical misalignment during experimental runs will occur resulting in the observed imprint of type II on the gasket. Figure 4.22 shows a schematic sketch of the consequence of this constructional problem on the resulting anvil positions and the observed gasket imprint. Figure 4.22A shows the initial position of the anvil-gasket-anvil assembly. If pressure is applied onto the anvils the lower anvil will tilt (Fig. 4.22B) due to the effect described above of non-uniform tightened adjusting screws in conjunction with the Belleville spring. As pressure is increased the upper culet face is imprinted stronger on that side of the tilted lower anvil indicated through the small red arrow in figure 4.22B. Figure 4.22C shows a cross section of the resulteing gasket imprint as it is observed after the experiments and test runs. This analysis can explain the tilt and half imprint of the lower anvil on the gasket and the entire imprint of the upper anvil with one side imprinted deeper into the gasket material.
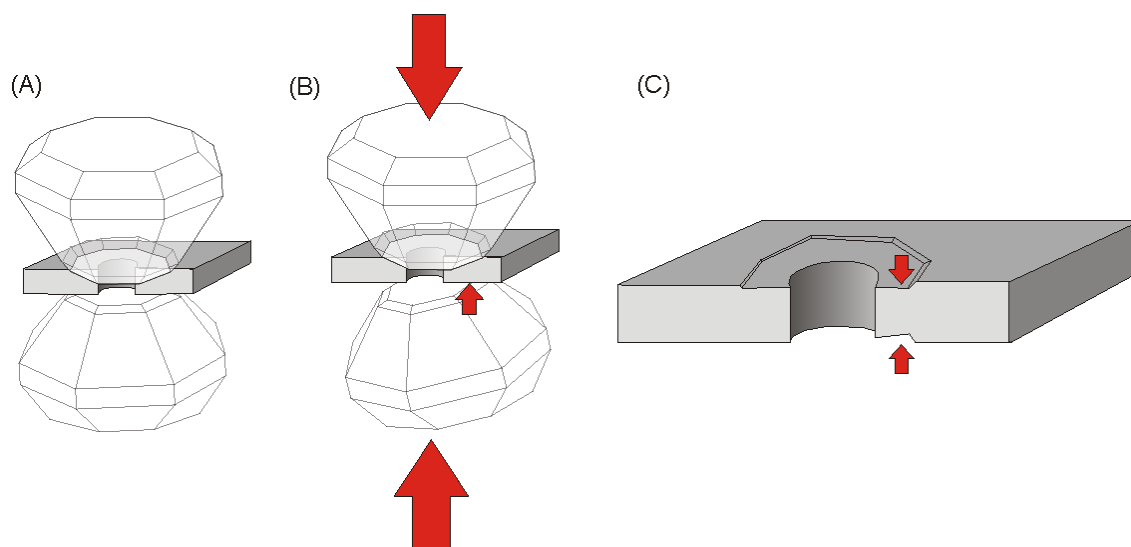
Fig. 4.22: Schematic sketch of the second type of gasket imprint caused by the second constructional problem. **(A)** If pressure is applied onto the anvils the lower anvil is tilted due to the non-uniformly tightened adjusting screws. **(B)** As the pressure is increased the culet faces are imprinted stronger on the side of the tilted lower anvil indicated through the small red arrow. **(C)** Resulting culet imprint as it is observed after the experiments and test runs. The upper anvil culet is entirely imprinted on the upper gasket side, but more deeply on the side of the tilted lower anvil (indicated through the small red arrows). The lower anvil culet is imprinted only half.

4.2.3.2.3 Technical solutions and results

The first constructional problem of the Belleville spring with respect to the upper adjustable seat was solved by aligning the cell in an upside-down position. In this way the upper platen cannot fall down when the adjusting screws are loosened by the alignment procedure. Axial alignment can be carried out correctly without a rocking movement in the Z-direction.

In order to solve the constructional problem of the Belleville springs with respect to the adjusting screws, it was necessary to reconstruct the core of the Burchard-Zaitsev Cell completely. To avoid that the adjusting screws loosen when applying pressure onto the diamond anvils and consequently do not keep the adjustable seats in place, and to prevent movement of either the upper or lower adjustable seat due to a possible push of the unevenly tightened adjustable screws, it is necessary to relocate the Belleville springs. It was found to be best to relocate the springs from the inner to the outer cell body. Thus, they cannot compress the adjustable screws while pressure is being applied, and therefore the position of the adjustable seats remains stable. Alignment of the anvils would remain stable even under pressure. However, due to the

fact that the outer parts of the cell could not be remachined, this option had to be discarded.

As an alternative solution, the Belleville springs were reduced to one spring. This spring was placed in the upper part of the cell. Figure 4.23 shows a schematic sketch of the new construction of the upper part of the inner cell. Mechanical drawings are located in the Appendix III. The Belleville spring (a) is placed between a small inner hollow cylinder (b) and the larger outer hollow cylinder (c). The outer hollow cylinder sits on a washer (d). This washer had to be placed inside the HDAC, because small holes were detected in the upper cell design. These holes led to water leakage from the cooling system. The washer was therefore glued to the cell base of the upper part to seal the outflow. This washer should not be needed for the new construction and operation of an intact HDAC.
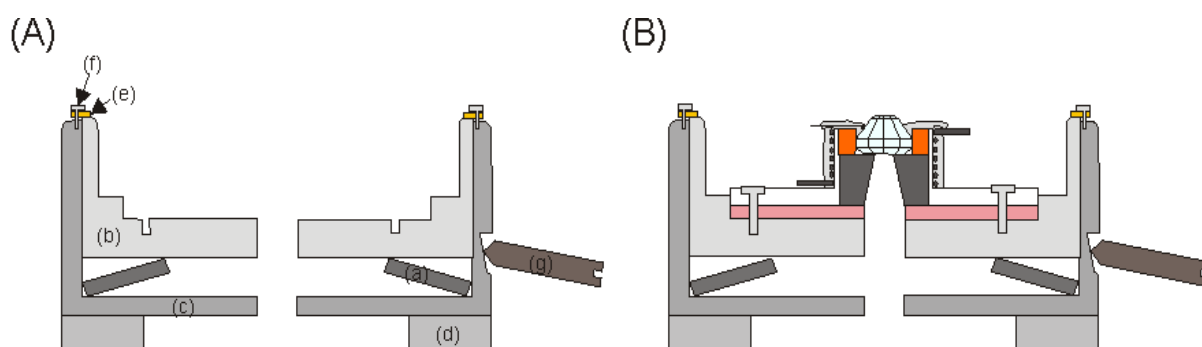
Fig. 4.23: (A) Schematic cross-section of the newly constructed inner part of the upper cell; (a) Belleville spring; (b) small hollow cylinder; (c) large hollow cylinder; (d) sealing washer; (e) small washer; (f) screw; (g) adjustable screw. **(B)** Schematic sketch of the new constructed part of the upper cell with built in heating device.

The small cylinder fits exactly into the large hollow cylinder. It is fixed by three screws (f) on top of the large cylinder to make sure it will not fall out when the upper cell part closes the lower cell part. If parts are machined there will always be a limit to the precision that can be achieved. Imprecision of a few μm are enough to allow for slight tilting movements of the inner hollow cylinder. Exact alignment under pressure will not be assured. Therefore small washers (e) were placed beneath the screws on top of the outer cylinder (Fig. 4.23A) that push the inner hollow cylinder tightly onto the Belleville spring, setting the spring under slight pressure. Thus, the small cylinder pre-

centers itself into the large cylinder and a tilting movement when applying pressure onto the anvils will be avoided.

The lower part of the cell was also totally reconstructed. Figure 4.24 shows a schematic sketch of the lower inner part of the HDAC. Mechanical drawings are located in the Appendix III.
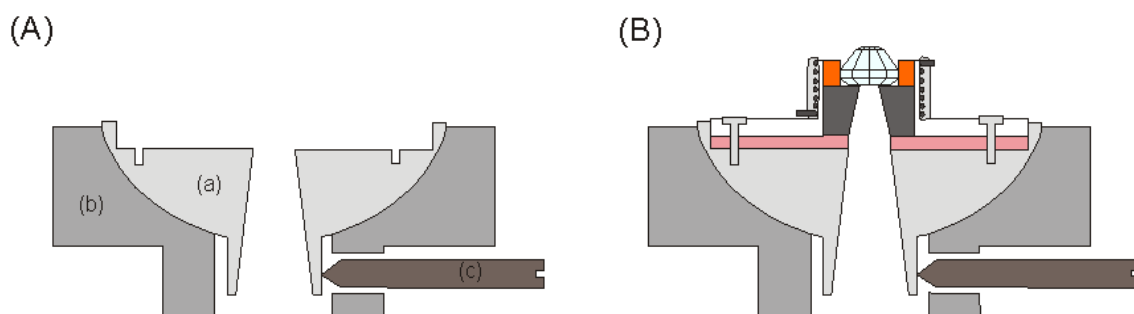
Fig. 4.24: (A) Schematic cross-section of the new constructed lower inner part of the HDAC. A hemisphere (a) sits in a bearing (b). The hemisphere has a small protrusion at its bottom for the adjusting screws (c) which can move the hemisphere in a rocking motion. **(B)** Schematic cross-section of the newly constructed lower inner parts of the HDAC with built-in heating device.

A hemisphere and its corresponding bearing were constructed for the lower part and no Belleville spring was used. This makes the construction much more stable. The Belleville spring is taken out of the lower construction and therefore the effect of any loosening of the adjusting screws when pressure is applied is minimized. Therefore the bottom of the hemisphere is constructed cylindrically instead of spherically as in the old construction. Even if the material itself is easing slightly under pressure, this new construction will avoid the problem that the adjusting screws will loosen if pressure is applied onto the HDAC.

With the newly constructed inner parts of the HDAC it is now possible to align the diamond anvils exactly, and to keep the alignment stable even when pressure is applied.

4.2.3.3 Guiding system

4.2.3.3.1 Critical requirements

The polished pin (see Fig. 3.9, section 3.3.2) was identified as a third constructional problem. During this study it was noticed that the pressurizing nut could

47

be moved in-plane with respect to the lower platen. As a result the upper adjustable seat and diamond anvil also moved strongly in-plane. It was not possible to carry out axial alignment procedures correctly.

4.2.3.3.2 Error analysis

The reason for this problem is the position of the pin holes of the upper and lower platen. The two holes are not located exactly upon each other. Consequently, both platens move on slightly different circular paths when the pressurizing nut is turned. In-plane movement of the upper platen is the result that one guiding pin can not compensate for.

4.2.3.3.3 Technical solutions and results

Two more guiding pins were introduced into the cell design. Therefore, two of the contact screws were taken out and their holes were broadened by spark erosion. These were used to insert the new guiding pins (see Fig. 4.27). In a second HDAC used, the contact screws were also left in place and new holes were drilled with a special drill for hardened steel. This procedure was very time-consuming and is not recommended for routine usage. Nevertheless, the holes are of good quality and can be used to insert the guiding pins.

The increase from one to three guiding pins is sufficient to fix the upper platen even if both platens move on slightly different circular paths. Rotation of the upper platen is avoided or at least minimized.

4.2.3.4 Pressurizing mechanism

4.2.3.4.1 Critical requirements

The fourth constructional problem is the pressurizing nut itself. During this study it was noticed that the pressurizing nut has too much play with respect to its worm. When the upper cell body is rocked, the upper platen and therefore the adjustable seat and the anvil, also move in a rocking motion. Parallel alignment using interference fringes is not possible in a precise manner.

The fifth constructional problem comprises the worm gear. Usually the cell is closed manually until the diamond anvils enclose the gasket between them tightly. Further pressure is induced by turning the worm gear. The anvils were aligned and

positioned before pressure was applied but type I of imprints on the gaskets (see Fig. 4.7) showed just half of the culet faces of both anvils.

4.2.3.4.2 Error analysis

The imprints of type I indicate critical misalignment of not only the lower anvil, explained through the second critical constructional problem with the Belleville springs and the adjusting screws, but also misalignment of the upper anvil during applied pressure. Figure 4.25 shows the schematic sketch of the analysis of the resulting imprint type I and anvil positions resulting from this analysis. Figure 4.25A shows the initial position of the anvils. As pressure is induced (Fig. 4.25B, indicated through the red arrows) both anvils will tilt and only one side of the culet faces will be pressed in the gasket. The result is displayed in the cross section of the gasket in figure 4.25C. Only half of the culet faces is observed on the gasket. This consideration is approved through the real gasket imprints (see Fig. 4.7).
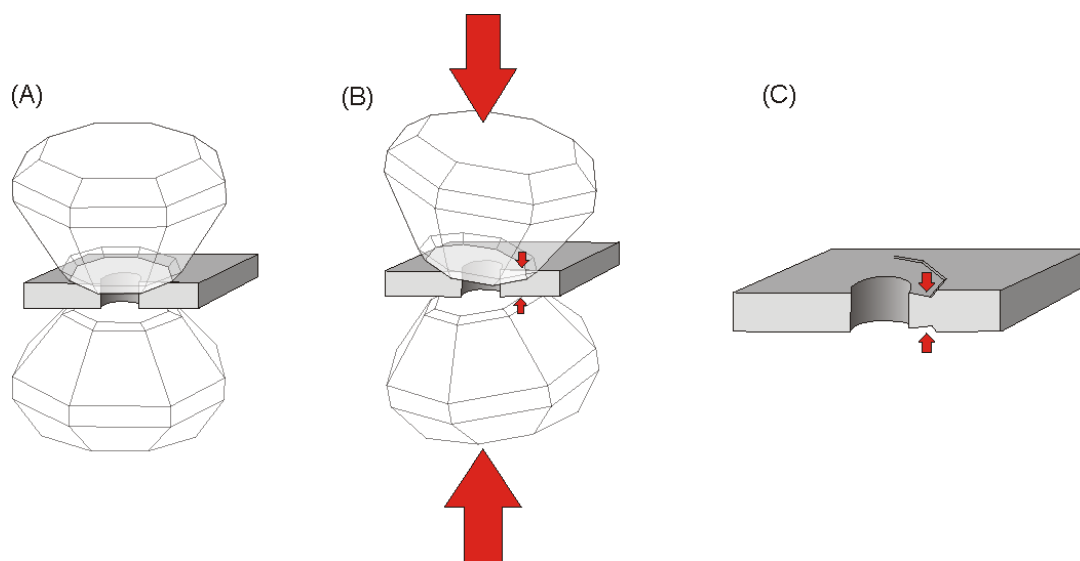
Fig. 4.25: Schematic sketch of the analysis of the first type of gasket imprints in conjunction with the fifth constructional problem: the pressurizing system. **(A)** Initial position of the diamond anvils. **(B)** Pressure is applied (indicated through the large red arrows) resulting in increased force onto the gasket on just one side, indicated through the small red arrows. **(C)** Cross section of the resulting gasket imprint.

To identify where the critical misalignment comes from, the worm gear was inspected closer. The diamond anvils were aligned and the cell manually closed, without a gasket lying between the anvils, until the anvils were touching each other. One uniform color of the interference fringe produced was observed, indicating correct

parallel alignment. Then the worm gear was turned and pressure induced very carefully. As soon as the worm gear started to turn new interference fringes formed between the two anvils, indicating that at least one of the anvils was being forced to tilt. This means that critical misalignment is also induced by the worm gear. An explanation is provided from the interaction of the pressurizing nut and worm gear. The worm gear touches the pressurizing nut at just one point (red circle in Fig. 4.26A), and the thread angle of the worm gear does not exactly match the thread angle of the pressurizing nut. Thus the upper platen is forced to tilt in the z-direction when the worm gear is turned (Fig. 4.26C). Additional shear stress is initiated on the gaskets and the diamond anvils to pressures that can also lead to leakage and lateral movement of the gasket itself. Another negative effect is that the worm gear wears off extremely rapidly so that increasing force is needed to turn the worm gear further.
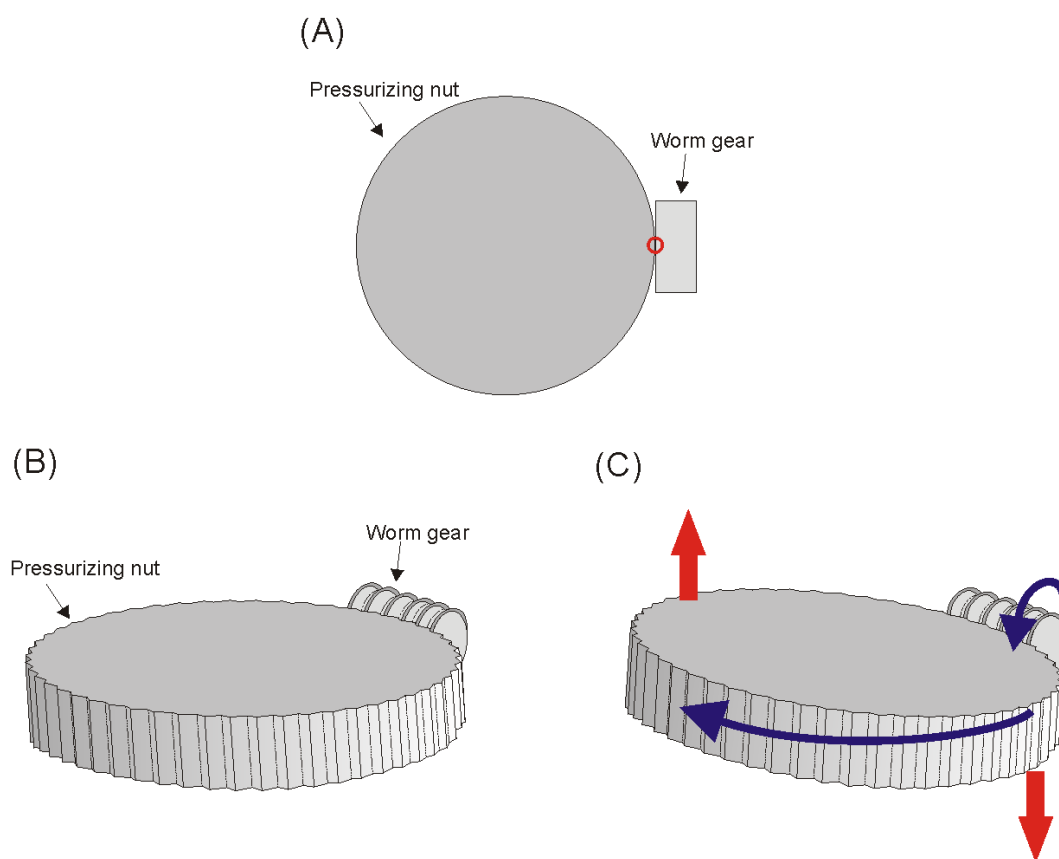
Fig. 4.26: (A) Simplified schematic sketch of the pressurizing nut with worm gear, top view. The worm gear touches the nut at just one point (red circle). **(B)** 3-Dimensional view of the pressurizing nut with worm gear, initial position. **(C)** By turning the worm gear, the nut is turned (indicated through the blue arrows) and the upper platen is forced to tilt in the z-direction (indicated by the red arrows).

4.2.3.4.3 Technical solutions and results

The outer parts of the basic cell design based on a pressurizing nut and the worm gear could not be changed due to the fact that the cell is made out of hardened steel. These cannot be remachined in order to change the design. Other solutions had to be found to overcome the constructional problems involved.

The first problem with respect to the play of the nut was solved by inserting three coil springs. The coil springs (Fig. 4.27) were wrapped around the three new polished pins guiding the upper platen.
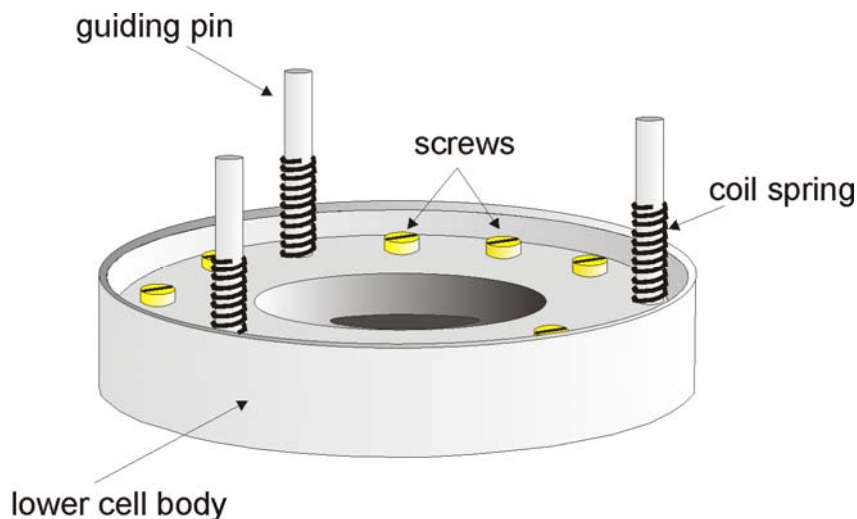
Fig. 4.27: Schematic sketch of the lower cell body. Coil springs are placed around the guiding pins to lift the upper cell body.

The coil springs will be under pressure from the first approach of the upper platen, pushing it against the ball-bearing of the pressurizing nut. Figure 4.28 gives a schematic overview of the function of the coil springs.
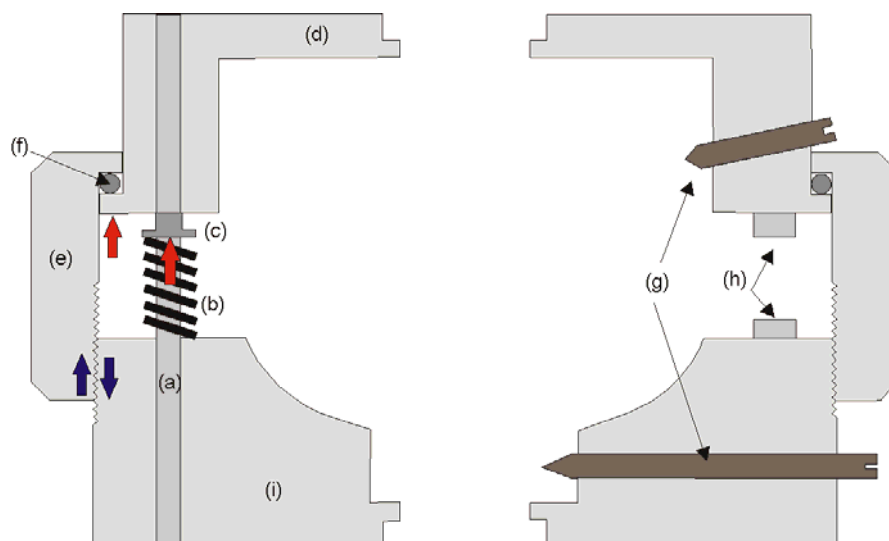
Fig. 4.28: Schematic cross-section of the modified HDAC. The coil springs (b) wrapped around the guiding pin (a) push the upper platen (d) against the ball bearing (f), as indicated by the red arrows pointing upwards. A metal cap (c) on top of the coil springs prevents them from being pressed against the inner adjustable seat (not drawn in this sketch) so it will not be moved (mechanical drawing in Appendix III). The pressurizing nut (e) now fits more tightly and centers itself in its worm from the lower platen (i) indicated by the blue arrows.

As a result the upper platen fits more firmly onto the ball-bearing and cannot tilt in a rocking motion when it is touched any more.

The coil springs were also constructed for a second positive effect that is the play of the nut. While the coil springs push the upper platen more firmly onto the ball-bearing, the pressurizing nut is also lifted up slightly. Therefore, it is pushed against its worm and centers itself in the worm (indicated by the blue arrows in Fig. 4.28). The play of the nut is reduced with this construction. Of course a stronger force is now needed to turn the pressurizing nut, but this is still acceptable. The upper platen cannot move in-plane any longer and the alignment of the diamond anvils can now be carried out precisely.

To solve the problem with the worm gear, no technical solution with respect to changing and/or machining the worm gear and nut could be applied, because of the hardened steel. A simple solution was found. Instead of applying pressure with the worm gear it is now applied by turning the nut with a chain pipe-wrench, and the HDAC is clamped in a three jaw drill chuck (Fig. 4.29).
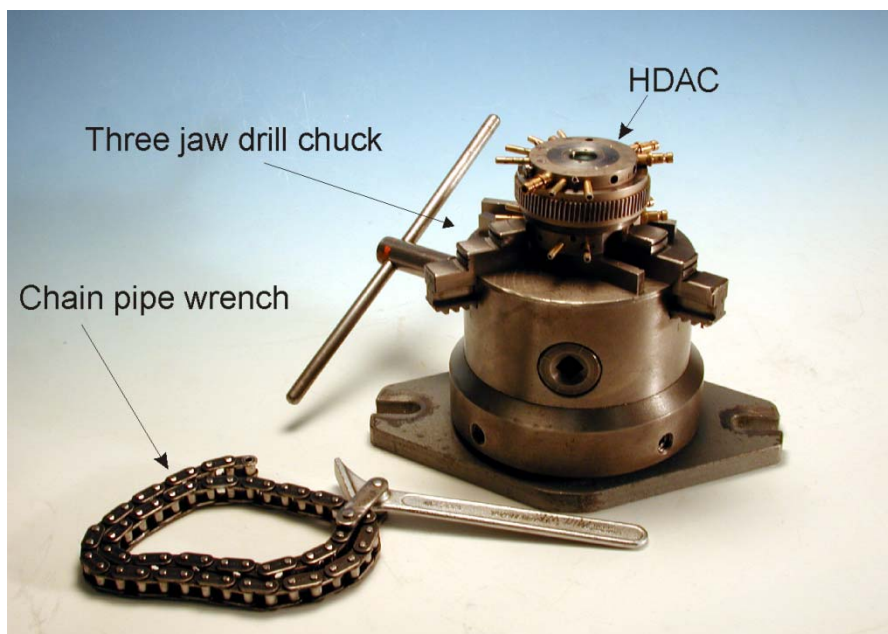
Fig. 4.29: HDAC clamped in a three jaw chuck. The chain pipe-wrench is used to apply pressure onto the diamond anvils.

The chain pipe wrench is laid around the nut of the HDAC and turned. Pressure is applied to the diamond anvils. Using a chain pipe-wrench to apply the pressure has the advantage that it intertwines with the nut at an infinite number of points indicated by the red line in figure 4.30A. Figure 4.30 shows a schematic sketch of the use of the chain pipe-wrench and its effect.
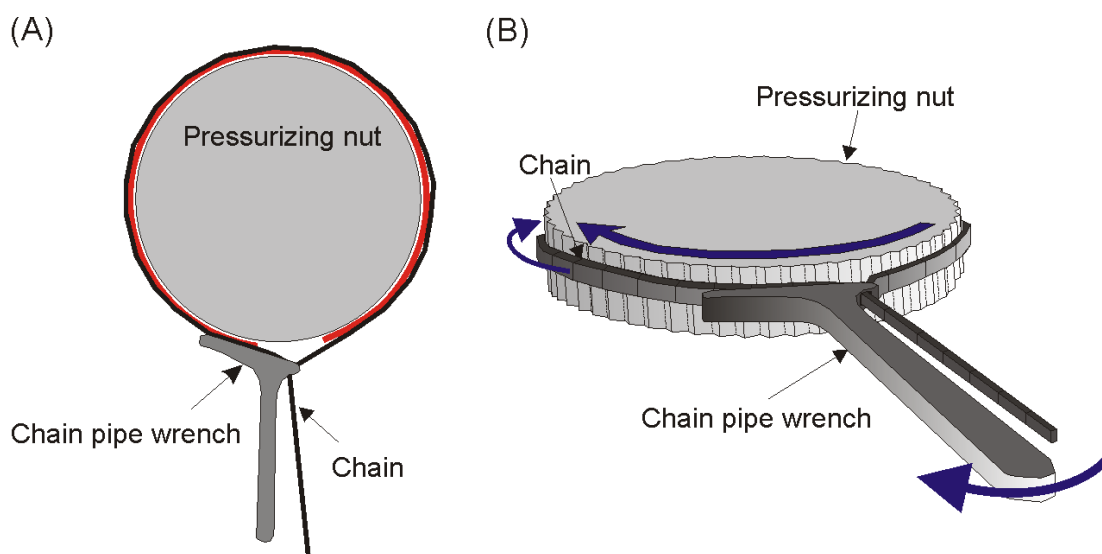
Fig. 4.30: Schematic sketch of the use of the chain pipe-wrench to induce pressure. **(A)** Top view; the red line indicates where the chain touches the nut. **(B)** 3-dimensional view of the nut. By turning the chain pipe-wrench, the chain will move and the nut will turn. Pressure is applied to the diamond anvils.

The pressurizing nut is now not affected by the worm gear anymore. Because the chain of the wrench intertwines along the whole nut the upper platen does not tilt in z-direction.

A more elegant solution would be to replace the worm gear and the nut with a six to eight edged nut (Fig. 4.31). A linked screw wrench would then be used for applying pressure.
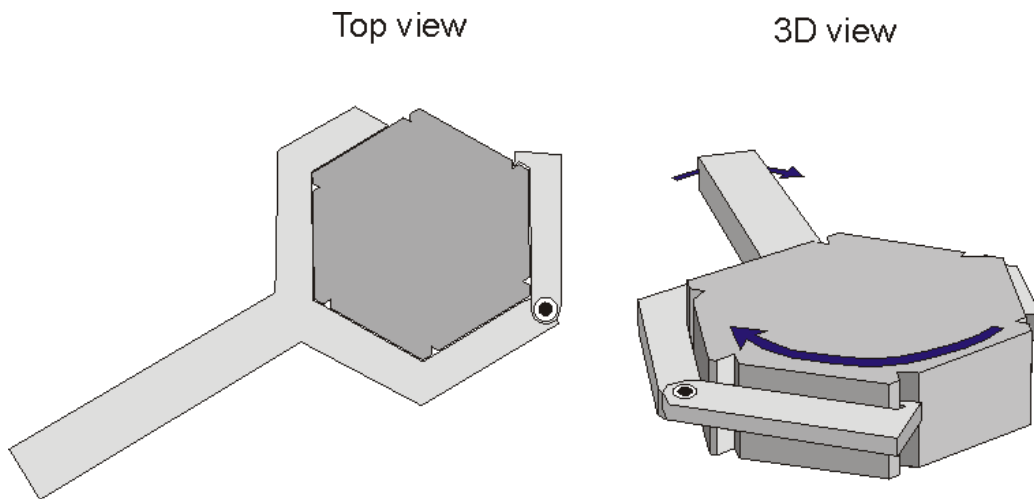
Fig. 4.31: Schematic sketch of a more elegant solution of the pressurizing mechanism. A six-sided nut is used that can be moved with a linked screw wrench, top view and 3-dimensional view.

4.2.3.5 Parallelism of diamond anvils and machined parts

To exclude that the surface of the diamond anvils and the machined parts are tilted and therefore being responsible of the observed critical deformations of the gasket and sample chamber, a method had to be found to measure the accuracy of parallelism of the provided material surfaces *e.g.* the diamond anvils and the machined parts of the HDAC.

4.2.3.5.1 Technical solutions

For this purpose the optical method of auto-collimation was found to be a useful tool. By using this technique it is possible to determine very small angle deviations with respect to exactly perpendicular reflectance of an incident light beam (Paul, 1999).

As shown in figure 4.32 a cross, which is situated in a back focal plane of a reflected light microscope, can be observed using a conoscopical ray path. Rotating the microscope stage does not affect the observed cross position when the reflectance is

exactly perpendicular. As soon as the reflectance is slightly oblique the cross centre moves on a circle (see Fig. 4.33). The circle diameter is a measure of obliquity.
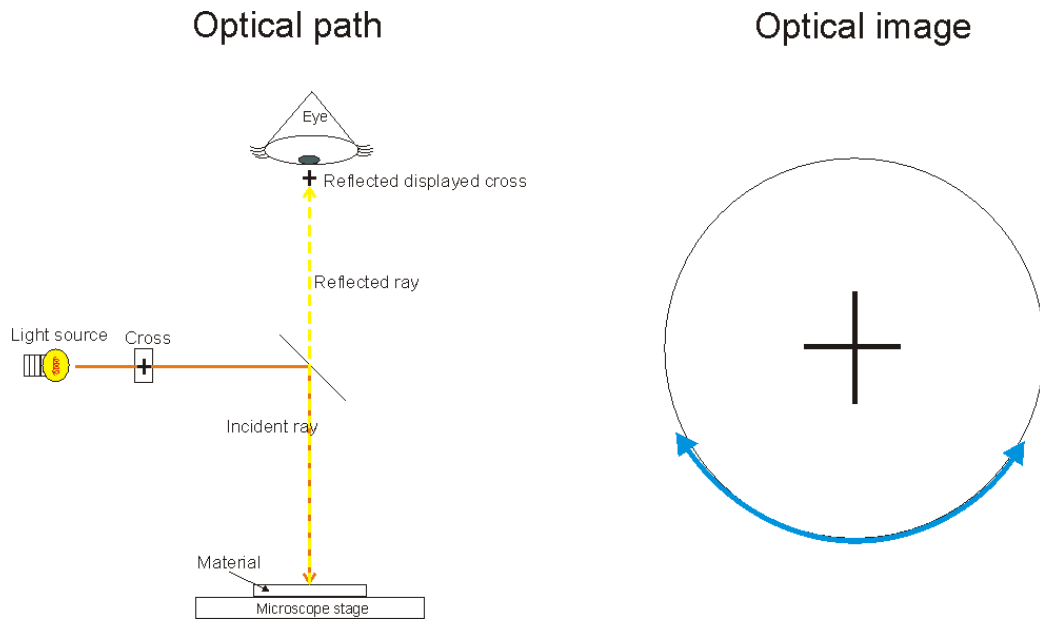
Fig. 4.32: Simplified schematic sketch of the optical ray path using the auto-collimation technique. If the tested material has parallel faces the reflectance is exactly perpendicular and the observed cross remains at its position when turning the microscope stage.
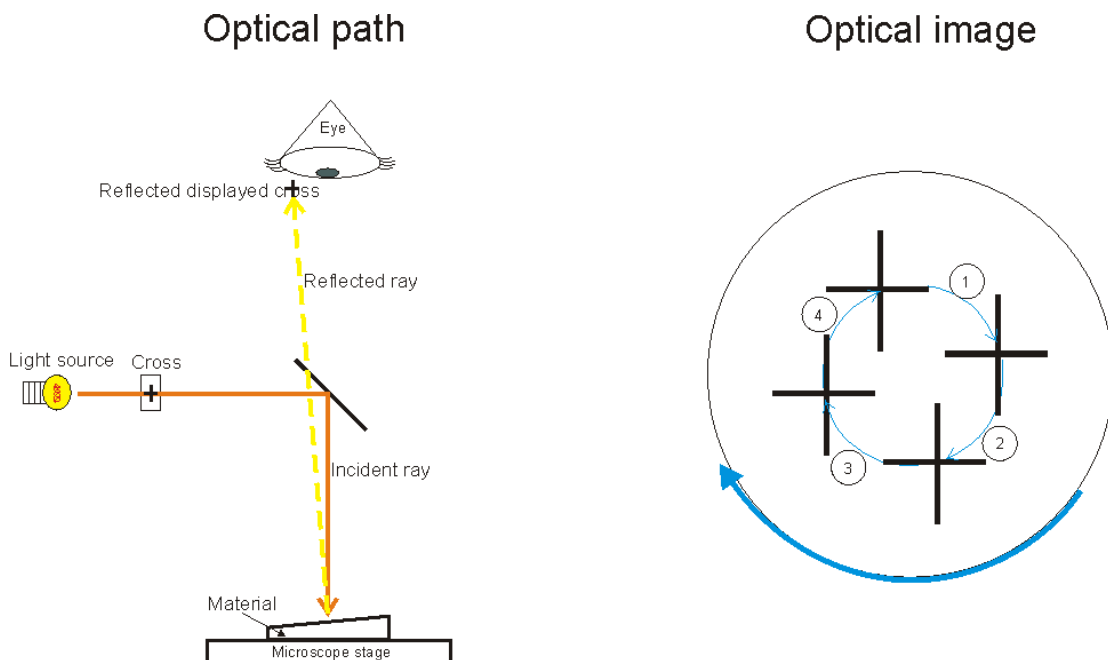
Fig. 4.33: Simplified schematic sketch of the optical ray path using the auto-collimation technique. If the tested material surfaces are not exactly parallel to each other the reflectance is not perpendicular hence when the microscope stage is rotated the locus of the cross centre is a circle – depicted here for 4 different stage positions.

4.2.3.5.2 Results

The auto-collimation technique was found to be a very sensitive tool for measuring the parallelism of the material surfaces. A calibration of the auto-collimation technique is only possible for determining relative changes in the inclinations because the length of the reflected path is slightly variable. Therefore, the calibration was done roughly to determine at least the magnitude of inclination. Different angles of inclination ranging from 0° to 0.05° were produced by placing different materials of known thicknesses under the edge of a glass plate (Fig. 4.34) with parallel surfaces. The diameter of the circle the cross described upon reflection was then calibrated against the inclination angles. Table 4.1 shows the materials used with their specifications, inclination angles and produced observed circle diameters.
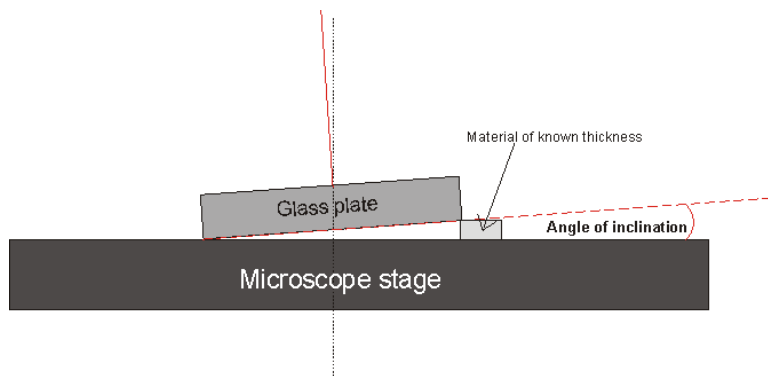
Fig. 4.34: Schematic sketch of the method used to calibrate the auto-collimation technique

All machined parts of the old cell e.g. the cell body, the adjustable seats and tables and also the Belleville springs, and the newly constructed parts e.g. the hemisphere and the bearing, the washers and the two cylinders were tested for parallelism. It turned out that all machined parts were parallel except one Belleville spring that showed an inclination angle around 0.001°. The parts that did not meet the quality expenses were reworked. Also the diamond anvils were tested upon the parallelism of the culet face with respect to the table face. It turned out that some anvils are of better quality than others, but all of them lie within the error specification of the producing company that is 0.0833°.

Table 4.1: Materials used for rough calibration of the auto-collimation system with their specifications, inclination angles and produced circle diameters.

Material of known thickness	Thickness (mm)	Length of reference material (mm)	Diameter of circle path (mm)	Angle of inclination (°)
Reference glass plate	0.000	28	3.44	0.0000
Mica plate	0.025	28	3.78	0.0009
Wire	0.050	28	9.37	0.0018
Thin gasket	0.060	28	11.26	0.0021
Paper	0.100	28	20.14	0.0036
Cover-glass	0.150	28	25.63	0.0054
Diamond good quality*			10.57	0.0018-0.0021
Diamond bad quality[#]			24.35	ca. 0.0054

*,# Classification of quality by author, all anvils lie within the error specification of the producing company. Error specification of the company of the parallelism of the culet face with respect to the table face is $\leq$ 5 min $\cong$ 0.0833°.

4.2.4 Conclusion

The combination of all these reconstructions led to a very good quality adjustment of the diamond anvils. The result can be observed in figures 4.35 and 4.36. Figure 4.35 shows a selection of imprints onto the gasket as they appeared before the reconstruction of the HDAC. In figure 4.36 a selection of imprints onto the gasket after the reconstruction can be examined. The culet faces of the diamond anvils are nicely and evenly imprinted onto the gasket. Shear stress of the diamonds and the gasket is prevented and leakage of the fluid is minimized with the new construction.
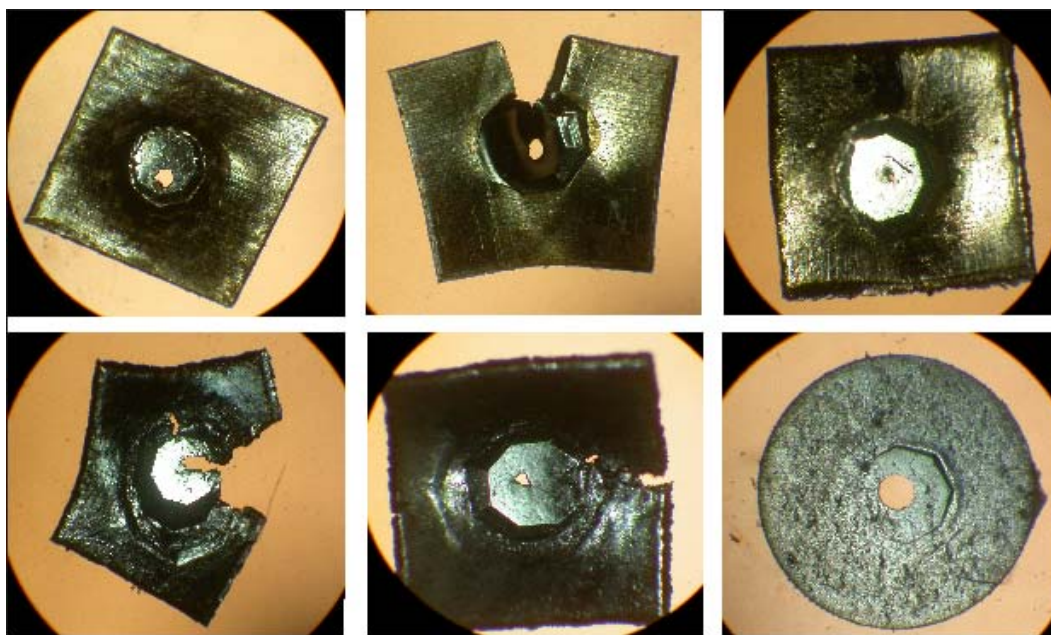
Fig. 4.35: Selection of inconsistent culet face imprints onto gaskets as they appeared before the reconstruction of the HDAC due to critical misalignment. Leakage of the fluid, loss of the sample and sheared sample chambers were the consequence.
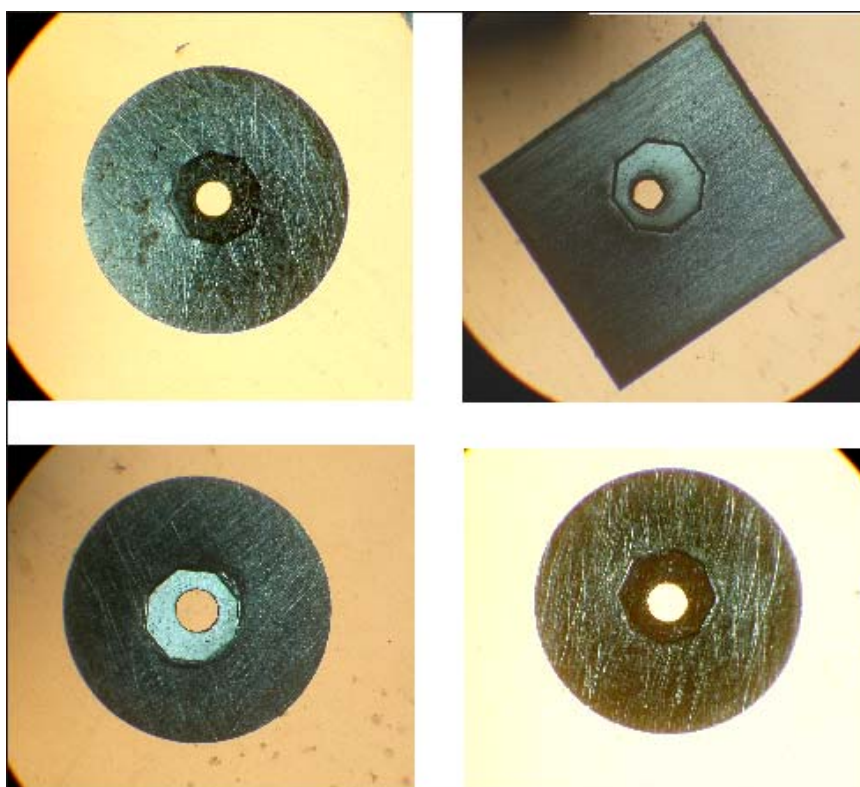
Fig. 4.36: Selection of culet face imprints onto gaskets. The imprints are nicely and evenly imprinted onto the gasket.

Figure 4.37 and 4.38 show the overall changes in design made and the technical reconstruction of the newly designed HDAC compared to the original HDAC. In figure 4.37 the solid red parts of the original HDAC are replaced by the newly constructed parts now outlined in red. Figure 4.38 shows the detailed inner parts of the previous HDAC (Fig. 4.38A) and the newly constructed inner parts of the HDAC (Fig. 4.38B).
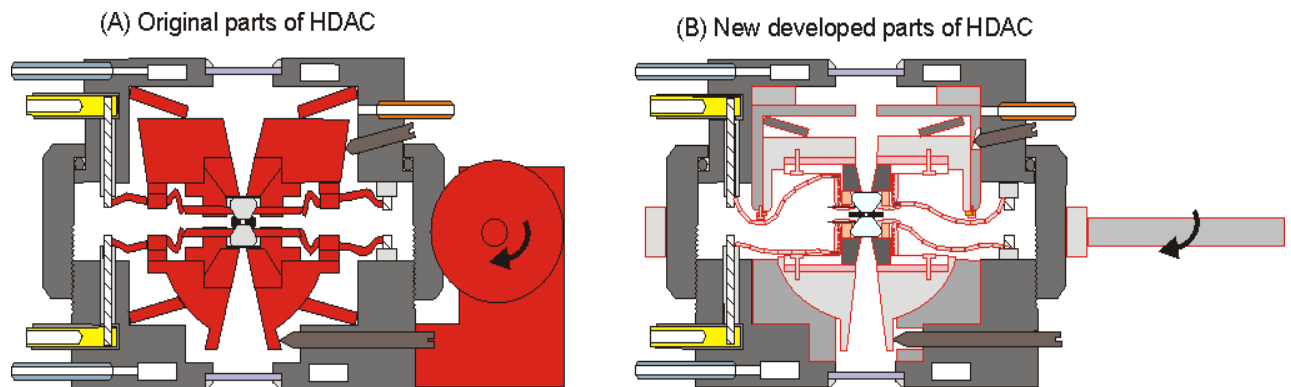
Fig. 4.37: (A) Schematic sketch of the original HDAC. Parts shown in solid red are all reconstructed and replaced by the parts outlined in red in **(B)**. Mechanical drawings of the new constructed inner cell are in Appendix III.
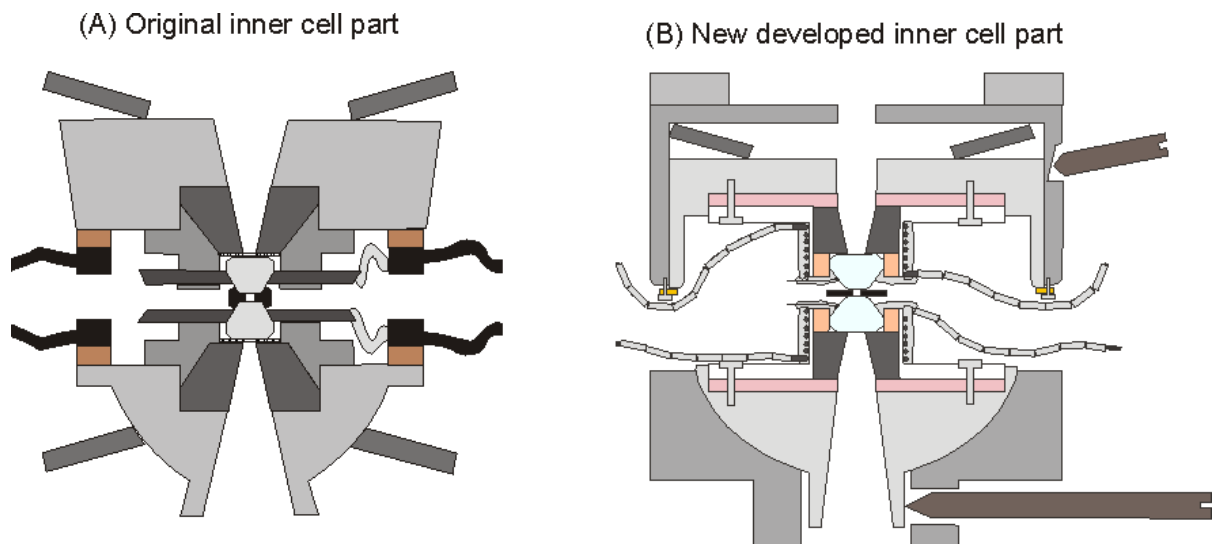
Fig. 4.38: (A) Schematic sketch of the previous design of the inner part of the original HDAC; **(B)** newly constructed design of the inner parts of the HDAC. Mechanical drawings of the new constructed inner cell and heater cell are in Appendix III.

4.3 A new heating system for the Burchard-Zaitsev Cell

The heating system of the Burchard-Zaitsev Cell also poses some critical requirements that need to be considered.

4.3.1 Critical requirements

The heating system of the Buchard-Zaitsev Cell was original designed for the use of i-Anvils. Such diamond anvils were not available at the beginning of this study. Although initially a single diamond anvil set, consisting of two diamonds, was boron-implanted during this study, it turned out that this type of heating system is not yet suitable for routine experimental runs for the following reasons.

(1) The ion implantation of diamonds is a time-consuming, complicated and expensive procedure. About two weeks are needed to prepare the laboratory assembly and the diamonds to make sure that the implantation in the Dynamitron Tandem Accelerator (DTL, Ruhr-University of Bochum) will be successful.

(2) After successful implantation the contact terminals have to be exposed in the diamond. A thin layer of diamond glass is produced during the implantation of the contact terminals. These act like insulators. Therefore, this layer has to be penetrated for electric current to flow. Usually, this penetration is done by sending a strong electric current directly onto the contact terminals. During this study, the equipment needed for such penetration was not available.

(3) The holders where the diamonds sit within the HDAC ensure robust electrical connections via the tungsten carbide needles. With this solution, however, the anvils themselves are not firmly and reliably held. They move relative to each other even while pressure is being applied. Furthermore, an exact adjustment is very difficult to attain and misalignments are common.

For these reasons it became necessary to create a new heating system that would fit into this special type of HDAC and also function in routine experiments.

4.3.2 Technical solutions and results

Figure 4.39 shows a schematic sketch of the heating system developed in this study from the first attempt to the final solution. A Mechanical drawing of the final heater can be found in the Appendix III. Basically, a wire (g/j) is wound around a macor ceramic cap (b) that serves as resistance heater. The ends of the wire are double-layered

to keep them cool, so that only the wire parts wound around the ceramic cap will serve as the actual heater. The ceramic cap is placed on top of the diamond (a) sitting on the backing plate (c). Ceramic glue (k) is used to fix the diamond (a). An insulating material (f, l) underneath the whole heating device including the backing plate avoids too much loss of heat. Several different specifications had to be developed during this study to optimize the heating system. Different wire materials, wire lengths, insulating materials, shapes of the ceramic cap, ceramic glues, heat transport systems and fixations of the diamond had to be developed and tested during this study. Figure 4.39 shows the first and the last type of heater developed. Eight different varieties were developed before the best working one was found. Table 4.2 gives an overview of the heater specifications.
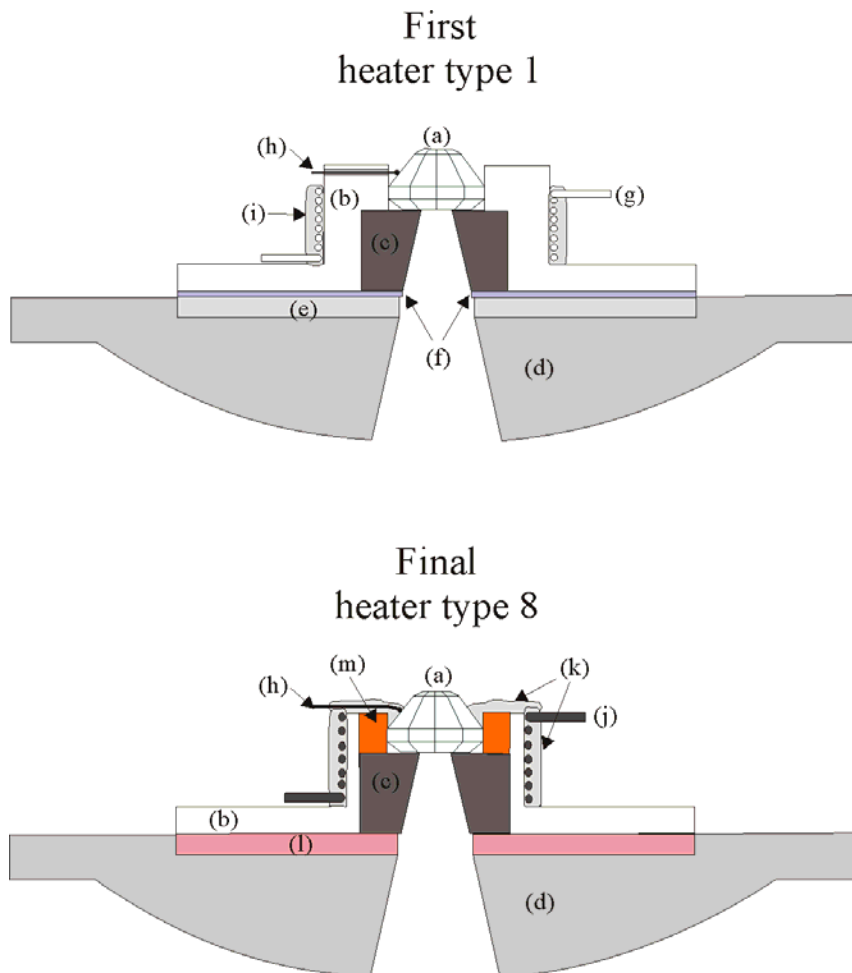
Fig. 4.39: Schematic sketch of the first and final heater type. (a) diamond; (b) macor ceramic plate; (c) backing plate; (d) adjustable seat; (e) hardened steel inlet; (f) mica sheet; (g) platinum-wire; (h) thermocouple; (i) macor ceramic nut; (j) molybdenum wire; (k) different types of ceramic glue; (l) hardened pyrophyllite plate; (m) copper plate.

Table 4.2: Specifications of the different heater types developed during this study.

Type	Type 1	Type 2	Type 3	Type 4	Type 5	Type 6	Type 7	Type 8	Type 9
Wire material	Platinum	Molybdenum	Molybdenum	Molybdenum	Molybdenum	Molybdenum	Molybdenum	Molybdenum	Molybdenum
Windings	10	10	9	9	9, up to the end	9	8	9	10
Wire length (mm)									40
Ceramic cover (mm)	2	2	2	2	2	2	1	none	none
Wall thickness of cap (mm)	1	1	1	0.5	1	0.5	0.5	0.5	0.5
Insulator	mica	mica	mica	mica	mica	mica	mica	pyrophyllite	pyrophyllite
Glue	no	no	ceramabond 865	ceramabond 865	ceramabond 865	ceramabond 865	ceramabond 571	ceramabond 571	ceramabond 571
Extras						copper ring	copper plate	copper plate	copper plate
Maximum temperature reached	343.4°C	629°C	574.1°C	91.1°C burned through	203.1°C burned through	485°C		700°C 900°C (assumed)	
Schematic sketch	1: Pt Wire	2: Mo-Wire	3: Less winding	4: Thinner wall	5: Winding until the end	6: Copper ring	7: Copper plate, thinner ceramic cover	8: no ceramic cover, pyrophyllite insulation	

62

During the development of the heater, a significant change was introduced by imposing a copper ring into which the diamonds were pressed. This construction has two positive advantages. It pre-centers the diamond in the middle of the heating system, and therefore in the middle of the cell body axis. It also keeps the diamond in place, preventing it from moving. Critical axial misalignments due to slight shifts of the diamond out of the cell body axis are minimized with this construction. Nevertheless, the ring was later changed to a 1 mm thick, flat, round copper plate (Fig. 4.39 (m)) with an outer diameter of 9 mm and an inner diameter of 3.9 mm. This construction has in addition a most important advantage. Since copper is a material with very good heat conductivity, the copper plate ensures a maximum of heat transfer from the ceramic towards the diamonds (Fig. 4.40).
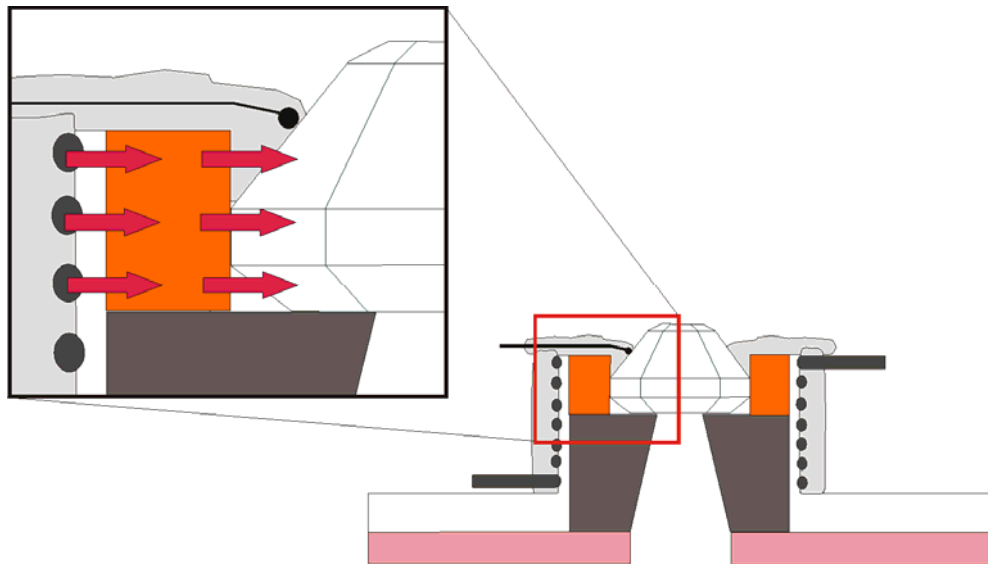
Fig. 4.40: Schematic sketch of the heating device with enlarged sketch of the copper plate. The red arrows indicate the heat transfer from ceramic heater through the copper towards the diamond.

The wires that are normally used for the resistance heater have the disadvantage that they slowly evaporate at higher temperatures. The performance of the heaters will thus deteriorate after each experiment, so that they can only be used a few times before breaking. To minimize evaporation, the wire was covered either by ceramic glue (around the ceramic cap) or by ceramic capillary tubes (Fig. 4.41) that covered the ends of the wire.
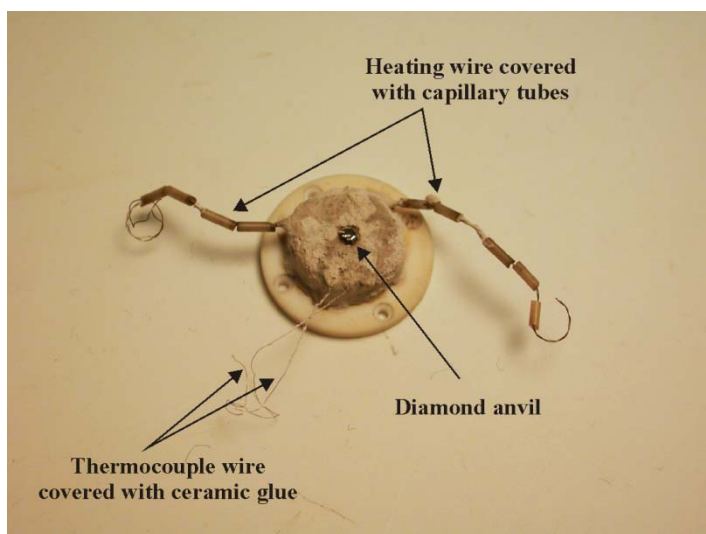
Fig. 4.41: New developed heating device inside the upper part of the HDAC with covered heating wires and thermocouples to minimize evaporation of the wire material.

Figure 4.42 shows a molybdenum heating wire after an experimental run. It can easily be noticed that the uncovered part evaporated. The covered part (indicated through the red arrow) is still intact.
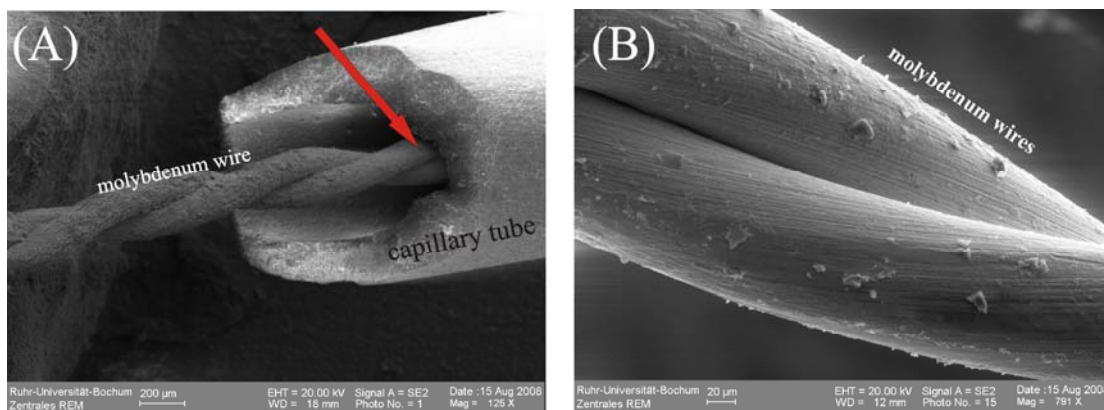
Fig. 4.42: SEM images: **(A)** Evaporation has started at the uncovered part of the molybdenum wires. The area covered by capillary tubes (indicated through the red arrow) is still intact. **(B)** Enlarged picture of swirled molybdenum wire that was covered by capillary tubes throughout the experiments. The wires are still of very good quality.

The loss of too much wire material is problematic, because the diameter of the wire will decrease. Consequently, the resistance will increase and worsen the ratio between

voltage and current. Maximum temperatures can no longer be reached. If the diameter becomes too small the heater is likely to burn through. During the development and optimization of the heating device, several changes had to be introduced to find the resistance heater with the best performance. A key constraint in this regard was the fact that the power supplies for the heaters are ideally able to produce 300 watts, with a maximum of 30V and 10A. Therefore the heater wire used had to have an electrical resistivity appropriate for ideally reaching 30V at a current of 10A in order to capitalize on the available power. Figure 4.43 shows the different heater types (see Table 4.2) with their maximum temperatures reached and their associated capacities.
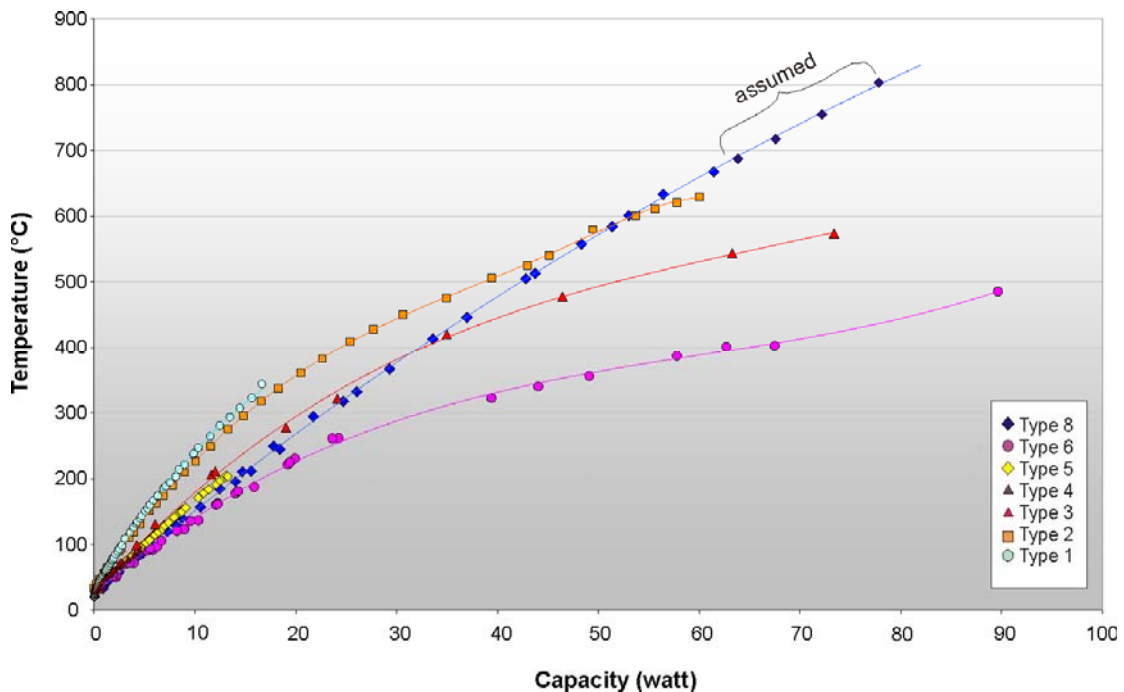
Fig. 4.43 Plot of the maximum temperature reached against the capacity of the different heater types (see Table 4.2). Temperature regulated via the applied current. Heater types 3 and 4 burned through before their capacity was reached. Heater type 8 was not heated to the possible maximum; the small blue diamonds indicate the assumed temperature that could be reached. The dotted lines are the trend lines for the different heaters. A complete list of the heater types with the temperature and capacity measurements are located at the Appendix IV.

The platinum wire resistance heater (type 1) had a resistance that was too high. Therefore, it was possible to reach a maximum temperature of only 343.4°C before the maximum of 30 V was reached. Molybdenum wire was used instead. Heater types 3 and 4 burned through before maximum conditions were reached. The molybdenum heater of

type 8 yielded the best results. The maximum capacity was not completely exploited, and the projected maximum temperature is at least 800°C.

In accordance with this result, a wire length of about 35mm and a diameter of 0.1mm is the most efficient wire specification for the available power supply in conjunction with the specifications of heater type 8 (Table 4.2).

Initially, thin mica plates drilled out of a single crystal were used as insulating material. However, it turned out that a 0.025 mm thick mica plate is not sufficient to stop the loss of heat. A thicker plate had several disadvantages. Because, the mica plates are made from a natural single crystal, it was not possible to get exactly parallel-sided sheets out of it, and critical misalignment was the result. Another disadvantage was the compressibility of the mica sheets when applying pressure onto the backing plate. Adjustment of the diamonds was almost impossible. The interference fringes moved over the culets even when pressure was not being applied or released. The delayed relaxation and compression of the mica sheets are responsible for this effect. After changing the insulating material from mica to pyrophyllite, this effect disappeared. Pyrophyllite has the advantage that it can be burned to absolute hardness, and it also has very efficient properties in avoiding heat loss. A plate of 1mm thickness is enough to minimize heat loss.

In figure 4.44 a direct visual comparison of the original and the new developed heating device is shown. Mechanical drawings of the new heater can be found in the Appendix III.

(A)

(B)
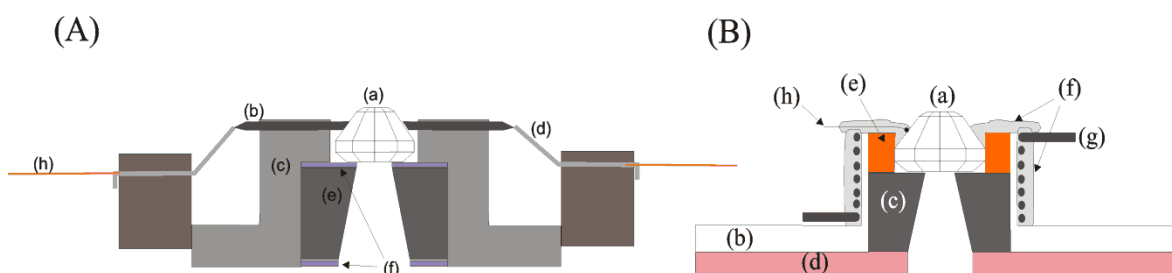
Fig. 4.44: Comparison of the original and new designed heating device. **(A)** Schematic sketch of the original heating device present in the Burchard-Zaitsev HDAC: (a) diamond anvil; (b) tungsten carbide rod electrodes; (c) disk-shaped hardened steel holder; (d) steel wire springs; (e) backing plate; (f) mica sheet; (h) electric connecting wires. **(B)** Schematic sketch of the new heating device developed in this study, (a) diamond anvil; (b) ceramic cap; (c) backing plate; (d) isolating pyrophyllite plate; (e) copper plate; (f) ceramic glue; (g) molybdenum wire; (h) thermocouple.

4.4 Optical equipment

Besides the principal item of the experimental apparatus, the hydrothermal diamond anvil cell, there is additional optical and technical equipment that is very important. The available optical equipment did not meet the requirements of this study for measuring optical phase differences, for keeping the HDAC in the field of view, and for monitoring the experimental run continuously. Hence, it was necessary to change and optimize the available instrumentation.

4.4.1 Microscopes

The HDAC is inserted into the optical path of a polarizing microscope (Leitz, LaborLux). To measure the optical path-length difference of the investigated sample (see section 5.2.2), a Babinet-Soleil compensator had to be integrated into the microscope (Fig. 4.45). Such compensators are primarily used for optical benches, hence the microscope had to be modified to allow insertion of the compensator into the optical path. Figure 4.46 gives an overview of the optical path of the microscope together with the position of the integrated compensator. The compensator is situated behind the rear focal plane of the objective and ahead of the analyzer. The microscope has an UMK32 objective with an overall magnification of 20x.
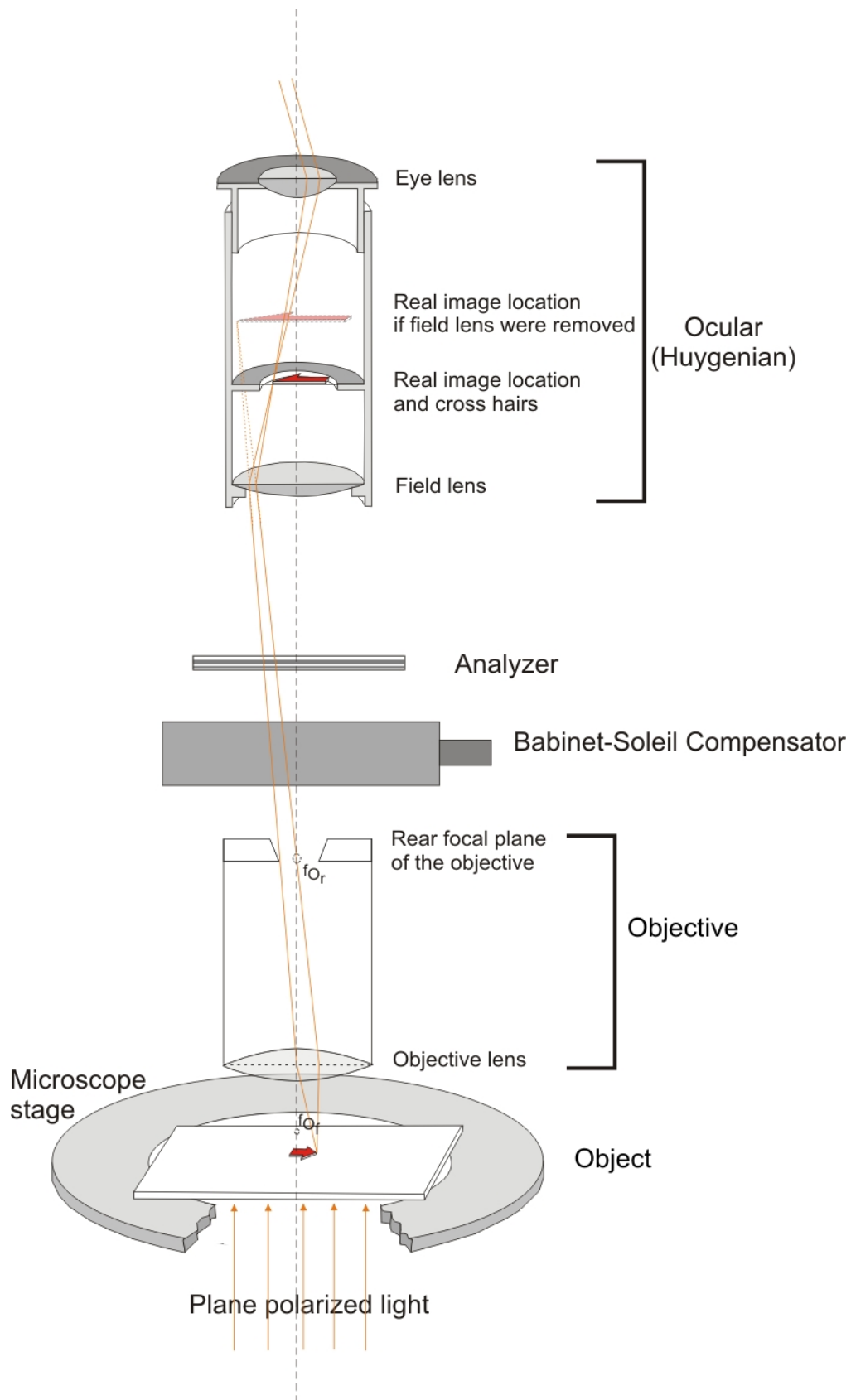
Fig. 4.45: Optical path of the microscope used with integrated Babinet-Soleil compensator. f_{Of} = front focal plane of the objective, f_{Or} = rear focal plane of the objective. The object is indicated by the red arrow.

68

A specially designed plate is integrated into the rotating microscope stage to ensure that the HDAC is centered exactly in the middle of the field of view. A long term alignment of the inside of the sample chamber with respect to the optical path of the microscope is not necessary anymore. This device also ensures that the HDAC will not move out of sight while turning the stage (Fig. 4.46). This is important for the later development of the new *in situ* mass-loss approaches for determining solubility where the image taken needs to show exactly the same detail during the whole experimental run.
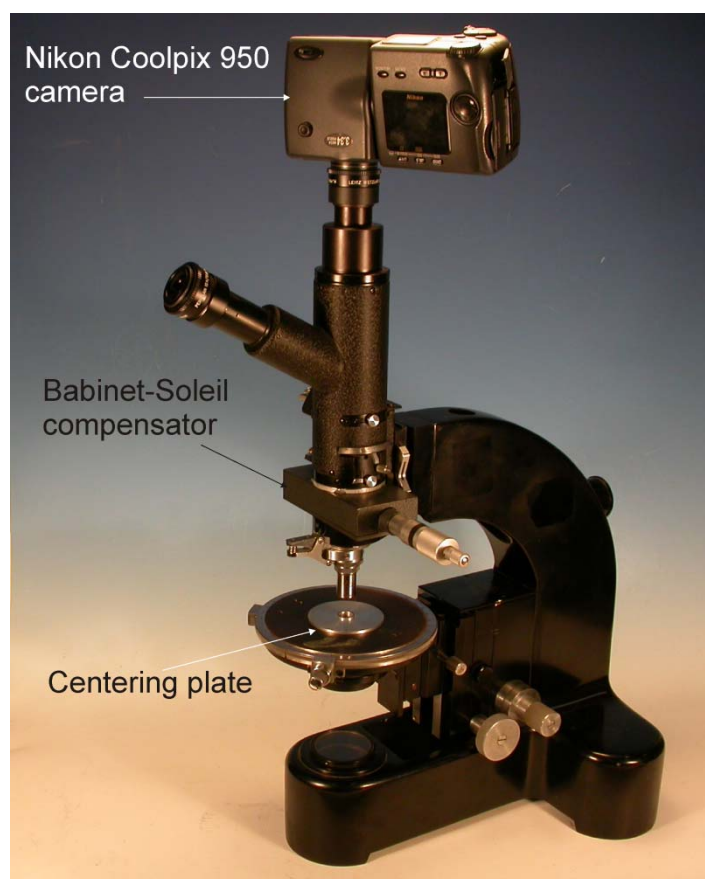
Fig. 4.46: Optimized microscope with Babinet-Soleil compensator, centering plate and a Nikon Coolpix camera.

4.4.2 Camera, receiver, recorder

To take pictures of the sample chamber during experimental runs, a camera (Nikon Coolpix 990) is placed on top of the microscope (see Fig. 4.47). It is connected to a video splitter. Here the signal coming from the camera screen is split and distributed to a large monitor screen and to a computer (Fig. 4.47). The latter permits

continuous monitoring of the reaction path inside the sample chamber and records everything directly to the hard drive. It has the advantage of creating a digital movie at the end of the record. The screen allows direct observation of the sample chamber during the experimental run. A computer program called "Diatronic.exe" (Burchard, personal communication, 2007) overlays the image signal coming from the camera screen with the temperature of the two anvils and the exact time before it is displayed on the large monitor screen and recorded with the first computer. Therefore, it is possible to know the temperature at any time segment of the movie created at the end of an experimental run. Figure 4.47 illustrates a simplified presentation of the optical parts and apparatuses connected to each other as described above, Figure 4.48 shows a zoomed section of the HDAC connected to the temperature regulators and power supply.
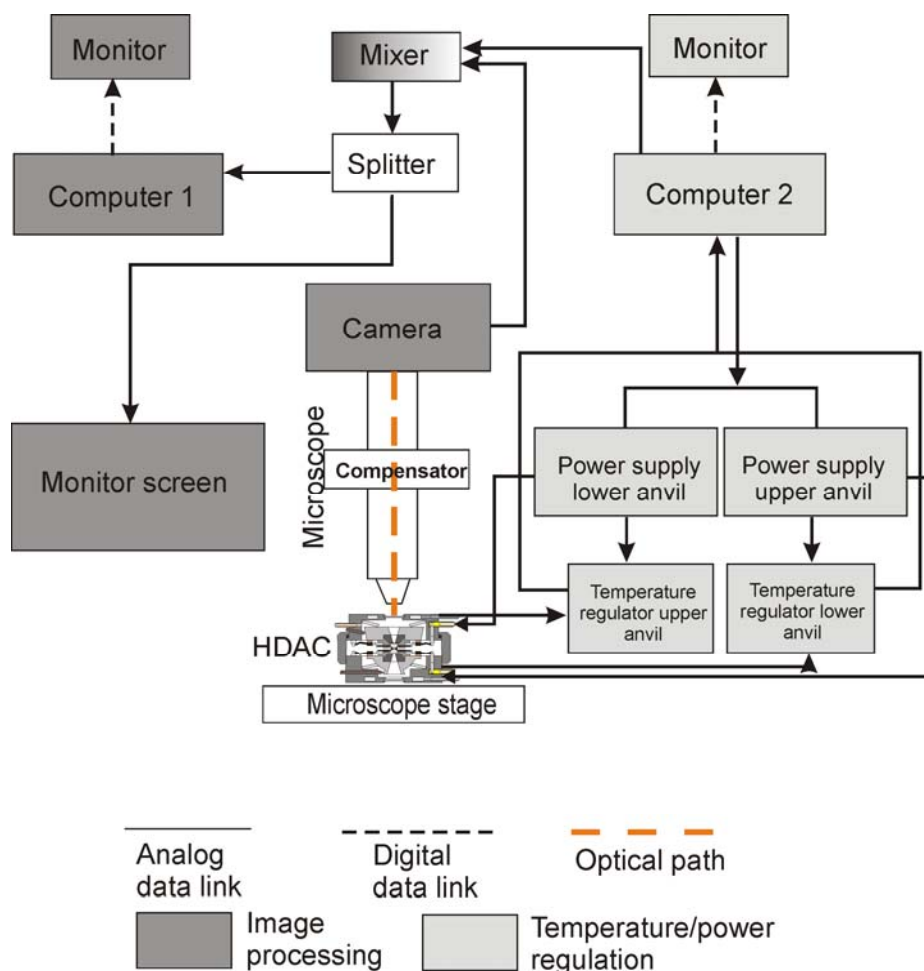
Fig. 4.47: Simplified overview and flow chart of optical and technical equipment as well as their interconnection.
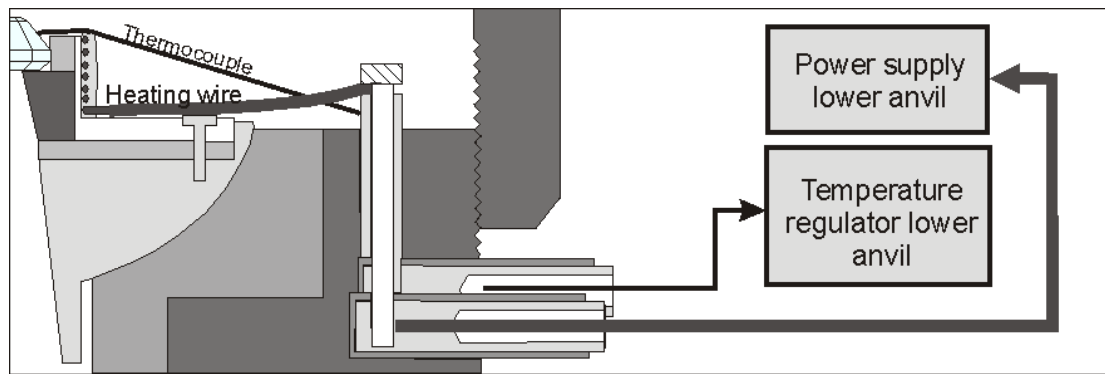
Fig. 4.48: Zoomed detail of part of he HDAC and its connections to the temperature regulator and power supply.

4.5 Micro-spark erosion

Micro-spark erosion or MEDM (Micro Electro Discharge Machining) is considered to be a machining process with a high potential for manufacturing small-size components. It is an electro-thermal process that utilizes spark discharges to erode a conductive material, and is characterized by extremely exact tolerances (Descoeudres, 2006). The tool electrode is mechanical almost unloaded, because there is no mechanical contact between the tool electrode and the workpiece. Therefore, the process is efficient, particularly in the machining of difficult-to-cut materials (Öpöz *et al.*, 2006). All kinds of electrically conductive materials can be machined, irrespective of their hardness and machinability (Braun et al., 1992). This method is therefore especially appropriate for machining materials like hardened steel or rhenium that would be extremely difficult or impossible to handle with any other method.

4.5.1 Theory

The principle of MEDM is to use the eroding effect of controlled electric sparks created between two electrodes (of which one is the workpiece to be machined, while the other is a "consumable tool" = electrode) which are placed in a dielectric medium. The resulting plasma channel vaporizes or melts the electrodes at the point of contact between the electrode material and the dielectric medium. Under controlled conditions, a precise impression of the tool electrode can be duplicated on the workpiece. Figure 4.50 gives a simple overview of the erosion process of a single MEDM discharge.

The workpiece and electrode are connected to the current source. An electrical potential is applied between the workpiece and tool (Fig. 4.49A). Where the electric

71

field is strongest, a discharge is initiated (Behrens and Witzak, 1997). In this electric field, electrons and positive free ions are accelerated to high velocities and rapidly form an ionized channel that conducts electricity. The current flows between the electrode and workpiece, is causing a great number of collisions between the particles. Due to the high current densities a plasma zone is created (Fig. 4.49B). The plasma zone reaches very high temperatures of approximately 8000°C to 12000°C. This causes instantaneous local melting of a certain amount of the material at the surface of the two conductors (Fig. 4.49C).
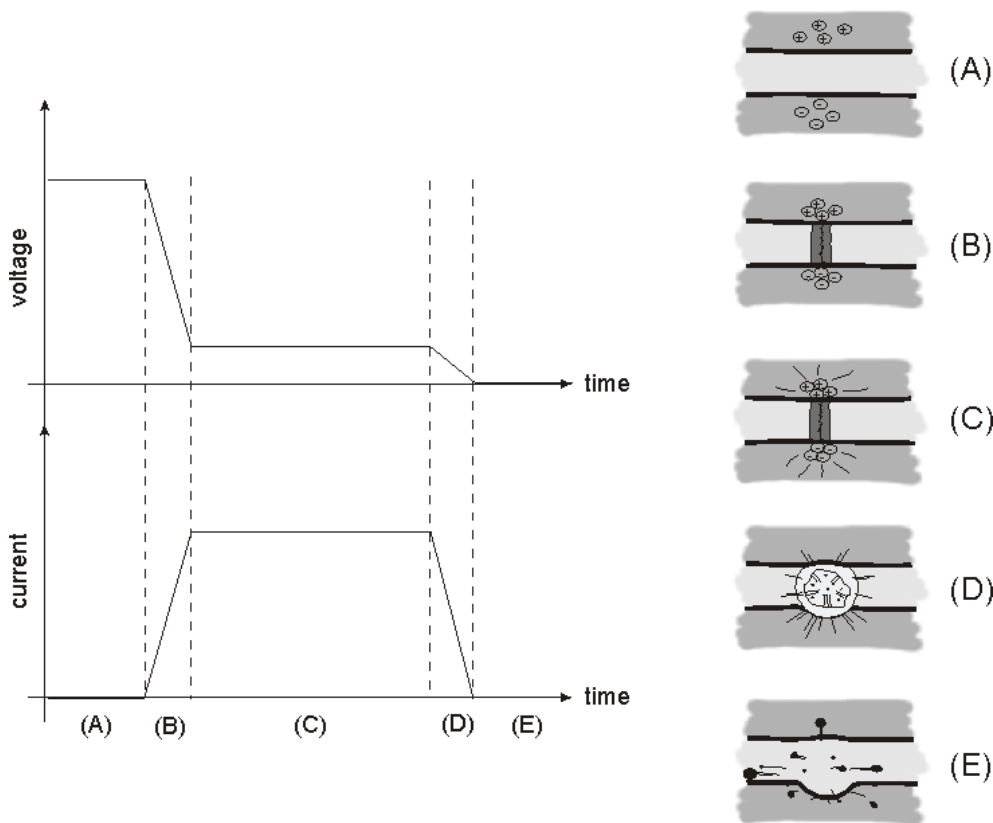
Fig. 4.49: Principle of the MEDM process. **(A)** Voltage applied between electrode and workpiece; **(B)** dielectric breakdown, creation of the plasma channel; **(C)** discharge: heating, melting and vaporizing of the workpiece material; **(D)** end of discharge: plasma implosion, removal of the molten metal pool; **(E)** post-discharge: solidifying and flushing of the eroded particles by the dielectric medium (modified from Descoeudres, 2006).

When the current is cut off, the sudden reduction in temperature and pressure imposed by the surrounding dielectric medium causes the plasma to implode (Fig. 4.49D), which projects the melted material away from the workpiece, leaving a tiny crater (Fig. 4.49E) (Descoeudres, 2006). The eroded material resolidifies in the

dielectric medium in the form of small spheres and is removed with the dielectric medium. Hence, under controlled conditions, a precise impression of the electrode can be duplicated on to the work piece.

4.5.2 Optimization of the construction

The gasket material used in this study was mainly rhenium. The gaskets were initially mechanically drilled in the workshop of the Institute of Geology, Mineralogy and Geophysics, Ruhr-University of Bochum. Nevertheless, the resulting sample chamber was not of good quality (Fig. 4.50). The hole dimensions that are needed to calculate the sample-chamber volume are not defined exactly enough. In addition, the rim of the chamber is wavy and cratered. For good-quality volume calculations this method of drilling the sample chamber is very unsatisfactory.
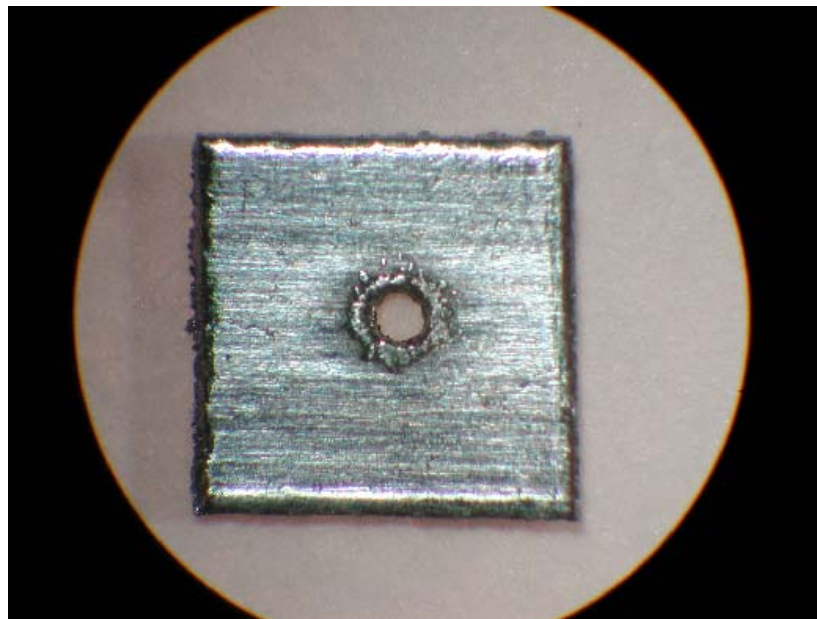
Fig. 4.50: Rhenium gasket drilled mechanically. The resulting sample chamber dimensions (e.*g.* the hole dimensions) are insufficient for good-quality volume determinations. The hole is not round and the rim of the hole is cratered and wavy.

In order to erode gaskets made of rhenium, an old microscope was converted into a micro-spark erosion apparatus (Fig. 4.51). Prof Ahsbahs of the Philipps University of Marburg had invented a micro-spark erosion apparatus which served as the basic principle (Ahsbahs, personal communication, 2008). To meet the requirement that the workpiece (rhenium gaskets) actually had to be viewed, a light source (b) was installed into the microscope between the nose-piece (d) and the oculars (a) to obtain

reflected light. The gasket is placed inside a small container (f) which is filled with the dielectric fluid during the erosion process. This container was provided by Prof. Ahsbahs. The gasket must be centered underneath the reflected-light beam. Therefore a table (h), moveable in x, y direction, was installed on which the container (f) is attached on a holder (g) and insulated. The tool electrode (e), made of copper or tungsten carbide, is screwed into a centering nosepiece (d). This system, in conjunction with oculars having centering rings (a), ensures that the electrode can be centered exactly to guarantee that the resulting sample chamber will be located in the middle of the gasket. Thus, gasket failure and the loss of sample and pressurizing fluid are minimized during experiments.
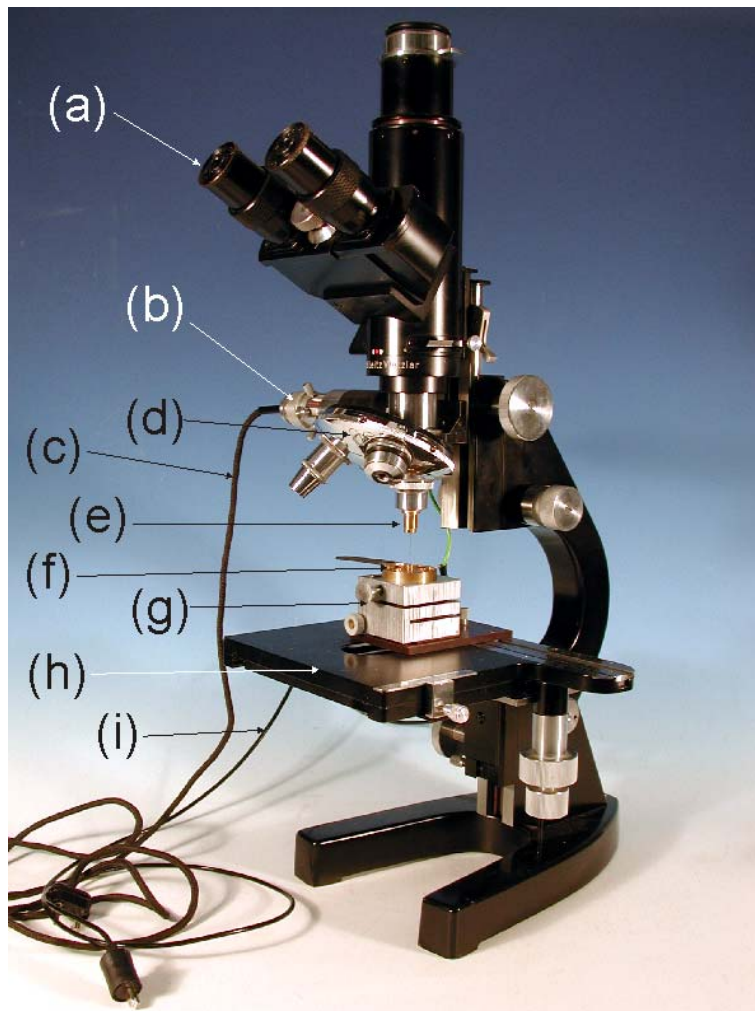
Fig. 4.51: Micro-sparking erosion apparatus. (a) Oculars with centering rings; (b) reflected light; (c) its connection to electric current source; (d) centering nosepiece; (e) tool electrode; (f) container with gasket (work piece) and dielectric fluid; (g) container holder; (h) movable table in x, y direction; (i) apparatus connection to the current source. The current source and the electric source for the reflected light are not displayed in this image.

Using liquid mineral-oil derivatives as dielectric fluid has considerable advantages. Disruptive strength is greater. Smaller spark gaps can be used, making higher precision possible. Spark frequency can be increased and metal particles can be removed without difficulty. Therefore, petroleum was used as the dielectric fluid. The electrical system for this micro-spark erosion apparatus was provided by Prof. Ahsbahs.

Figure 4.52 shows a comparison between rhenium gaskets drilled mechanically and those drilled by using the optimized micro-spark erosion apparatus of this study. It can easily be seen that using micro-spark erosion will result in perfectly round and sharp-edged sample-chamber dimensions.
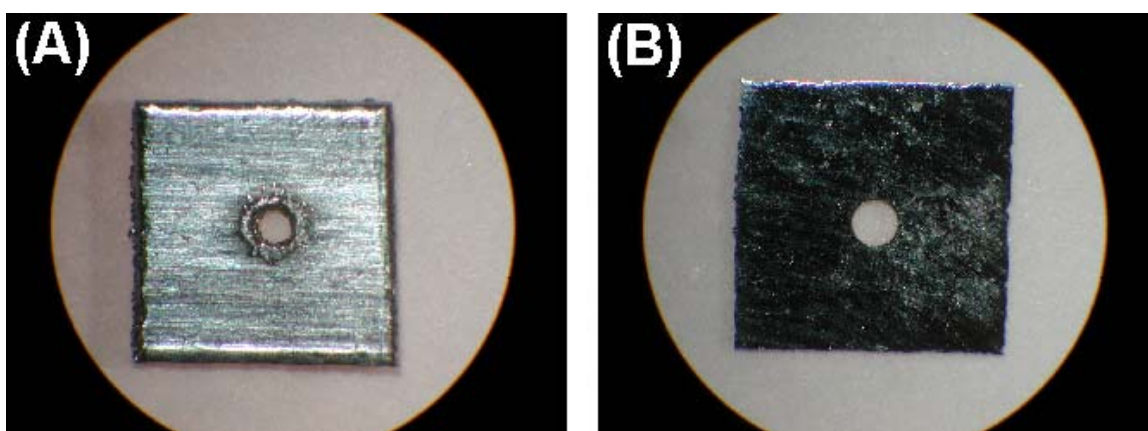
Fig. 4.52: Comparison between rhenium gaskets. **(A)** Rhenium gasket drilled mechanically; **(B)** rhenium gasket drilled by using the optimized micro-spark erosion apparatus.

4.6 Experimental procedure and method

After the alignment of the diamond anvils, the two type-K thermocouples which are attached to the diamonds must be calibrated. This was done using the following melting points: $S_2 = 112.8°C$, $NaNO_3 = 306.8°C$ and $CsCl = 645°C$ (Fig. 4.53).
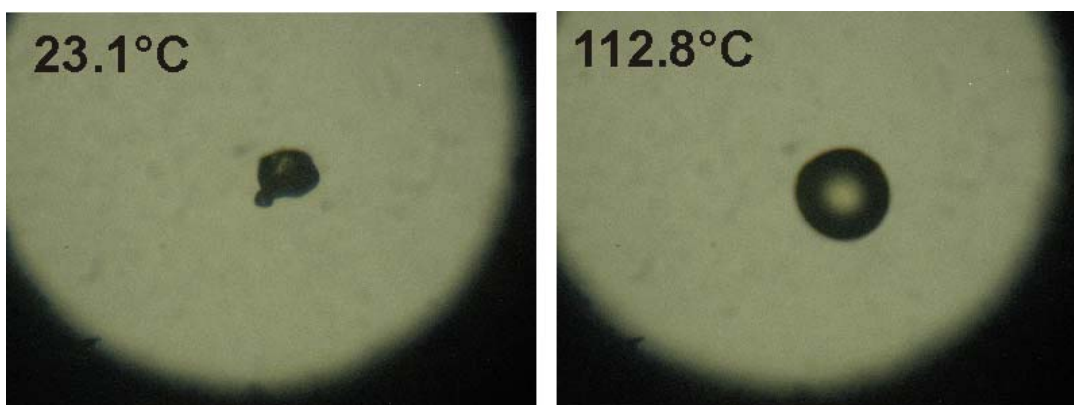
Fig. 4.53: Calibration of thermocouples: Melting of sulphur. At 23.1°C: solid; at 112.8°C liquid sulphur.

After calibration of the thermocouples, a pre-indented gasket is placed on top of the lower anvil with its hole exactly centered in the middle of the culet. The hole inside the gasket serves as the actual sample chamber. During this study it turned out that it is best to glue the edges of the gasket to the ceramic cement on top of the heater (Fig. 4.54).
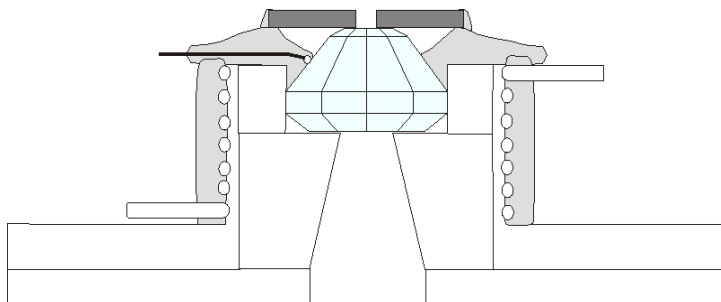
Fig. 4.54: Schematic sketch of a gasket glued onto the ceramic cement covering the top of the heating device.

This procedure prevented the gasket from falling or sliding away from its culet position when the cell is moved. With this technique, sample and fluid can be held inside the chamber easily while closing the cell. With the help of a very thin needle, or a piece of thermocouple wire, the initial sample is then loaded into the sample chamber (i.e. the hole in the middle of the gasket). Great care has to be taken not to contaminate the chamber while loading the sample. The pure doubly distilled water is placed in the chamber indirectly. To do this a water droplet is placed on top of the upper culet. The adhesive power will keep the droplet in place when the upper cell part is turned upside-down. This part of the cell then closes the cell and the upper anvil seals the sample chamber, confining the water inside the chamber. The closing procedure has to be done very quickly to prevent the fluid from evaporating before the upper anvil seals the chamber. The manually closed HDAC is then quickly clamped in a three-jaw drill chuck. By turning the pipe wrench laid around the nut of the HDAC, force is applied onto the anvils.

Temperature can be directly obtained from the thermocouple readings. Pressure can be calculated indirectly by using the equation of state of water (see section 3.5.3). In order to do so an air-bubble inside the sample chamber is required. Sometimes an air-bubble is present after closing the sample chamber. Unfortunately, when applying pressure small air-bubbles will homogenize with the fluid before the pressure is great enough to seal the sample chamber. If this happens and if no air-bubble is present from the beginning, a leakage has to be caused. Therefore, the sample chamber is heated to

about 100°C and the HDAC slowly opened until enough water vapor has vanished from the chamber. An air-bubble will appear which will grow depending on the amount of leaked water. If the air-bubble is large enough for the pressure to be attained, the sample chamber is closed quickly and pressure can be applied.

The cooling system will keep the cell body near room temperature. A water pressure as low as 1 bar is sufficient enough. During experiments, the cell is flushed with argon gas with 5% hydrogen to prevent oxidation of the diamonds and the molybdenum heater at higher temperatures.

5 Development of new *in situ* mass-loss approaches for determining mineral solubility

5.1 Crystal volume computation method

5.1.1 Theory

In 2004, Wang *et al.* developed an *in situ* mass-loss method for determining solubility of SiO_2 with a classical Bassett-type HDAC. Natural quartz samples were abraded into spherical shapes and then reacted with pure water. The spherical shapes were treated as ellipsoids. The mass of the ellipsoids was calculated based on the length of the two principal axes. Wang *et al.* (2004) determined the solubility within a range of 126-490°C and up to 8.9 kbar (Fig. 5.1).
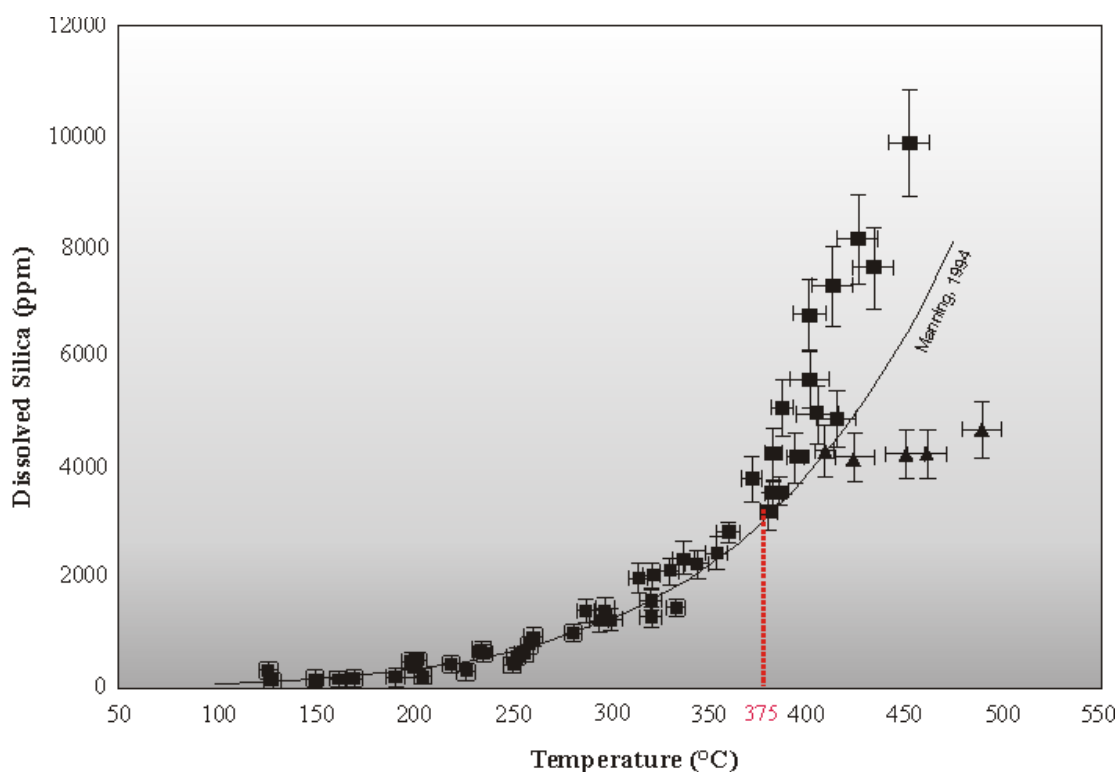
Fig. 5.1: Modified after Wang *et al.* (2004). Solubility curve for isochoric experiments at $\rho = 0.99$ g/cm^3. Squares and triangles represent experimental data; solid black line represents a fit to experimental solubility data (Manning, 1994).

The solid line in Figure 5.1 is the quartz saturation curve calculated from experimental data by Manning (1994). In the study of Wang *et al.* (2004), accurate experimental determination of SiO_2 solubility was limited to temperatures below 375°C,

because of over- and underestimation of the solubility above this temperature. The refaceting of the spheres to approach a trigonal habit at temperatures above 350°C was the major contribution to this deviation from the trend expected from Manning (1994).

The new approach developed in this study makes use of the fact that quartz crystals will attempt to attain a trigonal habit at temperatures above 350°C, as shown by Wang *et al.* (2004) and also by experiments in the present study. An idiomorphic quartz crystal is placed in the sample chamber together with pure water and a vapor bubble (Fig. 5.2). During heating the initial grain partially dissolves into the solution. During cooling of the system SiO_2 reprecipitates and refacets the grain into a trigonal habit (Fig. 5.2). However, in this study it has also been observed that the quartz crystals will refacet not only during cooling but also during heating if the crystal has enough time to equilibrate (between 20 minutes to almost an hour are needed to refacet, depending on temperature and pressure).
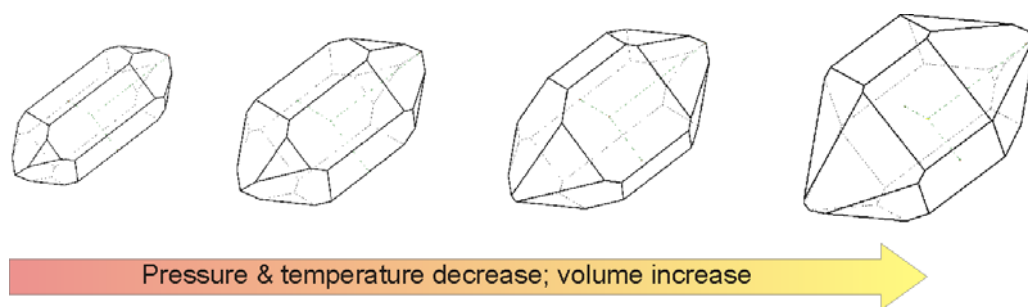
Fig. 5.2: Schematic sketch of the evolution of a quartz crystal. During cooling the SiO_2 reprecipitates and refacets the grain. The volume increases.

A single idiomorphic crystal is used as starting material whose geometric shape is determined before the experimental run. With this prior knowledge of the original volume and mass, absolute solubility can be determined. By comparing masses at various P, T conditions relative changes in solubility can also be determined.

This method allows multiple and reversible determinations along a given fluid isochore. It also yields information about the kinetics of growth and dissolution processes.

5.1.2 Requirements

In order to determine the crystal's shape and geometry accurately, technical equipment is required as well as a computer program to model the crystal's shape.

The technical requirements for the equipment are good-quality lighting to illuminate the crystal inside the sample chamber. Great care has to be taken in choosing the light source to prevent total reflection on the crystal faces from insufficient illumination. A camera is also needed to obtain images of the different crystal shapes at various P, T conditions. A video system is required to make digital movies from the experimental run with overlaid temperature and corresponding time to yield information about kinetic processes.

In order to model the crystal while its geometry is changing a computer program is needed. In this program the user is required to trace all faces of the crystal separately, and also to take into account any deformation of faces. In order to trace all faces correctly, it is necessary to upload the digital images of the crystal that were taken during the experimental run. An algorithm is then required to calculate the volume of the modeled crystal.

Legends of symbols and abbreviation can be found in the Appendix I and II.

5.1.3 Solutions and results

5.1.3.1 Technical equipment

To facilitate the illumination requirement described above, the use of a microscope is necessary. For an optimal quality of the microscope image, it is important that the object field be illuminated homogeneously. Consequently it is necessary to align the optical system in order to achieve a parallel optical path. Therefore the system (light-source—collector—condenser—microscope and stage—objective—ocular) is aligned along one common axis and the illumination system is adjusted according to Köhler (Müller and Raith, 1993).

A digital camera (Nikon Coolpix 990) is placed on top of the microscope to provide images of the crystal's geometry. An automatic release is provided to ensure sharp images.

A video system is connected to the camera consisting of two computers, an interface and splitter (Fig. 5.3). The first computer is provided with a program called "Diatronic.exe" (Burchard, personal communication, 2007) to record the time of the experimental run. It also records the temperature measured by the thermocouples and sends the time and temperature information to the interface. Here the time and temperature measurements are synchronized with the digital image provided from the camera and sent to a splitter. The splitter distributes the generated image information to

different output sources: the second computer and a video screen. The second computer is provided with a program to record the generated image, to create a digital movie out of it and to save it on an external hard drive. The video screen is used for monitoring the inside of the sample chamber.
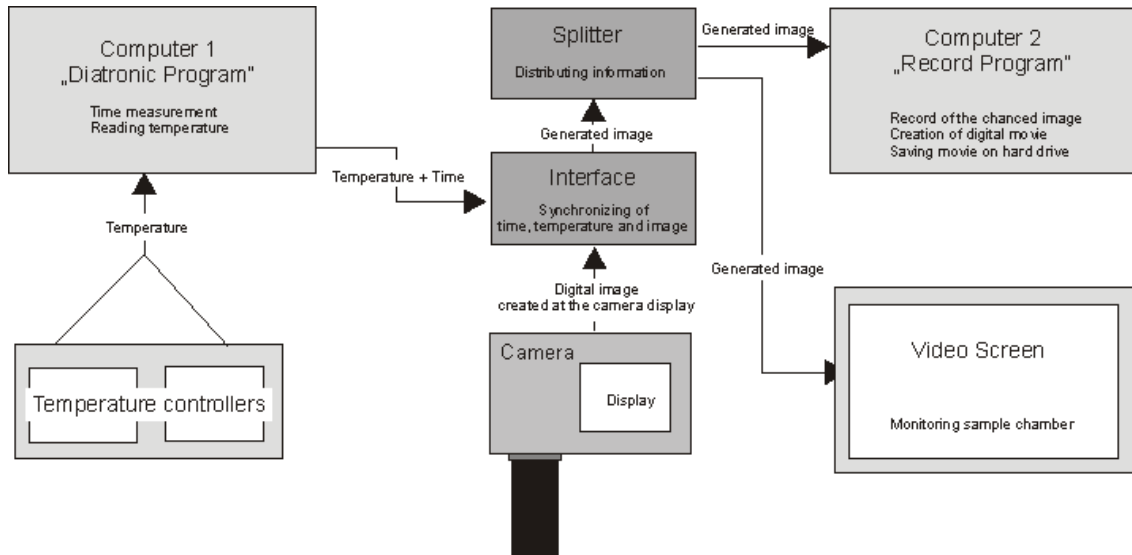
Fig. 5.3: Schematic sketch of the assembled video system connected to the camera used in this study. For explanations see text.

5.1.3.2 "Kristall2000" software

To model the crystal's shape, a computer program called "Kristall2000" is used. It combines crystal forms in all crystal classes to model single crystals in different morphologies (*German:* Tracht) and various habits (Schilling, 2008).

Idiomorphic crystals are defined by smooth and even crystal faces which correspond with the crystal's internal structure of atoms. Each crystal face is defined by its intersections with an internal axial system with 3 axes a, b and c and the interaxial angles α, β and γ, which represents the crystal's symmetry (e.g. a = b =c, and α = β = γ = 90° for the cubic system). The intersections of the face with these axes are called Weiss parameters, their reciprocal values, cleared of fractions, are the Miller indices. There are seven principal crystal systems that are further divided in 32 crystal classes which differ in their symmetry (according to the 32 point groups of crystal lattices). A crystal form is the sum of all crystal faces which are generated from one face by the symmetry operations required in the symmetry class of the crystal. For an idealized crystal drawing three basic informations are needed:

(1) the symmetry class of the crystal

(2) the different crystal forms involved

(3) the relative size of the crystal forms.

The latter can easily be described by the distance from the virtual centre of the crystal – a rapidly growing crystal form has a larger central distance and consequently is smaller. This distance value is specified with a parameter "T" within the program (Schilling, personal communication, 2009). A plane with "T"=0 then passes through the origin of the axial coordinate system (Fig. 5.4).
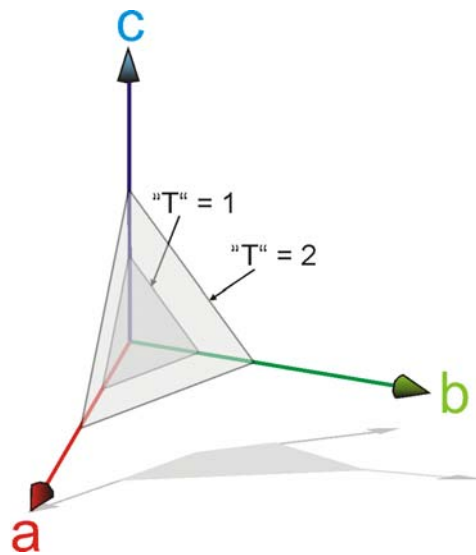
Fig. 5.4: Sketch of axial coordinate system with two planes of similar declination but different distance (described by the parameter "T"; see text) with respect to the origin of the axial system. (modified from Schilling, 2009, personal communication)

The advantage of the "Kristall2000" software is the fact that also malformed or misshaped crystals can be generated. This is accomplished by the fact that the central distance for each face – even if they belong to the same crystal form – can individually be defined.

The "Kristall2000" program was upgraded for the present study to calculate the volume of a crystal. Every crystal face forms the base of a pyramid (Fig. 5.5), whose vertex is located in the origin of the axial coordinate system of the modeled crystal. The sum of all pyramid volumes gives the volume of the entire crystal (Schilling, personal communication, 2009). This method can only be applied to convex bodies, such as single crystals. Therefore it is not possible to calculate the volume of twins, for example.
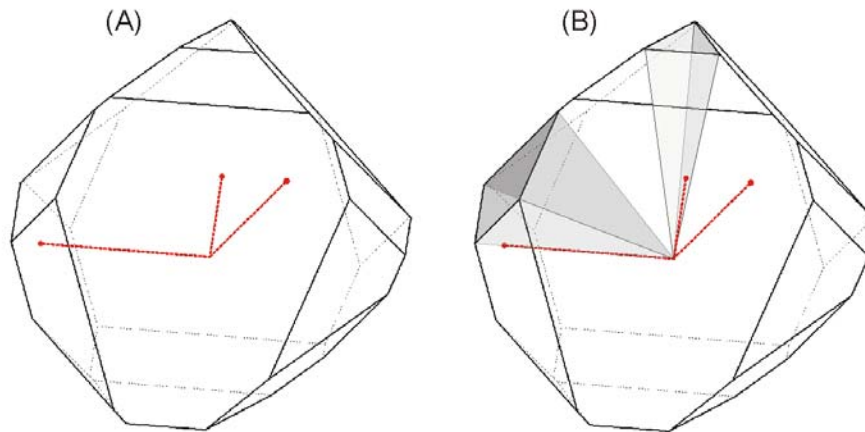
Fig. 5.5: (A) Schematic sketch of a modeled quartz crystal. The red lines represent the internal axial coordinate systems. **(B)** The same crystal with two exemplarily volume pyramids. The crystal faces form the bases of the pyramids and the vertexes are located at the origin of the axial coordinal system. For further explanations see text.

It should be emphasized that, once the morphology of the crystal has been completely described in terms of the above aspects, it is sufficient to determine the dimension of just one crystal edge to calculate the entire volume of the crystal.

5.1.3.3 Error analysis

To gauge the accuracy of the approach, Herkimer quartz crystals were photographed, weighed and then modeled. The calculated masses were then compared to the actual weights determined by direct weighing. The same methodology was used for all weight determinations, and all crystal masses were determined with the crystal volume computation (CVC) method. Thus it can be assumed that the random errors should be similar for all measurements. Uncertainties can therefore be established by pooling repeated mass determinations through the equation

$$\sigma = \sqrt{\frac{1}{n-1}\sum_{i=1}^{n}(x_i - \bar{x})^2} \qquad (E5.1)$$

where σ is the standard deviation, n is the number of mass determinations of one crystal, x_i is the ith determination and $\bar{x}$ is the mean of the mass determinations.

The crystal masses (M) are of course not obtained directly from the Kristall2000 program, which yields crystal volume, but from the relationship $M = \rho \cdot V$, where the density ρ, a well-known parameter, is taken from the literature.

If the result of the determination is a function of multiple measurements, i.e. $f(x_1, x_2, x_3,..)$, every measurement x_i will cause an error $(\sigma f)_i$ in f due to their own errors σx_i. Assuming that $|\sigma x_i| << x_i$ or $|\sigma f_i| << f_i$ the resulting error σf_i is then:

$$(\sigma f_i) = f'(x_i) \cdot \sigma x_i = \frac{\partial f}{\partial x_i} \cdot \sigma x_i \qquad (E5.2)$$

When solving for the derivative $\partial f / \partial x_i$ the remaining parameters $x_{j(\neq i)}$ are held constant. This is permissible if the parameters are independent of each other. The total error σf is then calculated from the Gaussian error propagation:

$$\sigma f = \sqrt{(\sigma f_1)^2 + (\sigma f_2)^2 + ... + (\sigma f_i)^2}$$

$$= \sqrt{(\frac{\partial f}{\partial x_1})^2 \cdot (\sigma x_1)^2 + (\frac{\partial f}{\partial x_2})^2 \cdot (\sigma x_2)^2 + ... + (\frac{\partial f}{\partial x_i})^2 \cdot (\sigma x_i)^2} \qquad (E5.3)$$

Because of the quadratic loading of the errors in equation (E5.3), the largest error will be reflected strongest.

In order to calculate the total error of the new method, a Herkimer quartz crystal was chosen, because of its large number of different faces. To get a well-defined standard deviation an overall number of 64 volume determinations of this crystal were obtained.

Due to optical refraction (Fig. 5.6A) the lower crystal face edges appear in several various positions, highlighted by the dashed colored lines in figure 5.6B.
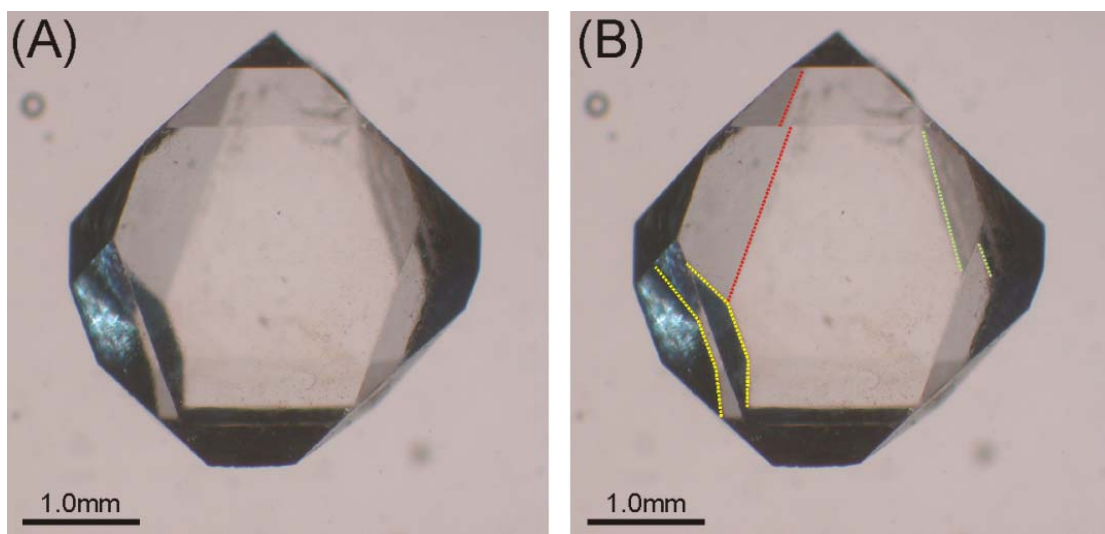
Figure 5.6: Herkimer quartz crystal. **(A)** Original image of the crystal; **(B)** Due to optical refraction the lower face edges are displayed in various positions (indicated by the colored lines).

Therefore, depending on the chosen position of the lower face edges, two different shapes can be obtained for the crystal (Fig. 5.7). In figure 5.7A the lower crystal face is modeled based on the assumption that its edges that are refracted upon the inner upper crystal faces represent the true edge positions. The modeled shape in figure 5.7B is based on the assumption that the positions of the lower crystal face edges, refracted on the outer upper crystal faces, represent the correct ones.
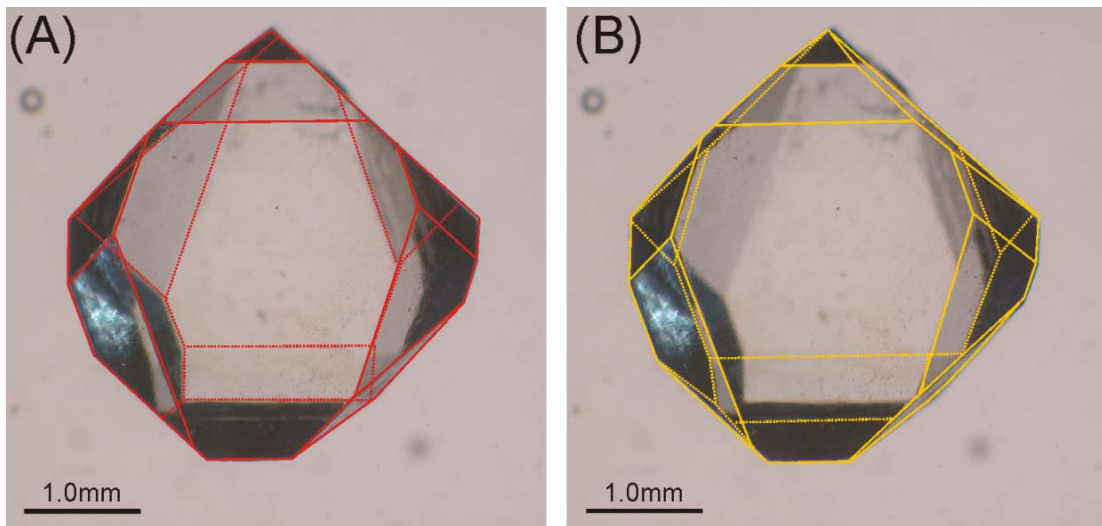
Fig. 5.7: Herkimer quartz crystal with overlaid modeled shape obtained with the Kristall2000 program. Two different shapes are displayed depending on which lower crystal face edges are chosen. **(A)** Shape based on modeling the inner lower faces edges; **(B)** shape based on modeling the outer lower faces edges.

Based on these two principal shapes, multiple remodeling of the same crystal was undertaken. By comparing the resulting masses with the actual weight, it turned out that the calculated masses determined with the second approach (Fig. 5.7B) are significantly too low (see Fig. 5.8). A complete list of the remodeled volume and mass of the Herkimer crystal using the two different principal shapes can be found in the Appendix V.
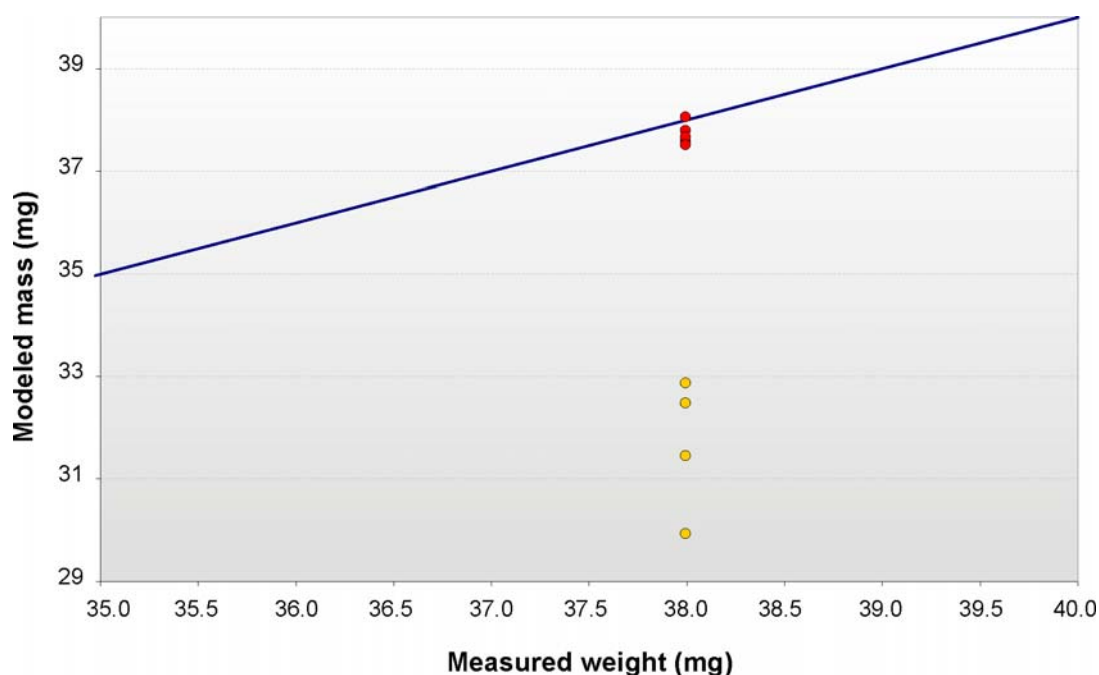
Fig. 5.8: Plot of the modeled masses vs. the actual weight of a Herkimer quartz crystal. The solid red dots are based on the modeled approach shown in Fig. 5.7A, while the yellow dots are based upon the second crystal shape approach (Fig. 5.7B). The blue solid line represents the 1:1 correspondence.

Closer inspection of the second modeled image (yellow crystal shape, Fig. 5.7B) reveals that this shape does not fit well. The arrows in figure 5.9 indicate the position of the face edges where they should be located based on the above conclusion. It can be clearly noticed that the modeled edges, indicated by the red dashed line in figure 5.9, do not coincide with these concluded positions. In addition, assuming that the positions of the lower crystal face edges are refracted on the outer upper crystal faces, will make the lower face larger, meaning that this face will have a smaller distance to the virtual centre of the crystal thus making the whole crystal thinner. This conclusion explains why the modeled masses appear to be too low.
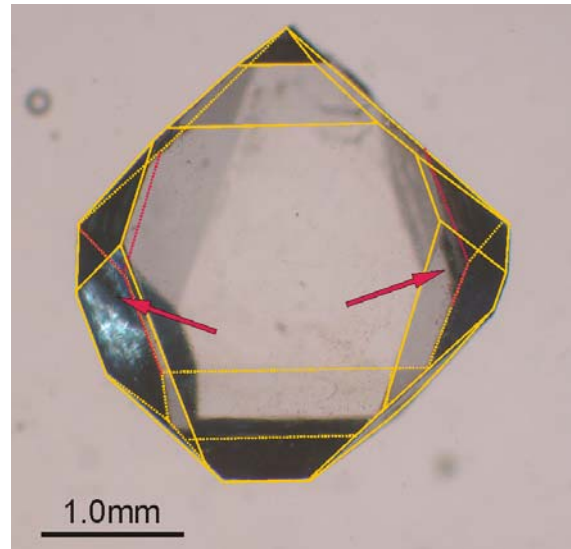
Fig. 5.9: Modeled shape of the Herkimer quartz crystal that is based on the second assumption of modeling. The red arrows indicate the edges that are assumed to be displayed in the true position. The red dotted lines indicate the modeled position of the edges.

A second consideration proves that the first model of the image (red modeled shape, Fig. 5.7A) represents the true shape of the quartz crystal. This conclusion is based on the assumption that the central upper and lower faces of this quartz crystal are coplanar with respect to each other (Fig. 5.10, indicated by the red lines). Based on the consideration that light will not be refracted if travelling through a coplanar medium, the position of the underlying face edges displayed in the image are identical with the true position of these faces. This is also confirmed by the comparison of the masses determined by weighing to those modeled by the CVC method (see Figure 5.8).
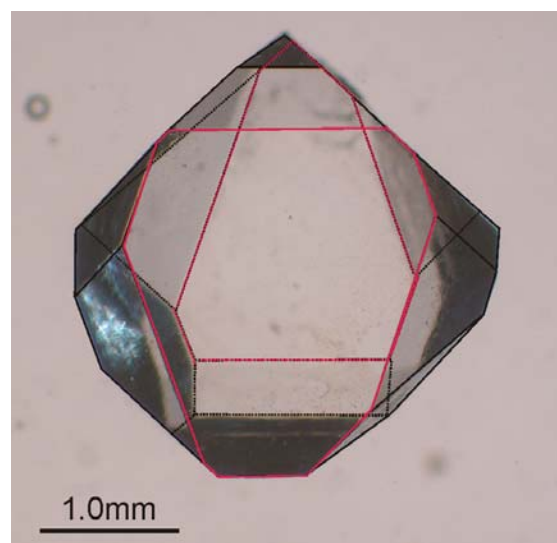
Fig. 5.10: Modeled shape of the Herkimer quartz crystal (black solid and dashed line). The central upper and central lower faces, indicated by the red lines, are coplanar with respect to each other.

In order to calculate the total error of this technique the first modeling approach shown in Fig. 5.7A was choosen. Recall that one measurement of any one crystal face edge uniquely determines the volume of the crystal. A data set was compiled in which the same Herkimer quartz crystal was remodeled 5 times. For each model seven to eight crystal face edges were measured to obtain a good statistic quality of the volume. The result was a set of 36 model/edge combinations that led to 36 unique volume and therefore mass determinations. A standard deviation (σ) of 0.38% using equations E5.1 – E5.3 was yielded. Table 4.1.1 shows an excerpt from this data set with examples of the calculated single data together with its error and the total error of the determined mass. In addition, a total error for the second approach to modeling the crystal shape (Fig. 5.7B) was calculated based upon a set of 28 volume and mass determinations by remodeling the Herkimer crystal 4. This yielded a standard deviation of 6.78%. If both approaches are taken together, a standard deviation of σ = 9.64% would be the result based on a set of 64 mass and volume determinations of 9 re-modelings of the Herkimer crystal. Based on the considerations described above, a σ = 0.38% is assumed to be the real, most representative standard deviation that can be attained with this new method. A table listing all determinations can be found in the Appendix V.

Table 4.1.1: Exemplary compendium of 36 sets of volume and mass determinations of 5 replicated crystal shapes.

Crystal shape type 1	Herkimer no.1a		Herkimer no.2		Herkimer no.6		Herkimer no.8		Herkimer no. 1		Mean value
Edge No.	2	4	1	6	1	3	1	6	3	7	
Volume V (mm^3)	14.243	14.568	14.205	14.321	14.460	14.184	14.100	14.264	14.709	14.232	14.235
ΔV (mm^3)											0.008
Density* ρ (mg/mm^3)	2.650	2.650	2.650	2.650	2.650	2.650	2.650	2.650	2.650	2.650	2.650
$\Delta\rho$ (mg/mm^3)											0.010
Resulting mass M (mg)	37.744	38.605	37.643	37.950	38.318	37.586	37.364	37.799	38.980	37.714	37.722
Total error ΔM$_{total}$ (mg)											0.144
Total error ΔM$_{total}$ (%)											0.382

* Density data is taken from Tröger (1982).

5.1.3.4 Testing the crystal volume computation method

The applicability of this approach was tested on a set of five idiomorphic crystal types: quartz, calcite, anhydrite, smithsonite, gypsum and natrolite. For quartz, calcite and natrolite, crystals of different sizes were also selected. The crystals were quite different in symmetry, shape, weight and complexity of forms. They were selected to test the method for a broader range of morphologies. All grains were weighed 10 times to assure good quality measurements. After weighing the samples, images were obtained with a Nikon Coolpix 990 mounted on a microscope. Each crystal was modeled once. To get a good average of volume for each model, the dimensions of three to five different crystal edges were determined. Hence three to five unique volume and therefore mass determinations for every crystal model were determined. Figure 5.11 plots the measured weight determined with an electronic balance versus the modeled mass from the newly developed approach. The numerical data are given Table 5.2. Densities are taken from Tröger (1982)
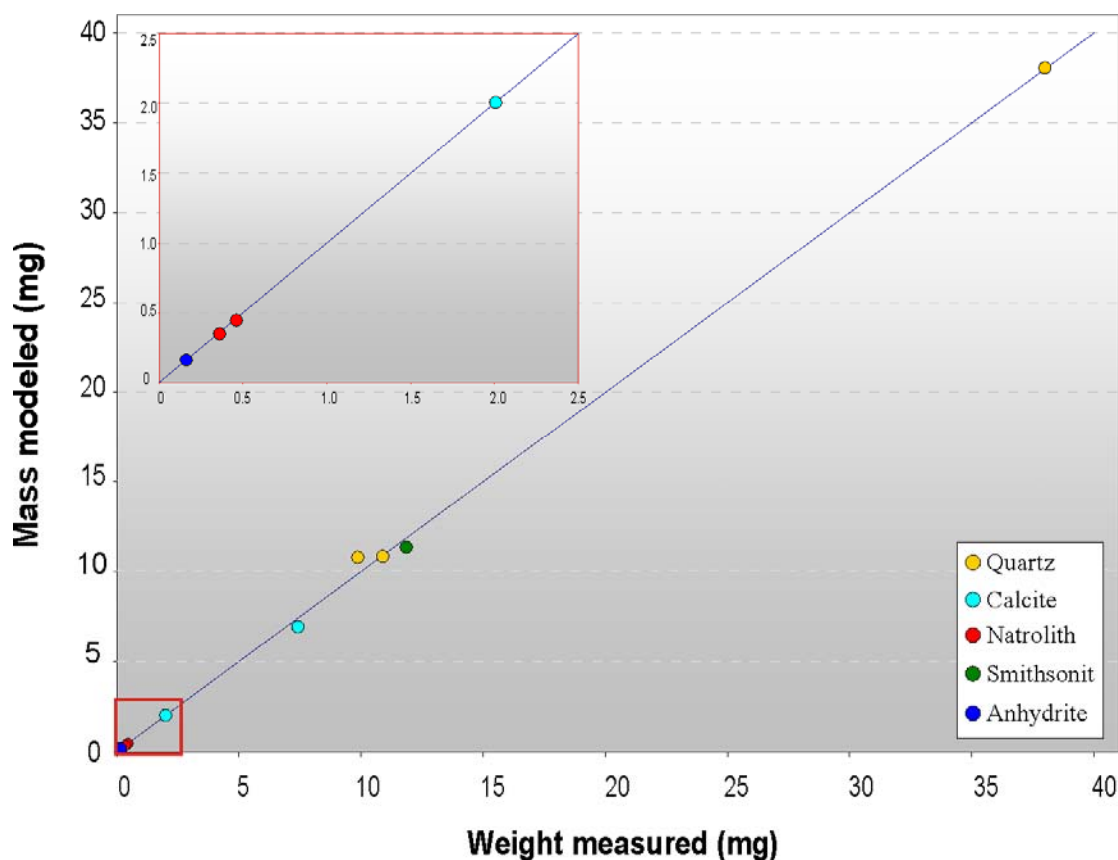
Fig. 5.11: Plot of calculated model mass versus measured weight for a set of five different crystal types.

Table 5.2: Weights and modeled masses for the different crystals of the test set.

Crystal type	Measured weight (mg)	Modeled mass (mg)
Quartz 1	37.992	38.061
Quartz 2	9.871	10.782
Quartz 3	10.833	10.889
Calcite 1	2.007	2.006
Calcite 2	7.417	6.927
Natrolite 1	0.461	0.446
Natrolite 2	0.360	0.349
Smithsonite	11.850	11.346
Anhydrite	0.162	0.162

It should be emphasized that the calcite, anhydrite, natrolite and smithsonite crystals measured are cleavage fragments from larger crystals. Therefore their shape was not exactly idiomorphic (see Fig. 5.12) in the sense assumed by the Kristall2000 program. Because cleavage fragments are not perfect, their modeled weight must be an approximation of the real weight. Nevertheless, as is evident from figure 5.11, the agreement with the true weights is excellent. To model the weight of good quality idiomorphic crystals with complex morphologies, three additional Herkimer quartz crystals were selected, weighed and modeled.
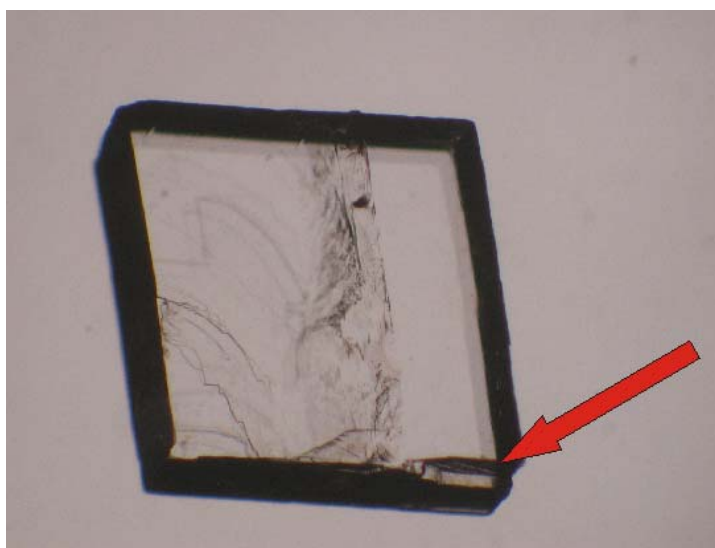
Fig. 5.12: Cleavage fragment of smithsonite. The fragment shows defects due to chipping (red arrow).

5.2 Birefringence mapping

The method of birefringence mapping to obtain the volume of crystal fragments is a totally new approach developed for the first time in this study. Nevertheless, it is based on several rather simple considerations. The mass of a crystal is given by:

1. $$M = \rho \cdot V \tag{E5.4}$$

with M as the mass, ρ the density and V the volume of a crystal and

2. $$V = d \cdot A \tag{E5.5}$$

with d as the mean or integrated thickness and A as the surface of a crystal.

For most common substances the density is known from literature with high precision, and therefore the mass can be determined with the volume as the only unknown variable. Hence a method for determining the thickness and surface area of a crystal can be an appropriate method for calculating crystal mass in a diamond anvil cell. In this study such an approach has been developed for the very first time, based on the quantification of the birefringence seen in mineral crystals and fragments.

5.2.1 Theory

This method uses the fact that non-cubic crystals show birefringence in polarized light. Birefringence is a phenomenon that occurs when linearly polarized light is incident on a transparent anisotropic plate. In general the light is then split into two rays with different properties: a fast ray (extraordinary ray; lower index of refraction (n')) and a slow ray (ordinary ray; higher index of refraction (n'')), both of which are polarized with their vibration direction perpendicular to each other.

Upon emergence from the plate, an optical path difference has developed because of the different velocities of transmission. The slow ray now lags behind the fast ray. If the path difference is designated as Γ, then

$$\Gamma = (\mid n'-n'' \mid)d \tag{E5.6}$$

where Γ is the path difference, n' and n'' are the refractive indices for the components transmitted by the plate and d is the thickness of the plate. The expression ($n'-n''$) is called the birefringence and usually expressed Δn. Therefore, the magnitude of the phase difference depends on the thickness of the crystal plate and the birefringence.

Between crossed polarizers, birefringent materials extinguish 4 times during a full rotation (360°) of the microscope stage in an angle distance of exactly 90°, when the vibration direction of the light transmitted by the sample is parallel to that of the

light transmitted by either the polarizer or the analyzer. These extinction positions of the sample are called "the normal position". Between each of the four extinction positions the sample appears bright; maximum brightness occurs at the halfway position (45° rotation) between two extinctions. The orientation of maximum brightness is called "the diagonal position".

The birefringence of a mineral or other material is generally known from the literature (e.g. Tröger, 1982). Hence, if the phase difference at every point on a crystal can be measured, the thickness of the crystal at every such point can be determined. Therefore, the thickness distribution can be mapped and the volume calculated from equation (E5.5).

5.2.2 Requirements

5.2.2.1 Measurement of path difference

The path difference can be measured in several ways. These methods of measurement are almost exclusively based on compensation that means that the vibrations are produced by birefringent plates, whether they are circular, elliptical, or linear, to linear vibrations oscillating perpendicular to the plane of vibration of the analyzer. The general mechanism of compensation is indicated in figure 1.
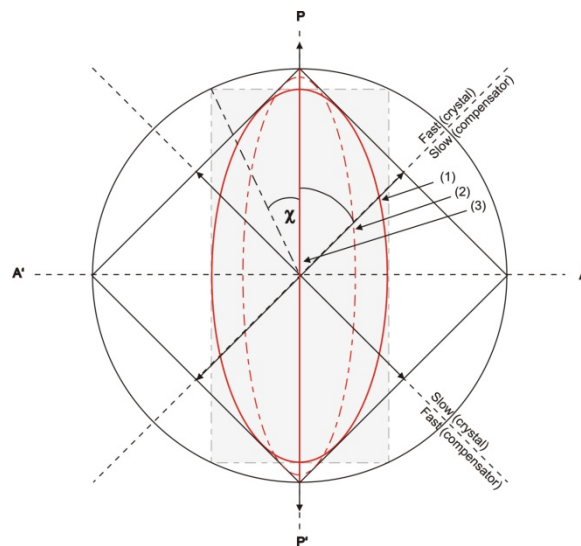
Fig. 5.13: Partial and complete compensation. (1) Initial elliptical motion, (2) effect of introducing ¼ λ plate, (3) complete compensation. AA' :vibration plane of the analyzer; PP': vibration plane of the polarizer.

To get compensation the direction of vibration of the slow component of the compensator must be parallel to the fast direction of the crystal plate so that the

compensator can reduce the path difference produced by the crystal plate. Therefore, phase differences can be measured in the diagonal position only.

At complete compensation the path difference has been reduced to zero and the vibration reaching the analyzer is a linear oscillation parallel to the plane of vibration of the polarizer (PP' in Fig. 5.13). In each position of compensation the intensity of the light passing through the analyzer can be estimated according to the following relationship:

$$I_A = \sin^2 \chi \qquad \text{(E5.7)}$$

With I_A as the intensity of the light leaving the analyzer, and χ measuring the ellipticity. At complete compensation $\chi = 0$ and $I_A = 0$ hold.

In this study compensation of the path difference was measured with two different compensators as described below.

5.2.2.2 Berek compensator

This type of compensator consists of a plate of a uniaxial crystal with perfectly known optical properties, cut perpendicularly to the optical axis and mounted on a horizontal rotating axis in a metal holder. Classical Berek compensators were equipped with calcite plates, more modern designs feature MgF_2. Due to lower birefringence the MgF_2 type is easier to produce in correct orientation and thickness and does not require individual corrections as does the calcite compensator. The Berek compensator used in this study is made of a 1.52 mm thick MgF_2 plate. In the zero degree position the compensator crystal is oriented with its optical axis parallel to the transmitting light-the path difference produced by this orientation is zero. Turning the rotating dial on the compensator in either direction (right-left) inclines the prism relative to the optical axis, lengthens the optical path, and increases the difference between the index of refraction of the ordinary rays (n_0) and extraordinary rays (n_e), which in turn increases the phase difference as shown in figure 5.14.
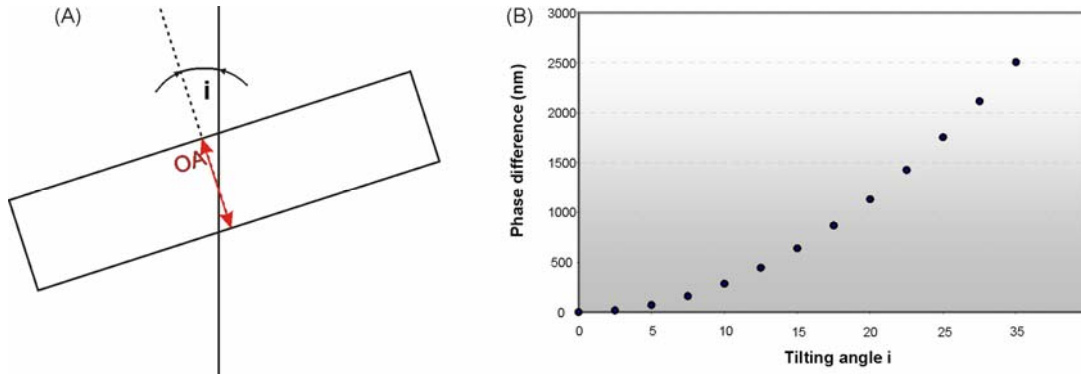
Fig. 5.14: (A) Angle (i) of prism inclination of the Berek compensator (OA) optical axis; **(B)** plot of its phase difference vs. the tilting angle (i).

This results in a dark compensation stripe which moves through the field of view. To measure the phase difference correctly, the compensation stripe has to be aligned with the crosshairs of the ocular.

The phase differences corresponding to the tilt of the compensator plate through the angle *i* are determined according to the equation:

$$\Gamma_\lambda = d \cdot n_o \left(\sqrt{1 - \frac{\sin^2 i}{n_e^2}} - \sqrt{\frac{\sin^2 i}{n_e^2}} \right) \tag{E5.8}$$

with Γ_λ, *d*, n_o, n_e and *i* as the phase difference in nm, the thickness in nm of the compensator plate, the refractive index of the ordinary ray, the refractive index of the extraordinary ray, and tilting angle of the compensator plate, respectively. The compensator equation (E5.8) is strictly spoken only valid if the compensator is located in a parallel optical beam. If the beam is not parallel the interference stripes will be slightly dislocated. This displacement depends on the tilting angle of the compensator plate and on the distance of the compensator with respect to the image plane. In this case a correction value has to be taken into account.

5.2.2.3 Babinet-Soleil compensator

In principle, the Babinet-Soleil compensator is itself a combination of two crystal plates in subtraction position, one of them variable in thickness and the other with a fixed thickness. In the classical Babinet design, change of thickness was achieved by moving a wedge laterally with respect to the parallel crystal plate. As in the case of the Berek

compensator, this results in a dark compensation stripe which moves through the field of view.

To overcome this problem and to create homogeneous compensation throughout the whole field of view, the Babinet-Soleil compensator is a sandwich of three crystal plates (Fig. 5.15). The quartz plate A is cut in such a way that its optical axis is parallel to its long dimension (indicated in Fig. 5.15 by the arrow).
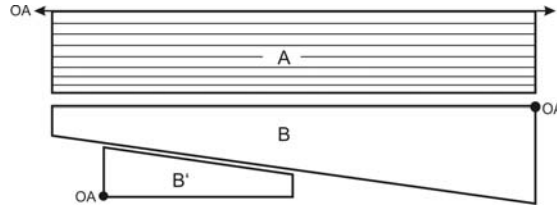
Fig. 5.15: Cross section of a Babinet-Soleil compensator. OA = optical axes.

The optical axes (OA) of the two wedges B and B' are parallel to the edges of the wedges as indicated by the black dots in Fig. 5.15. The wedges are arranged in such a way that they result in a coplanar plate. Therefore, the compensator produces homogenous compensation over the field of view.

The lower quartz wedge is adjustable underneath the upper wedge and either thickens or thins the resulting coplanar plate. With this arrangement the slow (n_o) and fast (n_e) component of one coplanar plate oppose the fast and slow components of the other coplanar plate.
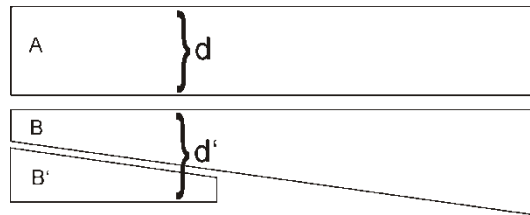
Fig. 5.16: Thickness d and d' of the traversed plates. If d =d' compensation is produced.

If the thicknesses of the traversed plates are called d and d' (Fig. 5.16) the phase difference of the upper plate (Γ_u) according to equation (5.6) is then given by

$$\Gamma_u = d(n_e - n_o) \tag{E5.9}$$

and the phase difference of the lower plate (Γ_l)

$$\Gamma_l = d'(n_o - n_e) \tag{E5.10}$$

Where the light passes through the same thickness in both plates (d=d') no path difference is produced for the emerging light, and compensation is complete according to:

$$\Gamma_u + \Gamma_l = d(n_e - n_o) + d'(n_o - n_e) = 0 \qquad (E5.11)$$

This wedge position is called zero setting.

If the lower wedge is now moved underneath the upper wedge, the thickness of the resulting plate is then d'+ Θ >d (Fig. 5.17).
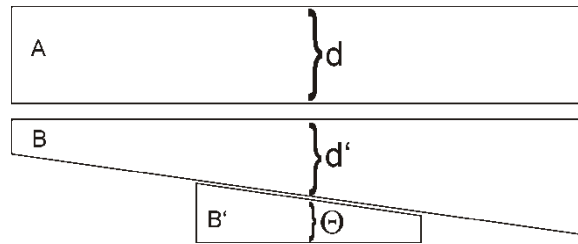
Fig. 5.17: Thickness d' of the resulting lower coplanar plate compared to the thickness d of the upper plate. Θ indicates the excess in thickness of d' - d.

The excess (Θ) of the thickness over the plate is crucial for the phase difference according to:

$$\Gamma_u + \Gamma_l = d(n_e - n_o) + (d'+\Theta)(n_o - n_e) = \Theta(n_o - n_e) \qquad (E5.12)$$

5.2.3 Solutions

5.2.3.1 Determination of the crystal thickness

According to equation E5.5, it is necessary to determine a crystal's thicknesses in order to calculate its volume, and, as described above, the thickness can be measured with the help of a compensator. This next section describes a new procedure for mapping out the thicknesses of a crystal. Both compensator types described above in section 5.2.2 were tested in detail. The unequivocal "best choice" turned out to be the Babinet-Soleil compensator, a preference best demonstrated when all the details of data acquisition have been presented. Thus, the following section will concentrate on measuring procedures using the Babinet-Soleil compensator.

By turning the micrometer scale of the Babinet-Soleil compensator, the small quartz wedge of the compensator will be moved underneath the upper quartz wedge and will thicken the resulting coplanar plate of the compensator (see Fig. 5.16 and 5.17). At some point the resulting phase difference of the compensator will compensate the phase

difference of the studied crystal. If the crystal has a homogeneous thickness (e.g. in a thin section), then the whole crystal will appear dark. If the crystal has an inhomogeneous thickness, as is generally the case with a fragment of a larger crystal, a dark area would appear within the crystal that represents that part of the crystal's thickness that has been compensated. By turning the micrometer scale of the compensator further, this dark compensated area would travel over the surface of the crystal, and thus the thickness of the whole crystal can be mapped. Figure 5.18 shows a quartz wedge as it would appear under the microscope if the micrometer scale of the compensator is turned. The dark area moves from the thinnest part of the crystal through to the thickest part.
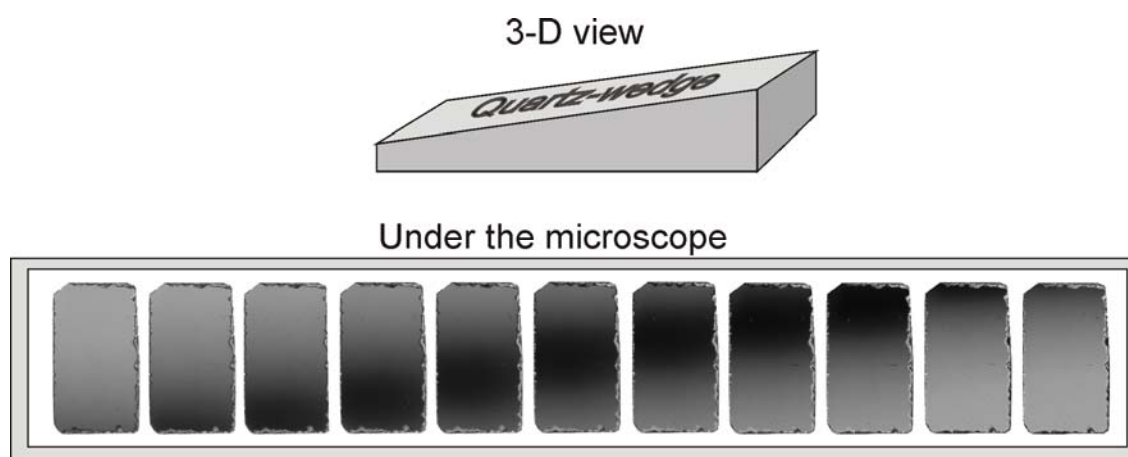
Fig. 5.18: 3-Dimensional view of a hypothetical quartz wedge and a sequence of images of a real crystal wedge (gray-scale) that would be observed under a microscope as the Babinet-Soleil compensator is adjusted. The black area (that part of the crystal that has been compensated) moves from the thinnest part of the wedge (start of the sequence at left) towards the thickest part of the wedge (at the right).

For each compensator position a photograph is taken. In the case of Figure 5.18 it would be 11 images. Great care has to be taken that the shutter speed and aperture produced by the camera have the same value for each image, to ensure comparable images. Therefore, the camera setting is fixed. In the manual program of the camera the user must control the shutter speed and aperture. The focus is set to infinite in order to ensure the same focus for each image taken.

For each image the corresponding phase difference of the compensated part (Γ_i) is known from the micrometer scale of the compensator and hence the thickness of this compensated part of the crystal can be calculated by converting equation (E5.6) into

$$d_i = \frac{\Gamma_i}{\Delta n_j} \qquad \text{(E5.13)}$$

with d_i = thickness of the area i of a crystal j; x_i = phase difference of the area i of a crystal j and Δn_j = birefringence of a crystal j.

Thus, if the surface of the compensated areas can be quantified, the volume of the crystal can be calculated (equation E5.5). In Figure 5.19 the procedure is shown schematically together with the required equations.

The thickness of the crystal is then the sum of all thickness parts of the crystal.

$$d_j = \Sigma d_i \qquad \text{(E5.14)}$$

with d_j = thickness of the whole crystal. In figure 5.19 the procedure is shown schematically together with the equations needed.
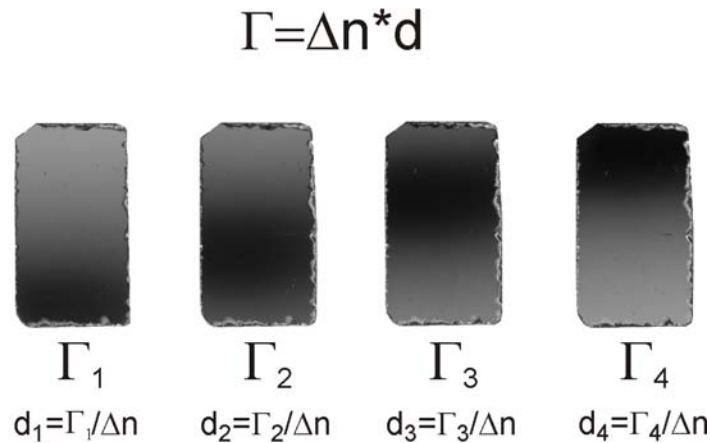
Fig. 5.19: Four pictures taken at different compensator positions with resulting positions of the dark compensated area with equation to calculate the thickness of that crystal part.

In Figure 5.18 it can be seen that that the dark area has diffuse rims. In order to define these areas precisely, the images are converted with the help of a defined threshold value. The threshold value turns pixel with a brightness value above or below this threshold into either white or black. A black and white image is produced with a defined width of the dark area (Fig. 5.20).
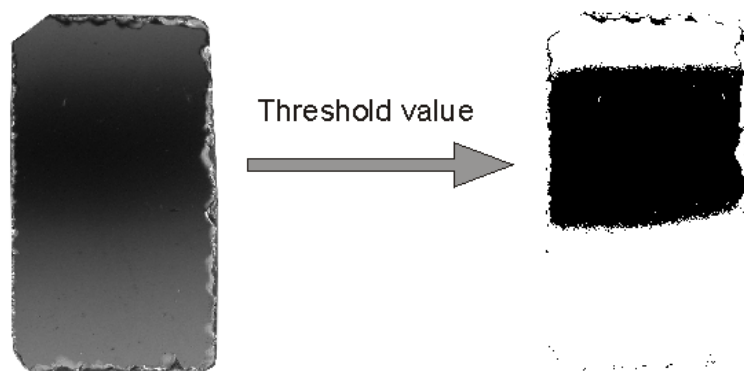
Fig. 5.20: Original picture of a quartz wedge with the black stripe (the compensated thickness part of the crystal) that is converted with a threshold value. Pixel values above or under the threshold are turned into white and black.

Figure 5.18 shows that the dark areas overlap each other. The overlap is the average of the overlapping images and hence has to be taken into account. In order to determine the width of the overlap all the images are coded with different colors. The overlap can now be determined precisely and again is color-coded. Figure 5.21 shows an example of the determination of the overlap width by coloring the two overlapping images differently.
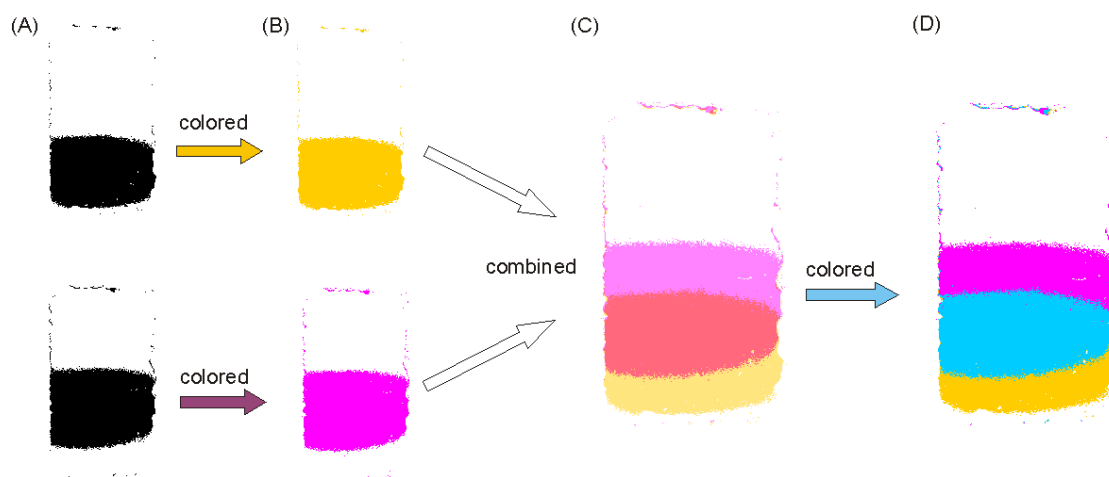
Fig. 5.21: Sketched example of the determination of the width of the overlap produced by two images. **(a)** Original black and white images with the defined black areas; **(b)** the two images are colored-coded; **(c)** enlarged image of the combination of the two images which defines the overlap (red area); **(d)** the overlap is again color-coded (blue area).

Each color thus stands for a defined phase difference, and hence for a definable thickness of the crystal. The thickness of the "overlap-color" can be calculated, as it is the average of the thicknesses of the colored areas that produced the interaction. This

procedure is carried out for every image taken, and as a result a summary image is created that represents a map of the thickness distribution of the crystal (Fig. 5.22). The 24 Bit RGB color model is used and hence a maximum of 24 pictures can be taken for one crystal.
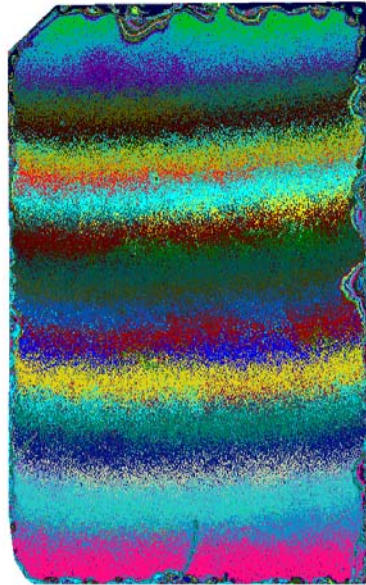
Fig. 5.22: The resulting image of the quartz wedge after the coloring and combination procedure. Each color stands for a defined thickness of the crystal.

The requirement for the combination and overlap of all images is that the crystal section and the field of view be absolutely the same for all images. As soon as the position of the crystal in the pictures taken is not longer constant, it will not be possible to calculate its volume exactly, because the combination of the pictures will result in an incorrect overlap of the colored black and white images.

5.2.3.2 Determination of the absolute crystal surface area

In the previous section it was shown how thickness at a given point can be determined and how the relative distribution of areas of the same thickness can be mapped, nevertheless it is still necessary to obtain an absolute measure of the surface area in order to calculate crystal mass via equation E5.4 and E5.5. The absolute surface area is determined by counting the numbers of pixels that constitute the specific colored regions of the crystal. Knowing the surface area of one pixel allows the surface areas of the colored regions to be calculated, and hence the volume of the colored regions can be

determined according to equation E5.5. The sum of the volumes of the colored regions is the whole volume of the crystal.

Each image should contain the same defined number of pixels. This can be achieved by cutting the images with the help of a mask (indicated by the red box in figure 5.23A), which contains a defined pixel number (Fig. 5.23B).
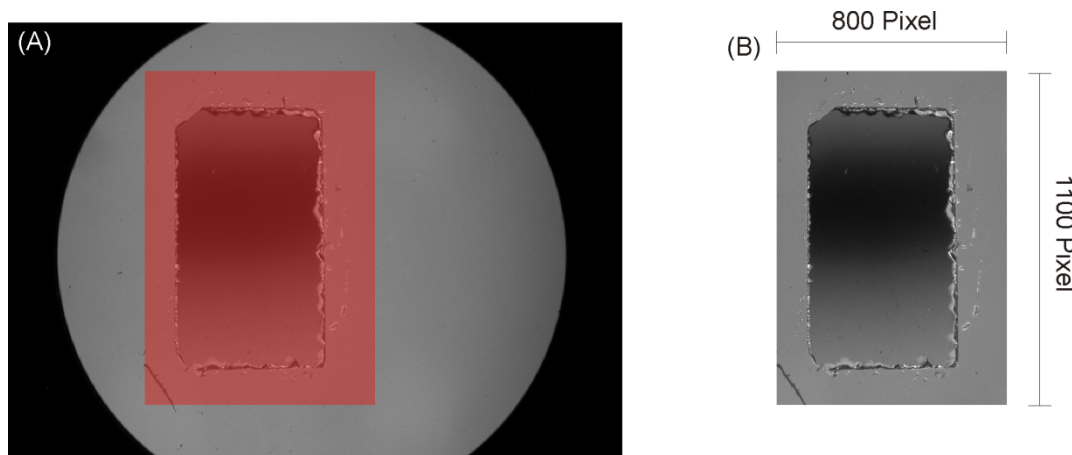
Fig. 5.23: (A) The original picture taken of the crystal is cut into an image with defined dimensions of pixel numbers with the help of a mask (indicated by the red box). **(B)** Example with dimensions of 800x1100 pixels of the cut image.

To determine the dimensions of one pixel, a calibration picture of a measuring scale (an object micrometer is recommended) has to be taken with the exact same camera settings used for all other photographs. The calibration image was cut into the same pixel dimensions as the other images. With the scale of the object micrometer displayed on the image and the information on the pixel dimensions of the image the dimensions of one pixel can be calculated. The width and the length of each pixel were determined separately. For this reason two pictures of the object micrometer scale were taken, one horizontally and the other vertically.

With this information on the dimensions of one pixel, its surface area can be calculated according to

$$A_{pixel} = Pixel_L \cdot Pixel_W \qquad (E5.15)$$

with A_{pixel} as the surface area of one pixel, $Pixel_L$ as the length of one pixel and $Pixel_W$ as the width of one pixel. With the surface area of one pixel and the number of pixels that constitute a specific color, the surface of that area of the crystal can be calculated according to

$$A_{colour} = N_{pixel-color} \cdot A_{pixel} \qquad \text{(E5.16)}$$

with A_{color} as the surface area of the specific colored part of the crystal and $N_{pixel-color}$ as the number of pixels that constitute that specific color. Figure 5.24 shows an image of the quartz wedge of figure 5.22 with a schematic sketch of one pixel dimension and the equations needed to calculate the surface and volume of a specific colored part of the crystal.
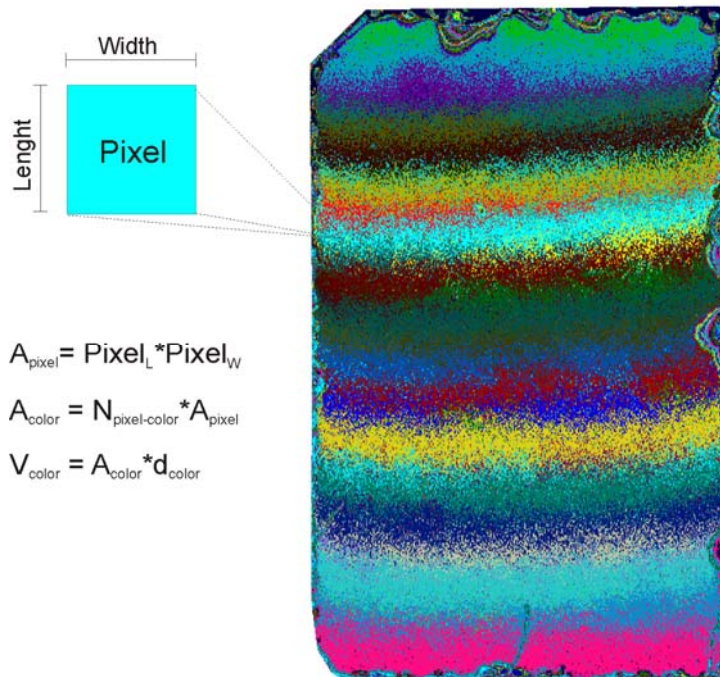
Fig. 5.24: Summary image of the quartz crystal of figure 5.22 with a schematic sketch of the dimensions of one pixel and the equations that are needed to calculate the volume under a specific color area. A_{pixel} = surface area of one pixel; A_{color} = surface area of a specific color; $N_{pixel-color}$ = number of pixels that constitute a specific color; V_{color} = volume of the specific color; d_{color} = thickness of the specific color.

The sum of the volumes of all colored regions is the volume of the whole crystal:

$$V_{crystal} = \Sigma V_{colour} \qquad \text{(E5.17)}$$

with $V_{crystal}$ = volume of the whole crystal and V_{color} = volume of the colored parts of the crystal. With this information on the volume and the thickness of the crystal, its mass can be determined according to equation (E5.4).

Source codes for modeling were developed in collaboration with Dr. Michael Burchard, University of Heidelberg, and can be found in the Appendix XII.

5.2.4 Critical aspects and results

5.2.4.1 Berek and Babinet-Soleil compensators

In order to calculate the volume of a crystal precisely and hence to determine its mass correctly, great care has to be taken in choosing the type of compensator used. The Berek compensator produces a dark stripe according to the tilt angle of the magnesium fluoride crystal. The points of same phase differences are located on a curve (Berek, 1913) and hence the adjustment is controlled only by the coincidence of one point of the compensation stripe with the intersection point of the ocular cross hairs (Berek, 1913). That means that only the part of the crystal that coincides with the intersection point of the ocular cross hairs is compensated correctly. Therefore, if the Berek compensator is used for measuring the phase difference of a crystal it will always lead to a rounded or oblique surface, even if the crystal has a homogeneous thickness (see Fig. 5.26). Consequently, calculating a crystal's mass from its phase difference determined with the Berek compensator yields incorrect data.

In addition, the Berek compensator produces a lateral displacement of the image according to the tilt angle of its magnesium fluoride crystal. Consequently, the position of the crystal sample on the images taken is not constant. The combination and overlap of the images will then result in falsified images and incorrect volume data. This lateral displacement can be overcome by reworking the images to reconstruct the original position of the crystal sample on every single image. This procedure is very time-consuming and not sufficient.

The Babinet-Soleil compensator creates a homogeneous field of view of compensation by using two coplanar plates. This has two advantages:

(1) The phase difference of the crystal is measured precisely at every point of the crystal, independent of its position within the field of view.

(2) No lateral displacement of the image is produced, and the crystal's position is constant at all times.

The comparison of a crystal (Fig. 5.25) measured with the Babinet-Soleil compensator (Fig. 5.25B) and the Berek compensator (Fig. 5.25C) clearly shows the great difference between the resulting images. From the graphic comparison of the two created images it can be noticed immediately that the Berek compensator does not report the thickness and surface structure of the crystal in a correct way.
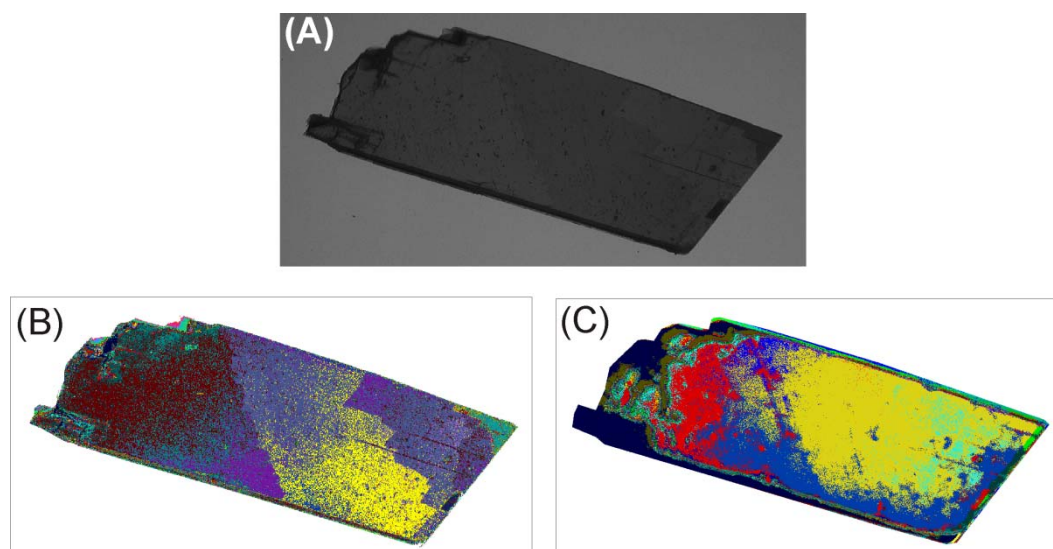
Fig. 5.25: Comparison of the modeled images of a gypsum crystal created with the methods outlined in this study on the basis of the two different compensators considered. **(A)** Gypsum crystal crossed polarizers (gray-scale image); **(B)** The modeled gypsum crystal image using the Babinet-Soleil compensator; **(C)** Same modeled gypsum crystal image using the Berek compensator.

By using crystals of constant thickness, such as a mica crystal, the differences between the created images becomes even more obvious (Fig. 5.26).
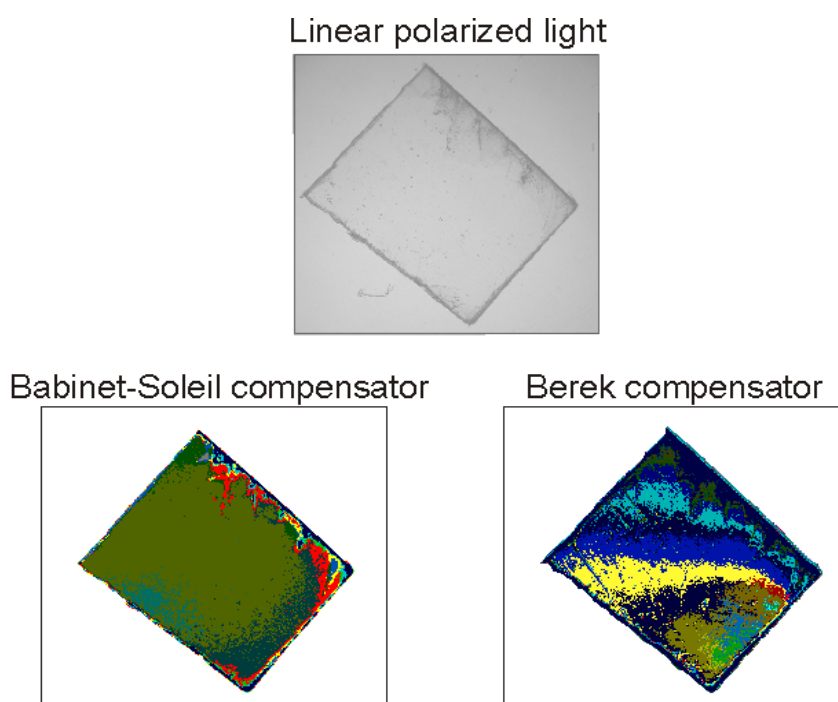
Fig. 5.26: Mica crystal with relatively homogeneous thickness under linear polarized light (top image). Comparison between the two resulting images measured with the Babinet-Soleil compensator (left image) and measured with the Berek compensator (right image) shows significant differences.

By measuring the phase difference of a gypsum crystal using the two compensators different masses are obtained. To improve the comparability of the two modeled images a crystal of appropriate size was picked and weighed to additionally obtain its exact weight. Table 5.3 presents the modeled mass and measured weight of the gypsum crystal. The data of the modeled mass using a Babinet-Soleil compensator lies within the standard deviation of the measured weight while the Berek compensator will also yield incorrect mass data.

Table 5.3: Weight measured vs. modeled mass of a gypsum crystal obtained by the Berek- and Babinet-Soleil compensator.

Mean measured (mg)	Standard deviation (σ) of 10 measurements (mg)	Mass modeled by compensation (mg)	
		Berek	Babinet-Soleil
0.3636	±0.0041	0.3055	0.3602

With the above information about the two compensators it is clearly demonstrated that the Babinet-Soleil compensator is the better choice for measuring the path difference of a crystal and hence it was used throughout this study.

5.2.4.2 Calibration of compensator

The Babinet-Soleil compensator used in this study was not designed for microscopic use but for optical benches. Therefore, it was necessary to calibrate the micrometer scale of compensation of the Babinet-Soleil compensator against known wavelengths in order to get correct results of compensation. Five to six known interference filters were used for measurement. Table 5.4 gives an overview of the filters used, their wavelength and the compensator scale.

The principal measuring technique is quite simple. A filter of known wavelength is placed between the light source of the microscope and the compensator. Then the micrometer scale of the Babinet-Soleil compensator is turned to move the small quartz wedge of the compensator into the position of total compensation. The field of view turns dark. The position of total compensation is now displayed on the micrometer scale.

Two approaches were used to measure the compensation. In the first approach the human eye measures the total compensation (that is the darkest color occurring). The human eye is very sensitive to detecting small differences in dark shades. Therefore, it is suitable for measuring the total compensation. In order to control this measurement the compensation was also measured two times with a photomultiplier that detects low intensity of radiation. Therefore, the lowest detection of the photomultiplier represents total compensation. To prevent that the room light is a source of irritation and not to adulterate the result, measurements with the photomultiplier were carried out in darkness.

Table 5.4: Calibration of the micrometer scale of the Babinet-Soleil compensator versus known wavelengths of up to six interference filters. The dark point was determined using the human eye and a photomultiplier.

Method	Filter	λ (nm)	Scale
Eye	Blue	432	8.178
	Green	526	10.271
	Green	546	10.624
		1092*	21.432
	Orange	589	11.555
		1178*	23.158
	Red	617	12.173
Photomultiplier	Blue	432	8.630
	Green	526	10.381
		1052*	20.859
	Green	1092*	21.524
	Orange	589	11.982
		1178*	23.369
	Red	617	12.325
Photomultiplier	Blue	432	8.435
	Green	526	10.674
		1052*	21.255
	Green	546	10.692
		1092*	21.489
	Green	548	10.920
	Orange	589	12.060
		1178*	23.725
	Red	617	12.400

* 2nd order interference of the wavelength. It can be assumed as the doubled wavelength.

In figure 5.27 the wavelength of the phase difference is plotted versus the micrometer scale of the compensator for all three measurements. It can be noticed that the results determined with the human eye are almost the same as to the results obtained with the photomultiplier. The dashed black line represents the best fit. Its correlation coefficient is $R^2 = 0.9988$. The resulting linear equation:

$$\lambda = 50.324 x_{compensator-scale} + 2.9965 \qquad \text{(E5.18)}$$

with λ = axis of ordinates; $x_{compensator-scale}$ = axis of abscissa, can be used for calculating the phase difference of compensation by the given micrometer scale.
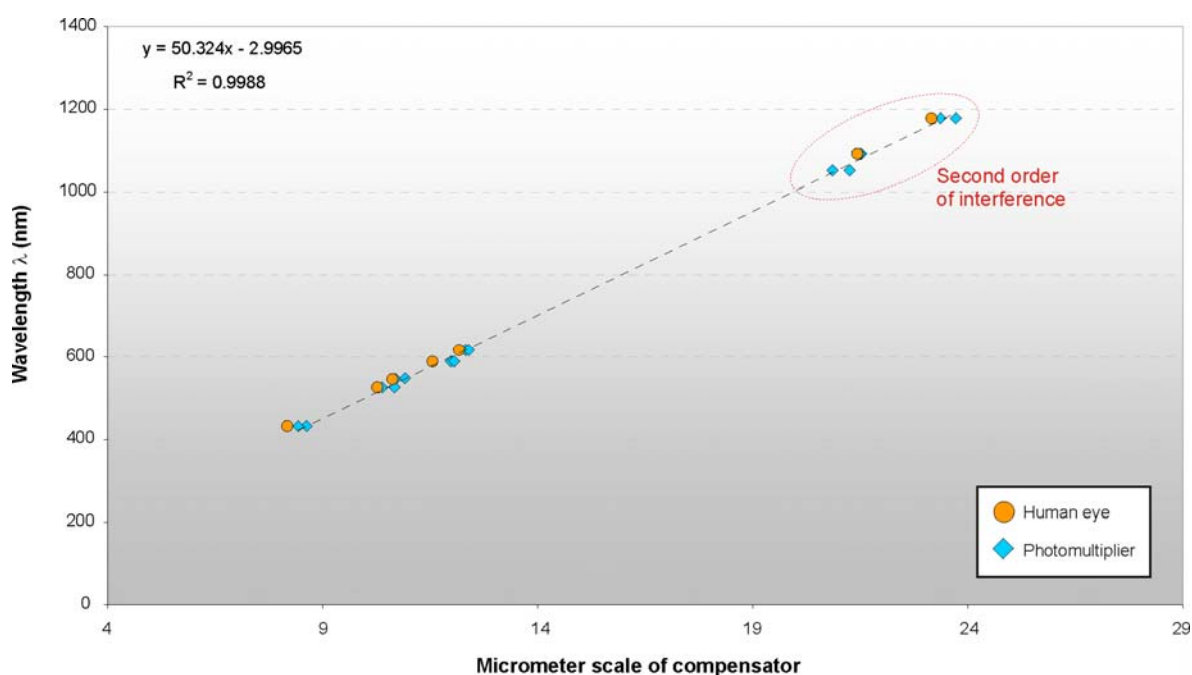
Fig. 5.27: Wavelength of the phase difference (nm) vs. micrometer scale of the compensator for compensation. Orange filled circles are measurements determined with human eyes; blue filled diamonds are the results obtained with photomultiplier. The dashed black line represents the line of best fit. The equation for the best fit line is displayed in the upper left corner together with the correlation coefficient R^2.

5.2.4.3 Threshold value

As explained in chapter 5.2.3.1, the dark area of compensation upon a crystal appears to have diffuse rims and the images are converted into black and white images with the help of a defined threshold value. Figure 5.28 (middle panel) shows a crystal wedge with a defined black area obtained from a threshold value number 12 for this example. The values in figure 5.28 are fictive numbers to show the effect of variation of the

threshold on the images. If the threshold value is set smaller the black area becomes narrower (left image), if it is set larger the black area becomes wider (right image). Therefore the threshold value defines the width of the resulting black areas. The critical question that arises from this conclusion is:

Does the variation of the threshold value affect the resulting crystal volume?
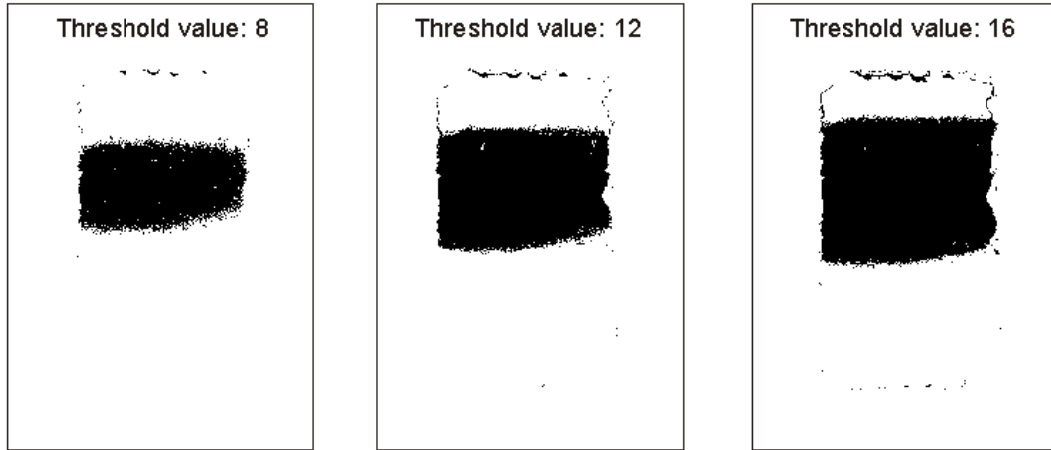
Fig. 5.28: Black and white images of a crystal wedge with varied threshold values.

In order to answer this question a theoretical crystal wedge was created (Fig. 5.29). This wedge has well defined variables and its volume and therefore its mass can calculated according to equations (E5.4) and (E5.5). Its birefringence was set to $\Delta n = 1$. Therefore the phase difference of the crystal wedge according to equation (E5.6) is:

$$\Gamma = d$$

with Γ as the phase difference and d as its thickness or in this example as its height.
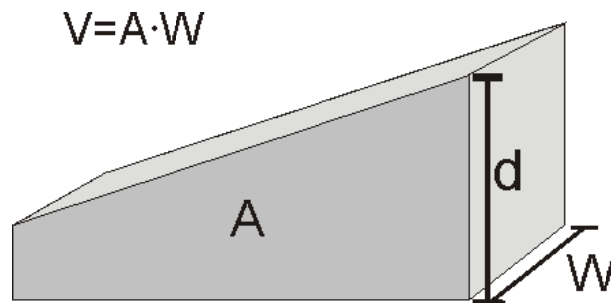
Fig. 5.29: Theoretical crystal wedge with a width=W, a surface area=A and the thickness/height=d. Its volume can be calculated with V = A*W.

The surface is calculated (Fig. 5.30) by forming the integral of the linear equation with its boundary conditions u_1 and u_2:

$$A = \int_{u_1}^{u_2} f(u)\,du$$

(E5.19)

with $f(u) = mu + c$ as the linear equation; u_1, u_2 as the boundary conditions on the axis of abscissa and A as the surface.
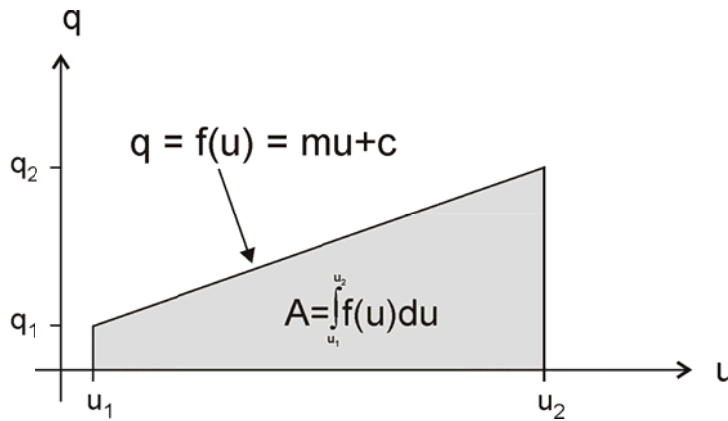
Fig. 5.30: Plot of the linear equation f(u) and the integral that is needed to calculate the surface A between the linear equation and u_1 and u_2 of the axis of abscissa.

Table 5.5 represents the assumed dimensions of the theoretical crystal wedge. Its theoretical volume is calculated to V= 45 mm^3.

Table 5.5: Assumed dimensions of the theoretical crystal wedge and the linear equation variables to calculate its surface and volume.

Linear equation				Surface	Width	Volume
(u_1/q_1)	(u_2/q_2)	m	c	A (mm^2)	W (mm)	V (mm^3)
(0/1)	(9/4)	0.33	1	22.5	2	45

It was assumed that images were taken at seven different theoretical compensator positions (q-values) indicated by the black dots (Fig. 5.31). The variation of the threshold value is achieved by varying the length of the theoretical dark areas indicated by the green and red line in figure 5.31B. The black dots are taken as the center of the variation and values are added and subtracted from this position (q-axis) indicated through the colored numbers in figure 5.31B. For example the compensator position is q=2. The green colored line represents a threshold value of 1; the red colored line represents the threshold value of 4. The width of each black area displayed on the u-axis

(green and red line in Fig. 5.31C) can exactly be calculated with the linear equation $f(u) = m \cdot u + c$.
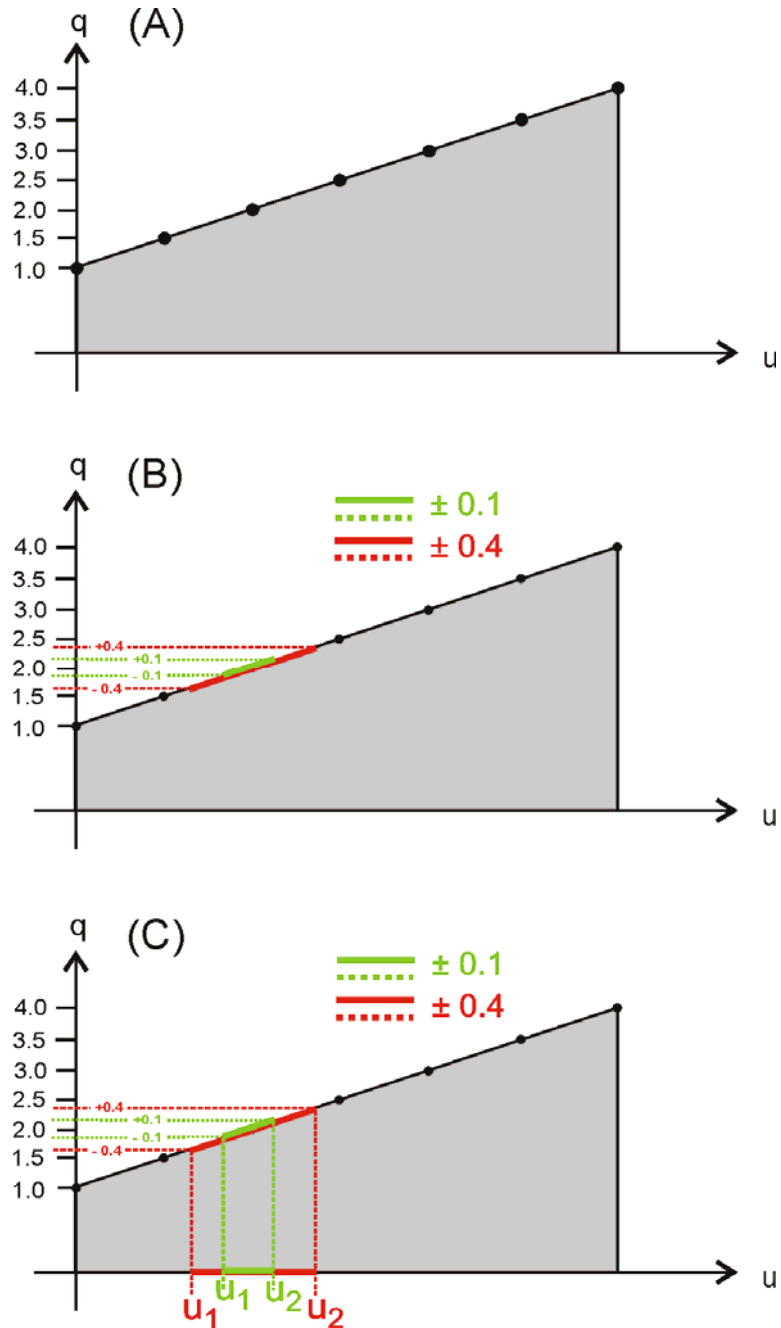
Fig. 5.31: **(A)** Seven assumed compensator positions from 1.0 to 4.0 in 0.5 steps. The black dots represent the compensator positions and hence the dark areas of compensation on the crystal wedge. **(B)** Variation of the threshold value is achieved by varying the thickness of the theoretical black area. The green colored line represents a threshold value of 1; the red colored line represents the threshold value of 4. To achieve thickening of the black area, values were added and subtracted from the center position (q-axis) indicated through the colored numbers. The center in this example is q=2. **(C)** Width of the black area as it appears in the u-axis of abscissa. The green line represents the width of the threshold value 1; the red line represents the threshold value 4. The boundaries for each width are u_1 and u_2 painted in their corresponding colors.

111

Seven black and white images will result in black areas at different positions on each image (Fig. 5.32A). Each stripe is then color-coded (Fig. 5.32B). Existing overlaps are taken into account and also color-coded (see 5.2.3.1). The result (Fig. 5.32C) is a colored image with each color representing a defined thickness/height of the crystal wedge (Fig. 5.32D). In figure 5.32E the result is sketched schematically as a 3-dimensional view of the modeled crystal.

Knowing the width W of the wedge (see Fig. 5.29) and the calculated thickness/height from the phase difference, the volume of each colored area can be calculated. The sum of all volumes is the total volume of the theoretical crystal wedge.
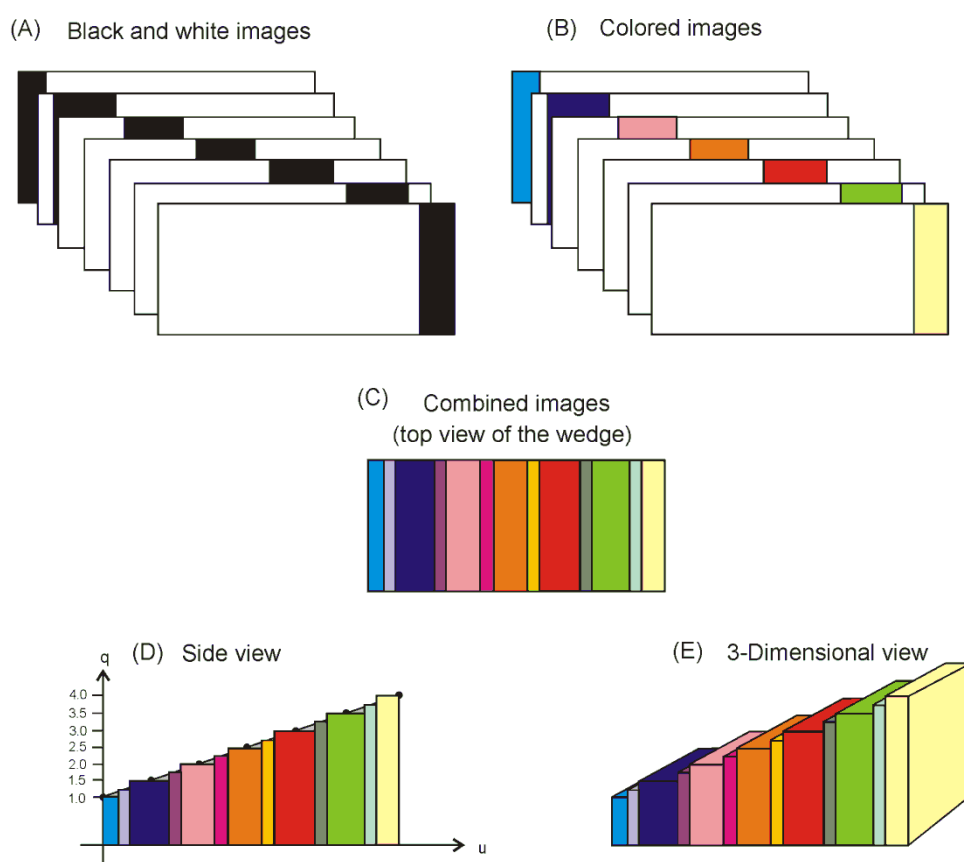
Fig. 5.32: **(A)** Black and white images with black areas in different positions on each image. **(B)** Each image is color-coded according to the procedure of the new approach. For detailed explanations of the procedure see text. **(C)** Resulting image of the seven combined images. Existing overlap was taken into account and colored differently. This view is the top view of the crystal wedge as it would be seen under the microscope (not colored there). **(D)** Each color represents a defined thickness/width of the crystal according to the phase difference. **(E)** 3-Dimensional view of the theoretical modeled crystal wedge.

Figure 5.33 shows how the calculated volume of the theoretical crystal wedge (yellow filled circles) is affected by varying the threshold value. The real volume of the

theoretical wedge is indicated by the red solid line. If the value of the threshold is too small, the resulting width of the black areas will be very narrow. Thus the areas do not touch or overlap each other and the resulting volume is too low (Fig. 5.33; threshold value 1 and 2). At some point the threshold value is large enough to produce black areas that will touch each other (Fig. 5.33; threshold value 3) and a "high plateau" is reached. Further variations of the threshold value do not affect the resulting volume anymore. A complete table of volume determinations with given threshold values can be found in Appendix VI.
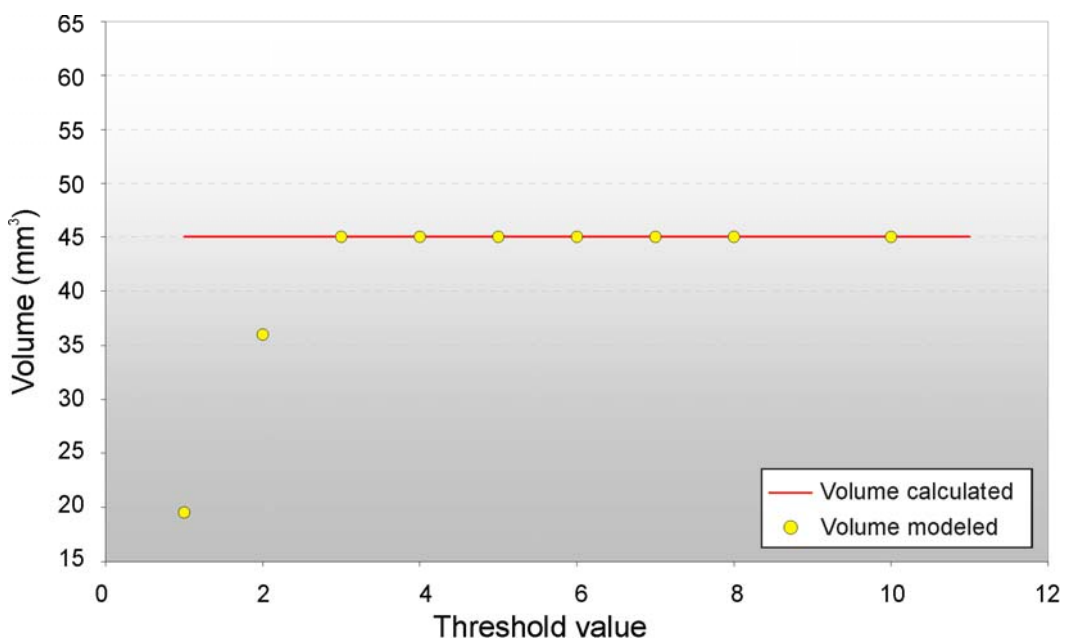
Fig. 5.33: Plot of the theoretical crystal wedge volume vs. the variation of the threshold value. Yellow filled circles indicate the volume determined with the new approach, red solid line represents the volume calculated from the crystal dimensions.

To confirm if this conclusion is valid for real crystals this procedure was applied to a quartz wedge (see figure 5.22 and/or 5.24). Figure 5.34 plots the resulting modeled volume of the quartz wedge versus the variation of the threshold value. The volume of the quartz wedge behaves as predicted. From this plot it can be concluded that the variation of the threshold value will not affect the determined crystal volume as soon as the "high plateau" is reached. A table with the quartz and image specifications and the given threshold values can be found in Appendix VII.
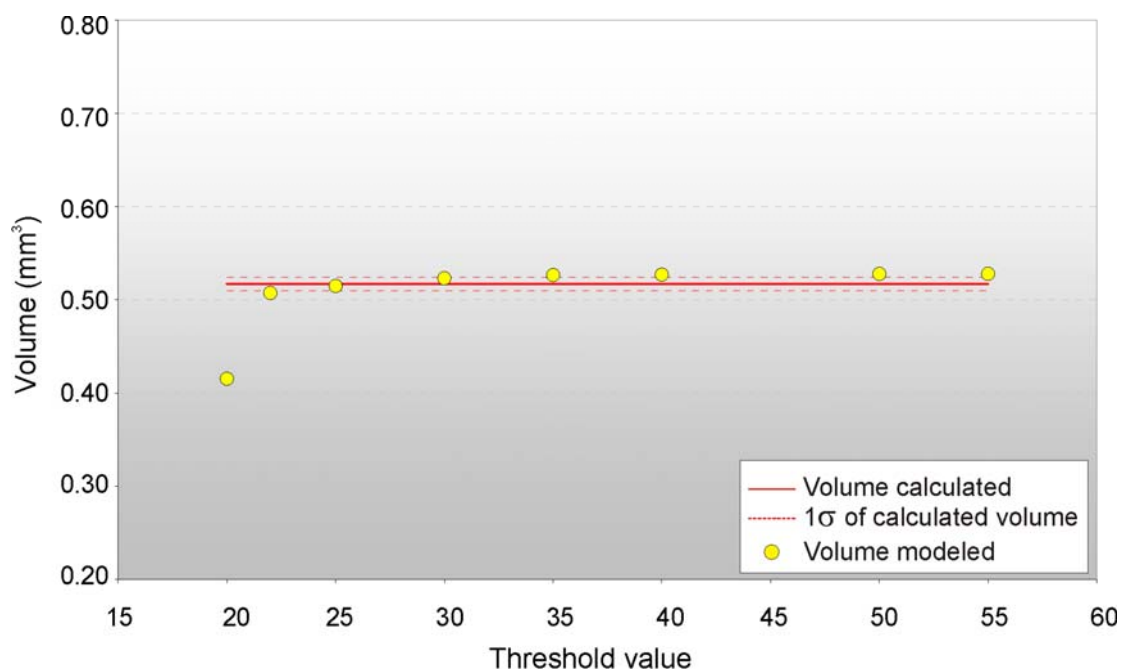
Fig. 5.34: Plot of a quartz crystal wedge vs. the variation of the threshold value. Yellow filled circles indicate the volume determined with the new approach, red solid line represents the volume determined from its weight; red dashed lines represent its standard deviation.

The method was also tested for a broader range of morphologies to see whether the results are reproducible. Crystals of appropriate size were taken to get additional information about the real weights and volumes and to improve the comparability. Figure 5.35 shows a gypsum crystal under linear polarized light (Fig. 5.35A) and the same crystal modeled (Fig. 5.35B).
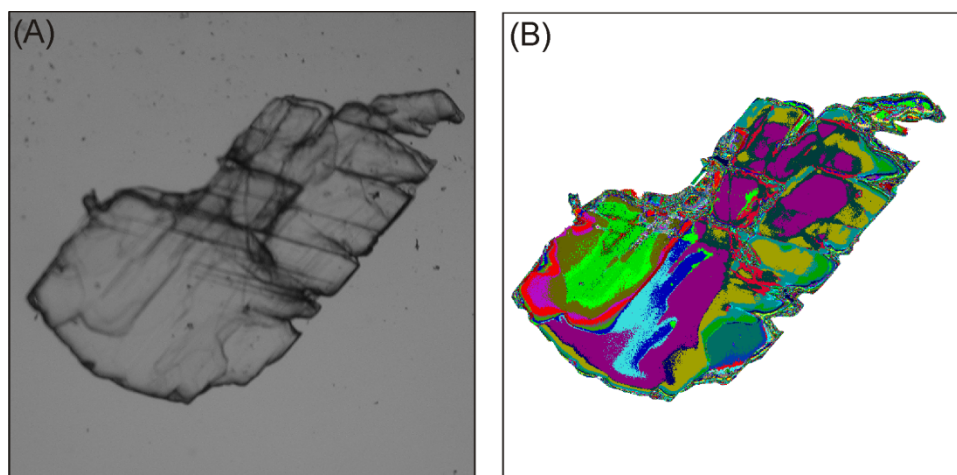
Fig. 5.35: (A) Gypsum crystal under linear polarized light; **(B)** same gypsum crystal modeled, each color stands for a specific thickness of the crystal.

In figure 5.36 the calculated volume of the gypsum crystal using its weight (red solid line) and its determined modeled volume (yellow filled circles) are plotted versus the variation of the threshold value. A table of the calculated values can be found in Appendix VII. The modeled volume behaves the same way as predicted: as soon as the high plateau is reached the volume does not change perceptibly. Nevertheless, by closer inspection of the determined volume data it was noticed that at higher threshold values (threshold value 70) the volume is getting lower. This determination becomes more obvious if the threshold is set to a very large value (threshold value = 80).
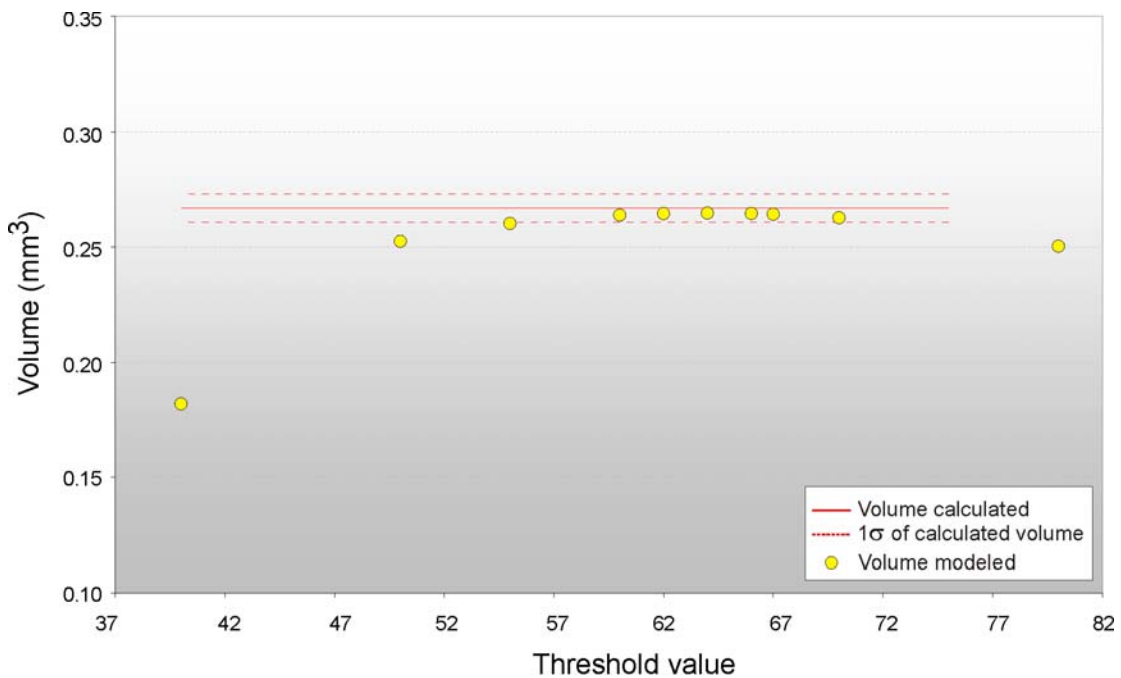
Fig. 5.36: Plot of a gypsum crystal vs. the variation of the threshold value. Yellow filled circles indicate the volume determined with the new approach, red solid line represents the volume determined from the crystal's weight; red dashed lines represent the standard deviation of the volume determined from the crystal's weight.

The predicted behavior of the modeled crystal volume is based on the assumption that its shape can be described by a linear equation (see Fig. 5.30). As long as this condition is fulfilled the modeled crystal volume agrees very well with the predicted theoretical volume. Nevertheless, as soon as the shape cannot be described by a linear equation the behavior of the modeled crystal volume will deviate from the predicted theoretical behavior at larger threshold values.

To explain this different behavior, a theoretical crystal wedge was created whose shape (Fig. 5.37) can be described through a second degree polynomial equation:

$$q = -0.1081u^2 + 0.9726u + 0.9781 \qquad\qquad (E5.20)$$

The surface and therefore the volume of this theoretical crystal can be calculated precisely by solving the integral of the polynomial function:

$$A = \int_{u_2}^{u_1} (-0.1081u^2 + 0.9726u + 0.9781)\,du = |F(u_2) - F(u_1)| \qquad (E5.21)$$

with u_1 and u_2 as the boundary conditions and $F(u)$ as the antiderivative from the function $f(u)$ and A as the surface.

In Table 5.6 the assumed dimension of the theoretical crystal and the variables of the polynomial equation are specified. The difference to a wedge is that in one compensator position, two black areas will appear upon the crystal's surface (Fig. 5.37). The red dots in figure 5.37 represent the corresponding second black area of one compensator position (black dots). Besides this difference, the theoretical crystal underwent the same procedure as the theoretical crystal wedge described earlier, for calculating the volume in variation with the threshold value.

Table 5.6: Assumed dimensions of the theoretical crystal wedge and the variables of the polynomial equation to calculate its surface and volume.

Polynomial equation		Surface	Thickness	Volume
(u_1/q_1)	(u_2/q_2)	A (mm^2)	d (mm)	V (mm^3)
(0/0.98)	(9/0.98)	21.92	2.00	43.85
(1/1.84)	(8/1.84)			
(2/2.49)	(7/2.49)			
(4.5/3.23)	(4.5/3.23)			

Images at five different theoretical compensator positions were assumed to be taken. Since the birefringence is set to $\Delta n = 1$, the compensator positions (q-values) represent the thickness of the theoretical crystal.
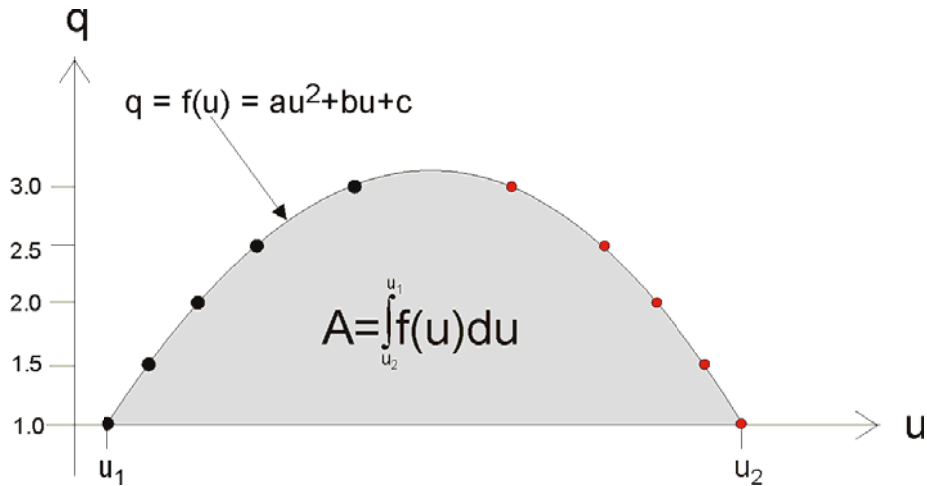
Fig. 5.37: Theoretical crystal whose shape is described through a second degree polynomial function with the equation to calculate its surface.

In figure 5.38 the calculated volume of the theoretical crystal (yellow filled circles) versus the variation of the threshold value is plotted together with the calculated real volume (red solid line). It can be noticed immediately that the behavior of the theoretical volume reflects the behavior of the gypsum crystal volume seen in figure 5.36 very accurately.
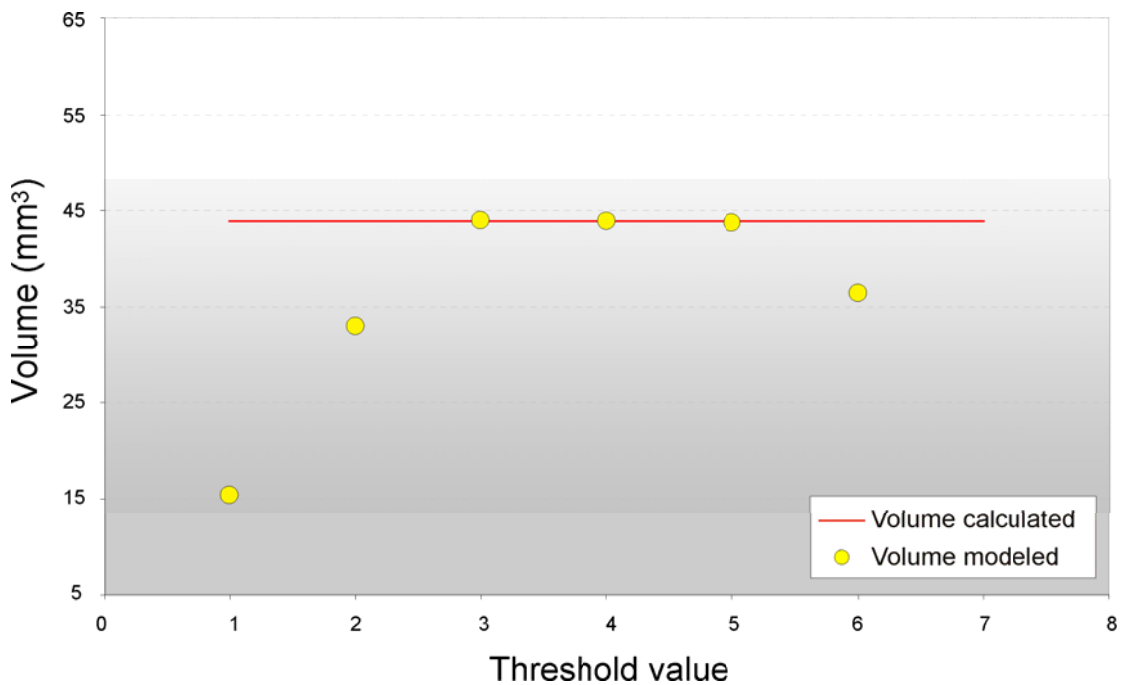
Fig. 5.38: Plot of the theoretical crystal vs. the variation of the threshold value. Yellow filled circles indicate the volume determined with the new approach, red solid line represents the volume calculated with the crystal dimensions.

However, As soon as the calculated volume of the second degree polynomial equation reaches the "high plateau" the volume doesn't change perceptibly. This agrees very well with the calculated volume of the gypsum crystal. Therefore any threshold value of the high plateau can be used for determining a crystals volume independently from the crystal's shape. A list of the calculations can be found in the Appendix VI.

5.2.4.4 Birefringence of investigated material and diamond anvils

In the new developed approach, the accurate determination of the volume and therefore the mass of a crystal depends on its birefringence. For most minerals the birefringence is known precisely from literature (Tröger, 1982). Nevertheless most of these minerals are pure end-members. Unfortunately in nature crystals have variable compositions and therefore exhibit variable birefringence according to their composition. For example, the birefringence of muscovite varies from 0.036 for the iron-free end-member to 0.054 for the iron-rich end-member. Other crystals such as topaz have variable birefringence due to their fluorine content. Variation within the birefringence leads to incorrect volume and mass determinations. Table 5.7 represents the determined volume of a muscovite crystal calculated with the birefringence for the iron-free end-member as well as for the iron-rich end-member. The resulting volumes and masses differ strongly from each other.

Table 5.7: Volume and mass data obtained with the birefringence for an Fe-free end member (*) and an Fe-rich end member (#) of muscovite.

Birefringence (a-b plane)	Volume (mm^3)	Mass (mg)
0.006*	0.432	1.248
0.005$^{\#}$	0.518	1.497

Therefore it is recommended to determine a crystal's birefringence before the experimental run. According to equation (E5.6) the birefringence depends on the thickness of the crystal and the phase difference. The latter can be measured with the Babinet-Soleil compensator. The thickness of a crystal can be determined in different ways:

(1) The spindle stage. The crystal is glued to a glass nod and mounted on a spindle stage. Its dimensions can be measured very precisely now (see Figure 5.46 as example).

(2) The thin section. A thin section with known thickness is made from the crystal sample or the sample itself is polished down to a known thickness.

In either case the birefringence can be determined exactly (equation E5.6). As long as the exact indicatrix position within the crystal is known its birefringence can be calculated. However, a slight rotation of the crystal about the angle of rotation ω will lead to a new value for the effective index $n_e^{'}$ (Medenbach, 1984) which can easily be obtained from the relation

$$n_e^{'2} = \frac{n_o^2 \cdot n_e^2}{n_0^2 \cdot \sin^2 \omega + n_e^2 \cdot \cos^2 \omega} \qquad \text{(E5.22)}$$

Another critical aspect may be the temperature dependence of the birefringence. For quartz this was studied by several authors and summarized by Hintze (1915). It is reported that the variation of the birefringence with increasing temperature becomes noticeable in the 5th decimal at temperatures above 200°C. Hence the temperature dependence of the birefringence is negligible with respect to the present study.

Measuring the birefringence of minerals is based on the consideration that the supporting material (e.g. object glass plate) is optically isotropic. Otherwise the birefringence of the support will affect the birefringence of the sample because the measured birefringence will be a combination of both materials.

However, during experimental runs the investigated crystal is located on the lower culet face of the diamond anvils confining the sample chamber. Based on the consideration that diamond is a cubic material it should be optically isotropic and therefore the birefringence of the sample should not be affected. Nevertheless, diamonds show more or less stress birefringence (Seal, 1987). Figure 5.39 and 5.40 shows the mapped and calculated stress birefringence of two opposing diamond anvils that is visible through the sample chamber. In figure 5.39A the stress birefringence of the two diamonds is mapped and calculated with the new method at 22°C. The distributed force applied over the diamond anvils is unknown due to losses of internal friction. The rotation of the pressurizing nut was ½ rotations. Figure 5.39B shows a numerical calculation based on the mapped stress birefringence of the same diamond

anvil culets. The two images remind remarkably of an uniaxial conoscopic image of a crystal.

Stress birefringence
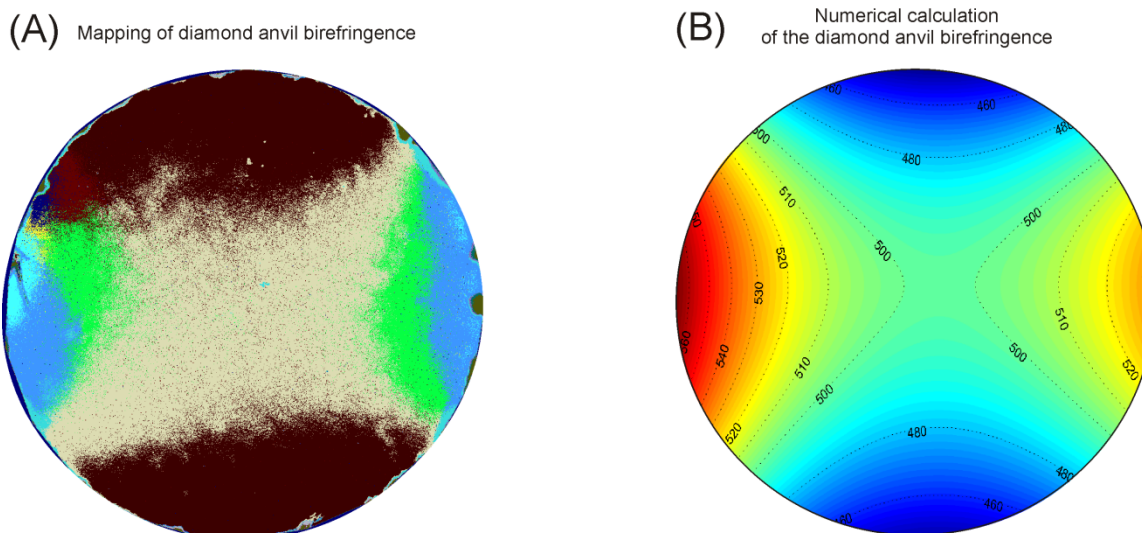
Fig. 5.39: (A) Mapped stress birefringence of the diamond anvils at 22°C and applied pressure of ½ rotation of the pressurizing nut. **(B)** Numerical calculation based on the mapped stress birefringence image.

This can be explained with the behavior of objects that are exposed to a centered, external stress. Figure 5.40A show an image taken from a hemisphere under crossed polarizer that was pressed onto a plane. A rotation-symmetric interference image is the result. The dark center in the middle of the image represents the center of the stress. The areas of the interference image that vibrate parallel to polarizer and analyzer appear extinguished. Due to the orientation of the Babinet-Soleil compensator the polarizers in the used microscope are oriented in a 45° position, rather than NS-EW as in standard polarizing microscopes. Comparison of the two images shows that the stress birefringence of the diamond anvils can be exactly described with this conclusion.
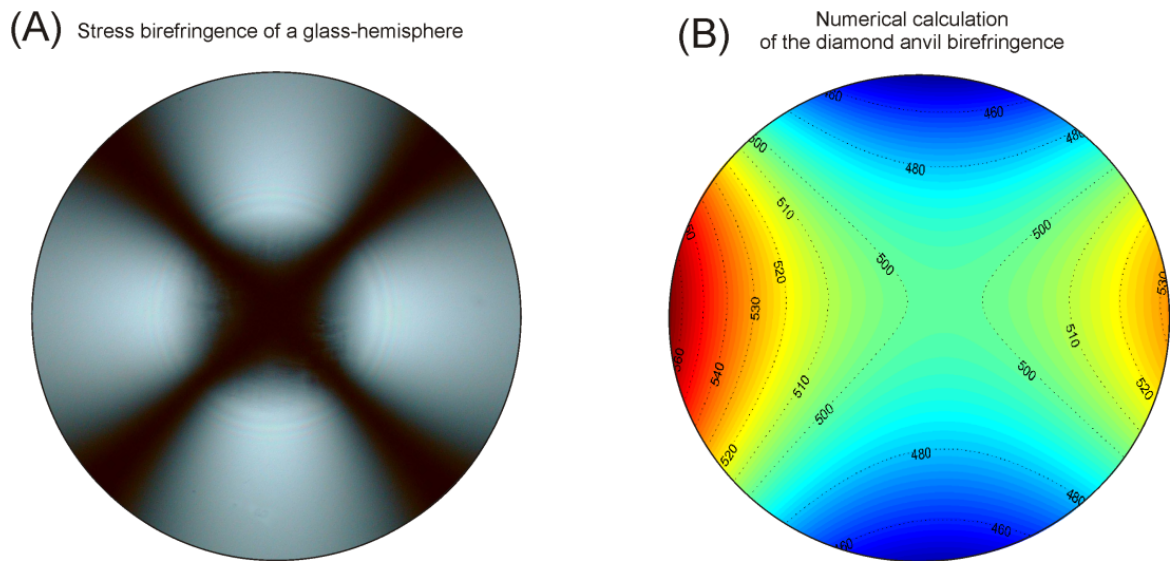
Fig. 5.40: (A) Stress birefringence of a hemispherical glass lens pressed onto a glass plate causing an external, centered stress under crossed polarizers. For explanations see text. **(B)** The numerical calculation of the stress birefringence of the diamond anvils from figure 5.39B. Both images are comparable (see text).

Two critical questions arise from this conclusion:

(1) Does the stress birefringence change with changing P, T conditions?

(2) Does this stress birefringence affect the resulting volume of the measured crystal?

To solve the first question the stress birefringence was measured in dependence of pressure and various pressure and temperature conditions and also calculated numerically. Therefore the HDAC was loaded with a rhenium gasket filled with pure water and an air bubble so pressure could be calculate at various stages of temperatures from the EOS of water. Different starting conditions were applied in the mean of applied pressures, which are the turns of the pressurizing nut. The distribution of the force over the anvil is unknown and losses due to internal friction cannot be quantified exactly therefore the calculated pressures from the EOS of water and also the rotations of the pressurizing nut can only be an approximation of the real pressure. Figure 5.41 shows the stress birefringence in dependence of the applied pressure, specified by the rotation turns of the pressurizing nut. The complete list of determinations can be found in the Appendix VIII.
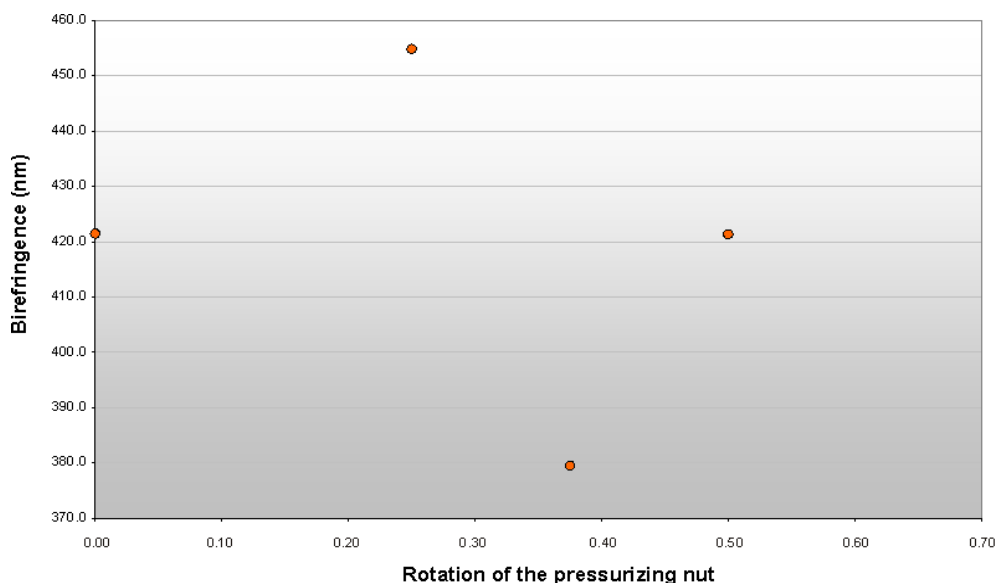
Fig. 5.41: Plot of the stress birefringence versus the pressure applied onto the diamond anvils. The pressure is specified by rotations of the pressurizing nut.

In Figure 5.42 the stress birefringence was calculated in dependence of various temperature conditions and different starting pressures. In addition the stress birefringence was also measured during a heating and cooling cycle of the HDAC.
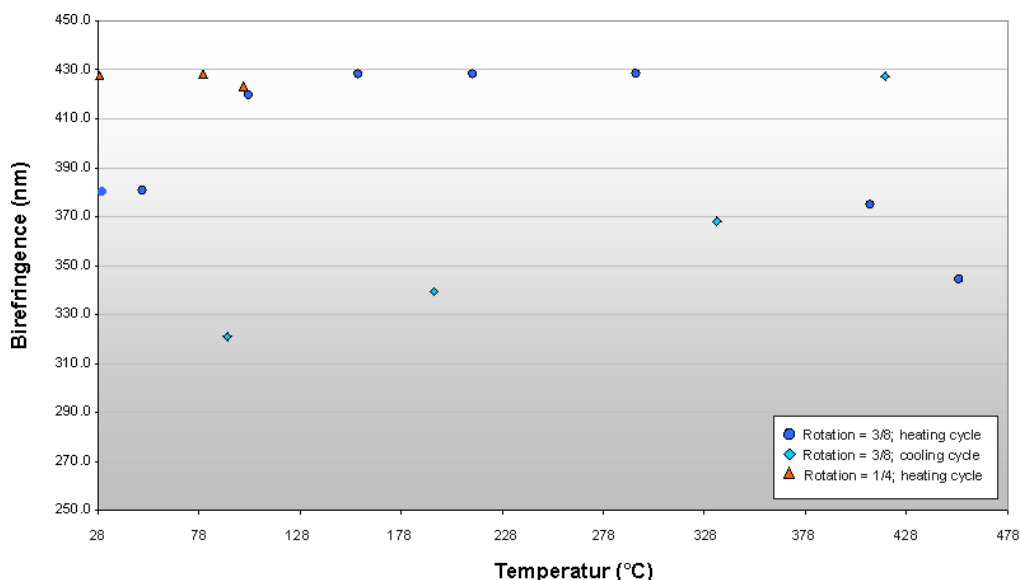
Fig. 5.42: Plot of the Diamond anvil stress birefringence versus various temperature conditions in conjunction with different starting pressures.

Numerical calculations of the stress birefringence of such a heating cycle display the variation of the birefringence at various temperature and pressure conditions graphically. Pressures are calculated from the EOS of water and do not represent the actual force applied onto the anvils.
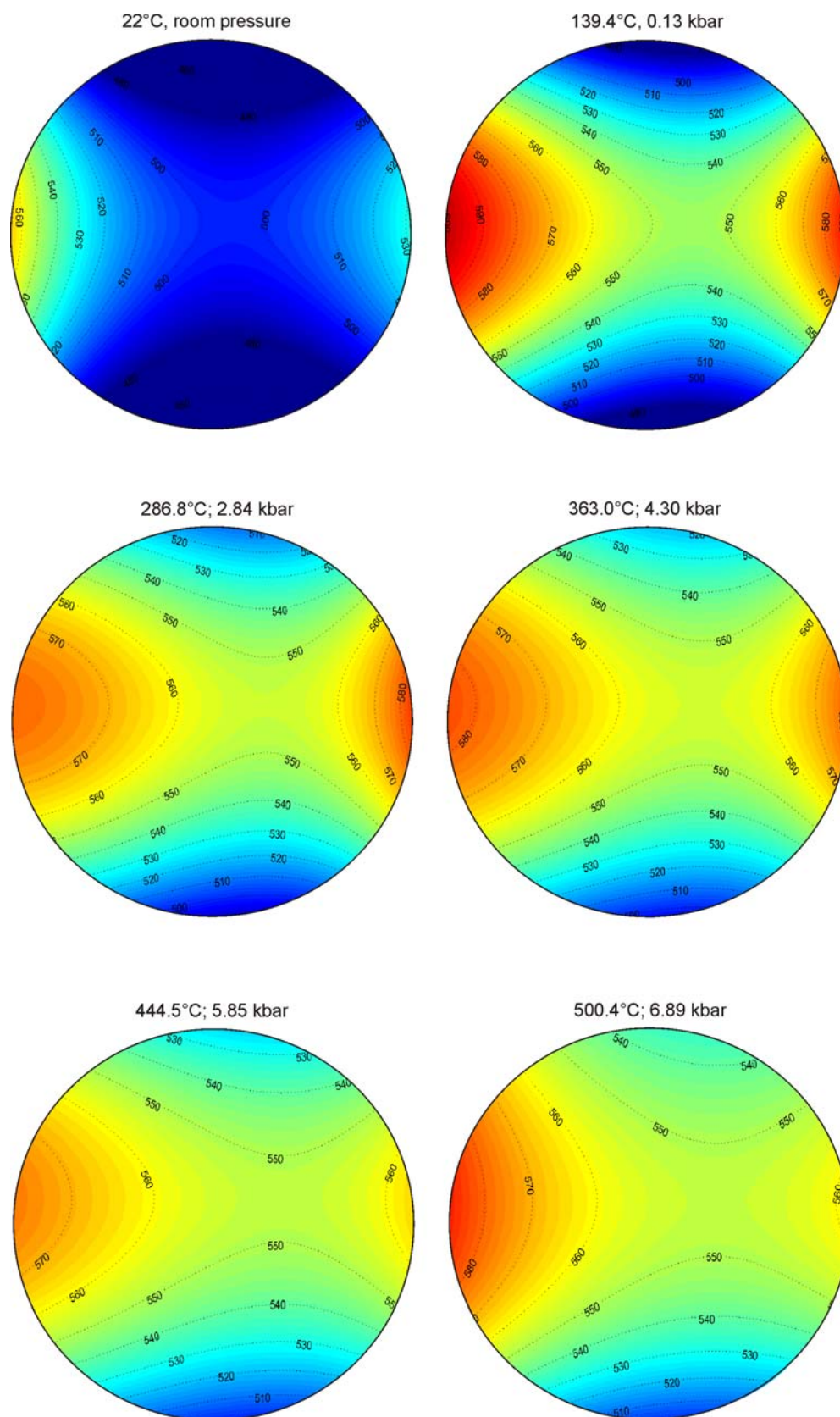
Fig. 5.43: Numerical calculation of mapped diamond anvil stress birefringence at various stages of temperature and pressure. The pressure was calculated using the EOS of water. However it does not represent the actual force affecting the diamond anvils (see text).

From Figures 5.41, 5.42 and 5.43 it can be concluded that the stress birefringence of diamond anvils is changing with changing P,T conditions. In addition the stress birefringence is not a constant value and thus can not be predicted, demonstrated by Figures 5.41 and 5.42.

The second question was solved by determining the volume of a quartz crystal outside the HDAC, lying on an objective plate and comparing it to its volume that was determined when the crystal was loaded inside the HDAC.
Table 5.8 represents the two volumes derived from the different location the quartz crystal was situated on.

Table 5.8: Volume and mass of a quartz crystal that was determined when the crystal was within the HDAC and outside the HDAC, lying on an objective plate.

	Within HDAC	On objective plate
Volume (mm^3)	0.00184	0.00204
Mass (mg)	0.00488	0.00537

The volumes of the crystal determined within and without the HDAC are different. Therefore the conclusion can be drawn that the diamond anvils do affect the resulting volume. Closer considerations about the measured phase difference can explain this effect. The diamond anvils produce an offset on the crystal's phase difference because the measured phase difference is the sum of the crystal's phase difference and the phase difference of the supporting substance, in this case the diamond anvil. If a 546 nm green filter is used, the compensator will extinguish the incoming light by 546 nm or a multiple of this wavelength (n*546 nm). Table 5.9 represents the phase difference of a theoretical crystal, of the diamond anvils and the measured phase difference. The combination of the phase difference of the crystal and the offset of the diamond will exceed 546nm and compensation will result in a false phase difference (Fig. 5.44), in this case a too small phase difference. Figure 5.44 shows this consideration in a graphical way.

Table 5.9: Phase differences of the theoretical crystal, the diamond anvil, the combination of both and the resulting phase difference as it would be measured with the compensator.

Phase difference

x-value	"Real" Diamond anvils	"Real" Crystal	Combination (Diamond + crystal)	Measured (Diamond + crystal)
1	320	0	320	320
3	320	0	320	320
5	320	0	320	320
7	320	170	490	490
9	320	210	530	530
10	320	230	550	4
11	320	250	570	24
13	320	275	595	49
15	320	289	609	63
17	320	300	620	74
19	320	300	620	74
21	320	300	620	74
23	320	300	620	74
25	320	300	620	74
27	320	300	620	74
29	320	300	620	74
31	320	280	600	54
33	320	260	580	34
35	320	230	550	4
37	320	190	510	510
39	320	150	470	470
41	320	0	320	320
43	320	0	320	320
		231.7**		169.5**

** = average phase difference from x = 5-41.

At the beginning of the measured phase difference the offset of the diamond anvils will lead to a phase difference that is too high. As soon as the combination of both phase differences will exceed 546 nm the measured phase difference will result in a minimum. This plot clearly demonstrates that the averaged phase difference measured is too low and hence the calculated volume of the crystal will be too low as well.
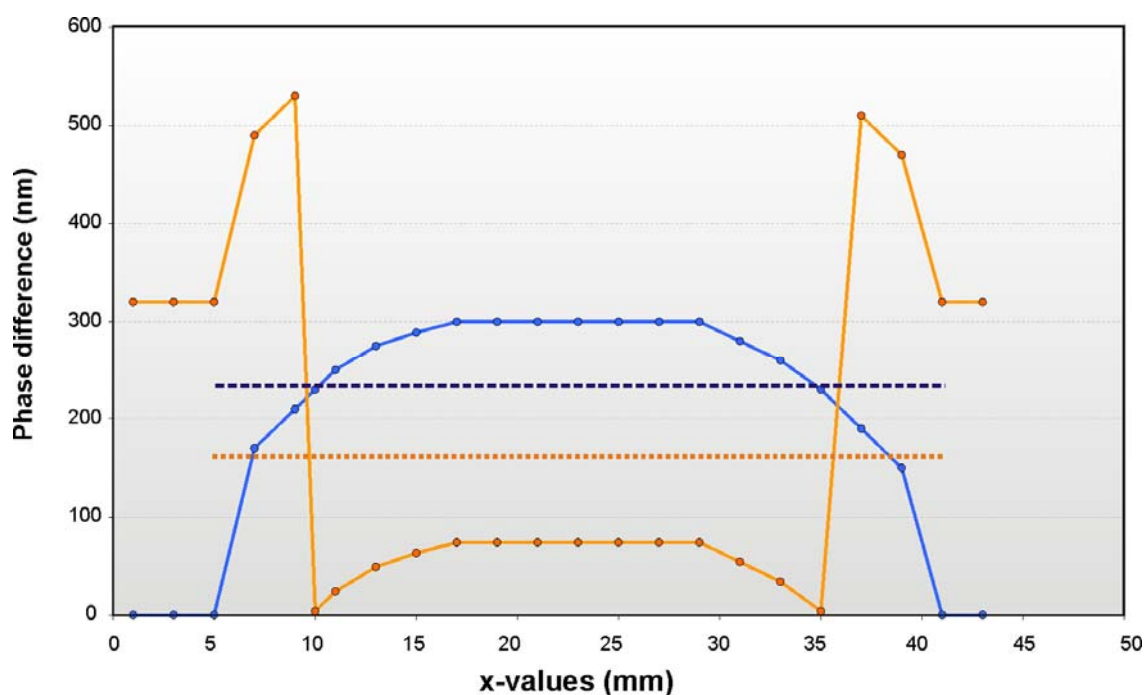
Fig. 5.44: Plot of the real phase difference of a theoretical crystal (blue dots and line) and measured phase difference of the combination of diamond anvils and crystal (orange dots and line). The blue dashed line represents the real average phase difference of the crystal; the orange dotted line represents the measured average phase difference of the crystal.

The resulting conclusion of this consideration is that the offset of the diamond anvils needs to be subtracted from the measured phase difference in order to calculated the volume and mass of a crystal correctly. Therefore not only the phase difference of the crystal but the phase difference of the diamond anvils has to be measured as well. Both images, the crystal and the diamond anvil, will run through the same procedure described above. Two color-coded images will be the result (Fig. 5.45) one for the background (Fig. 5.45B) and one for the crystal (Fig. 5.45C).
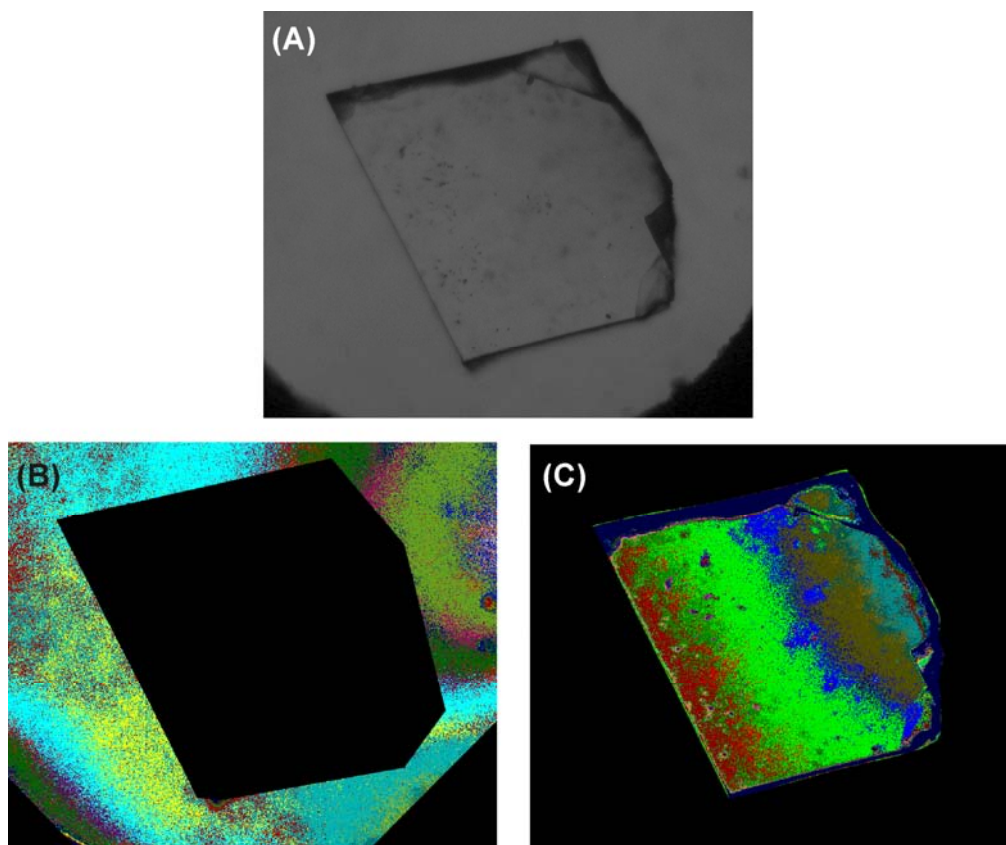
Fig. 5.45: (A) Original image cut into a box with defined pixel length and width. **(B)** Resulting color-coded image for the background (that is the diamond anvil). **(C)** Resulting color-coded image for the crystal.

In addition, for both resulting images matrix output and data output files are created. In these files every single pixel, in its x-,y-location on the image, is dedicated a phase difference value (a z-value) and put in a matrix. These data files for the background are the base to calculate a regression which describes the 3-dimensional behavior of the phase difference in a two dimensional (x, y) space. That means this regression predicts the behavior of the phase difference underneath the crystal. Therefore a correction factor can be determined for the imported x-, y-, phase difference (z)-values of every single crystal surface pixel. The volume and mass of the crystal can now be calculated with the corrected average phase difference. The source code for this calculation was developed in collaboration with Dr. Michael Burchard, University of Heidelberg. Table 5.11 represents the corrected volume and mass data of the quartz crystal compared to the data determined without the HDAC. The corrected volume is slightly higher than the volume of the crystal determined without the HDAC (Table 5.10). This can be explained by the regression equation. The calculated regression is a source of error

because the true regression describing the behavior of the phase difference in the 2-Dimensional room is unknown. By using different kinds of regressions, e.g. linear, 2nd degree, 3rd degree, the resulting volume differs slightly (Table 5.11). The true regression might be more complex than the assumed ones. Source codes are found in the Appendix XII.

Table 5.10: Comparison between the volume and mass of a quartz crystal determined within and without the HDAC.

	Within HDAC corrected	On objective plate
Volume (mm^3)	0.00214	0.00204
Mass (mg)	0.00567	0.00537

Table 5.11: Corrected volume and mass of the quartz crystal determined within the HDAC.

	Linear regression	2nd degree regression	3rd degree regression
Volume (mm^3)	0.00212	0.00214	0.00216
Mass (mg)	0.00562	0.00567	0.00572

5.2.4.5 Error analysis

The accuracy of this method depends on a couple of variables. The mass (M) of a crystal is calculated according to equation (E5.4) with the volume and density as variables. Both of them have errors themselves and which have to be taken into account. To calculate the error in the volume the Gaussian error propagation is used. The volume of a crystal is calculated from its thickness (d) and the crystal's surface (A) according to equation (E5.5). The thickness of the crystal is calculated from:

$$d = \frac{\overline{\Gamma}}{\Delta n} \qquad (E5.23)$$

with $\overline{\Gamma}$ as the average phase difference and Δn as the birefringence of the crystal. The crystal's surface ($A_{crystal}$) is calculated from:

$$A_{crystal} = \Sigma(N_{pixel-mask} \cdot A_{pixel}) \tag{E5.24}$$

with N_{mask} as the number of pixel of one color and A_{pixel} the surface of one pixel. The variable $\overline{\Gamma}$ is calculated from

$$\overline{\Gamma} = \frac{\Sigma(\Gamma_{color} \cdot N_{pixel-color})}{N_{pixel-mask}} \tag{E5.25}$$

with Γ_{color} as the phase difference of the specific color and $N_{pixel-color}$ as the number of pixels in the specific color. The surface (A_{pixel}) of one pixel is calculated from the pixel's length and width:

$$A_{pixel} = Pixel_L \cdot Pixel_W \tag{E5.26}$$

with $Pixel_L$ as the length and $Pixel_W$ as the width of one pixel.

By combining equations x1-x4 the volume of the crystal can be calculated:

$$V = \Sigma(\Gamma_{color} \cdot N_{pixel-color}) \cdot \frac{1}{\Delta n} \cdot Pixel_L \cdot Pixel_W \tag{E5.27}$$

The variables Γ_{color}, $Pixel_L$ and $Pixel_W$ are sources of error and will cause an error in the total error of the resulting volume. By assuming that Δn of a crystal and $N_{pixel-color}$ are constants, the total error of the volume (σV) based on the Gaussian error propagation is then:

$$\sigma V = \sqrt{\Sigma((\frac{\partial V}{\partial \Gamma_{color}}) \cdot \sigma\Gamma_{color})^2 + ((\frac{\partial V}{\partial Pixel_L}) \cdot \sigma Pixel_L)^2 + ((\frac{\partial V}{\partial Pixel_W}) \cdot \sigma Pixel_W)^2} \tag{E5.28}$$

The dimension length and width of one pixel are calculated by counting the numbers of pixel that build up the length and width scale of object micrometer images that have the same image dimensions as the crystal image. Γ_{color} is calculated from the calibrated compensator position with respect to the wavelength from the linear regression:

$$\Gamma_{color} = mx_{compensator-position} + c \tag{E5.29}$$

with m = 50.324 as the slope value and c = 2.9965 as the y-intersection (see section 5.2.4.2). This calibration is also a source of error which has to be taken into account. The total error of the phase difference of one color ($\sigma\Gamma_{color}$) based on the Gaussian error propagation is then:

$$\sigma\Gamma_{color} = \sqrt{((\frac{\partial \Gamma_{color}}{\partial m}) \cdot \sigma m)^2 + ((\frac{\partial \Gamma_{color}}{\partial c}) \cdot \sigma_c)^2} \tag{E5.30}$$

The standard deviations of the slope (σ_m) and the y-intercept (σ_c) as well as the degree of y-value scatter about the line of best fit (σ_y) need to be calculated as well. The degree of y-value scatter is then given by

$$\sigma_y = \sqrt{\frac{\sum (mx_k + c - y_k)^2}{n-2}} \qquad (E5.31)$$

with n numbers of the value pairs (x_k, y_k). The standard deviation of the slope is calculated from

$$\sigma_m = \sigma_y \sqrt{\frac{n}{n\sum x_k^2 - (\sum x_k)^2}} \qquad (E5.32)$$

The standard deviation of the y-intercept is

$$\sigma_c = \sigma_y \sqrt{\frac{\sum x_k^2}{n\sum x_k^2 - (\sum x_k)^2}} \qquad (E5.33)$$

Applied to the present method the degree of y-value scatter is $\sigma_y = \pm11.13$nm; the standard deviation of the slope is $\sigma_m = \pm 0.418$ and the standard deviation of the y-intercept is then $\sigma_c = \pm 6.57$nm.

The error of the dimensions of one pixel ($\sigma Pixel_L$; $\sigma Pixel_W$) can be determined statistically be measuring the number of pixel of a known scale in x- and y-direction several times. 10 to 15 measurements are recommended.

A total accuracy of the method alone can not be gauged because it depends on variables such as the dimensions of the image, the number in pixel and the birefringence of the crystal. Hence the error has to be calculated for every single crystal separately.

5.2.4.6 Testing the birefringence mapping method

The applicability of this approach was tested on a set of seven crystals with variable symmetries, morphologies, densities, birefringence and weights. These crystals are: quartz, anhydrite, gypsum, natrolite and mica. All grains were weighed 10 times to assure a good quality of their weights. Anhydrite however was too small for weighing. Its dimensions were determined by gluing the grain to a thin glass nod (Fig. 5.46) and mounting it on a spindle stage. Turning the spindle resulted in different positions of the grain, its dimensions were measured with an object micrometer and the volume could be determined precisely.
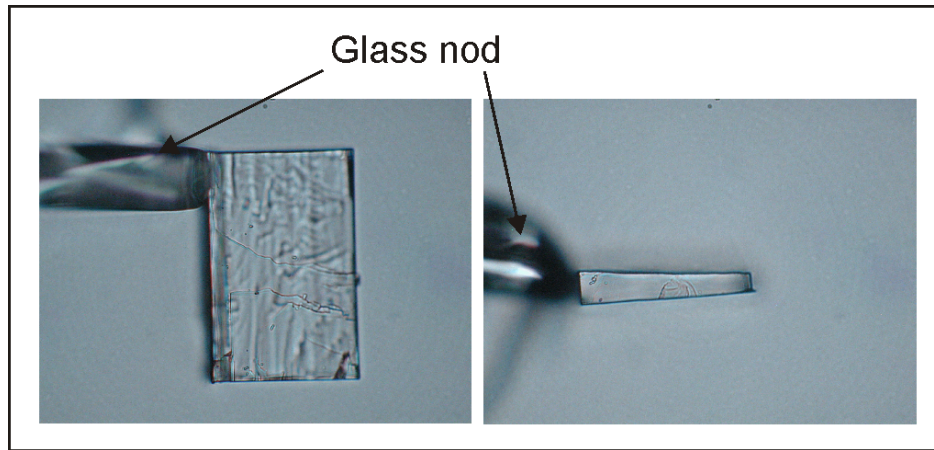
Fig. 5.46: Anhydrite crystal glued to a thin glass nod (indicated by the two arrows) and mounted on a spindle stage to determine its dimensions.

After weighing the samples, for every single crystal a set of 24 pictures was taken with a Nikon Coolpix 990 mounted on a microscope, one picture per compensator position. The volumes of the crystals were then modeled based on the new developed approach according to the procedures described above. Figure 5.47 plots the measured weights versus the modeled masses.
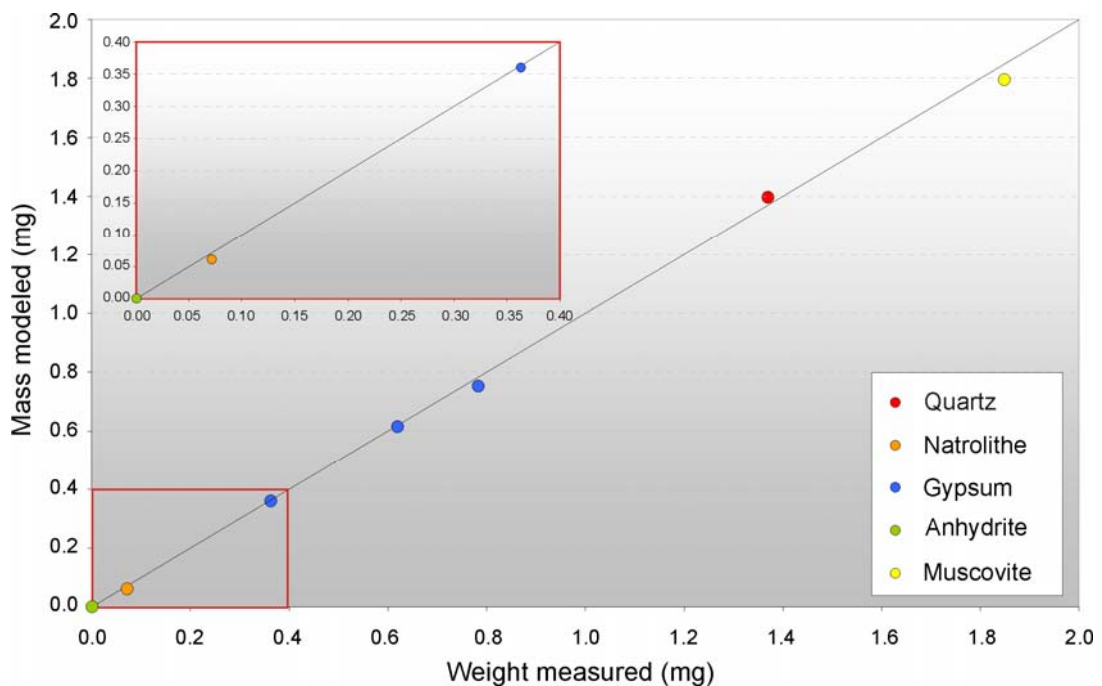
Fig. 5.47: Modeled masses versus measured weights for a set of five different crystal types. The black solid line is the 1:1 correspondence.

The sample masses, determined with the new approach, are compared to their weights. In table 5.12 the weights, determined volume, densities and calculated masses are represented.

Table 5.12: Measured weights compared to the modeled masses and volumes of six different crystals. In addition the densities are also stated. Densities are taken from Tröger (1982).

Crystal type	Volume modelled (mm3)	Density	Mass modelled (mg)	Weight measured (mg)
Quartz	0.527	2.65	1.397	1.370
Natrolite	0.028	2.20	0.062	0.072
Gypsum no.1	0.155	2.32	0.360	0.363
Anhydrite	0.000	2.96	0.001	0.001
Muscovite	0.635	2.83	1.796	1.849
Gypsum no.2	0.325	2.32	0.753	0.783
Gypsum no.3	0.265	2.32	0.615	0.62

The modeled masses of the crystals agree very well with the measured weights. However, the masses of muscovite and natrolite vary slightly from the measured weights. A natural muscovite sample was used to test the method. Its unknown iron-content affects the birefringence. To determine the correct birefringence the thickness of the muscovite crystal was measured with the spindle stage. Unfortunately the crystal had not a constant thickness over its whole surface and it was not possible to determine the thickness of the crystal precisely. Consequently the determined birefringence is only an approximation of its real birefringence and the modeled mass differs from its weight.

Natrolite on the other hand is a very small grain and its weight lies almost within the error of the electronic balance. Additionally it has a very high birefringence and the compensator reached its limitation. These two aspects may explain the larger difference between the measured weight and the calculated mass.

Therefore, it can be assumed that the volume is best fitting if the compensator is not used to its upper limit and if the birefringence is known exactly for the sample that is to be modeled. Figures 5.48 to 5.50 illustrate the resulting crystal images corresponding to

the data in figure 5.47 and table 5.12. All modeled images can be found in the Appendix IX.

Muscovite
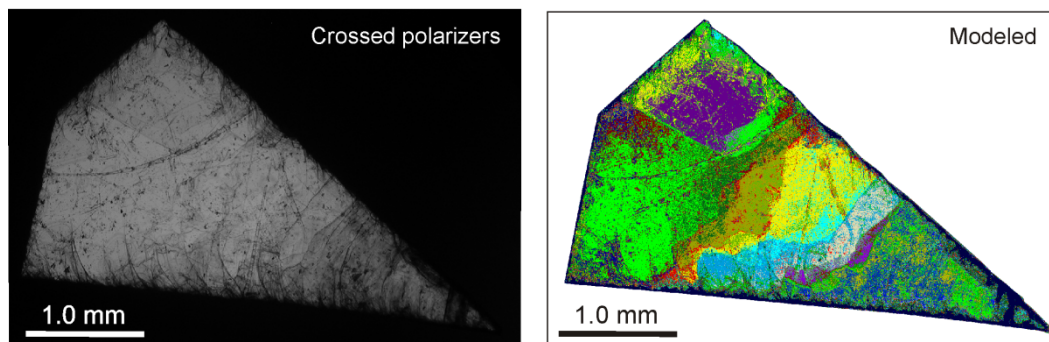
Fig. 5.48: Muscovite crystal under crossed polarizers and modeled.

Anhydrite
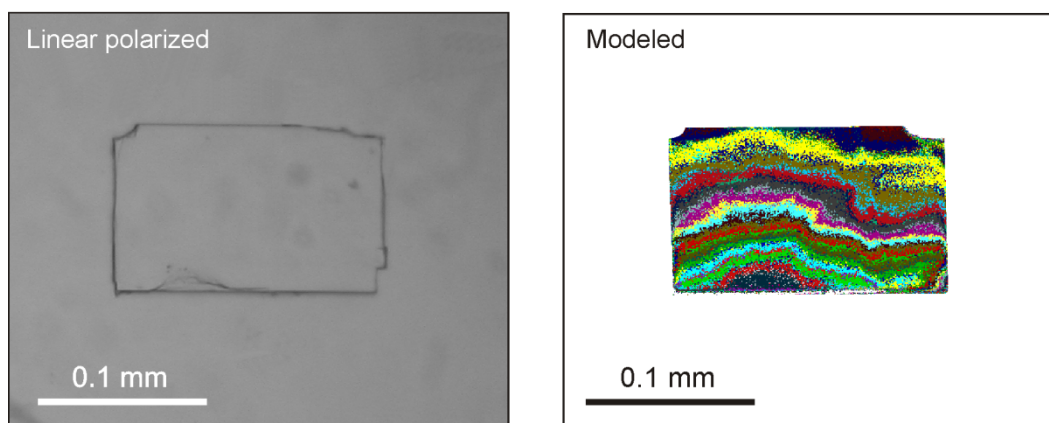
Fig. 5.49: Anhydrite crystal under crossed polarizers and modeled.

Gypsum no. 2
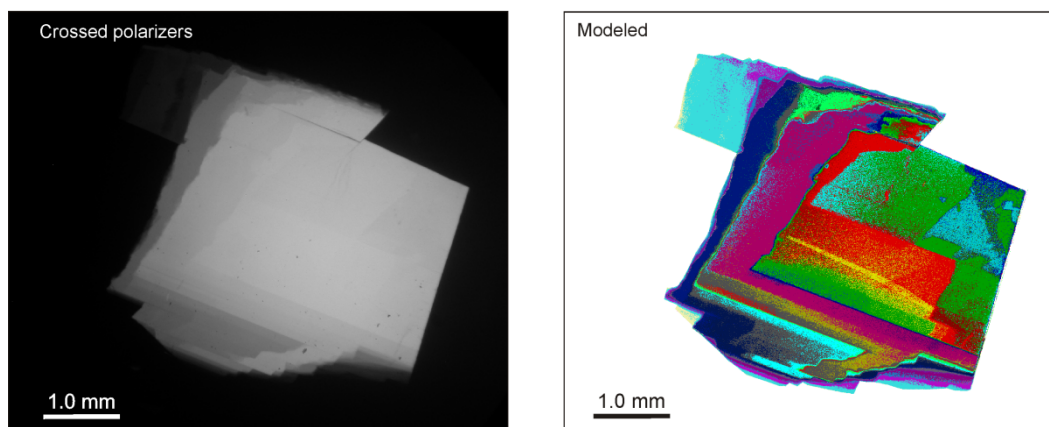
Fig. 5.50: Gypsum crystal no. 2 under crossed polarizers and modeled.

5.3 Practical applications

5.3.1 Quartz solubility

5.3.1.1 Introduction

The solubility of quartz in aqueous solutions is of fundamental importance to geochemistry and petrology. Because quartz solubility increases with pressure at a given temperature, Si metasomatism is particularly important in metamorphic and igneous processes at high pressures (Manning, 1994). The magnitude and variation of quartz solubility in H_2O result in a strong potential for local to large-scale redistribution of Si during fluid-rock interaction in diverse geologic environments (e.g. Wood and Walther, 1986).

The major sources of information on quartz solubility as a function of pressure and temperature are experimental studies in pure water, starting with the low-pressure studies of Kennedy (1950) and Morey and Hesselgesser (1951). Studies at high pressures include the work of Anderson and Burnham (1965) to 9 kbar and 900°C and that of Manning (1994) to 20 kbar and 900°C. All of these studies used the weight-loss method. A ground fragment or crushed aggregate of natural quartz was equilibrated with pure water for hours to days and then cooled to room temperature within several seconds to tens of minutes, depending on the type of apparatus. The combined dataset of earlier observations was summarized by Manning (1994) in a single equation, in which the solubility of quartz is expressed as an empirical function of temperature and water density. In 2004 Wang *et al.* studied the solubility of quartz *in situ* in pure water between 25°C and 490°C and 1 bar to 8.9 kbar in a hydrothermal diamond anvil cell using the optical weighing method introduced by Matthews and Davis (1999). They abraded natural quartz into ellipsoids and calculated the weight of each grain by measuring the two principal axes from taken images. The results agree with those of Manning (1994) up to about 370°C, but not above this temperature, because of under- and overestimation. The refaceting of the ellipsoids to approach a trigonal habit was the major contribution to the overestimation. This optical weighing technique is therefore limited in determining quartz solubility up to 370°C (Wang *et al.*, 2004). It is designed for spherical objects and is not suitable for longer prismatic crystals (Matthews and Davis, 1999).

The new approach developed and described in this study can overcome the limitations of the optical weighing method described by Wang *et al.* (2004) by using the geometry of a crystal's morphology to determine its volume and mass.

5.3.1.2 Experimental methods

Because the Burchard-Zaitsev hydrothermal diamond anvil cell was not yet ready for operation, the solubility experiments were carried out in an externally heated Bassett-type of hydrothermal diamond anvil cell (Bassett *et al.*, 1993) in Paris, France, and Potsdam, Germany. The sample is contained in a rhenium gasket compressed with two type-I diamonds with 1 mm culets. The initial diameter of the borehole in the gasket is 0.5 mm. Heating is achieved by passing a high electrical current through the molybdenum wires around the tungsten carbide seats below the diamonds. During operation, the cell is flushed with an argon–hydrogen (3%) mixture to prevent oxidation of the diamonds and the molybdenum heater. Temperature is measured by two type-K thermocouples attached to the diamonds. The temperature in the sample chamber was calibrated against these thermocouples by measuring the melting points of $NaNO_3$, CsCl, and sulphur in the cell at room pressure, or the α-β quartz transition (574°C) at room pressure observed by a slight visible change in birefringence. Accuracy in temperature measurement was ± 1.5°C in Potsdam, ± 2°C up to 400°C in Paris and our own laboratory which increases to ± 7°C for measurements above 400°C.

The pressure medium in all experiments was pure bi-distilled water. The pressure inside the sample chamber was calculated from the equation of state of water from Wagner and Pruß (2002). After cooling, the bulk density of the pressure medium was determined by measuring the homogenization temperature.

For each CVC experiment an idiomorphic quartz crystal is needed to determine its volume and mass before the experimental run. Such crystals were grown with hydrothermal synthesis. Crushed natural quartz from Brazil was filled in a gold capsule together with SiO_2 gel and double deionized water. The gel is used to assure fast over-saturation of the fluid. The gold capsule rims were closed by arc-welding. Minimization of fluid loss is assured with this welding technique. Capsule length, ratio between crushed SiO_2 and SiO_2 gel, water content and time were varied to get a maximum of good quality idiomorphic SiO_2 crystals. The best results were achieved with a capsule length of at least 25 mm, a ratio of crush crystals to SiO_2 gel of 1:1 and duration of the

experiments of three weeks. In table 5.13 the experimental run conditions are displayed together with the capsule specifications.

Table 5.13: Specifications of the experiments for hydrothermal SiO_2 crystal growth.

Number	Capsule length (mm)	Ratio crushed: gel	Weight H_2O (mg)	P (kbar)	T (°C)	Duration (days)
1	20	1:93	0.098	2	550 to 450 in 20/day	7
2	20	1:50	0.070	2	550	7
3	15	1:1	0.059	2	550	3
4	20	1:1.5	0.103	2	550	10
5	15	1:2	0.054	2	550	17
6	20	1:2.3	0.174	2	550	21
7	20	1:1.2	0.109	2	550	21
8	15	1:0.7	0.059	2	550	21
6+7	15	1:0.7	0.096	2	550	21
9	15	1:5.7	0.050	2	550	8
10	10	1:2	0.080	2	600	8
11	10	1:0.7	0.110	2	600	15
12	15	1:0.5	0.061	2	550	20
13	15	1:1	0.077	2	550	20
14	15	1:1.5	0.069	2	550	20
15	15	1:2	0.061	2	550	20
16	25	1:1	0.212	2	550	21
17	25	1:1	0.159	2	550	21

A single idiomorphic quartz crystal was used as starting material whose volume and mass had been determined before the experimental run to assure an accurate initial mass. The spindle stage was found to be a useful tool in identifying the crystal geometry very accurately. The cell was then loaded with the crystal, doubly distilled pure water and an air bubble and heated to the desired maximum temperature (Fig. 5.51). The sample was left to equilibrate for about 20 min. The temperature was then slowly

decreased to the various desired temperatures and the sample left to equilibrate for up to 15 to 20 min. Digital images were taken of the crystal by using a UTK objective. The optical path was oriented vertically from the top to the bottom diamond surface. The loss of mass was estimated by calculating the crystal volume at different stages of temperature as described in chapter 5.1.
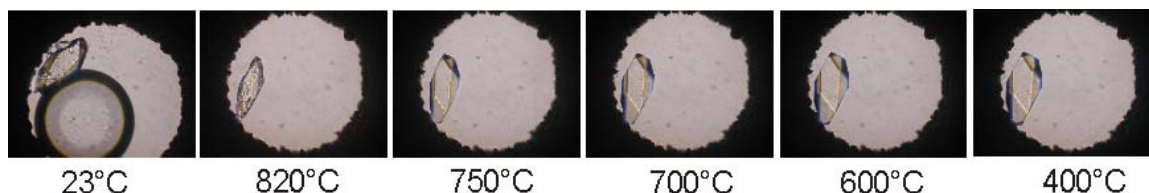
Fig. 5.51: Experimental run with quartz. A single quartz crystal is placed in the sample chamber with an air-bubble and pure water. During the cooling cycle the dissolved SiO_2 reprecipitates and refacets the grain into a trigonal shape.

For the birefringence mapping method a cropped piece of a quartz plate was instead of an idiomorphic crystal used whose indicatrix position was known exactly to calculate its birefringence. The procedure of the experiments was the same as for the CVC method, except that up to 24 pictures were taken at up to 24 different compensator positions at the desired temperature.

5.3.1.3 Results

The solubility data of quartz were collected between a temperature range of 31°C to 750°C and a pressure range of up to 11.7 kbar for bulk densities of 0.7807-0.9933 g/cm^3 for the CVC method. The results are plotted in Figure 5.52 - 5.57 and are summarized in table 5.14. The total data set can be found in the Appendix X. The circles indicate the solubility derived in this study and are compared to the solubility curve calculated using the equation of Manning (1994) (blue solid line) and Gerya *et al.* (2005) (red solid line). In addition two experiments at densities of $\rho = 0.97$g/cm^3 and $\rho = 0.99$g/cm^3 can be directly compared to experimental data from Wang *et al.* (2004) and are plotted in figure 5.58.
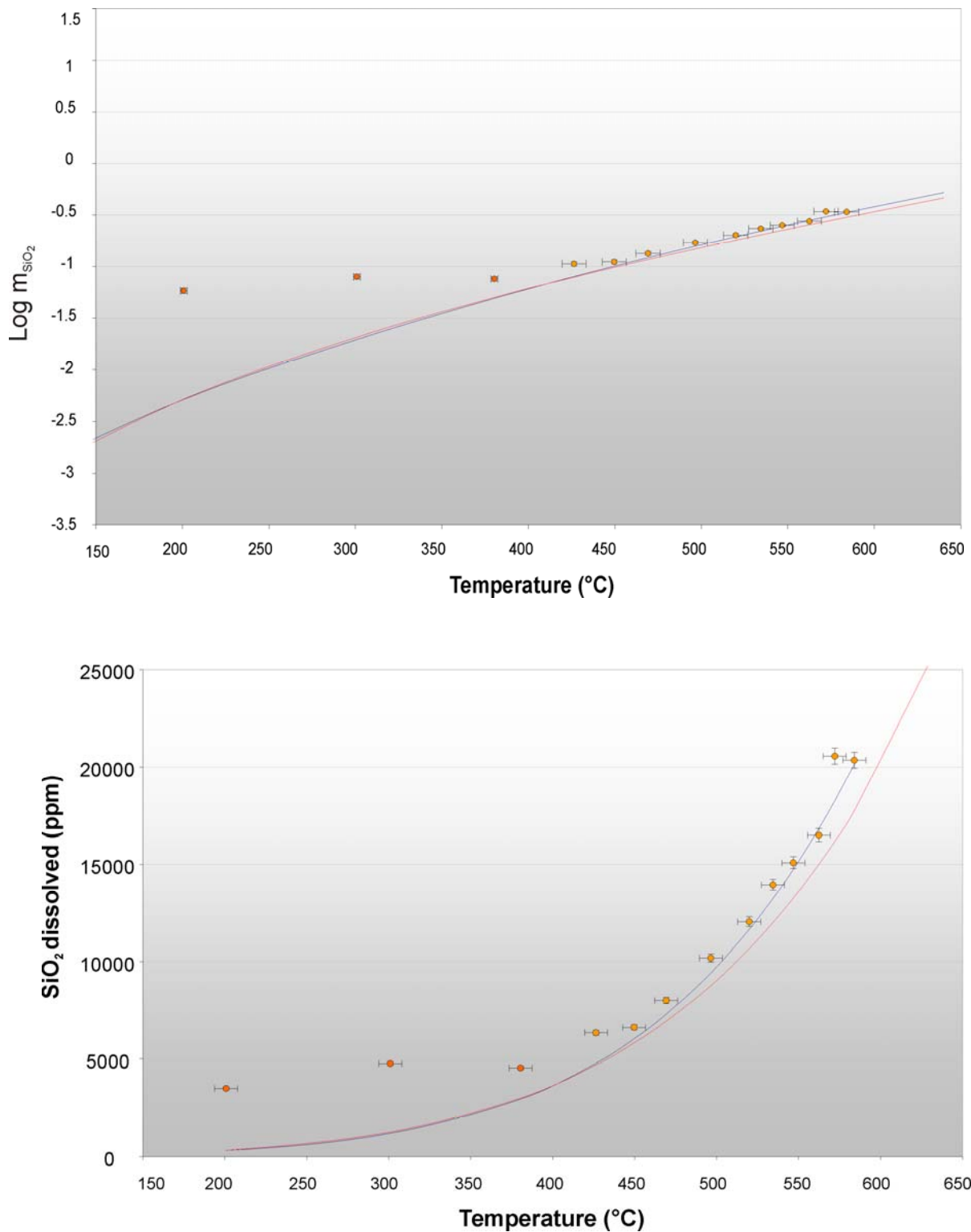
Fig. 5.52: Isochoric experiments at ρ = 0.9656 g/cm^3. Red circles indicate solubility data derived from this study, blue solid line indicates the calculated solubility from Manning (1994), red solid line indicate the calculated solubility from *Gerya et al.* (2005). m= molality. Standard deviation is displayed as 2σ.

138
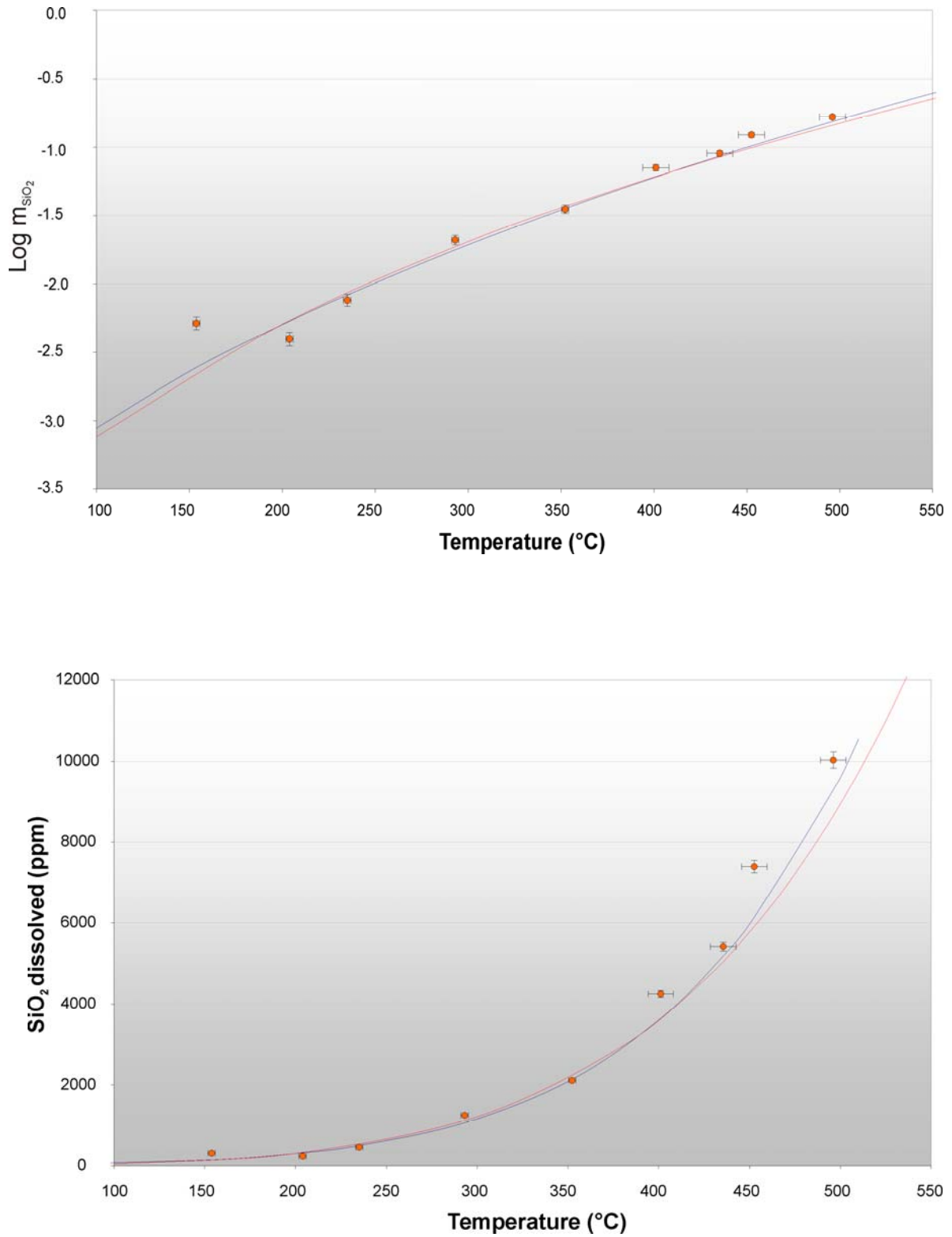
Fig. 5.53: Isochoric experiments at $\rho = 0.9614$ g/cm^3. Red circles indicate solubility data derived from this study, blue solid line indicates the calculated solubility from Manning (1994), red solid line indicate the calculated solubility from Gerya *et al.* (2005). m= molality. Standard deviation is displayed as 2σ.
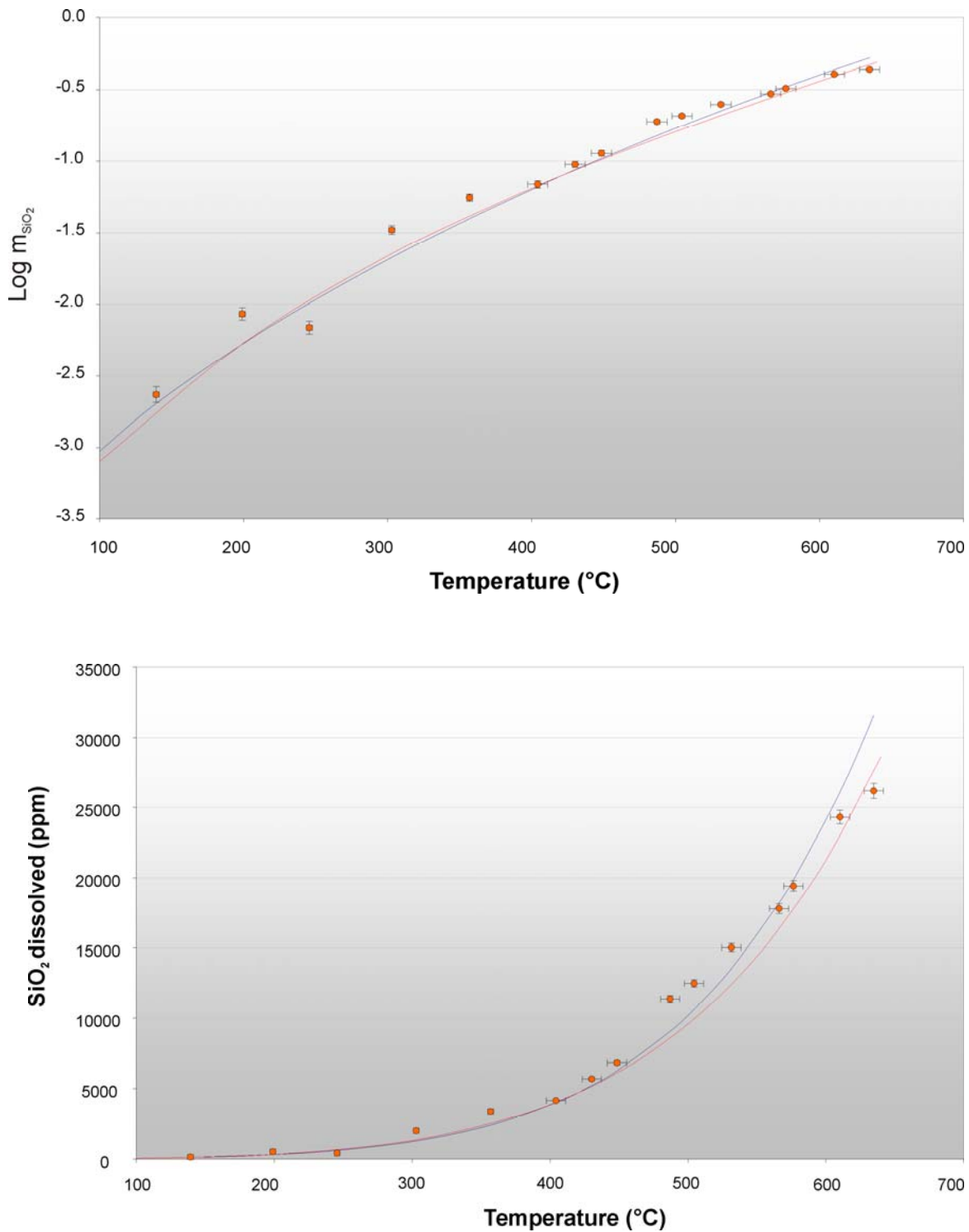
Fig. 5.54: Isochoric experiments at $\rho = 0.9876$ g/cm^3. Red circles indicate solubility data derived from this study, blue solid line indicates the calculated solubility from Manning (1994), red solid line indicate the calculated solubility from Gerya *et al.* (2005). m= molality. Standard deviation is displayed as 2σ.
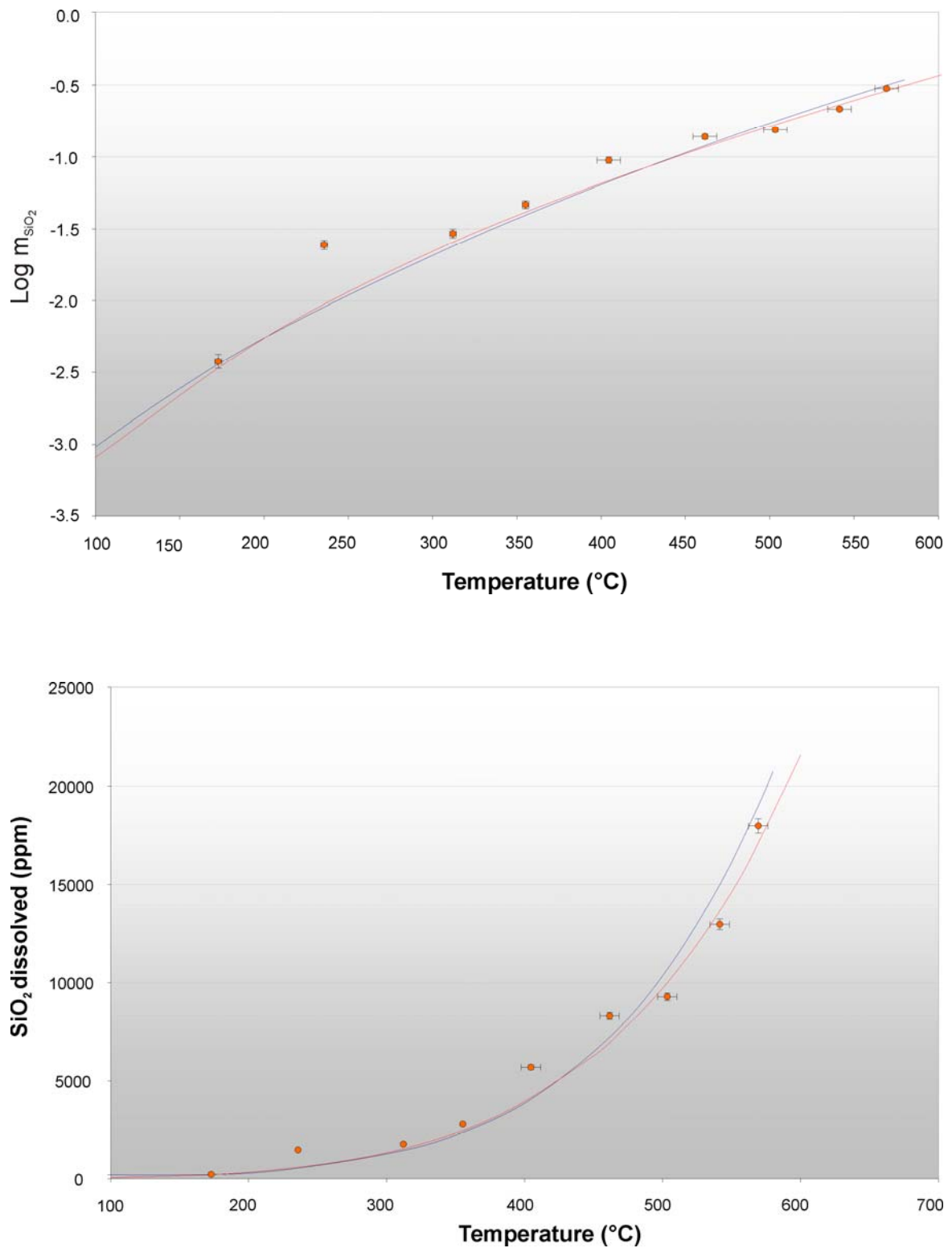
Fig. 5.55: Isochoric experiments at ρ = 0.9933 g/cm^3. Red circles indicate solubility data derived from this study, blue solid line indicates the calculated solubility from Manning (1994), red solid line indicate the calculated solubility from Gerya *et al.* (2005). m= molality. Standard deviation is displayed as 2σ.
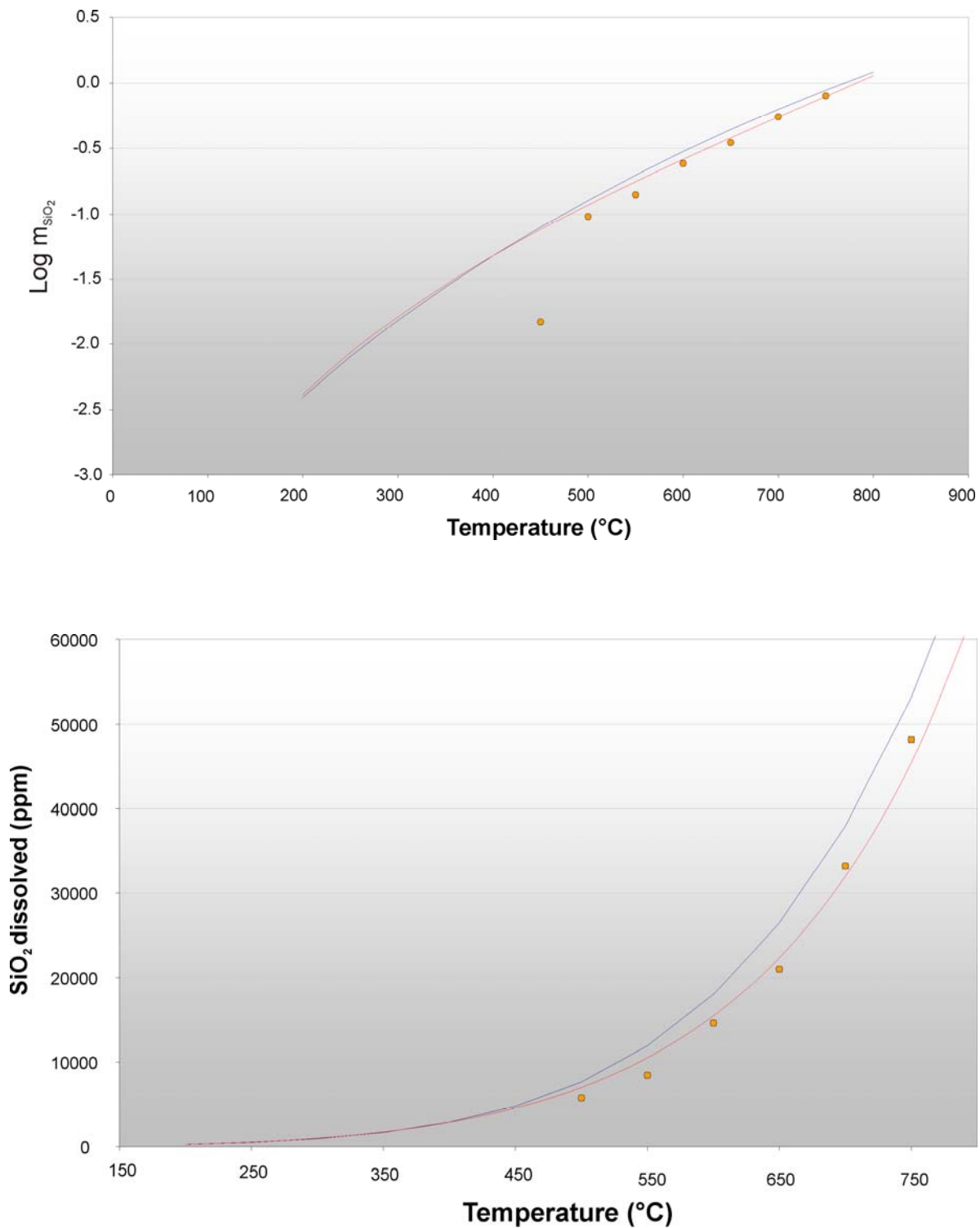
Fig. 5.56: Isochoric experiments at ρ = 0.8633 g/cm^3. Red circles indicate solubility data derived from this study, blue solid line indicates the calculated solubility from Manning (1994), red solid line indicate the calculated solubility from Gerya *et al.* (2005). m= molality. Standard deviation is displayed as 2σ.
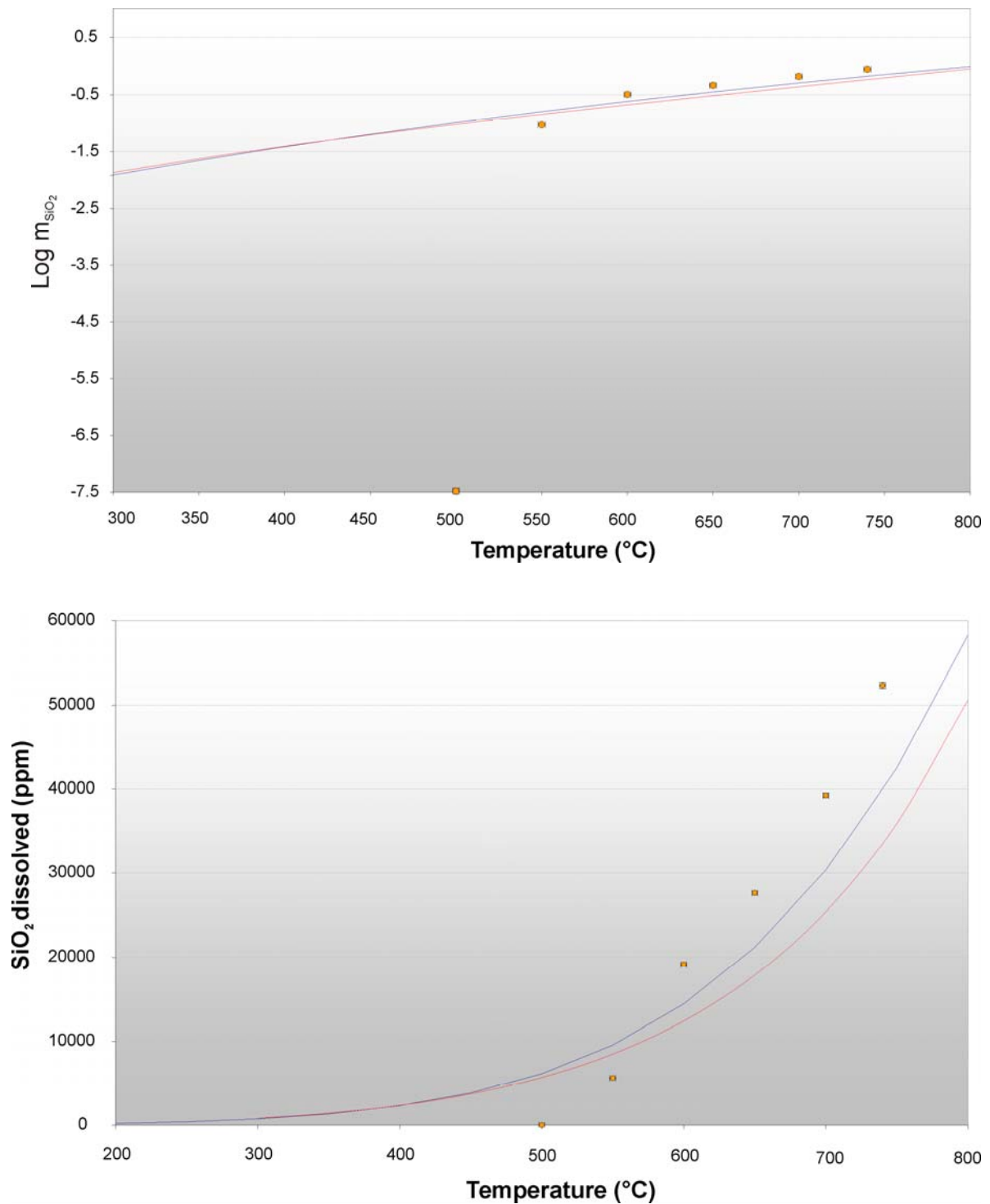
Fig. 5.57: Isochoric experiments at ρ = 0.97797 g/cm³. Red circles indicate solubility data derived from this study, blue solid line indicates the calculated solubility from Manning (1994), red solid line indicate the calculated solubility from Gerya *et al.* (2005). m= molality. Standard deviation is displayed as 2σ.
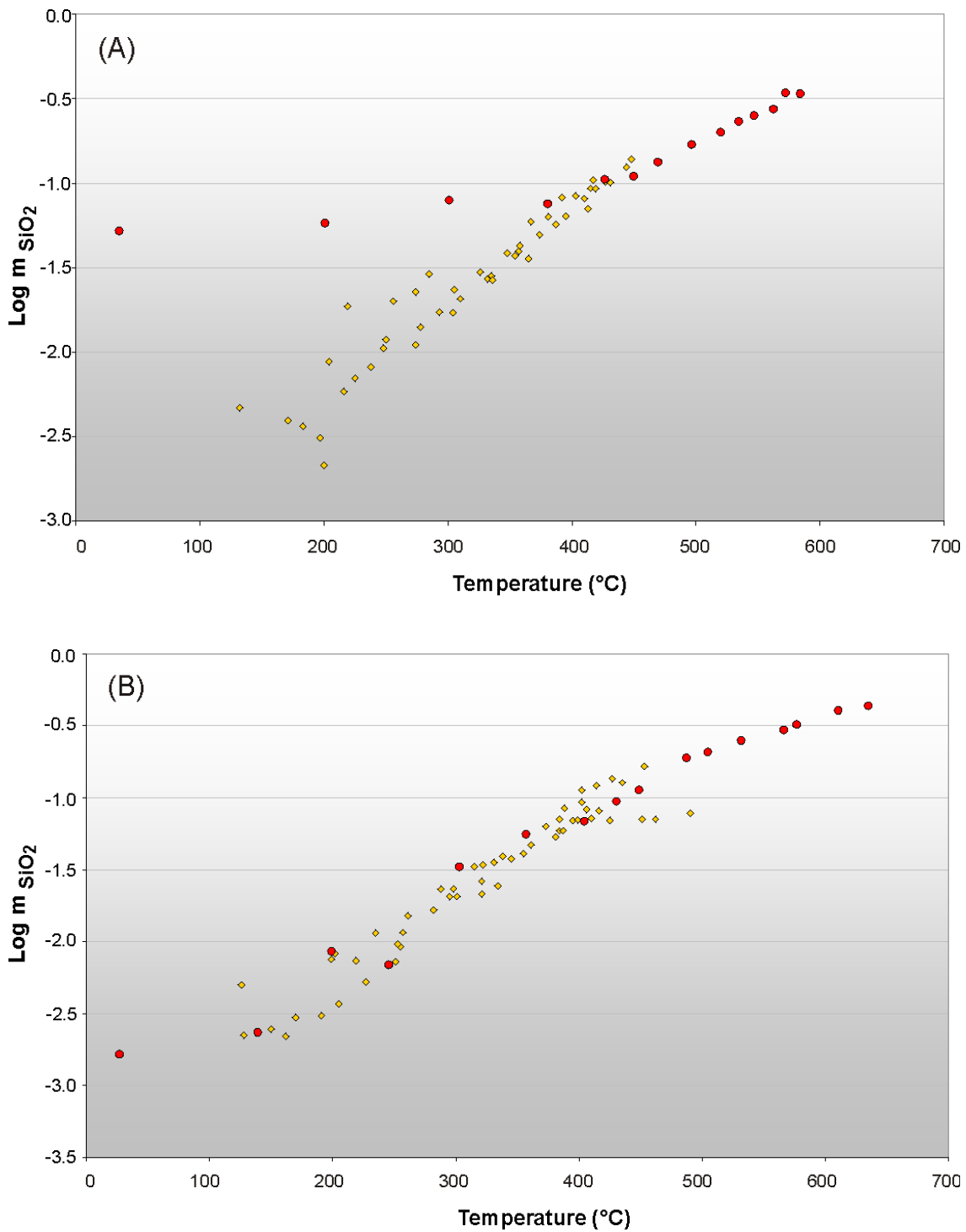
Fig. 5.58: Comparison of the solubility data derived in this study (red circles) with the data from Wang *et al.* (2004) (yellow diamonds). **(A)** Solubility data for the isochoric experiment at $\rho = 0.97 \text{g/cm}^3$. **(B)** Solubility data for the isochoric experiment at $\rho = 0.99 \text{g/cm}^3$. m= molality.

Table 5.14: Extracted solubility data derived in this study with the CVC method. The total data set can be found in Appendix X.

	Temperature (°C)	Pressure (kbar)	Qtz loss (μg)	Solubility (mol/kg)	Solubility (ppm)	Volume H_2O (mm^3)
Bulk density ρ = 0.9656;	T_H 89.5					0.02065
	584	9.7	0.4058	0.3388	20356	
	562	9.3	0.3289	0.2746	16500	
	450	7.1	0.1319	0.1101	6615	
	201	2	0.0696	0.0581	3493	
Bulk density ρ = 0.9614;	T_H=95.7					0.02073
	496	7.8	0.1999	0.1669	10029	
	352	5	0.0421	0.0352	2113	
	154	1	0.0062	0.0052	310	
Bulk density ρ = 0.9876;	T_H = 50.8					0.01780
	635	11.7	0.4600	0.4355	26169	
	610	11.2	0.4274	0.4047	24316	

All experiments were carried out within similar HDACs and all solubility data were determined with the newly developed volume computational approach using the Kristall2000 (Schilling, 2008) method. Therefore, it can be assumed that sources of random error are similar for all measurements. The volume of water in the HDAC could not be measured directly. Instead it was assumed that the amount of water is equal to the dimensions of the sample chamber. Shen *et al.* (1992) determined that the sample volume does remain relatively constant during cooling of the system from an elevated temperature and compression of the gasket results in a change of volume of only 0.5%. Therefore, measurements were made during the cooling part of the heating cycle.

The corrected water volume represents a difference of 0.5% from the original calculated volume. The accuracy of the homogenization temperature is measured within ± 1.5°C for the experiments done in Potsdam and ± 2°C for experiments derived from Paris which corresponds to a maximum density uncertainty of 0.2%. Consequently, the maximum uncertainty for the calculated mass of H_2O is 0.54%.

The accuracy of the solubility data is also based on the quality of the images taken. For the experiments derived in Potsdam good quality images were taken and the

accuracy of the calculated masses of the quartz grains is assumed to be 0.38% (see chapter 5.1.3.3). The accuracy of the solubility data based on the Gaussian error propagation is 0.7%.

For experiments derived in Paris the quality of the images is not so good, because strong total reflection arose. Therefore, 27 sets of volume and mass determinations of 5 replicated crystal yielded a standard deviation of σ = 1.96% using the equations E5.1-E5.3. This results in an accuracy of the solubility data of 2.04% based on the Gaussian error propagation.

With the birefringence mapping method solubility data of quartz were collected between a temperature range of 139.4°C to 500.4°C and a pressure range of up to 6.89 kbar for a bulk densitiy of 0.9332 g/cm^3. The results are plotted in figure 5.59. A table of the summarized data can be found in the Appendix XI. The circles indicate the solubility derived in this study and are compared to the solubility curve calculated using the equation of Manning (1994) (blue solid line) and Gerya *et al.* (2005) (red solid line).

The accuracy of the solubility data is based on the same assumptions made for the CVC method for the water density and volume of sample chamber deviations. The accuracy of a pixel length was statistically determined to an error of 0.3%. The standard deviation of the average phase difference was calculated based on the Gaussian error propagation and the equations E5.23 to E5.33 to 2.23%. The volume and mass standard deviations of the crystal are than 2.33% and 2.36% which leads to a standard deviation for the solubility data of 2.42%. The birefringence of the diamond anvils does affect the resulting volume and mass determinations and will cause a stronger error. Based on the volume determinations of a quartz crystal within and without a HDAC this error is assumed to be about 5.6%. Therefore the total error in the solubility data is calculated to 5.6%.
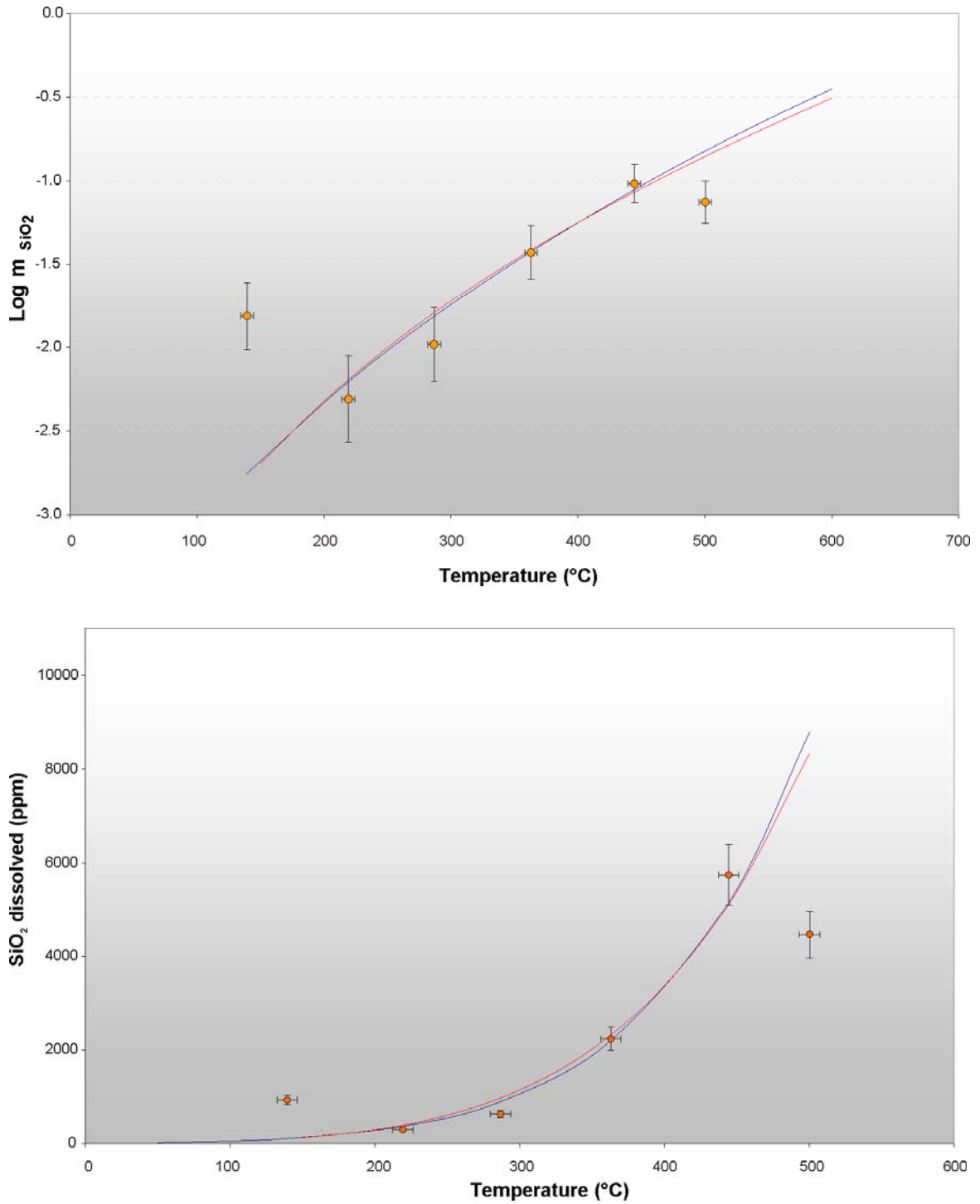
Fig. 5.59: Isochoric experiments at ρ = 0.97797 g/cm³ obtained with the birefringence mapping method. Red circles indicate solubility data derived from this study, blue solid line indicates the calculated solubility from Manning (1994), red solid line indicate the calculated solubility from Gerya *et al.* (2005).

5.3.1.4 Discussion

The solubility data derived in this study with both methods (CVC and BM) agree very well with published data from Manning (1994), Gerya *et al.,* (2005) (Fig. 5.52 – 5.57) and also Wang *et al.* 2004 (Fig. 5.58). For any given isochoric experiment, the solubility of quartz increased with increasing temperatures as predicted by previous studies (Manning, 1994; Gerya, *et al.*, 2005).

However, for experiments derived with the CVC method the 0.9656 g/cm^3 isochor deviates at temperatures below 400°C (Fig. 5.52 and Fig. 5.58A). Closer inspection of the images revealed that at temperatures below 400°C amorphous quartz and whisker-like quartz crystals precipitated on the lower diamond anvil and the gasket wall (Fig. 5.60).
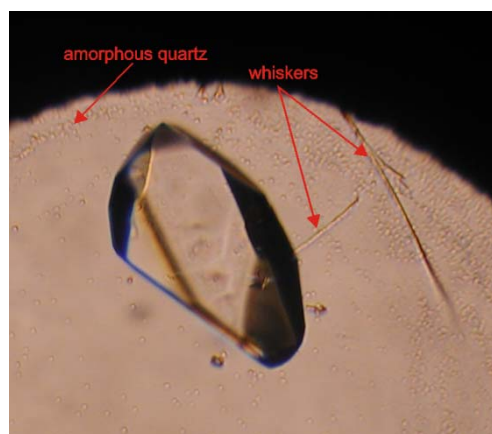
Fig. 5.60: Idiomorphic quartz crystal re-precipitated from the isochoric experiment ρ = 0.97g/cm^3 with amorphous and whisker-like quartz that crystallized on the lower diamond anvil and the gasket wall at temperatures below 400°C.

Therefore, the initial quartz grain did not grow as much as predicted. This re-precipitation is most likely due to the fact that the temperature drop between the different temperature stages was too fast below 400°C. Also a thermal gradient between the upper and lower diamond was caused on purpose to prevent tiny quartz crystals to re-precipitate onto the upper anvil as reported by Wang *et al.* (2004). To keep the lower diamond a few °C cooler the dissolved SiO$_2$ should re-precipitate on the existing quartz grain, allowing it to grow. The thermal gradient >5°C was probably too large and in conjunction with the rapid temperature drop it caused amorphous quartz and whisker-grains to re-precipitate on the lower anvil and the gasket wall. Unfortunately there is no accurate way of determining the amount of the re-precipitated phases inside the cell (Wang *et al.*, 2004). The crystals are usually too small and too numerous to be measured. Also tiny crystals might re-precipitate at the gasket wall where they will not

be noticed during experimental runs. Nevertheless, heating the cell to over 600°C resulted in total dissolution of the unintentional grains. The gradient was reduced to ca. 2°C difference and the system was cooled more slowly below 400°C. Re-precipitation other then the growing initial quartz grain was minimized or eliminated.

Solubility measurements are also limited by the quality of the images taken. Total reflections of the grains complicate modelling the correct geometry and therefore the exact volume. The accuracy of the method decreases. Using a microscope for the experiments as optical equipment can reduce this effect.

For CVC experiments at $\rho = 0.8633$ and $\rho = 0.7797$ (see Fig.5.56 and 5.57), carried out in Potsdam, a microscope was used. Total reflection was minimized. However, data for the 0.8633 g/cm^3 isochor deviate from the calculated solubility predicted by Manning (1994) but fits quite well with the data calculated from Gerya *et al.* (2005). Data for the density of 0.7797g/cm^3 plot above the predicted data from Manning (1994) and Gerya *et al.* (2005). It has to be noticed that both experiments carried out in Potsdam did not run according to plan. The quartz crystals used as starting material were not perfectly idiomorphic. However, the crystals refaceted during the experimental runs while the system was cooled down. Both experiments were terminated at 400°C ($\rho = 0.8633$g/cm^3) and 450°C ($\rho = 0.7797$g/cm^3). Unfortunately the images taken of the quartz grains were not scaled after the experiments. The quartz crystals were recovered after the experimental runs and measured with the spindle stage to calculate the initial volumes and masses. Images were taken from different orientations of the crystals and modeled with the new developed CVC method. These images were then scaled with an object micrometer. The so calculated volumes were assumed to be equal to the 400°C and 450°C volumes of the quartz grains and used as starting material. This is not accurate. At temperatures of 400 and 450°C some dissolved SiO_2 still is in solution. Also after cooling of the system to room temperature SiO_2 can still be in the solution as metastable fluid (Burchard personal communication, 2008). The determined masses of the crystals recovered after the experiments are therefore not equal to the initial start masses of the crystals. Therefore, the mass and volume changes are only approximations of the real solubility. This can explain the deviations of the predicted solubility from Manning (1994) and Gerya *et al.* (2005).

The solubility measurement derived with the birefringence mapping method was determined on the heating and cooling cycle of the experiment. Unfortunately during cooling the SiO_2 did not reprecipitate on the initial quartz grain. Instead small crystals

grew upon the quartz grain and the culet faces of the diamond anvils. Therefore only the heating cycle could be used for solubility analysis. At 139°C and 500°C the data points deviate from the predicted solubility curve. For the lower temperature data point the equilibrium time could be a source of error. Waiting times exceeded 20min but this might even not be enough. Zotov and Keppler (2002) showed through time dependent measurements in HDAC that the equilibrium is achieved seconds after heating to the respective temperature. This observation applies to temperatures above 400°C and it might not be applicable for lower temperatures. Nevertheless, Wang *et al.* (2004) showed that waiting times of 15 min are sufficiently long for equilibrium to achieve. Another possibility that can explain this deviation is the impact of the stress birefringence on the birefringence mapping method. The stress birefringence is pressure and temperature dependent and has to be corrected for every single data point. The assumed regression that describes the behavior of the stress birefringence underneath the crystal was expected to be relative simple and linear to 3rd degree regressions were used. These regressions are likely not to represent the true behavior but are much more complex and hence are a source of error. It could be possible that both data points would fit better to the predicted solubility curve if more complex regressions are used. This is a very time consuming procedure and needs to be reworked and adapted in the future.

Another source of error is the purity of the materials used. The observed tiny crystals that grew during the heating and cooling cycle of the experiment were measured with the scanning electron microprobe and turned out to be iron-silicates (Fig. 5.62 and 5.63). Therefore the pure, double-deionized water from our laboratory was tested since it could be the only source contamination. Measurement with a Unicam ICP 701 emission spectrometer revealed that our water has traces of iron (Fig. 5.61) of > 15ppb.
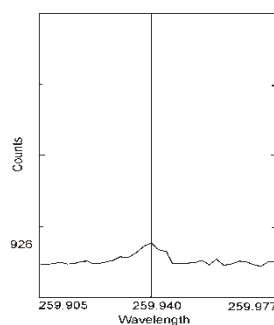
Fig.5.61: Iron peak of the analyzed water measured with an ICP 701 emission spectrometer. Standard measurements showed that 926 counts correlate to >15ppb iron.

If this water is funneled inside the sample chamber with a very thin injection needle, small amounts of water might remain within the injection needle and dry out resulting in reprecipitation of iron inside the needle. By using the same injection, even after cleaning it, the remaining iron will slightly concentrate and contaminate the water that is put inside the sample chamber. At some point the concentration of iron is sufficient to react with the dissolved quartz and tiny crystals will form on the initial crystal grain, the diamond anvil faces (Fig. 5.62) and also the gasket walls (Fig. 5.63).
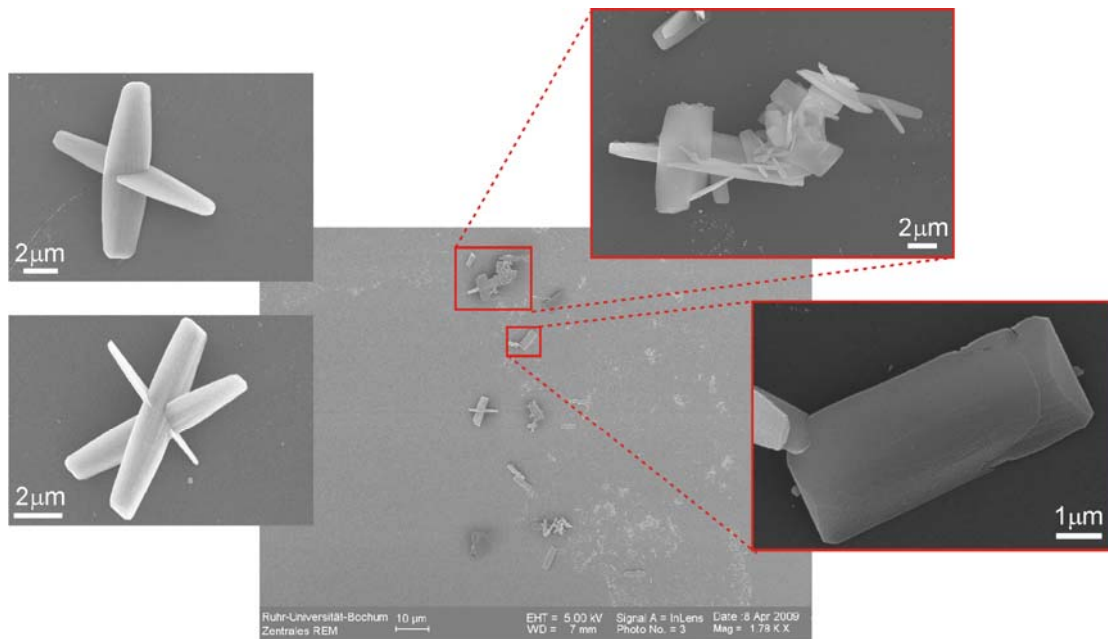
Fig. 5.62: Tiny, idiomorphic iron-silicates that precipitated on the culet faces of the diamond anvil.
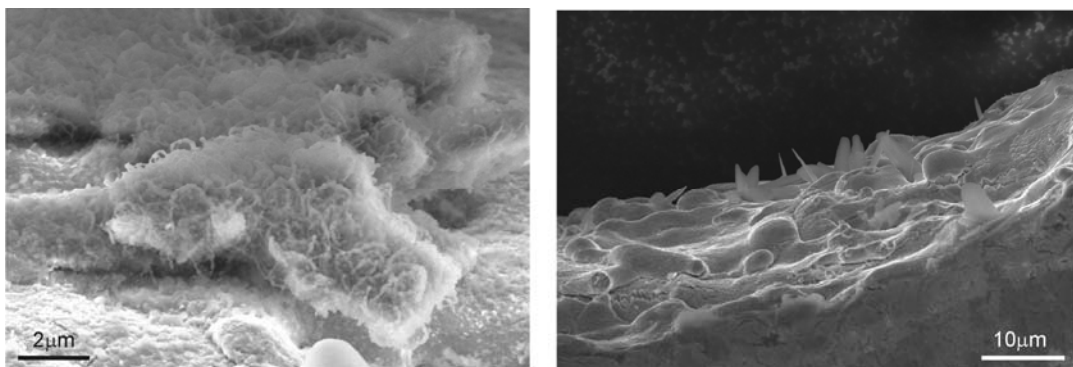
Fig. 5.63: Tiny iron-silicates that precipitated on the gasket walls lawn like.

5.3.2 Gypsum measurements

Gypsum (CaSO$_4$*H$_2$O) is one of the most common sulfate minerals, that forms in a variety of environments including hydrothermal vents near mid-ocean ridges, in diagenetically altered marine sediments and evaporate deposits (Knittle *et al.*, 2001). Solubility determinations of gypsum and its related sulfate phases Bassanite and anhydrite have been studied by several authors (e.g. Blount and Dickson, 1973).

To test the birefringence method on a broader range of morphologies, densities and birefringences, gypsum solubility data were determined within the HDAC. Experimental methods were the same as for the quartz solubility. Equilibrium waiting times were between 5 to 10 minutes. Solubility data were determined from 26°C-83°C at room pressure. Note that the temperature of the transition of gypsum to anhydrite is 40°C. At temperatures above 40°C gypsum is therefore strictly spoken in metastable solution However, the derived solubility data (yellow filled circles) could not reproduce the data from literature (pink filled triangles) (Fig. 5.64). Table 5.15 represents the determined solubility data.
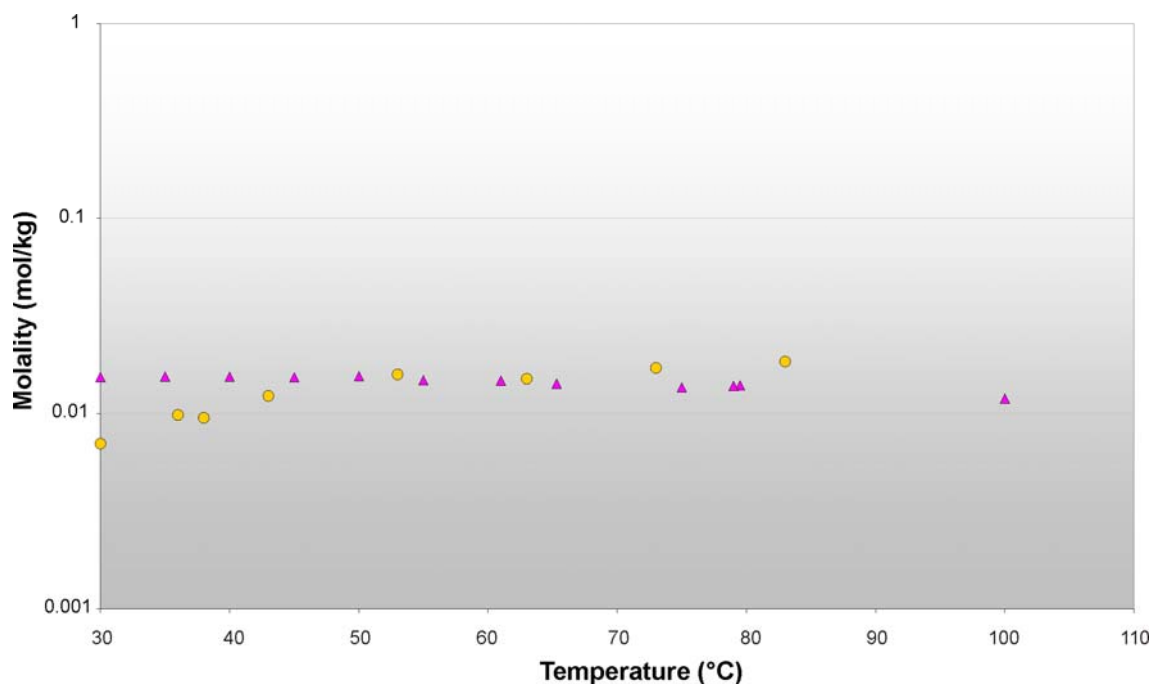
Fig. 5.64: Solubility data of gypsum (yellow filled circles) derived with the birefringence mapping method compared to the literature data (pink filled triangles) for solubility of gypsum. Data from literature are from Blount and Dickson (1973); Hullet and Allen (1902) and Marshall and Slusher (1966).

Table 5.15: Determined solubility data

Temperature (°C)	Gypsum loss (μg)	Solubility (mol/kg)	Solubility (ppm)	Volume H_2O (mm^3)
26	0.0256	0.0055	952	0.0278
30	0.0324	0.0070	1204	
36	0.0454	0.0098	1689	
38	0.0439	0.0095	1634	
43	0.0568	0.0123	2115	
53	0.0731	0.0158	2721	
63	0.0695	0.0150	2587	
73	0.0790	0.0171	2941	
83	0.0852	0.0184	3171	

At temperatures below 50°C the solubility was underestimated and above 65°C the solubility was overestimated.

The short waiting times to reach equilibrium could be responsible for the over- and underestimation. Dickson *et al.* (1963) reported that a time of 48 hours is required to reach equilibrium between anhydrite and the solution. Therefore it is possible that gypsum needs similar times to equilibrate. To see whether the equilibrium times within a HDAC of several minutes are too short, a time-dependent solubility measurement of gypsum was determined at 40°C and room pressure. In figure 5.65 the results are plotted and are displayed in table 5.16.
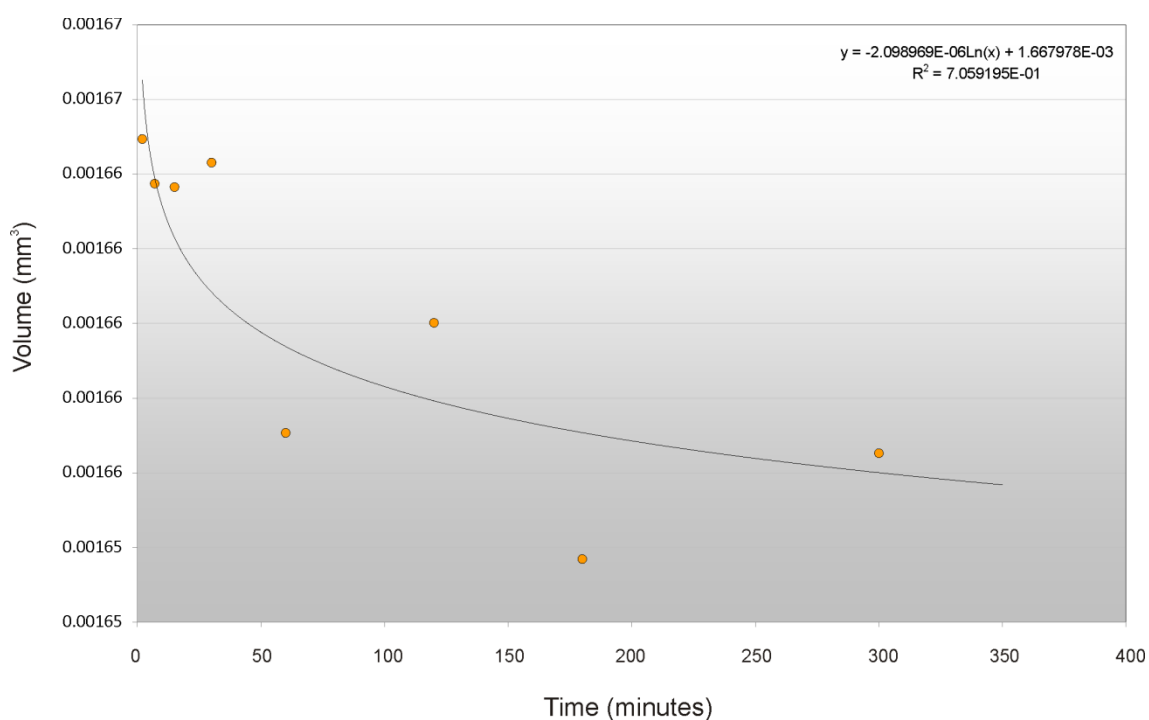
Fig. 5.65: Time dependent measurement of gypsum. The solid black line represents the line of best fit. The equation is displayed in the right upper corner with $R^2 = 0.706$.

Table 5.16: Determined solubility data for gypsum

Time (min)	Volume (10^{-3} mm^3)	Mass (10^{-3} mg)
2	1.665	3.863
7	1.664	4.409
15	1.664	4.409
30	1.664	4.410
60	1.657	4.391
120	1.660	4.399
180	1.654	4.382
300	1.657	4.390

From Figure 5.65 it can be clearly noticed that equilibrium was not reached even after 300 min. The volume data points deviate around a logarithmic function suggesting that either too much of the gypsum was dissolved or the crystal started to grow. However at times above 300 min. it seems that the system starts level out at one value.

154

This observation concludes that waiting times of 5-10 minutes are much too low to reach equilibrium for gypsum solubility measurements. This could explain the deviation of the determined solubility data compared to the literature.

5.3.3 Equation of state of water

Using the equation of state of pure water raises the question:
Is the PVT behavior of pure water the same as the PVT behavior of H_2O with dissolved silicate, such as SiO_2?

To answer this question the PVT behavior of water with dissolved SiO_2 was calculated from the equation of Gerya *et al.* (2005). Comparing the PVT behavior of pure water and of H_2O-SiO_2 solution demonstrates that there is not much difference in the PVT behavior of both fluids up to 2 GPa (Fig. 5.66). Therefore, using the equation of state of pure water will lead to the correct pressure. By reaching higher pressures >2 GPa, a small difference exists and the calculated pressure has to be corrected slightly.
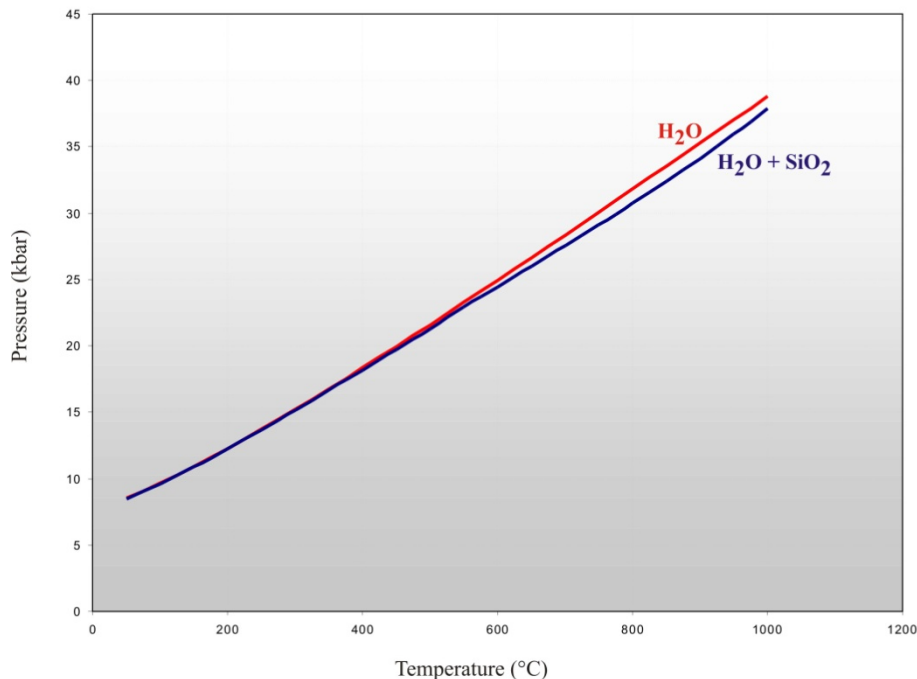
Fig. 5.66: Comparison of the PVT behavior of pure H_2O (red solid line) and a saturated H_2O-SiO_2 solution (blue solid line) using the EOS of Gerya *et al.* (2005).

6 Discussion and Conclusions

The capacity of a material to transmit fluid is a critical geological parameter, because migrating fluids play a fundamental role in heat and mass transport in petrologic processes in many medium- and high-pressure environments (e.g. Wyllie, 1979; Manning and Ingebritsen, 1999). In addition, H_2O is a powerful solvent at subduction zone conditions and can effectively mobilize many rock components (Manning, 2004a; Manning, 2004b).

It is therefore essential to understand the different elementary processes activated in response to different boundary conditions such as temperature, depth, rock composition and pore-fluid pressure. The basic atomistic mechanisms governing phenomenological rate laws for the rheological behavior of complex deforming rock-water systems at high pressures and temperatures, such as those typical for subduction zones, have been largely identified. But the quantification of characteristic rate-law parameters such as the solubility of rock forming minerals at high pressures and temperatures still remains problematic.

Two new promising, cutting edge approaches have been developed to determine solubility and quantify the amount of rock-forming minerals in solution. Both approaches are based on the use of a HDAC type which was developed earlier at the Ruhr-University of Bochum, called the Burchard-Zaitsev Cell.

This cell was used instead of the classical Bassett Cell, because the former was available at the beginning of the present study. In addition this cell had the advantage of an integrated cooling system. The cell body can be kept at room temperature even at high temperatures of the anvils. This results in minimization of undesired phenomena such as defocusing of the object due to thermal expansion of the objective. Another advantage is that pressures of at least 4 GPa can be reached with this type of cell as compared to the 2 GPa limit of the classical Bassett type of HDAC. However, it turned out that pressures of 4 GPa result in very strong deformation of the gasket and thus of the sample chamber. Pressures can no longer be calculated using the EOS of water. Phase transitions can be used for pressure calibration instead, but this technique was insufficient for the present study because pressure had to be calculated continuously during changing temperature conditions.

However, the Burchard-Zaitsev Cell had to be reconstructed and re-designed to allow routine experimental runs to be carried out. The possible changes to the cell were

limited by the given design of the hardened steel making up the outer cell body. All inner parts of the cell were entirely reconstructed. For reasons of economy of time and money these parts were machined out of high-grade stainless steel. The new construction was tested successfully and the critical problems that had arisen earlier were minimized or eliminated completely. Nevertheless, the new material did show signs of inelastic deformation. The inner cylinder of the upper adjustable seat sitting on the Belleville spring showed traces of yielding. Therefore, it is suggested that all parts of the cell should be made out of hardened steel in the future to minimize yielding effects that might result in additional sources of error.

The two new techniques developed in the present study for determining the solubility of minerals in a fluid combine the advantages of *ex situ* weight-loss and *in situ* approaches such as direct observation of the reaction path of the sample during changing P, T conditions while circumventing their obvious disadvantages, such as quench problems and overstepping of solubility isopleths. It results in much less ambiguity in the interpretation of the results as compared to the *ex situ* weight-loss method.

In the first method, called crystal volume computation (CVC), the crystal's volume and thus its mass is calculated by modeling its changing morphology during experimental runs. An idiomorphic crystal is used as starting material whose geometry and thus its volume and mass have been determined before the experimental run. By knowing the original volume and mass absolute solubilities can be calculated and by comparing masses at various P, T conditions relative changes in solubilities can be determined. The limitation of the CVC method lies in the fact that the starting material has to be idiomorphic. In addition, crystals with less complex symmetries cannot be modeled correctly inside a HDAC if their zone axis (indicated by the red line, Fig. 6.1) is parallel to the optical path (Fig. 6.1). The information on the length/thickness of the crystals parallel to the zone axis would be a critical missing parameter that cannot be retrieved from such 2-dimensional pictures (see Fig. 6.1B).
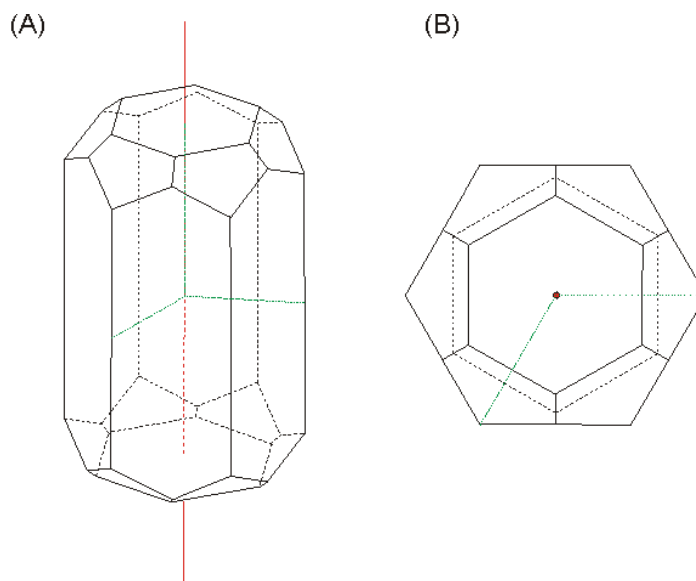
Fig. 6.1: (A) Beryl crystal in a general position with the zone axis indicated by the red line; **(B)** same crystal as would be seen inside a HDAC if the zone axis is parallel to the optical path (indicated by the red dot). The length/thickness of the crystal parallel to the zone axis cannot be determined from this 2-dimensional image. The green dashed lines indicate the a-, b-, c-axes in both cases.

The second approach uses the fact that minerals show birefringence in polarized light. The volume and thus the crystal's mass are determined by measuring its phase difference with a Babinet-Soleil compensator. A volume profile is created and relative changes of the crystal can be directly observed visually. By knowing the original volume and mass, again absolute solubilities can be calculated and by comparing masses at various P, T conditions relative changes in solubilities can be determined.

The advantage of the birefringence mapping method lies in the fact that any morphology of the starting crystal can be used, including cleavage fragments or chips of larger crystals. In addition, 3-dimensional information on the crystal is derived. With the profile created of the crystal, not only information about the dimensions of its surface, but also information about the thickness of every part of the crystal can be determined. This method is very sensitive down to the ppm-level, and therefore it is applicable to low-temperature experiments and time-dependent changes in solubility of crystals such as gypsum. The advantage is that changes can be observed visually from the volume profiles even before the actual changes are quantified by calculation.

The limitations of this technique lie in the accuracy of data on the birefringence of the material investigated and of the diamond anvils that enclose the sample chamber, and also in the limitations imposed by the compensator itself. Only materials that actually show birefringence can be used as starting materials, and thus crystals with

cubic symmetry as well as opaque materials are excluded. In addition, the compensator can only measure one-λ phase-difference correctly, otherwise two separate dark areas would appear upon the crystals surface in monochromatic light. This means that only crystals with birefringence of one order of interference can be used for monochromatic light. Using polychromatic light can overcome this limitation. Nevertheless, the compensator itself can only compensate birefringence of up to 1208 nm. Thus, minerals such as zircon and rutile are excluded unless they are polished down to very thin fragments.

Diamond is cubic in symmetry, but it shows stress birefringence that can affect the resulting calculated thickness to a certain degree. Thus, this stress birefringence has to be deducted from the result to obtain correct solubility data. This deduction is made by calculating a regression that describes the behavior of the diamond anvil birefringence in a two-dimensional space. With this regression a correction factor is calculated and the volume of the crystal can be determined accurately. Problematic is the degree of regression. For some crystal positions on the culet very complex regressions are needed to describe the birefringence behavior correctly (Fig. 6.2). Therefore it is recommended to place the crystal in the center of the sample chamber which itself should be centered in the middle of the diamond anvil where a simple regression such as a linear one is sufficient to describe the birefringence behavior (Fig. 6.2).
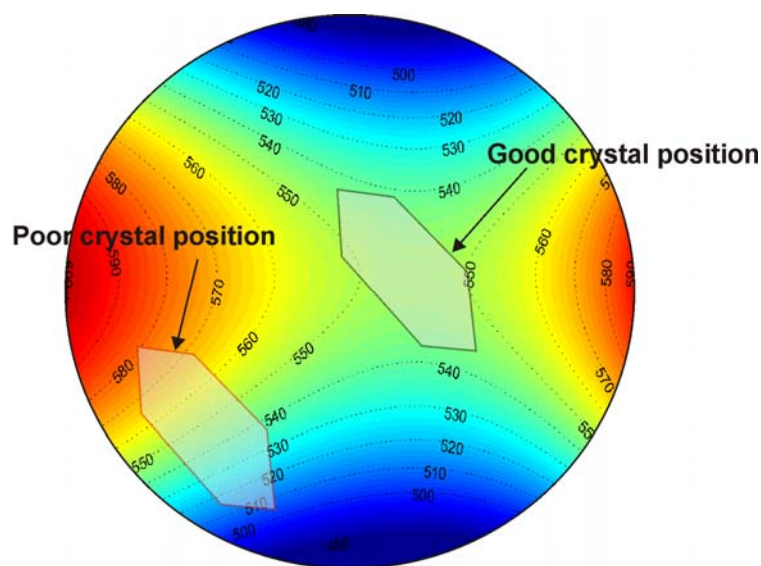
Fig. 6.2: Good and poor crystal positions on the diamond anvil in order to calculated a good quality regression. It can also be noticed that the sample chamber was not positioned exactly in the middle of the culet.

Another promising aspect of this birefringence mapping method can be that it can be tested during experimental runs if a crystal is under hydrostatic pressure or not e.g. if it touches both diamond anvils. This crystal will show the same rotation-symmetric interferences caused by the stress as seen by the diamond anvils. Therefore this method is also applicable for experiments where the investigated crystal needs to be under hydrostatic pressures conditions.

In addition, the combination of both methods can circumvent the disadvantages of the CVC method outlined above. Information on the length/thickness dimension in a crystal whose zone axis is parallel to the optical path can be retrieved from the calculated thickness of the crystal with the birefringence mapping method as long as the axis parallel to the optical path is not an optical axis. In the latter case the crystal would not show birefringence and the birefringence mapping method could not be applied. Nonetheless, time-dependent changes in crystal volume/mass can be calculated very precisely down to the ppm-level with both methods, and kinetic data such as dissolution/growth and/or diffusion rates could be derived very accurately.

Both new methods and the reconstructed HDAC were successfully tested on the basis of the voluminous published data on SiO_2 solubility. The data derived with the CVC method range from 139°C to 750°C and 1 kbar to 11.7 kbar. Determined SiO_2 solubility data reproduce the calculated SiO_2 solubility from Manning (1994) and Gerya *et al*. (2005) very well. In addition, this method provides more precise solubility data at higher temperature than the optical weighing method introduced by Matthews and Davis (1999) and tested by Wang *et al*. (2004) in HDAC runs. The accuracy of the CVC method based on the Gaussian error propagation is calculated to $\sigma = 0.38\%$. SiO_2 data derived with the birefringence mapping method range from 139°C to 500°C and up to 6.89 kbar and also reflect the predicted solubility of Manning (1994) and Gerya *et al*. (2005) quite well. Time-dependent changes in solubility can be calculated very precisely and observed visually through the created volume profile of the crystal. The accuracy of the birefringence mapping method based on the Gaussian error propagation is $\sigma = 2.42\%$.

Both methods show that the derived solubility data are compatible down to the ppm-level with the quartz solubility summarized by Manning (1994) and Gerya *et al*. (2005) for numerous literature sources. The approaches are promising techniques for

systematic investigations over a wide P- and T-range for both single-crystal and multi-phase systems that can be derived with limited effort and expense, but considerable accuracy. This makes both techniques very fitting and effective for future research.

7 References

Adams, D.M. and Shaw, A.C. (1982): A computer-aided design study of the behavior of diamond anvils under stress. *J. Phys. D. Appl. Phys.*, **15**, 1609-1635.

Anderson, G.M. and Burnham, C.W. (1965): The solubility of quartz in supercritical water. *Am. J. Sci.*, **263**, 494-511.

Asaumi, K., Kojima, S., Nakamura, T., (1980): Effect oft he hydrostatic pressure on the ferroelastic NDP5014. *J. Phys. Soc. Japan*, **48**, 4, 1298-1306.

Audétat, A. and Keppler, H. (2005): Solubility of rutile in subduction zone fluids, as determined by experiments in the hydrothermal diamond anvil cell. *Earth Planet. Sci. Lett.,* **232**, 393– 402.

Ayers, J.C., Watson, E.B. (1993): Rutile solubility and mobility in supercritical aqueous fluids. *Contrib. Mineral. Petrol.*, **114**, 3, 321-330.

Barnett, J.D., Block, S., Piermarini, G.J. (1973): An optical fluorescence system for quantitative pressure measurement in the diamond anvil cell. *Rev. Sci. Instrum.*, **44**, 1, 1-9.

Bassett, W.A. (1985): High pressure-temperature x-ray diffraction using synchrotron radiation. *Nucl. Instrum. Methods Phys. Res.*, **B10/11**, 309-312.

Bassett, W.A. (2003): High pressure-temperature aqueous systems in the hydrothermal diamond anvil cell (HDAC). *Eur. J. Mineral.*, **15**, 773–780.

Bassett, W.A., Takahashi, T and Stook, P.W. (1967): X-Ray diffraction and optical observations on crystalline solids up to 300 kbar. *Rev. Sci. Instrum.*, **38**, 37.

Bassett, W.A., Shen, A.H., Bucknum, M., Chou, I-M. (1993): Hydrothermal Studies in a New Diamond Anvil Cell up to 10 GPa and from -190°C to 1200°C. *PAGEOPH*, **141**, 2/3/4, 487-495.

Behrens, A. and Witzak, M.P. (1997): New arc detection technology for highly efficient electro-discharge machining. *Draft Papers Dies and Molds*.

Bell, P. M. and H. Mao, H.K. (1981): Degree of hydrostaticity in He, Ne, and Ar pressure-transmitting media. *Carnegie Inst. Washington Yearb.*, **80**, 404-406.

Bell, P.M., Mao, H.K., Goettel, K. (1984): Ultra high pressure-beyond 2 Megabars and the ruby flourescence scale. *Science*, **226**, 4674, 542-544.

Berek, M. (1913): Zur Messung der Doppelbrechung hauptsächlich mit Hilfe des Polarisationsmikroskops. *Centralblatt f. Min., Mitteilungen der Leitz-Werke*, **13**, 1-28.

Besson, J.M. (1997): Comment on "Metallization of Fluid Molecular Hydrogen at 140 GPa (1.4 Mbar)". *Phys. Rev. Lett.*, **78**, 26, 5026.

Bjørlykke, K. (1997): Lithological control on fluid flow in sedimentary basins. . *in* "Fluid flow and Transport in rocks, mechanisms and effects". Jamtveit, B., Yardley, B.W.D., eds. Chapman & Hall, London, 15-34.

Blount, C.W. and Dickson, F.W. (1973): Gypsum-Anhydrite equilibria in sytems $CaSo_4$-H_2O and $CaSO_4$-$NaCl$-H_2O. *Am. Mineral.*, **58**, 323-331.

Boehler, R., Nicol, M., Zha, C.S., Johnson, M.L. (1986): Superconductivity of arsenic at high pressure, *JETP Lett.*, **10**, 55-57.

Braun, H., Doll, W., Fischer, U., Heinzler, M., Höll, H., Ignatowitz, E., Kudlich, H., Nist, G., Röhrer, W., Schilling, K. (1992): Fachkunde Metall. Europa-Lehrmittel, Haan-Gruiten, 495 p.

Brown, P.E. and Lamb, W.M. (1989): P-V-T properties of fluids in the system $H_2O \pm CO_2 \pm NaCl$: New graphical presentations and implications for fluid inclusion studies. *Geochim. Cosmochim. Acta,* **53**, 1209-1221.

Burchard, M., Zaitsev, A.M., Meijer, J., Stephan, A. and Maresch, W.V. (2001): Electronic structuring of diamond anvils – new advances and possibilities for HP research. *EOS, Transactions, American Geophysical Union*, **82**, F1388.

Burchard, M., Zaitsev, A.M., Maresch, W.V. (2003): Extending the pressure and temperature limits of hydrothermal diamond anvil cells. *Rev. Sci. Instrum.,* **74**, 3, 1263-1266.

Burchard, M., Kubsky, S., Bureau, H., Somogyi, A., Malavergne, V., Menez, B., Munoz, M., (2006): X-ray transmission properties of intelligent anvils in diamond anvil cells. *High Pressure Research,* **26**, 3, 235–241.

Bureau, H. and Burchard, M. (2006): *In situ* characterization of geological materials at high pressure and temperature: techniques and observations – a special session at the 2005 AGU Fall Meeting, San Francisco, USA. *High Pressure Research,* **26**, 3, 233–234.

Bureau, H. and Keppler, H., (1999): Complete miscibility between silicate melts and hydrous fluids in the upper mantle: experimental evidence and geochemical implications. *Earth. Planet. Sci. Lett.,* **165,** 187–196.

Bureau, H., Burchard, M., Kubsky, S., Henry, S., Gonde, C., Zaitsev, A., Meijer, A. (2006): Intelligent anvils applied to experimental investigations: state-of-the-art. *High Pressure Research,* **26**, 3, 251-265.

Cartwright, J.A. (1997): Polygonal extensional fault systems: a new class of structure formed during the early compaction of shells. . *in* "Fluid flow and Transport in rocks, mechanisms and effects". Jamtveit, B., Yardley, B.W.D., eds. Chapman & Hall, London, 35-56.

Colón, C.F.J., Oelkers, E.H., Schott, J. (2004): Experimental investigation of the effect of dissolution on sandstone permeability, porosity, and reactive surface area. *Geochim. Cosmochim. Acta*, **68**, 4, 805–817.

Colthup, N.B, Daly, L.H., Wiberley, S.E. (1964): Introduction to infrared and raman spectroscopy. Academic Press, New York and London, 511 p.

Connolly, J.A.D. (1997a): Devolatilization-generated fluid pressure and deformation-propagated fluid flow during prograde regional metamorphism. *J. Geophys. Res., B*, **102**, 8, 149-173.

Connolly, J.A.D. (1997b): Mid-crustal focused fluid movement: thermal consequence and silica transport. . *in* "Fluid flow and Transport in rocks, mechanisms and effects". Jamtveit, B., Yardley, B.W.D., eds. Chapman & Hall, London, 235-250.

Decker, D.L. (1971): High-pressure equation of state for NaCl, KCl and CsCl. *J. Appl. Phys.*, **42**, 8, 3239-3244.

Descoeudres, A. (2006): Characterization of electrical discharge machining plasmas. Unpublished PhD Thesis. École Polytechnique Fédérale de Lausanne, Lausanne EPFL, 124p.

Diatschenko, V. and Chu, C.W. (1981): Melting of normal hydrogen under high pressures between 20 and 300 Kelvins. *Science*, New Series, **212**, 4501, 1393-1394.

Dickson, F.W., Blount, C.W., Tunell, G. (1963): Use of hydrothermal solution equipment to determine the solubility of anhydrite in water from 100°C to 275°C and from 1 bar to 1000 bars pressure. *Am. J. Sci.*, **261**, 61-78.

Doltsinis, N.L., Burchard, M., Maresch, W.V. (2004): Ab initio molecular dynamics simulations as a tool for interpreting vibrational spectra in aqueous fluids. *Bochumer Geowiss. Arbeiten*, **3**, 118-120.

Evans, B. and Kohlstedt, D.L. (1995): Rheology of Rocks. *in* Handbook of Physical Constants - AGU Reference Shelf , Vol. 3, Rock Physics and Phase Relations, 148-165.

Fockenberg, T., Burchard, M., Maresch, W.V. (2006): Experimental determination of the solubility of natural wollastonite in pure water up to pressures of 5 GPa and at temperatures of 400-800 °C. *Geochim. Cosmochim. Acta*, **70**, 1796-1806.

Fockenberg, T., Burchard, M., Maresch, W.V. (2008): The solubility of natural grossular-rich garnet in pure water at high pressures and temperatures. *Eur. J. Mineral.*, **20**, 845–855.

Gerya, T. Stöckhert, B., Perchuk, L.L. (2001): Development of a subduction channel and hydrated mantle wedge – 2D numerical simulation compared to the record high-pressure metamorphic rocks. EOS (abstract): 82(47): F1151.

Gerya, T.V., Podlesskii, K.K., Perchuk, L.L. Maresch, W.V. (2004a): Semi-empirical Gibbs free-energy formulations for minerals and fluids for use in thermodynamic databases of petrological interest. *Physics and Chemistry of Minerals*, **31**, 429-455.

Gerya, T., Maresch, W.V., Buchard, M., Zakhartchouk, V., Doltsinis, N.L., Fockenberg, T. (2004b): Semi-empirical thermodynamic modeling of mineral solubilities in water. *Bochumer Geowiss. Arbeiten*, **3**, 160-162.

Gerya, T., Maresch, W.V., Buchard, M., Zakhartchouk, V., Doltsinis, N.L., Fockenberg, T. (2005): Thermodynamic modeling of solubility and speciation of silica in H_2O-SiO_2 fluid up to 1300°C and 20 kbar based on the chain reaction formalism. *Eur. J. Mineral.*, **17**, 269-283.

Gerya, T., Gorczyk, W., Faccenda, M., Nikolaeva, K., Cantieni, C., Fossati, D., Connolly, J. (2007): Numerical modeling and visualization of subduction processes in multiple scales. *Bochumer Geowiss. Arbeiten*, **10**, 72-73.

Gross, J., Burchard, M., Schertl, H.-P., Maresch, W. V. (2008): Common high-pressure metamorphic history of eclogite lenses and surrounding metasediments: a case study of calcsilicate reaction zone (Erzgebirge, Germany). *Eur. J. Mineral.*, **20**, 757-775.

Haar, L., Gallagher J.S., Kell, G.S. (1984): NBS/NRC Steam Tables. Hemisphere, New York, 320 p.

Halbach, H. and Chatterjee, N.D. (1982): An Empirical Redlich-Kwong-Type equation of state for water to 1,000°C and 200 Kbar. *Contrib. Mineral. Petrol.*, **79**, 337-345.

Haselton, H.T., Jr., Chou, I-M., Shen, A.H., Bassett, W.A. (1995): Techniques for determining pressure in the hydrothermal diamond-anvil cell: Behavior and identification of ice polymorphs (I, III, V, VI). *Am. Mineral.*, **80**, 1302-1306.

Heinz, D.L. and Jeanloz, R. (1984): The equation of state of the gold calibration standard. *J. Appl. Phys.*, **55**, 4, 885-893.

Helgeson, H.C., Kirkham, D.H., Flowers, G.C. (1981): Theoretical prediction of the thermodynamic behavior of aqueous electrolytes at high pressures and temperatures, IV. *Am. J. Sci.*, **281**, 1241-1516.

Hintze, C. (1915): Handbuch der Mineralogie, Band 1, 2. Hälfte. Von Veit & Comp., Leipzig, 2674 p.

Holzapfel, W.B. and Isaacs, N.S. (1997): High-pressure techniques in chemistry and physics. Oxford University Press, New York, 388 p.

Huber, G., Syassen, K.and Holzapfel, W.B. (1977): Pressure dependence of 4f levels in europium pentaphosphate up to 400 kbar. *Phys. Rev. B,* **15**, 5123 – 5128.

Hullet, G.A. and Allan, L.E. (1902): The solubility of gypsum. J. *Amer. Chem. Soc.*, **24**, 667-679.

Jamtveit, B. and Yardley, B.W.D. (1997): Fluid flow and transport in rocks: an overview. *in* "Fluid flow and Transport in rocks, mechanisms and effects". Jamtveit, B., Yardley, B.W.D., eds. Chapman & Hall, London, 1-14.

Jayaraman, A. (1983): Diamond anvil cell and high-pressure physical investigations. *Rev. Mod. Phys.*, **55**, 1, 65-108.

Jayaraman, A. (1986): Ultrahigh pressures. *Rev. Sci. Instrum.*, **57,** 6, 1013-1031.

Jeanloz, R. and Heinz, D.L. (1984): Experiments at high temperature and pressure: laser heating through the diamond cell. *J. Phys. Colloque C8 Suppl.* 11, **45**, 83-92.

Kennedy, G.C. (1950): A portion of the system silica-water. *Econ. Geol.*, **45**, 629-653.

Kerrick, D.M. and Jacobs, G.K. (1981): A modified Redlich-Kwong equation for H_2O, CO_2 and H_2O-CO_2 mixtures at elevated pressures and temperatures. *Am. J. Sci.*, **281**, 735-767.

Kikegawa, T. (1987): X-ray diamond anvil press for structural studies at high pressures and high temperatures. *in* "High-Pressure Research in Mineral Physics", Manghnani, M.H. and Syono, Y., ed. Terra Scientific Publishing Company (TERRAPUB), Tokyo / American Geophysical Union, Washington, D.C., 61-68

Knittle E., Phillips W., Williams Q. (2001): An infrared and Raman spectroscopic study of gypsum at high pressures. *Phys.Chem.Minerals*, **28**, 630-640.

Kubsky, S., Burchard, M., Bureau, H. (2005): Intelligent diamond anvil cell (iDAC): First in situ x-ray measurements.Eos Trans. AGU **86**(52), Fall Meet. Suppl., Abstract MR23C-0080, San Francisco.

LeToullec, R., Pinceaux, J.P., Loubeyre, P. (1988): The membrane diamond anvil cell: A new device for generating continuous pressure and temperature variations. *High Pressure Research*, **1**, 77-90.

Liebenberg, D.H. (1979): A new hydrostatic medium for diamond anvil cells to 300 kbar pressure. *Phys. Lett.*, **73A**, 1, 74-76.

Manning, C.E. (1994): The solubility of quartz in HZ0 in the lower crust and upper mantle. *Geochim. Cosmochim. Acta*, **58**, 22, 4831-483.

Manning, C. E. and Ingebritsen, S. E. (1999): Permeability of the continental crust: Implications of geothermal Data and metamorphic systems. *Rev. Geophys.,* **37**, 1, 127-150.

Manning, C. E. (2004a): Polymeric silicate complexing in aqueous fluids at high pressure and temperature, and its implications for water-rock interaction, *in* "Water-Rock Interaction, Proceedings of the Eleventh International Symposium on Water-Rock Interaction", Wanty, R. B., and Seal, R. R., II, eds., London, Taylor & Francis Group, 45-49.

Manning, C.E. (2004b): The chemistry of subduction-zone fluids. *Earth Planet. Sci. Lett.*, **223**, 1-16.

Manning, C. E. (2007a): Book Review: Inside the Subduction Factory. *Geofluids*, **7**, 1-3.

Manning, C. E. (2007b): Solubility of corundum + kyanite in H_2O at 700°C and 10 kbar: evidence for Al-Si complexing at high pressure and temperature. *Geofluids*, 7, 258-269.

Manning, C.E. (2007c): New perspectives on subduction-zone fluids. *Bochumer Geowiss. Arbeiten*, **10**, 33.

Manning, C. E. and Boettcher, S. L. (1994): Rapid-quench hydrothermal experiments at mantle pressures and temperatures. *Am. Mineral.*, **79**, 1153-1158.

Mao, H. K. (1989): Static compression of simple molecular systems in the megabar range. *in* "Simple Molecular Systems at Very High Density", Loubeyre, P. and Polian, A., eds. Plenum Publishing Corp., New York, 221-236.

Mao, H. K. and Bell, P.M. (1976a): High-pressure research: 1-Mbar pressure on the ruby pressure scale. *Carnegie Inst. Washington Yearb.*, **75**, 827-828.

Mao, H. K. and Bell, P.M. (1976b): High-pressure physics: the 1-megabar mark on the ruby R1 static pressure scale. *Science*, **191**, 851-852.

Mao, H. K. and Bell, P.M. (1979): Observation of hydrogen at room temp. (25°C) and high pressure (to 500 kilobars).Science, 203, 4384, 1004-1006.

Mao, H.K., Bell, P.M., Shaner, J.W., Steinberg, D.J. (1978): Specific volume measurements of Cu, Mo, Pd, and Ag and calibration of the ruby R_1 fluorescence pressure gauge from 0.06 to 1 Mbar. *J. Appl. Phys.*, **49,** 6, 3276-3283.

Mao, H.K., Xu, J., Bell, P.M. (1986): Calibration of the Ruby Pressure Gauge to 800 kbar Under Quasi-Hydrostatic Conditions. *J. Geophys. Res.*, **91**, B5, 4673-4676.

Mao, H.K., Hemley, R.J., Hanfland, M. (1992): Stability of ruby in solid hydrogen at megabar pressures. *Phys. Rev. B*, **45**, 14, 8108-8111.

Maresch, W.V., Burchard, M., Fockenberg, T., Medenbach, O. (2002): Mass transport, densities, viscosities and kinetics of solution/reprecipitation in aqueous fluids coexisting with mineral assemblages. *in* "Rheology of the Earth – from the Upper Crust to the Subduction Zone. SFB526, Ruhr-Universität Bochum, Proposed budget 2002/2-2005/1, 357-382.

Marshak, S. (2008): Earth – Portrait of a Planet. Third Edition. W.W. Norton & Company, New York, 832 p.

Marshall, W.L. and Slusher, R. (1966): Thermodynamics of calcium sulfate dihydrate in aqueous sodium chloride solutions, 0-110°. *J. Phys. Chem.*, **70**, 4015-4027.

Matthews, W. and Davis, W.J. (1999): A practical image analysis technique for estimating the weight of abraded mineral fractions used in U-Pb age dating. *in* "Radiogenic Age and Isotopic Studies: Report 12". Current Research 1999-F. Geological Survey of Canada.

Medenbach, O. (1984): A new microrefractometer spindle-stage and its application. *Fortschritte der Mineralogie,* **63**, 1, 111-133.

Merrill, L. and Bassett, W.A. (1974): Miniature diamond anvil pressure cell for single crystal x-ray diffraction studies. *Rev. Sci. Instrum.*, **45**, 2, 290-294.

Miletich, R. (1998): Diamanten als Fenster zum Erdinneren - Experimentelle Hochdruckforschung in den Geowissenschaften. *Mitteilungen der Österreichischen Mineralogischen Gesellschaft*, **143**, 55-73.

Ming, L.C. and Bassett, W.A. (1974): Laser heating in the diamond anvil press up to 2000°C sustained and 3000°C pulsed at pressures up to 260 kilobars. *Rev. Sci. Instrum.*, **45**, 9, 1115-1118.

Ming, L.C., Manghani, M.H., Qadri, S.B., Skelton, E.F., Jamieson, J.C., Bologh, J. (1983): Gold as a reliable internal pressure calibrant at high temperatures. *J. Appl. Phys.*, **54**, 18, 4390-4397.

Moore, M.J., Sorensen, D.B., DeVaies, R.C. (1970): A simple heating device for diamond anvil high pressure cell. *Rev. Sci. Instrum.*, **41**, 1665-1666.

Morey, G.W. and Hesselgesser, J.M. (1951): The solubility of some minerals in superheated steam at high pressures. *Econ. Geol.*, **46**, 821-835.

Moss, W.C., Hallquist, J.O., Reichlin, R., Goettel, K.A., Martin, S. (1986): Finite element analysis of the diamond anvil cell: Achieving 4.6 Mbar. *Appl. Phys. Lett.*, **48**, 1258-1260.

Müller, G. and Raith, M. (1993): Methoden der Dünnschliffmikroskopie. *Clausthaler tektonische Hefte,* **Bd. 14**.

Mysen, B.O. and Acton, M. (1999): Water in H_2O-saturated magma–fluid systems: Solubility behavior in $K_2O–Al_2O_3–SiO_2–H_2O$ to 2.0 GPa and 1300°C. *Geochim. Cosmochim. Acta*, **63**, 22, 3799-3815.

Newton, R.C. and Manning, C.E. (2002a): Experimental determination of calcite solubility in H_2O-NaCl solutions at deep crust/upper mantle pressures and temperatures: implications for metasomatic processes in shear zones. *Am. Mineral.*, **87**, 1401-1409.

Newton, R.C. and Manning, C.E. (2002b): Solubility of enstatite - forsterite in H_2O at deep crust/upper mantle conditions: 4 to 15 kbar and 700 to 900°C. *Geochim. Cosmochim. Acta*, **66**, 23, 4165–4176.

Newton, R.C. and Manning, C.E. (2006): Solubilities of corundum, wollastonite and quartz in H_2O-NaCl solutions at 800°C and 10 kbar: Interaction of simple minerals with brines at high pressure and temperature. *Geochim. Cosmochim. Acta*, **70**, 5571-5582.

Öpöz, T.T., Ekmekci, B., Elkoca, O., Halkaci, H.S., Erden, A. (2006): Manufacturing of smaller holes by using micro-electrical discharge machining (Micro-EDM). The 12th International Conference on Maschine Design and Production, Kuşdasi, Turkey.

Paul, H. (1999): Lexikon der Optik A bis L. Spektrum Akademischer Verlag, Heidelberg and Berlin, 438 p.

Piermarini, G.J., Block, S., Barnett, J.D. (1973): Hydrostatic limits in liquids and solids to 100 kbar. *J. Appl. Phys.*, **44**, 12, 5377-5382.

Piermarini, G.J.and Block, S. (1975): Ultrahigh pressure diamond-anvil cell and several semiconductor phase transition pressures in relation to the fixed point pressure scale. *Rev. Sci. Instrum.*, **45**, 8, 973-979.

Ranalli, G. (1995): Rheology of the earth. Chapman & Hall, London, 413 p.

Saul, A. and Wagner, W. (1989): A Fundamental Equation for Water Covering the Range from the Melting Line to 1273 K at Pressures up to 25 000 MPa. *J. Phys. Chem. Ref. Data*, **18**, 4, 1537-1564.

Schmidt, C. and Ziemann, M.A. (2000): In-situ Raman spectroscopy of quartz: A pressure sensor for hydrothermal diamond-anvil cell experiments at elevated temperatures. *Am. Mineral.*, **85**, 1725–1734.

Schiferl, D., Nicol, M., Zaug, J.M.. Sharma, S.K., Cooney, T.F., Wang, S.-Y., Anthony, T.R., Fleischer, J.F. (1997): The diamond $^{13}C/^{12}C$ isotope Raman pressure sensor system for high-temperature/pressure diamond-anvil cells with reactive samples. *J. Appl. Phys.*, Volume **82**, 7, 3256-3265.

Schilling, K.J. (2008): Software: Kristall2000. www.kristall2000.de

Seal, M. (1987): Diamond Anvil Technology. *in* "High-Pressure Research in Mineral Physics", Manghnani, M.H. and Syono, Y., ed. Terra Scientific Publishing Company (TERRAPUB), Tokyo / American Geophysical Union, Washington, D.C., 35-40.

Seal, M. (1990): The Choice of Diamond for some Scientific Applications. *in* "Science and Technology of New Diamond", Saito, S., Fukunaga, O., Yoshikawa, M., eds. KTK Scientific Publishers / Terra Scientific Publishing Company, 311-317.

Shen, A.H., Bassett, W.A., Chou, I-M. (1992): Hydrothermal studies in a diamond anvil cell: Pressure determination using the equation of state of H_2O. *in* "High-Pressure Research: Application to Earth and Planetary Sciences, Syono, Y. and Manghnani,

M.H., ed. Terra Scientific Publishing Company (TERRAPUB), Tokyo / American Geophysical Union, Washington, D.C., 61-68.

Simon, G., Bureau, H., Kubsky, S., Datchi, F., Munsch, P., Foy, E., Meijer, J., Burchard, M. (2009): In situ pressure measurements with i-anvils. In preparation.

Todd, C.S. and Evans, B.W. (1993): Limited fluid-rock interaction at marble-gneiss contacts during Cretaceous granulite–facies metamorphism, Seward Peninsula, Alaska. *Contrib. Mineral. Petrol.*, **114**, 27-41.

Tropper, P., and Manning, C. E. (2005): Very low solubility of rutile in H_2O at high pressure and temperature, and its implications for Ti mobility in subduction zones. *Am. Mineral.*, **90**, 502-505.

Tröger, W.E. (1982): Optische Bestimmung der gesteinsbildenden Minerale, 5. Auflage. E. Schweizerbart'sche Verlagsbuchhandlung (Nägele und Obermiller), Stuttgart, 188 p.

Van Valkenburg, A. (1962): Visual Observations of High Pressure Transitions. *Rev. Sci. Instrum.*, **33**, 1462.

Verlaguet, A. and Brunet, F. (2007): Effect of incongruent dissolution on mineral solubility data derived from quench experiments. *Eur. J. Mineral.*, **19**, 783–789.

Verlaguet, A., Brunet, F., Goffé, B., Murphy, W.M. (2006): Experimental study and modeling of fluid reaction paths in the quartz–kyanite ± muscovite–water system at 0.7 GPa in the 350–550°C range: Implications for Al selective transfer during metamorphism. *Geochim. Cosmochim. Acta*, **70**, 1772–1788.

Vrolijk, P. and Myers, G. (1990): Fluid pressure history in subduction zones: Evidence from fluid inclusions in the Kodiak Accretionary Complex, Alaska. *in* "Studies in Geophysics: The role of fluids in crustal processes". Geophysical Study Committee, Commission on Geosciences, Environment, and Resources, National Research Council eds. National Academy Press, Washington, D.C., 148-157.

Wagner, W., Pruß, A. (2002): The IAPWS Formulation 1995 for the Thermodynamic Properties of Ordinary Water Substance for General and Scientific Use. *J. Phys. Chem. Ref. Data,* **31**, 387-585.

Wang, H.M., Henderson, G.S., Brenan, J.M. (2004): Measuring quartz solubility by in situ weight-loss determination using a hydrothermal diamond cell. *Geochim. Cosmochim. Acta*, **68**, 24, 5197-5204.

Watson, E.B. and Wark, D.A. (1997): Diffusion of dissolved SiO_2 in H_2O at 1 GPa, with implications for mass transport in the crust and upper mantle. *Contrib. Mineral. Petrol.*, **130**, 66-80.

Webb, A.W., Gubser, D.U., Towle, L.C. (1976): Cryostat for generating pressures to 100 kilobar and temperatures to 0.03 K. *Rev. Sci. Instrum.*, **47**, 1, 59-62.

Weir, C., Block, S., Piermarini, G. (1965): Single-crystal X-ray diffraction at high pressure. *J. Res. NBS*, **69C**, 4, 275-281.

Willner, A.P., Sebazungu, E., Gerya, T.V., Maresch, W.V. (2002): Numerical modelling of PT-paths related to rapid exhumation of high-pressure rocks from the crustal root in the Variscan Erzgebirge Dome (Saxony, Germany). *J. Geodyn.*, **33**, 281-314.

Wood, B.J. and Walther, J.V. (1986): Fluid-rock interactions during metamorphism. Advances in Physical Geochemistry, Vol. 5, Springer-Verlag, New York, 218 p.

Wyllie, P.J. (1979): Ultramafic and related rocks. R.E. Krieger Pub. Co, Huntington, New York, 464 p.

Xu, J.A., Mao, H.K., Bell, P.M. (1986): High-pressure ruby and diamond fluorescence: Observations at 0.21 to 0.55 terapascqal. *Science*, **232**, 1404-1406.

Yardley, B.W.D. and Valley, J.W. (1997): The petrologic case for a dry lower crust. *J. Geophys. Res., B*, **102**, 6, 173-185.

Yousuf, M. (1998): Diamond anvil cells in high-pressure studies of semiconductors. *in* "Semiconductors and Semimetals Volume 55", Willardson, R.K. and Weber, R., ed. Academic Press, 381-436

Zaitsev, A.M., Burchard, M., Meijer, J., Stephan, A., Burchard, B., Fahrner, W.R., Maresch, W. (2001): Diamond Pressure and Temperature Sensor for High-Pressure High-Temperature Applications. *Phys. Stat. Sol. (a)* **185**, 1, 59–64.

Zotov, N., Keppler, H. (2002): Silica speciation in aqueous fluids at high pressures and high temperatures. *Chem. Geol.,* **184,** 71–82.

Appendix

CVC – Crystal Volume Computation

DAC- Diamond Anvil Cell

EOS – Equation of State

HDAC – Hydrothermal Diamond Anvil Cell

i-Anvils – intelligent Anvils

MEDM – Micro Electro Discharge Machining

NBS – National Bureau of Standards

SEM – Scanning Electron Microscope

Wo I – Wollastonite I

Wo II – Wollastonite II

Qtz – Quartz

$\dot{\varepsilon}$ = Strain rate

Ω = Atomic volume

υ = Shear modulus

τ = Average grain diameter

F = Proportion by fluid volume

c_o = Solubility

D_F = Diffusion coefficient

η = Stess rate

T = Temperature

T_H = Temperature of homogenization

T_M = Temperature of melting

P = Pressure

k = Boltzmann constant

A = Constant

B = Constant

C = Culet diameter of diamond anvil

H = Height

X = Girdle diameter of diamond anvil

BC = Bevel angle of diamond anvil

b = Bevel diameter of diamond anvil

ρ = Density

"T" = Distance of a crystal face from the virtual center of the crystal

a,b,c = crystallographic axes

α,β,γ = Angles of crystal system

σ = Standard deviation; error

n = Number of determinations

x_i = i^{th} determination

$\bar{x}$ = mean of determinations

f(…) = Function of (…)

F(…) = Antiderivative of f(…)

M = Mass

V = Volume

d = Thickness

A = Surface

n_e, n′ = Extraordinary refractive index

n_o, n′′ = Ordinary refractive index

Δn = Birefringence

Γ = Phase difference

$\bar{\Gamma}$ = Average phase difference

I_A = Intensity of the light leaving the analyzer

X = Ellipticity

OA = Optical axis

I = Tilting angle of compensator

Θ = Excess in thickness

$Pixel_L$ = Pixel length

$Pixel_W$ = Pixel width

N = Number of pixel

Σ = Sum

W = Width

q = Height axis of coordinate system

u = Length axis of coordinate system

u_1, u_2 = Boundary conditions

x,y,z = coordinates in a 3-dimensional space; axes of these coordinates

x_k,y_k = Value pair

ω = Angle of rotation

m = molality

Mechanical drawing of the upper inner cell parts: Inner cylinder and outer hollow cylinder.
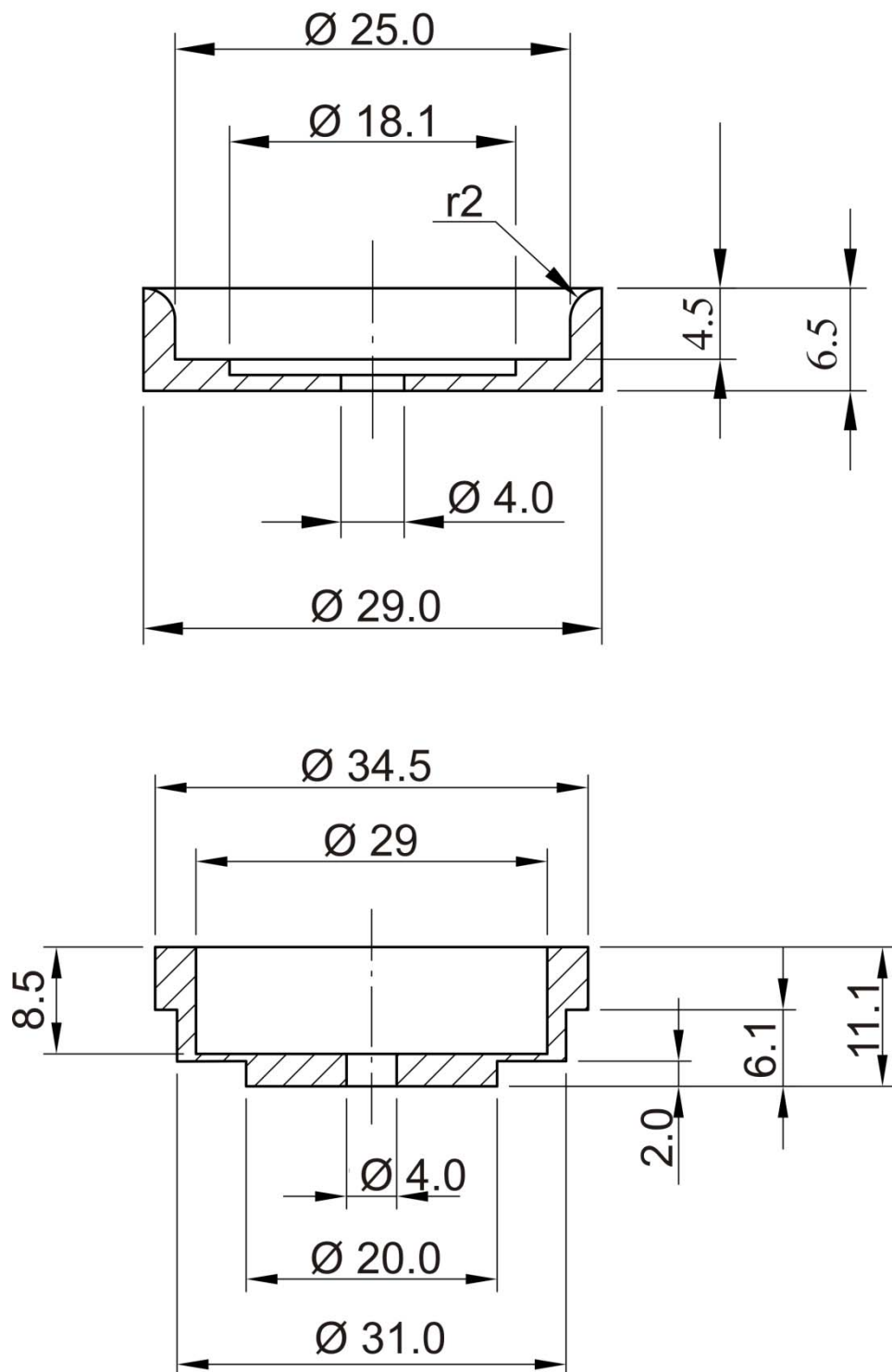
Drawings not true to scale. All specifications in mm.

Mechanical drawing of the lower inner cell parts: hemisphere and its corresponding bearing
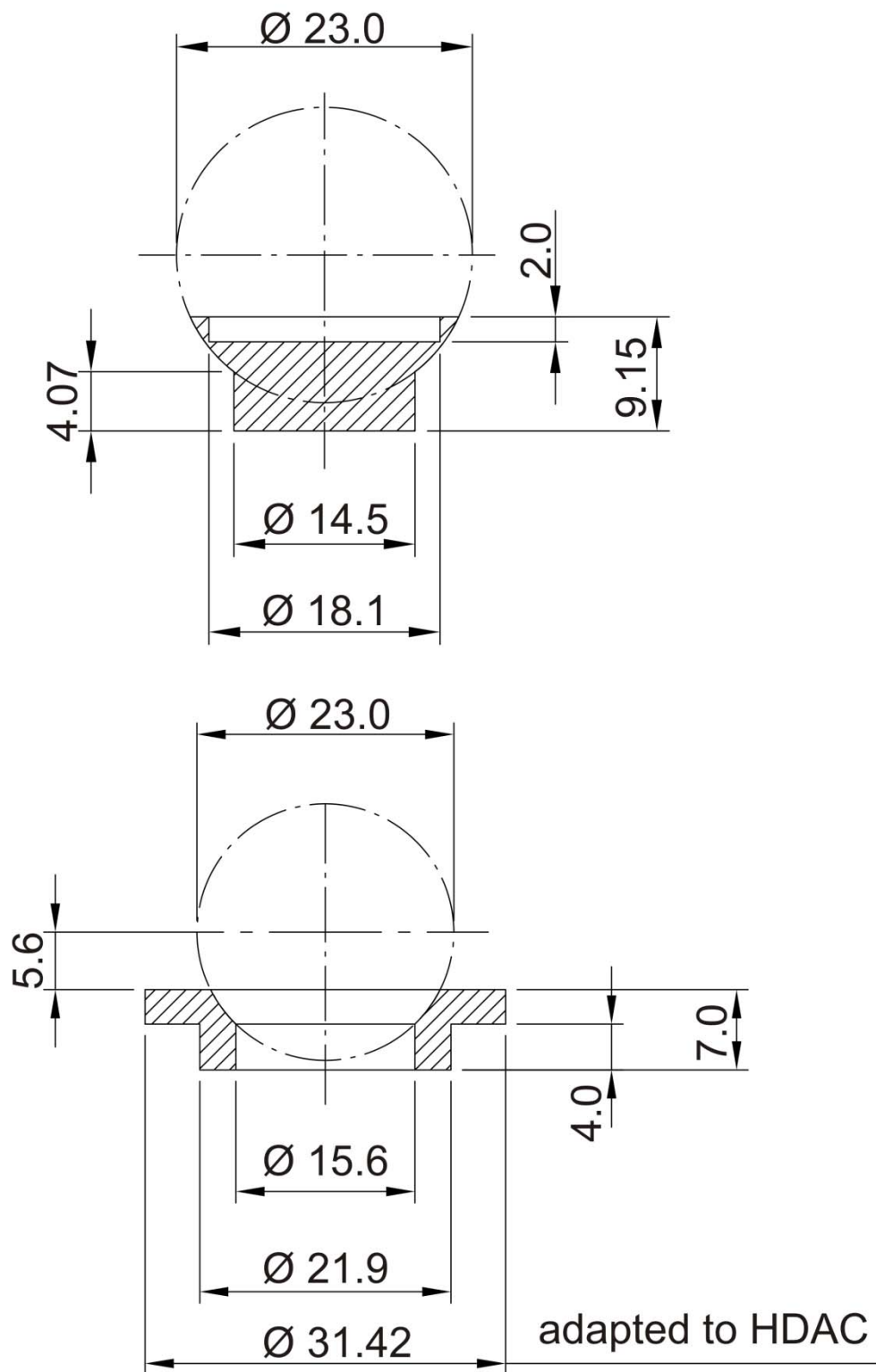
Drawings not true to scale. All specifications in mm.

Mechanical drawing of the metal cap

Ø 5.86

Ø 4.0

4.5

4.1

Ø 5.0
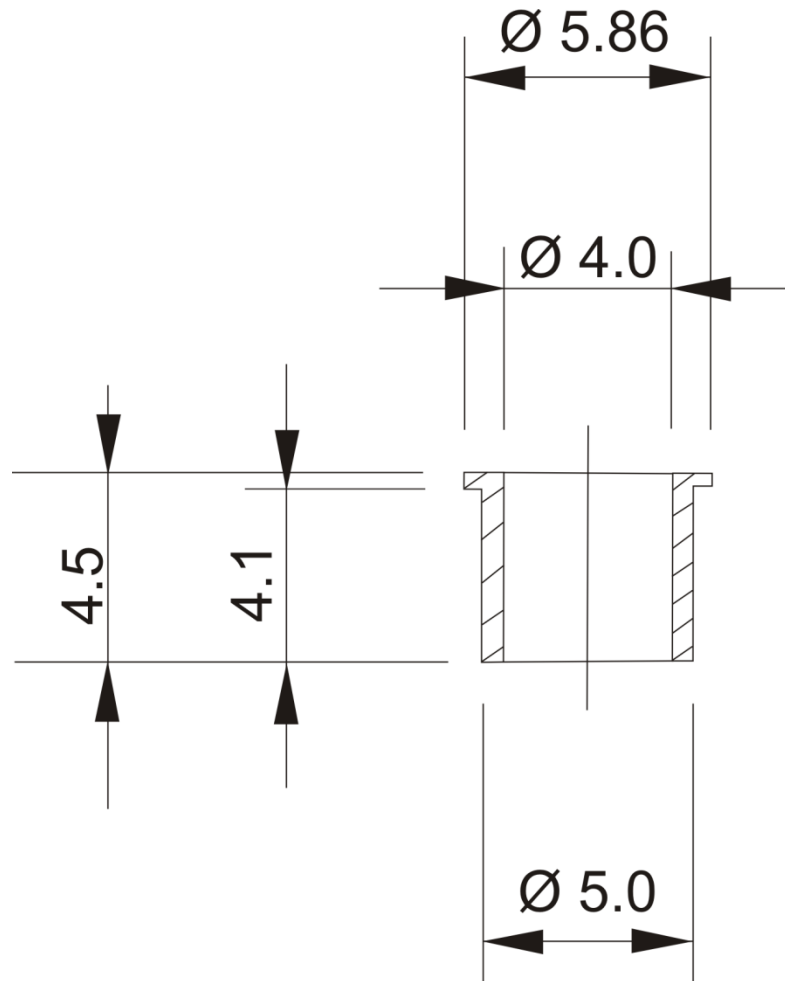
Drawing not true to scale. All specifications in mm.

Mechanical drawing of the copper plate and ceramic heater cap.
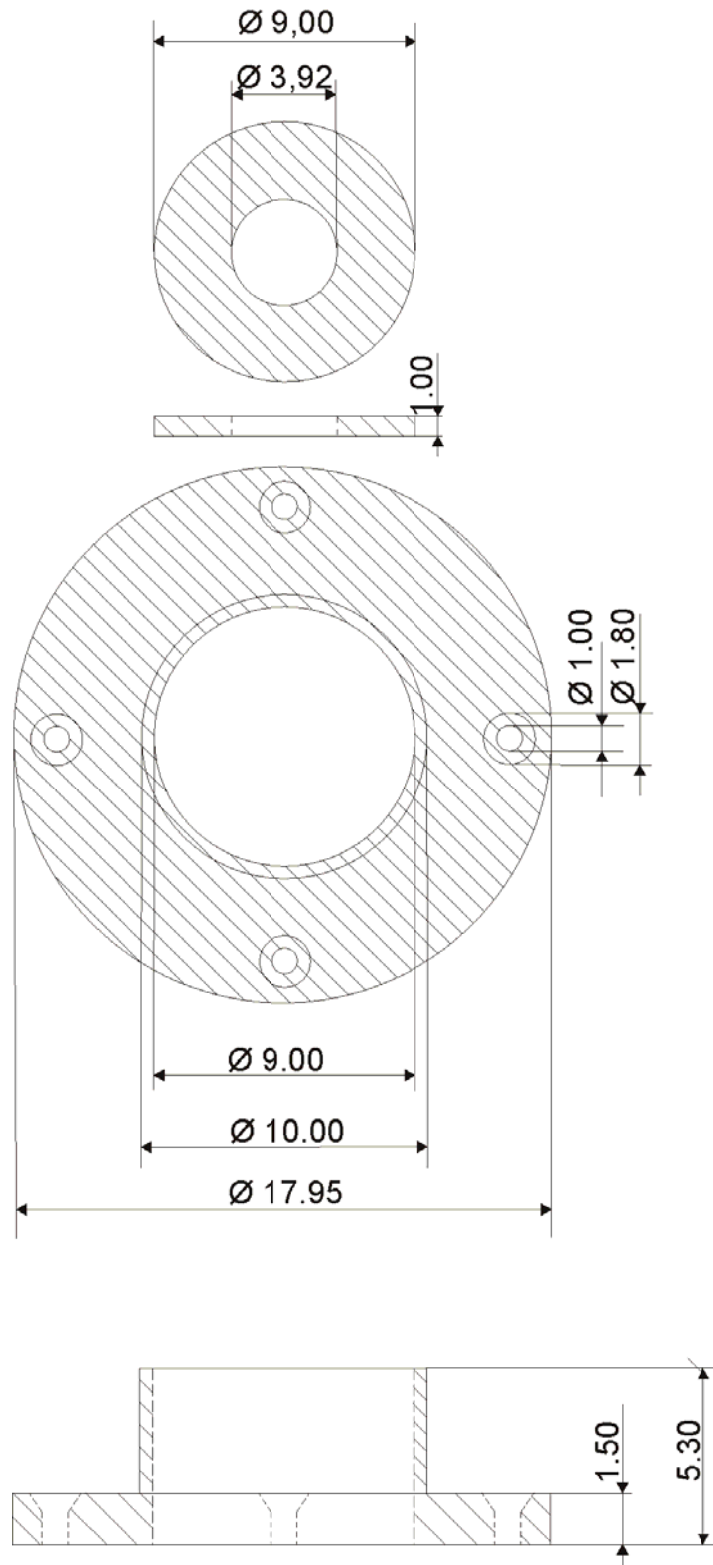
Drawings not true to scale. All specifications in mm.

Heater Type 1 and 2

Type 1			Type 2		
Resistance	Capacity	Temperature	Resistance	Capacity	Temperature
20.00	0.07	28.1	5.00	0.00	33.2
20.00	0.10	29.8	2.86	0.22	39.1
20.00	0.13	31.2	2.79	0.52	46.4
20.00	0.16	32.1	3.04	0.95	56.2
20.00	0.20	33.5	3.13	1.28	64.4
20.00	0.34	38.2	3.29	1.90	77.7
20.71	0.41	40.4	3.45	2.44	89.8
20.63	0.53	43.9	3.56	2.70	94.2
21.11	0.68	48.3	3.75	3.46	110.8
21.50	0.86	52.3	3.90	3.90	119.0
22.00	0.88	54.0	4.10	4.52	130.6
22.73	1.10	59.7	4.38	5.49	151.8
22.92	1.32	64.5	4.57	6.15	162.2
23.60	1.48	68.1	4.75	6.84	174.8
24.07	1.76	74.6	4.96	7.75	190.3
24.81	1.81	77.0	5.31	8.97	209.5
24.64	1.93	79.1	5.60	10.05	226.9
26.00	2.34	89.7	5.97	11.54	248.7
26.13	2.51	93.0	6.39	13.25	275.2
26.88	2.75	98.6	6.76	14.80	295.2
28.18	3.07	108.9	7.17	16.57	317.6
29.14	3.57	117.9	7.50	18.25	336.7
30.28	3.92	126.0	8.00	20.48	360.1
30.54	4.18	131.5	8.41	22.63	382.3
31.35	4.29	134.4	8.99	25.37	409.5
31.58	4.56	139.6	9.36	27.69	428.4
32.63	4.71	143.3	9.89	30.62	449.9
33.33	5.07	151.0	10.55	34.94	475.5
33.25	5.32	154.0	11.28	39.46	505.8
34.50	5.52	159.9	11.78	42.98	525.1
34.88	5.86	166.7	12.12	45.16	540.3
35.71	6.30	173.8	12.74	49.45	580.0
37.21	6.88	184.6	13.28	53.67	601.2
38.37	7.10	188.2	13.50	55.62	611.7
38.86	7.52	194.0	13.76	57.81	621.4
40.00	8.10	203.0	14.01	60.03	629.0
41.56	8.42	213.8			
42.39	8.97	221.1			
44.47	9.82	236.4			
44.68	9.87	238.0			
44.79	10.32	247.0			
47.96	11.52	264.1			
49.80	12.45	280.4			
51.76	13.46	293.2			
53.46	14.46	307.2			
55.66	15.64	322.3			
57.04	16.63	343.4			

Heater Type 3 and 4

Type 3			Type 4		
Resistance	Capacity	Temperature	Resistance	Capacity	Temperature
2.73	0.03	26.4	2.35	0.07	31.9
2.50	0.06	28.0	2.67	0.24	35.0
2.62	0.46	34.1	2.70	0.37	37.7
2.76	0.93	43.3	2.56	0.39	39.4
2.84	1.86	59.2	2.56	0.47	41.7
3.01	2.60	71.1	2.67	0.54	43.3
3.42	4.22	99.2	2.77	0.61	44.8
3.81	6.05	130.6	2.76	0.93	51.9
4.84	11.63	206.0	2.86	1.13	55.8
4.94	12.01	210.9	2.88	1.25	59.1
6.14	19.01	277.7	2.97	1.63	66.3
6.90	24.12	321.2	2.95	1.79	70.6
8.66	34.97	420.5	3.01	2.08	76.6
10.14	46.44	477.9	3.18	2.46	84.2
11.86	63.29	544.3	3.26	2.76	91.1
12.85	73.37	574.1			

Table 1: Mass determinations for error analyses for the first approach.

Herkimer Model no.	1a	1a	1a	1a	1a	1a	1a
Edge fictive [e]	426	474	285	231	462	518	357
Edge real [mm]	1.5	1.67	1	0.82	1.63	1.82	1.26
Volume [e3]	325681516.19	325681516.19	325681516.19	325681516.19	325681516.19	325681516.19	325681516.19
Volume real [mm^3]	14.218	14.243	14.069	14.568	14.303	14.126	14.319
Density [mg/mm^3]	2.65	2.65	2.65	2.65	2.65	2.65	2.65
Mass modeled [g]	0.038	0.038	0.037	0.039	0.038	0.037	0.038
Mass modeled [mg]	37.678	37.744	37.282	38.605	37.903	37.434	37.944
Weight measured [mg]	37.992	37.992	37.992	37.992	37.992	37.992	37.992

Herkimer Model no.	2	2	2	2	2	2	2
Edge fictive [e]	406	228	509	207	279	152.9	195.8
Edge real [mm]	1.43	0.8	1.79	0.73	0.98	0.54	0.69
Volume [e3]	325094369.31	325094369.31	325094369.31	325094369.31	325094369.31	325094369.31	325094369.31
Volume real [mm^3]	14.205	14.043	14.139	14.258	14.089	14.321	14.227
Density [mg/mm^3]	2.65	2.65	2.65	2.65	2.65	2.65	2.65
Mass modeled [g]	0.038	0.037	0.037	0.038	0.037	0.038	0.038
Mass modeled [mg]	37.643	37.215	37.468	37.784	37.335	37.950	37.702
Weight measured [mg]	37.992	37.992	37.992	37.992	37.992	37.992	37.992

Continuing table 1: Mass determinations for error analyses for the first approach.

Herkimer Model no.	6	6	6	6	6	6	6
Edge fictive [e]	418	246	518	198	379	119.9	189.2
Edge real [mm]	1.47	0.85	1.81	0.69	1.34	0.42	0.66
Volume [e3]	332458503.64	332458503.64	332458503.64	332458503.64	332458503.64	332458503.64	332458503.64
Volume real [mm^3]	14.460	13.715	14.184	14.070	14.694	14.290	14.113
Density [mg/mm^3]	2.65	2.65	2.65	2.65	2.65	2.65	2.65
Mass modeled [q]	0.038	0.036	0.038	0.037	0.039	0.038	0.037
Mass modeled [mq]	38.318	36.344	37.586	37.285	38.939	37.868	37.398
Weight measured [mg]	37.992	37.992	37.992	37.992	37.992	37.992	37.992

Herkimer Model no.	8	8	8	8	8	8	8	8
Edge fictive [e]	534	196	390	272	448	349	129.8	185.9
Edge real [mm]	1.89	0.7	1.38	0.96	1.58	1.24	0.46	0.66
Volume [e3]	318012385.41	318012385.41	318012385.41	318012385.41	318012385.41	318012385.41	318012385.41	318012385.41
Volume real [mm^3]	14.100	14.487	14.089	13.981	13.950	14.264	14.154	14.231
Density [mg/mm^3]	2.65	2.65	2.65	2.65	2.65	2.65	2.65	2.65
Mass modeled [q]	0.037	0.038	0.037	0.037	0.037	0.038	0.038	0.038
Mass modeled [mq]	37.364	38.390	37.336	37.051	36.968	37.799	37.509	37.712
Weight measured [mg]	37.992	37.992	37.992	37.992	37.992	37.992	37.992	37.992

X

Continuing table 1: Mass determinations for error analyses for the first approach.

Herkimer Model no.	1	1	1	1	1	1	1
Edge fictive [e]	525	193	426	379	159	125.4	201
Edge real [mm]	1.85	0.67	1.5	1.35	0.55	0.43	0.7
Volume [e3]	336935591.28	336935591.28	336935591.28	336935591.28	336935591.28	336935591.28	336935591.28
Volume real [mm^3]	14.743	14.096	14.709	15.228	13.946	13.585	14.232
Density [mg/mm^3]	2.65	2.65	2.65	2.65	2.65	2.65	2.65
							0.038
Mass modeled [q]	0.039	0.037	0.039	0.040	0.037	0.036	37.714
Mass modeled [mq]	39.069	37.355	38.980	40.353	36.956	36.000	0.727
Weight measured [mg]	37.992	37.992	37.992	37.992	37.992	37.992	37.992

Table 2: Mass determinations for error analyses for the second approach.

Herkimer Model no.	3	3	3	3	3	3	3
Edge fictive [e]	152.9	156.2	588	462	360	255	536
Edge real [mm]	0.54	0.55	2.06	1.63	1.27	0.9	1.89
Volume [e3]	271196210.63	271196210.63	271196210.63	271196210.63	271196210.63	271196210.63	271196210.63
Volume real [mm^3]	11.947	11.839	11.661	11.910	11.907	11.923	11.890
Density [mg/mm^3]	2.65	2.65	2.65	2.65	2.65	2.65	2.65
Mass modeled [q]	0.032	0.031	0.031	0.032	0.032	0.032	0.032
Mass modeled [mg]	31.658	31.374	30.903	31.562	31.552	31.596	31.508
Weight measured [mg]	37.992	37.992	37.992	37.992	37.992	37.992	37.992

Herkimer Model no.	4	4	4	4	4	4	4
Edge fictive [e]	403	240	533	195	385	149.6	179.3
Edge real [mm]	1.525	0.84	1.87	0.69	1.36	0.52	0.63
Volume [e3]	251867926.81	251867926.81	251867926.81	251867926.81	251867926.81	251867926.81	251867926.81
Volume real [mm^3]	13.648	10.799	10.877	11.159	11.102	10.578	10.926
Density [mg/mm^3]	2.65	2.65	2.65	2.65	2.65	2.65	2.65
Mass modeled [q]	0.036	0.029	0.029	0.030	0.029	0.028	0.029
Mass modeled [mg]	36.167	28.617	28.825	29.571	29.421	28.031	28.953
Weight measured [mg]	37.992	37.992	37.992	37.992	37.992	37.992	37.992

Continuing table 2: Mass determinations for error analyses for the second approach.

Herkimer Model no.	5	5	5	5	5	5	5
Edge fictive [e]	152.9	70.4	424	285	515	207	388
Edqe real [mm]	0.54	0.25	1.48	1.00	1.81	0.73	1.37
Volume [e3]	280518919.55	280518919.55	280518919.55	280518919.55	280518919.55	280518919.55	280518919.6
Volume real [mm^3]	12.357	12.562	11.930	12.118	12.178	12.303	12.34891161
Density [mq/mm^3]	2.65	2.65	2.65	2.65	2.65	2.65	2.65
Mass modeled [q]	0.033	0.033	0.032	0.032	0.032	0.033	0.032724616
Mass modeled [mq]	32.747	33.290	31.615	32.112	32.272	32.604	32.72461577
Weight measured [mg]	37.992	37.992	37.992	37.992	37.992	37.992	37.9924

Herkimer Model no.	7	7	7	7	7	7	7
Edqe fictive [e]	159.5	189.2	418	246	518	198	379
Edqe real [mm]	0.57	0.66	1.57	0.86	1.83	0.71	1.35
Volume [e3]	272019640.55	272019640.55	272019640.55	272019640.55	272019640.55	272019640.55	272019640.55
Volume real [mm^3]	12.415	11.547	14.414	11.622	11.994	12.542	12.294
Density [mg/mm^3]	2.65	2.65	2.65	2.65	2.65	2.65	2.65
Mass modeled [q]	0.033	0.031	0.038	0.031	0.032	0.033	0.033
Mass modeled [mq]	32.899	30.600	38.196	30.799	31.784	33.237	32.578
Weight measured [mg]	37.992	37.992	37.992	37.992	37.992	37.992	37.992

Table 3: Calculated effect of the threshold value variation on a theoretical crystal volume whose morphology can be described through a 3-degree polynomial equation.

$$y=-0.11x^2+0.97x+0.98$$

Polynomial equation

Theoretical surface A (mm^2)	Theoretical thickness d (mm)	Theoretical volume V (mm^3)
21.92	2.00	43.85

Threshold value	Volume calculated	Volume theoretical
1	15.43	43.85
2	33.05	43.85
3	43.98	43.85
5	43.73	43.85
6	36.47	43.85
4	43.90	43.85

Table 4: Calculated effect of the threshold value variation on a theoretical crystal volume whose morphology can be described through a linear equation.

Linear equation $y=0.33x+1$

Theoretical surface A (mm^2)	Theoretical thickness d (mm)	Theoretical volume V (mm^3)
22.50	2.00	45.00

Threshold value	Volume calculated	Volume theoretical
1	19.50	45.00
2	36.00	45.00
3	45.00	45.00
4	45.00	45.00
5	45.00	45.00
6	45.00	45.00
7	45.00	45.00
8	45.00	45.00
10	45.00	45.00

Table 5: Calculated effect of the threshold value variation on the volume of a quartz crystal wedge.

Crystal	Quartz-wedge							
Threshold value	20	22	25	30	35	40	50	55
Image								
Height (pixel)	900	900	900	900	900	900	900	900
Width (pixel)	600	600	600	600	600	600	600	600
Pixel								
Height (mm)	0.0041	0.0041	0.0041	0.0041	0.0041	0.0041	0.0041	0.0041
Width (mm)	0.0041	0.0041	0.0041	0.0041	0.0041	0.0041	0.0041	0.0041
Surface (mm^2)	1.68E-05	1.68E-05	1.68E-05	1.68E-05	1.68E-05	1.68E-05	1.68E-05	1.68E-05
Crystal								
Phase difference (mm)	4.17E-04	5.09E-04	5.17E-04	5.25E-04	5.28E-04	5.29E-04	5.29E-04	5.29E-04
Birefringence	0.0091	0.0091	0.0091	0.0091	0.0091	0.0091	0.0091	0.0091
Height (mm)	0.0458	0.0559	0.0568	0.0577	0.0580	0.0581	0.0582	0.0582
Volume (mm^3)	0.4156	0.5072	0.5148	0.5229	0.5264	0.5268	0.5277	0.5277

Table 6: Calculated effect of the threshold value variation on the volume of a gypsum crystal wedge.

Crystal	Gypsum											
Threshold value	40	50	55	60	62	64	66	67	70	80
Image										
Height (pixel)	800	800	800	800	800	800	800	800	800	800
Width (pixel)	800	800	800	800	800	800	800	800	800	800
Pixel										
Height (mm)	0.0041	0.0041	0.0041	0.0041	0.0041	0.0041	0.0041	0.0041	0.0041	0.0041
Width (mm)	0.0041	0.0041	0.0041	0.0041	0.0041	0.0041	0.0041	0.0041	0.0041	0.0041
Surface (mm^2)	1.66E-05	1.6569E-05	1.66E-05	1.66E-05	1.66E-05	1.66E-05	1.66E-05	1.66E-05	1.66E-05	1.66E-05
Crystal										
Phase difference (mm)	1.56E-04	2.17E-04	2.24E-04	2.27E-04	2.27E-04	2.27E-04	2.27E-04	2.27E+00	2.26E-04	2.15E-04
Birefringence	0.0091	0.0091	0.0091	0.0091	0.0091	0.0091	0.0091	0.0091	0.0091	0.0091
Height (mm)	0.0172	0.0238	0.0246	0.0249	0.0250	0.0250	0.0250	0.0250	0.0248	0.0236
Volume (mm^3)	0.1821	0.2524	0.2606	0.2642	0.2649	0.2651	0.2649	0.2646	0.2631	0.2508

Table 7: Pressure and Temperature dependence of diamond anvil stress birefringence

P,T dependence				
Rotation of nut	0.375		0.25	
Heating cycle				
	Birefringence (nm)	Temperature (°C)	Birefringence (nm)	Temperature (°C)
	380.36	29.8	427.55	28.7
	380.93	49.6	428.23	80.0
	419.89	102.2	423.30	100.0
	428.45	156.5		
	428.47	213.2		
	428.58	294.0		
	375.12	409.9		
	344.63	453.8		
Cooling cycle	321.06	91.9		
	339.44	194.2		
	368.18	334.2		
	427.31	417.5		

Table 8: Pressure and Temperature dependence of diamond anvil stress birefringence

P dependence	Birefringence (nm)	Rotation of nut
	421.46	0.00
	454.88	0.25
	379.54	0.38
	421.35	0.50

Natrolithe
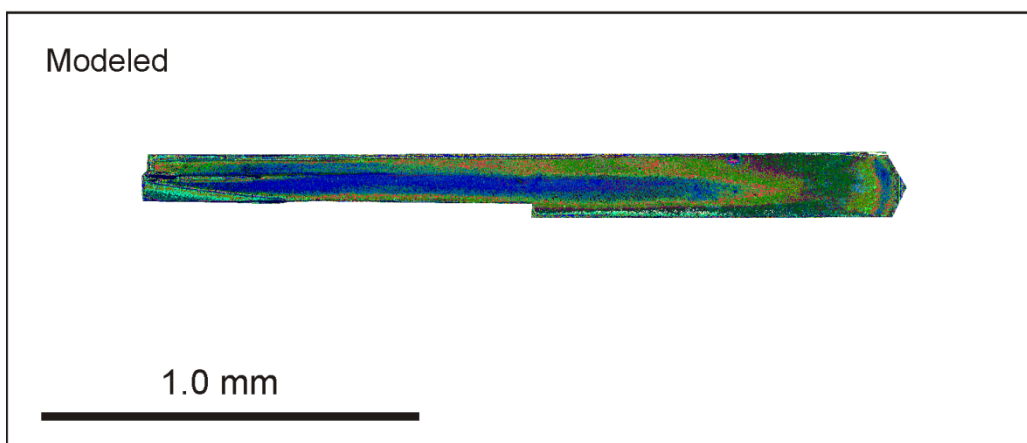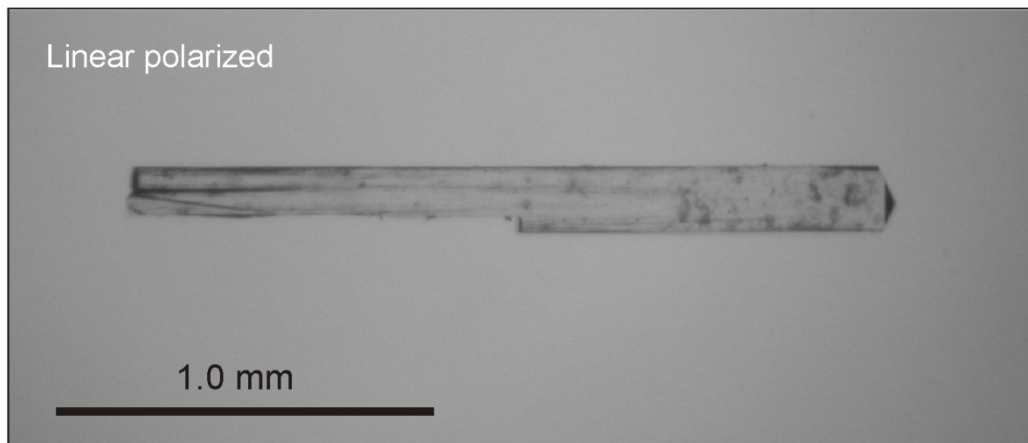
Natrolithe crystal under linear polarized light (upper image), same crystal modeled.

Anhydrite
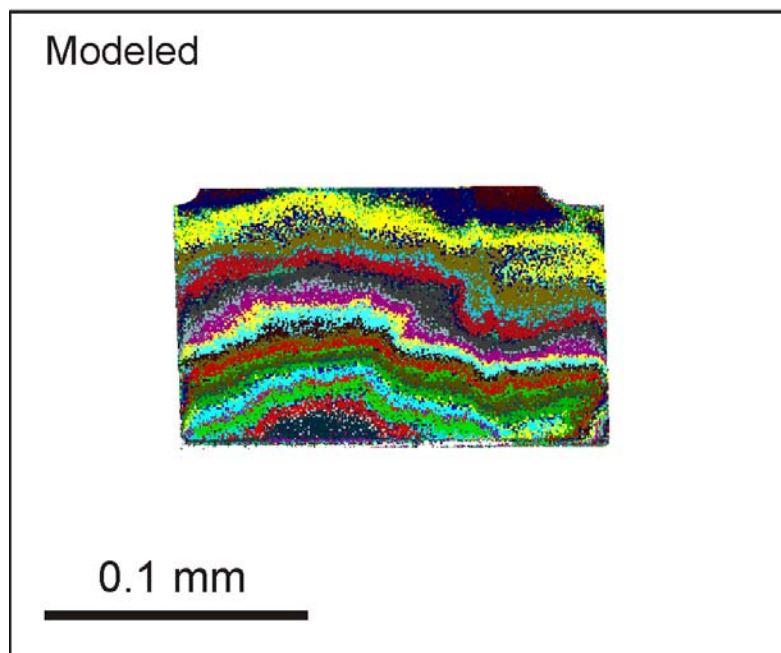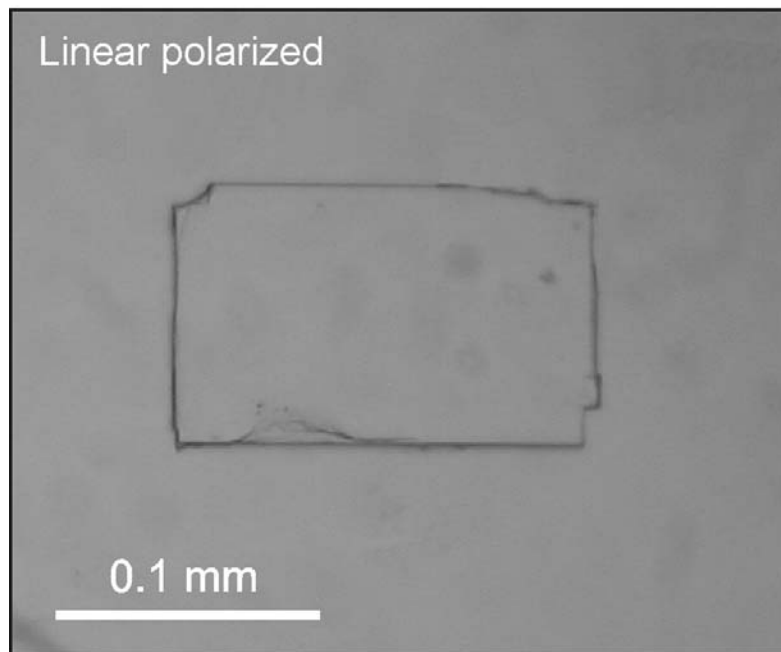
Anhydrite crystal under linear polarized light (upper image), same crystal modeled.

Gypsum no.1
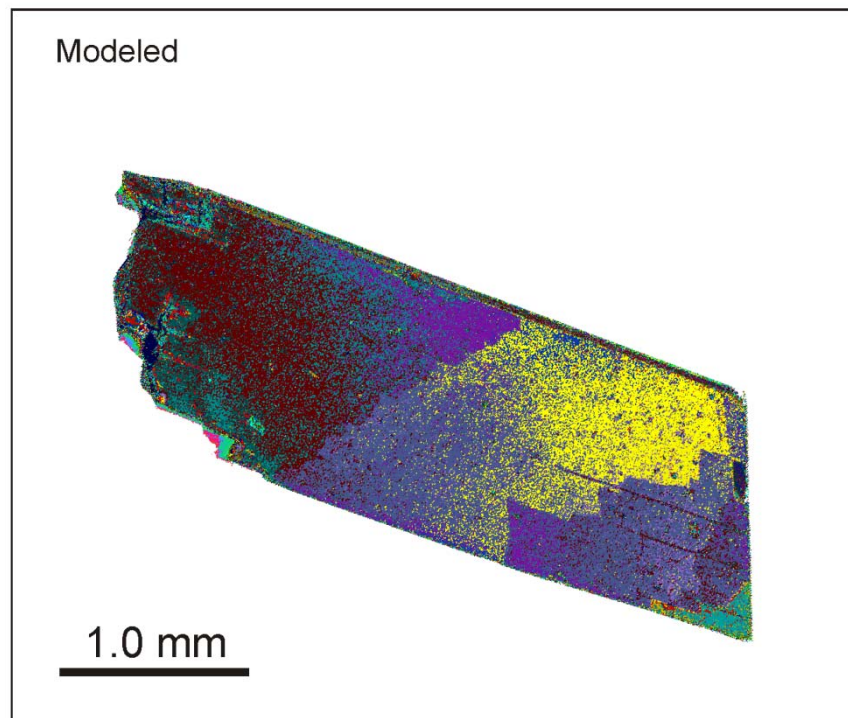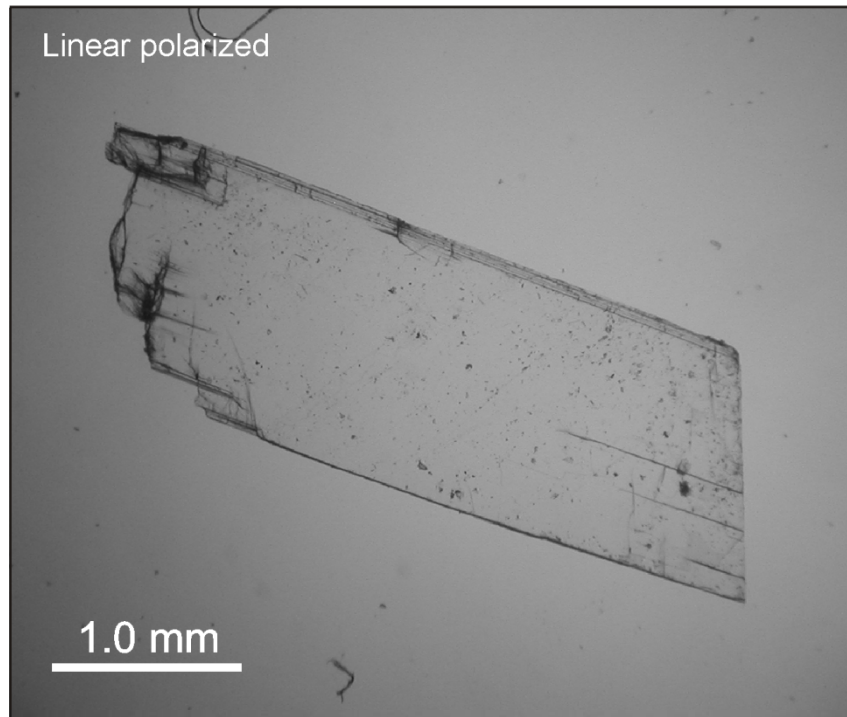
Gypsum crystal no.1 under linear polarized light (upper image), same crystal modeled.
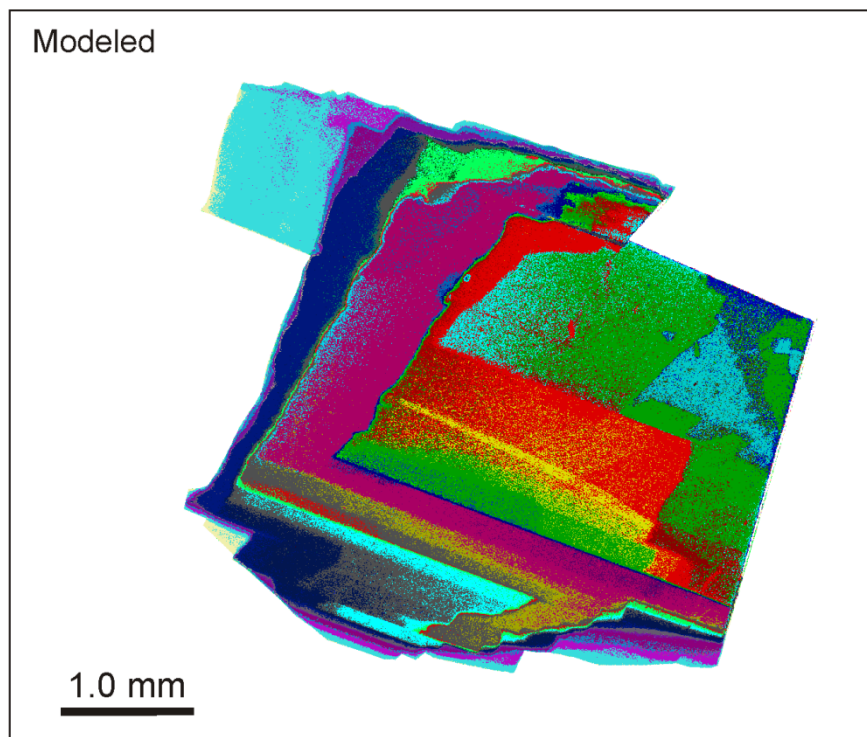
Gypsum no. 2

Gypsum crystal no.2 under crossed polarizers light (upper image), same crystal modeled.

Gypsum no.3
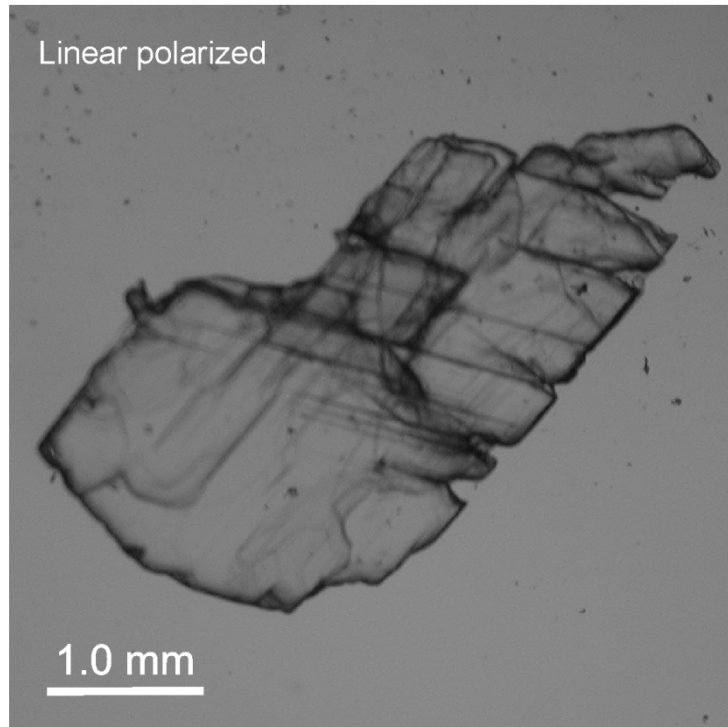
Gypsum crystal no.3 under linear polarized light (upper image), same crystal modeled.

Muscovite
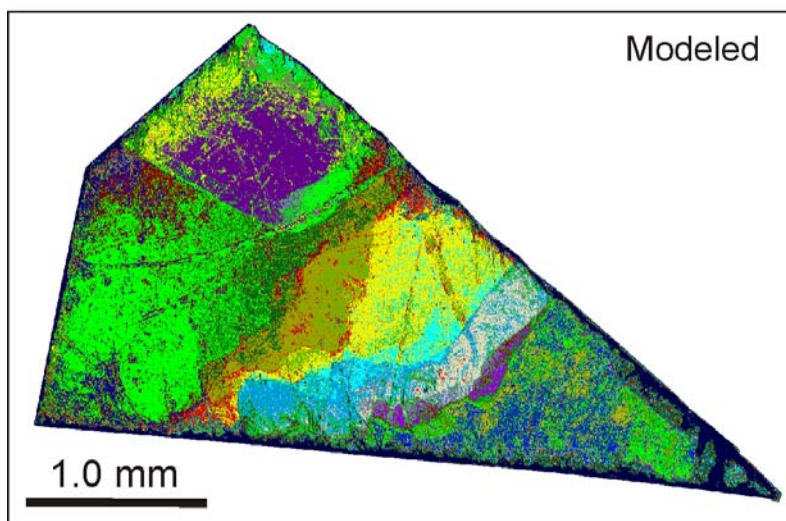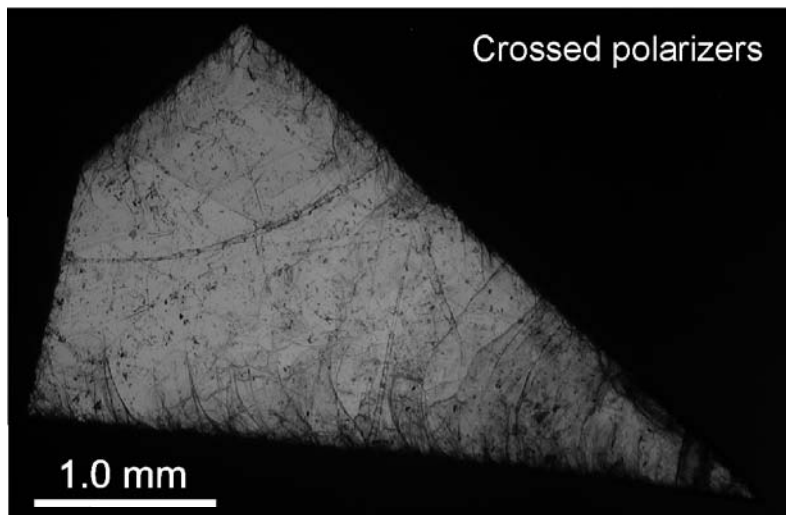
Muscovite crystal under crossed polarizers (upper image), same crystal modeled.

Quartz
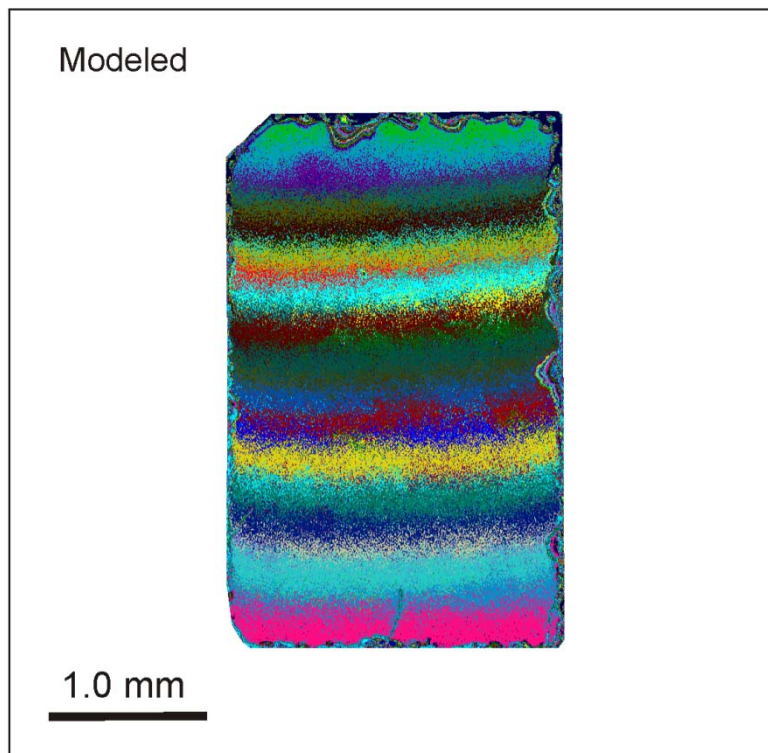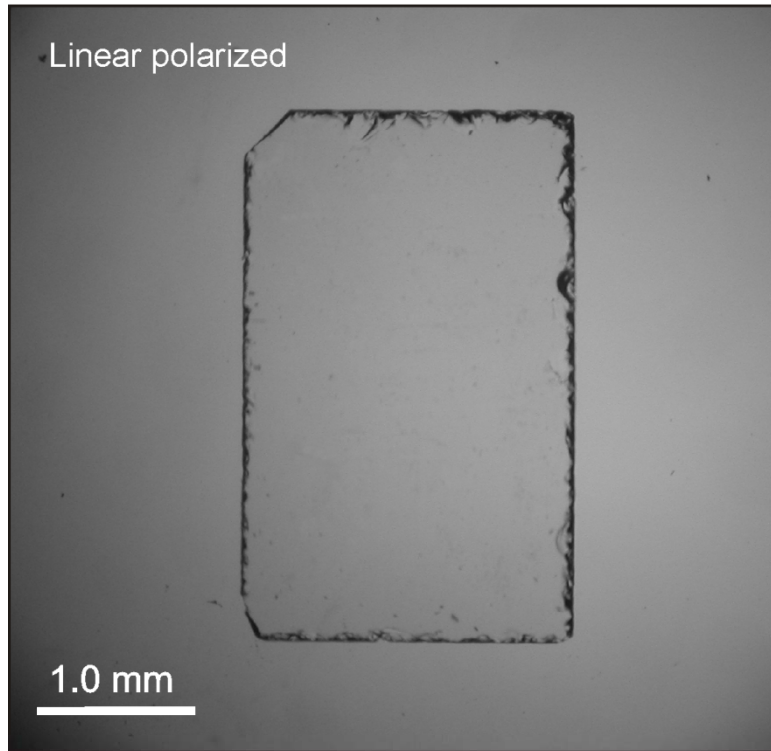
Quartz wedge under linear polarized light (upper image), same crystal modeled.

Table 9: Solubility data of quartz derived in this study with the CVC method.

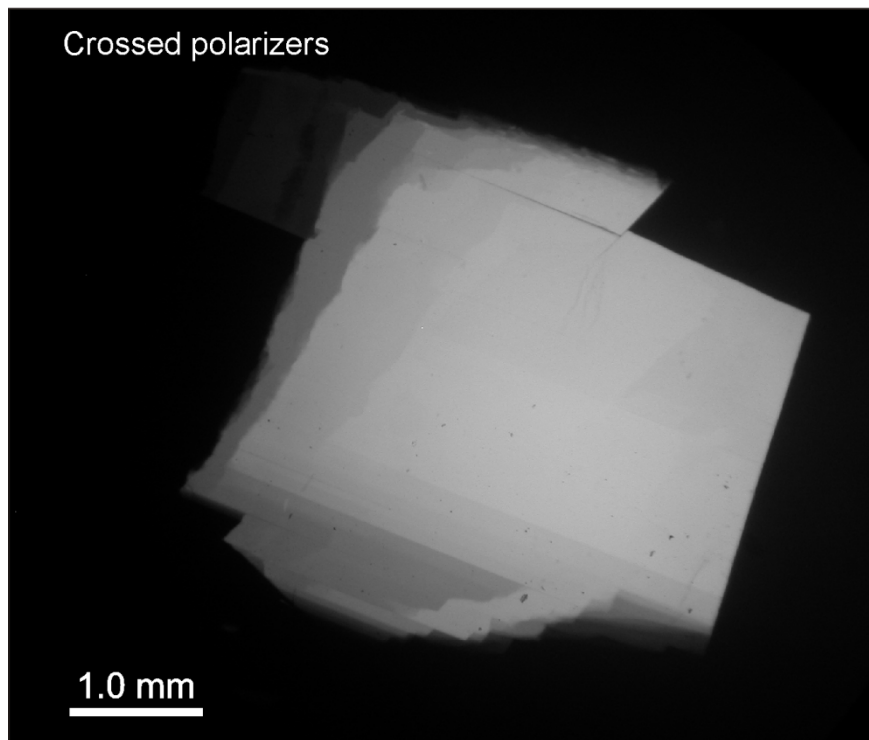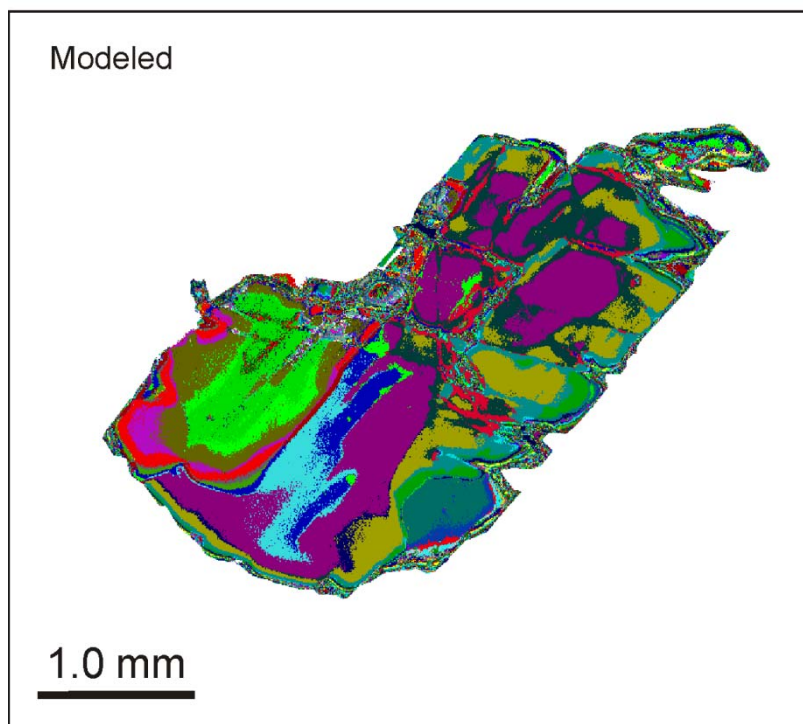|	Temperature (°C)	Pressure (kbar)	Qtz loss (µg)	Solubility (mol/kg)	Solubility (ppm)	Volume H_2O (mm^3)
Bulk density ρ	= 0.9656;	T_H 89.5				0.02065
	584	9.7	0.4058	0.3388	20356	
	572	9.5	0.4100	0.3423	20565	
	562	9.3	0.3289	0.2746	16500	
	547	9	0.3009	0.2512	15092	
	534	8.7	0.2781	0.2322	13952	
	520	8.5	0.2401	0.2005	12045	
	496	8	0.2031	0.1696	10189	
	469	7.5	0.1598	0.1334	8016	
	450	7.1	0.1319	0.1101	6615	
	426	6.6	0.1264	0.1055	6339	
	380	5.7	0.0905	0.0756	4542	
	301	4	0.0951	0.0794	4768	
	201	2	0.0696	0.0581	3493	
Bulk density ρ	= 0.9614;	T_H=95.7				0.02073
	496	7.8	0.1999	0.1669	10029	
	453	7	0.1474	0.1231	7396	
	435	6.6	0.1079	0.0901	5415	
	401	5.9	0.0848	0.0708	4254	
	352	5	0.0421	0.0352	2113	
	293	3.7	0.0250	0.0208	1253	
	235	2.6	0.0091	0.0076	458	
	204	1.9	0.0047	0.0040	237	
	154	1	0.0062	0.0052	310	
Bulk density ρ	= 0.8633;	T_H = 201.2				0.00954
	450	4	0.0073	0.0149	893	
	500	4.8	0.0472	0.0958	5754	
	550	5.6	0.0693	0.1406	8449	
	600	6.4	0.1197	0.2426	14579	
	650	7.1	0.1724	0.3496	21008	
	700	7.9	0.2727	0.5529	33221	
	750	8.6	0.3956	0.8022	48199	

Continuing table 9.

	Temperature (°C)	Pressure (kbar)	Qtz loss (µg)	Solubility (mol/kg)	Solubility (ppm)	Volume H$_2$O (mm^3)
Bulk density ρ = 0.9876;		T_H = 50.8				0.01780
	635	11.7	0.4600	0.4355	26169	
	610	11.2	0.4274	0.4047	24316	
	577	10.6	0.3412	0.3231	19410	
	566	10.3	0.3128	0.2962	17794	
	531	9.6	0.2641	0.2501	15026	
	504	9.1	0.2194	0.2077	12482	
	487	8.7	0.1999	0.1893	11371	
	449	7.9	0.1198	0.1134	6815	
	430	7.5	0.0997	0.0944	5673	
	404	7	0.0727	0.0688	4135	
	357	6	0.0589	0.0558	3354	
	303	4.8	0.0350	0.0331	1990	
	246	3.6	0.0073	0.0069	415	
	199	2.6	0.0091	0.0086	516	
	139	1.4	0.0025	0.0023	141	
Bulk density ρ = 0.9933;		T_H = 37.0				0.01773
	173	2.2	0.0040	0.0038	226	
	236	3.6	0.0259	0.0244	1762	
	312	5.2	0.0311	0.0293	3258	
	355	6.2	0.0493	0.0466	2799	
	405	7.3	0.1001	0.0945	8299	
	462	8.5	0.1463	0.1381	9276	
	503	9.4	0.1635	0.1544	12945	
	541	10.1	0.2282	0.2154	15184	
	569	10.7	0.3165	0.2988	17953	
Bulk density ρ = 0.7797;		T_H = 262.4				0.00862
	500	3.1	0.0000	0.0000	0	
	550	3.8	0.0379	0.0937	5627	
	600	4.4	0.1288	0.3186	19144	
	650	5	0.1858	0.4596	27616	
	700	5.6	0.2642	0.6536	39269	
	740	6.1	0.3522	0.8712	52347	

Table 10: Solubility data of quartz derived in this study with the birefringence mapping method.

	Temperature (°C)	Pressure (kbar)	Qtz loss (µg)	Solubility (mol/kg)	Solubility (ppm)	Volume H_2O (mm^3)
Bulk density ρ	= 0.9332;	T_H 131.9°C				0.0202
	139.3	0.13	0.0175	0.0154	924	
	219.3	1.56	0.0056	0.0049	294	
	286.8	2.84	0.0118	0.0104	624	
	363.0	4.31	0.0422	0.0372	2230	
	444.5	5.85	0.1091	0.0962	5749	
	500.3	6.89	0.0846	0.0746	4462	

Programm BifCalc
Programm zur Berechnung des Kristallvolumens aus Bildern mit unterschiedlichen Gangunterschieden und Berücksichtigung der Spannungsdoppelbrechung
(C) Juliane Groß & Michael Burchard 2009

```
###############################################################################
```
Berechnung der Korrekturfunktion für die Spannungsdoppelbrechung
```
###############################################################################
```

(Basiskoordinaten des Bildausschnittes im Bild für die Spannungsdoppelbrechung)
x1 = 560
y1 = 390
x2 = 1170
y2 = 870

(Daten für den Spannungdoppelbrechnungshintergund einlesen (Liste von x, y , Gangunterschied) und der Matrix D zuweisen)
D=dlmread('c:\daten_d.out',';');
(x Koordinate der Matrix D entnehmen)
x=D(:,1)+x1;
(y Koordinate der Matrix D entnehmen)
y=D(:,2)+y1;
(Gangunterschiede (z Werte) der Matrix D entnehmen)
z=D(:,3);

(Regression, Matrize aus x und y Potenzen bilden)
M=[ones(size(x)) x x.^2 y y.^2];
(lineare Regression von z über M das Ergebnis wird dem Vektor k zugewiesen)
*(Regression für die Funktion z = k(1)+k(2)*x+k(3)*x.^2+k(4)*y+k(5)*y.^2)*
k=M\z
(Spannungsdoppelbrechungshintergrund für gesamtes Bild berechnen)
(gleichmäßige Zahlenreihe für die y-Koordinate aufbauen und yy zuweisen)
yy = linspace(y1,y2,y2-y1+1);
(gleichmäßige Zahlenreihe für die x-Koordinate aufbauen und xx zuweisen)
xx = linspace(x1,x2,x2-x1+1);
(Gitter für xxx,yyy,zzz Plot aufbauen)
[yyy,xxx]=meshgrid(yy,xx);
(Spannungsdoppelbrechung für jede x,y Koordinate berechnen (zzz für jedes xxx,yyy Paar berechnen))
zzz = k(1)+k(2)*xxx+k(3)*xxx.^2+k(4)*yyy+k(5)*yyy.^2;

(2-D Colorplot für die berechnete Spannungsdoppelbrechung aufbauen)
(Grafikfenster öffenen und Handle zuweisen)
H=figure
(2-D Colorplot erzeugen)
pcolor(xxx,yyy,zzz);
(Farbeverlauf interpolieren)
shading interp
(Minimum und Maximum Wert der z-Achse definieren)
caxis([20 35]);
(Farbskala hinzufügen)
colorbar

```
################################################################################
Zeichnen eine 2D-Plots für die gemessene Spannungsdoppelbrechung
################################################################################
```

(Daten für des Spannungdoppelbrechnungshintergund einlesen (Matrize Ganguntterschied mit x*y Werten) und der Matrix d zuweisen)
```
d=dlmread('c:\matrix_d.out',';');#
```

(Anpassung des Koordinatensystems der Corel Photopaint Daten Matrix transponieren)
```
d=transpose(d);
```
(Richtung der y-Achse ändern)
```
d_=d;
sd=size(d_,2);
for i1 = 1:sd
  for i2 = 1: size(d_,1)
    d(i2,i1)=d_(i2,sd-i1+1);
  end
end
```

(2-D Colorplot für die gemessene Spannungsdoppelbrechung aufbauen)
(Grafikfenster öffnen und Handle zuweisen)
```
Hd=figure
```
(2-D Colorplot erzeugen)
```
pcolor(xxx,yyy,d);
```
(Farbeverlauf interpolieren)
```
shading interp
```
(Minimum und Maximum Wert der z-Achse definieren)
```
caxis([20 35]);
```
(Farbskala hinzufügen)
```
colorbar
```
(Anlegen von Konturlinien)
(Grafiksicherung an)
```
hold on
```
(Kontur hinzufügen)
```
[S H] = contour(xxx,yyy,d,[20 25 30 35],'-k');
```
(Beschriftung der Kontur hinzufügen)
```
clabel(S,H);
```
(Grafiksicherung aus)
```
hold off
```

```
################################################################################
Berechnung der Differenz zwischen gemessene und berechneter  Spannungsdoppelbrechung
(###############################################################################
```

(Differenz berechnen)
```
dz=zzz-d;
```

(2-D Colorplot für die Differenz zwischen gemessener und berechneter Spannungsdoppelbrechung)
(Grafikfenster öffnen und Handle zuweisen)
```
Hdz=figure
```
(2-D Colorplot erzeugen)
```
pcolor(xxx,yyy,dz);
```
(Farbeverlauf interpolieren)
```
shading interp
```
(Minimum und Maximum Wert der z-Achse definieren)
```
caxis([-30 30]);
```
(Farbskala hinzufügen)
```
colorbar
```

```
################################################################################
```
Zeichnen eines 2-D Plots der gemessenen Doppelbrechung des Kristalls
```
################################################################################
```

(Basiskoordinaten des Bildausschnittes im Bild für die Doppelbrechung des Kristalls)
x3 = 560
y3 = 390
x4 = 1170
y4 = 870

(Daten für des Doppelbrechung des Kristalls einlesen (Matrize Gangunterschied mit x*y Werten) und der Matrix C zuweisen)
C=dlmread('c:\matrix.out',';');

(2-D Colorplot für die Doppelbrechung des Kristalls)
(gleichmäßige Zahlenreihe für die x-Koordinate aufbauen und cxx zuweisen)
cxx=linspace(x3,x4,x4-x3+1);
(gleichmäßige Zahlenreihe für die y-Koordinate aufbauen und cyy zuweisen)
cyy=linspace(y3,y4,y4-y3+1);
(Gitter für cxxx, cyyy, C Plot aufbauen)
[cxxx,cyyy]=meshgrid(cxx,cyy);
(Grafikfenster öffnen und Handle zuweisen)
HC=figure
(2-D Colorplot erzeugen)
pcolor(cxxx,cyyy,C);
(Farbeverlauf interpolieren)
shading interp
(Minimum und Maximum Wert der z-Achse definieren)
caxis([0 150]);
(Farbskala hinzufügen)
colorbar
(Kontur hinzufügen)
[S H] = contour(cxxx,cyyy,C,[0 10 20 30 40 50 60 70 80 90 100 110 120 130 140 150],'-k');
(Beschriftung der Kontur hinzufügen)
clabel(S,H);
(Grafiksicherung aus)
hold off

```
################################################################################
```
Korrektur der Doppelbrechung des Kristalls um den Spannungsdoppelbrechungsanteil
```
(###############################################################################
```

(Matrix mit Korrektur werten aus Spannungsdoppelbrechungfunktion berechnen)
ZZZ = k(1)+k(2)*cxxx+k(3)*cxxx.^2+k(4)*cyyy+k(5)*cyyy.^2;
(Spannungsdoppelbrechung von der Kristalldoppelbrechung abziehen)
DD = C-ZZZ;

(2-D Colorplot für die korrigierte Doppelbrechung des Kristalls)
(Grafikfenster öffnen und Handle zuweisen)
HDD = figure;
(2-D Colorplot erzeugen)
pcolor(cxxx,cyyy,DD);
(Farbeverlauf interpolieren)
shading interp
(Minimum und Maximum Wert der z-Achse definieren)
caxis([0 100])
(Farbskala hinzufügen)
colorbar

```
##############################################################################
Berechnung des Kristallvolumens
##############################################################################

( Bildpixel des Kristalls zählen, Platzhalterzahle entfernen (Vorbereitung zur Bildung des Integrals))
U=DD;
dot=0;
for I1=1:size(U,1)
  for I2=1:size(U,2)
    if (U(I1,I2)<1000)
      if (U(I1,I2)> -1000)
        dot=dot+1;
      else
        U(I1,I2)=0;
      end
    else
      U(I1,I2)=0;
    end
  end
end
( Pixelanzahl ausgeben)
dot
( Doppelbrechung des Materials festlegen)
doppelbrechung=0.0091
( Umrechnungsfaktor auf gewünschte Volumeneinheit (1E6 ==> mm^3))
umrechnungmm=1e6
( Mittlere Dopelebrechung des Kristalls berechnen)
kristalldoppelbrechung= sum(sum(U))/dot
( Höhe des Kristalls berechnen für die Annahme das kein Vielfaches von Lambda vorliegt)
delta1=kristalldoppelbrechung/doppelbrechung/umrechnungmm
( Höhe des Kristalls berechnen für die Annahme das ein Vielfaches von Lambda vorliegt)
delta2=(kristalldoppelbrechung+546)/doppelbrechung/umrechnungmm
( Höhe des Kristalls Berechnen für die Annahme das kein Vielfaches von Lambda vorliegt und die
Diamantstempelzelle einen Phasensprung von lambda/4 verursacht)
delta3=(kristalldoppelbrechung+546+546/4)/doppelbrechung/umrechnungmm
( Pixelgröße festlegen)
Pixelgroesse=1.42992372787E-07
( Kristallfäche berechnen)
A=Pixelgroesse*dot
( Volumina für alle drei Deltas berechnen)
V1=delta1*A
V2=delta2*A
V3=delta3*A
(Stoffmenge des Kristallmaterials pro Kubikmillimeter festlegen )
molprokubikmm=4.410506659E-05
( Stoffmenge des Kristalls für alle drei Volumina berechen)
n1=molprokubikmm*V1
n2=molprokubikmm*V2
n3=molprokubikmm*V3
```

```
##########################################################################
Funktion ausschneiden_und_konvertieren
 Das Programm schneidet definierte Bereich aus eine Bilderfolge aus und wandelt diese in Schwarz-Weiß
Bilder um.

(C) Juliane Groß & Michael Burchard (2009)
##########################################################################

(Datenpfad)
Dim fpath As String
fpath = "C:\Gips300\"
(x,y Offset um relative Änderungen in der Position des Bildes zu kompensiren)
Dim offx As Long
Dim offy As Long
offx = 0
offy = 0
(Position des rechteckigen Ausschnitts)
Dim x1 As Long
Dim x2 As Long
Dim y1 As Long
Dim y2 As Long
x1 = 560
y1 = 390
x2 = 1170
y2 = 870
(Exportfilter Objekt)
Dim ef As ExportFilter
(Farbmodell)
Dim cm As Long
(Bildhöhe)
Dim dh As Long
(Bildbreite)
Dim dw As Long
(Dateinamen)
Dim filen As String
Dim filen1 As String
Dim filen2 As String
Dim filen3 As String
Dim filen4 As String
Dim filemask As String
Dim fileimage As String
(Corelskriptobjekt)
Dim cs As Object
(Corelskriptobjekt zuweisen)
Set cs = Application.CorelScript
(Steuerdatei öffnen)
Open fpath + "imagescript.txt" For Input As #1
(Dateiname der Maske lesen)
Line Input #1, filemask
(Schleife zum einlesen und bearbeiten der Bilder)
Do While Not EOF(1)
  (Bild dateiname lesen)
  Line Input #1, fileimage
  (Bild öffnen)
  Application.OpenDocument (fpath + fileimage)
  (Corelskriptobjekt an das Bild anbinden)
  cs.BindToActiveDocument
  (Neue Dateinamen generieren)
  filen = fileimage
  filen4 = fpath + Left(filen, Len(filen) - 4) + "_.jpg"
```

```
filen1 = fpath + Left(filen, Len(filen) - 4) + ".cpt"
filen2 = fpath + Left(filen, Len(filen) - 4) + "_mask.cpt"
filen3 = fpath + Left(filen, Len(filen) - 4) + "_shape.cpt"
```
(Rechteckmaske setzen)
```
cs.MaskRectangle x1, y1, x2, y2, 0, 0
```
(auf Maske zuschneiden)
```
cs.ImageCropToMask
```
(Neues Dokument speichern)
```
Set ef = ActiveDocument.SaveAs(filen4, 774)
ef.Finish
```
(Dokument schließen & wieder öffnenen ("Work around"))
```
Application.ActiveDocument.Close
Application.OpenDocument (filen4)
```
(Corelskript an Dokument binden)
```
cs.BindToActiveDocument
```
(Farbmodell zuweisen)
```
cm = cdrColorRGB
```
(Bildhöhe auslesen)
```
dh = cs.GetDocumentHeight
```
(Bildbreite auslesen)
```
dw = cs.GetDocumentWidth
```
(Maske einlesen
```
cs.MaskLoad fpath + filemask, 0, 0, dw - 1, dh - 1, 0
```
(freie Bereiche mit Weiß füllen)
```
cs.EditFill 15, 0, 0, 0, 1, 0, 0, 0, 0, 0, 0
cs.FillSolid cm, 255, 255, 255, 0
cs.EndEditFill
```
(Maske invertieren)
```
cs.MaskInvert
```
(Dokument Speichern)
```
Set ef = ActiveDocument.SaveAs(filen1, 1808)
ef.Finish
```
(in Schwarz-Weiß Grafik umwandeln (Thresholdvalue definiert die Grenze für Schwarz))
```
cs.BitmapEffect "Grenzwert", "ThresholdEffect
ThresholdChannel=0,ThresholdBiLevel=2,ThresholdLow=0,ThresholdHigh=255,ThresholdMid=8"
```
(Dokument abspeichern)
```
Set ef = ActiveDocument.SaveAs(filen1, 1808)
ef.Finish
```
(Maske speichern)
```
cs.MaskSave filen2, 1808, 0
cs.ColorMaskCreateMask 0, 1, 0, 0, False, 127, 0
cs.ColorMaskColor 0, 5, 0, 0, 0, 0, 20, 20, 20, 20
cs.EndColorMask
```
(Dokument schließen)
```
Application.ActiveDocument.Close
```
(Ende der Schleife)
```
Loop
```
(Steuerdatei schließen
```
Close #1
```
(Parameterdatei öffnen)
```
Open Path + "parameterk.out" For Output As #1
```
(Verwendeten Ausschnitt ausgeben)
```
Print #1, "X1:", x1
Print #1, "X2:", x2
Print #1, "Y1:", y1
Print #1, "Y2:", y2
```
(Parameterdatei schließen)
```
Close #1
End Sub
```

```
###############################################################
Funktion berechnen_und_auswerten
Das Programm kombiniert die Schwarz-Weiß Bilderfolge zu einem Bild, es
Berechnet die Gangunterschiede für jeden Bildpunkt und erstellt Eingabedateien für Matlab        .

(C) Juliane Groß & Michael Burchard (2009)
###############################################################

Dim fpath As String
fpath = "C:\Gips300\"
Dim ef As ExportFilter
(Farbmodell)
Dim cm As Long
(Bildhöhe)
Dim dh As Long
(Bildbreite)
Dim dw As Long
(RGB Rotwert)
Dim rgbr As Long
(RGB Grünwert)
Dim rgbg As Long
(RGB Blauwert)
Dim rgbb As Long
(RGB Rotwert)
Dim r As Long
(RGB Grünwert)
Dim g As Long
(RGB Blauwert)
Dim b As Long
(Zählvariablen)
Dim i As Long
Dim i1 As Long
Dim i2 As Long
Dim ic As Long
(Minimum Farben)
Dim ub As Long
(Dateinummer)
Dim fno As Long
(Pixelvariable)
Dim res As Boolean
(Dateinamen)
Dim filen As String
Dim filen1 As String
Dim filemask As String
Dim fileimage As String
(Objektvariable für Corelskriptobjekt)
Dim cs As Object
(Auswertungvariable für das Auszählen)
(der Bildpunkte und die Berechnung von Farbwerten, Gangunterschieden und Integralen)
Dim delta(24) As Double
Dim dotvalue As Double
Dim value As Double
Dim colors() As Long
Dim colorsdot() As Long
Dim colors1() As Long
Dim colorsdot1() As Long
Dim deltalist() As Double
Dim deltalistsum() As Double
Dim deltadots() As Long
Dim deltalist1() As Double
```

```
Dim deltalistsum1() As Double
Dim deltadots1() As Long
Dim maxdeltalist As Double
Dim maxdeltalistsum As Double
Dim maxdeltadots As Long
```
(Boolschevariable als Abruchbedingung)
```
Dim leave As Boolean
```
(Pixelcolor)
```
Dim pixco As Long
```
(2^16 Variable)
```
Dim ko As Long
```
(dynamisches Array für Blau- Grün und Rotwerte)
```
Dim rr() As Long
Dim gg() As Long
Dim bb() As Long
```
(ko initialisieren)
```
ko = 256& * 256&
```
(Arrays initialisieren)
```
ReDim colors(0)
ReDim colorsdot(0)
ReDim deltalist(0)
ReDim deltalistsum(0)
ReDim deltadots(0)
```
(Corelskriptobjekt initialisieren)
```
Set cs = Application.CorelScript
```
(Steuerdatei öffnen)
```
Open fpath + "imagescript6.txt" For Input As #1
```
(1. Datei öffnen)
```
Line Input #1, fileimage
Application.OpenDocument (fpath + fileimage)
filemask = fileimage
```
(Corelskript an Datei binden)
```
cs.BindToActiveDocument
```
(Farbmodel auslesen)
```
cm = cdrColorRGB
```
(Bildhöhe auslesen)
```
dh = cs.GetDocumentHeight
```
(Bildbreite auslesen)
```
dw = cs.GetDocumentWidth
```
(Maske lesen)
```
cs.MaskLoad fpath + filemask, 0, 0, dw - 1, dh - 1, 0
```
(Maske invertieren)
```
cs.MaskInvert
```
(freien Bereich mit Farbe 1 setzen)
```
cs.EditFill 15, 0, 0, 0, 1, 0, 0, 0, 0, 0, 0
cs.FillSolid cm, 0, 0, 1, 0
cs.EndEditFill
```
(Maske invertieren)
```
cs.MaskInvert
```
(freinen Bereich mit Farbe 0 füllen)
```
cs.EditFill 0, 0, 0, 0, 1, 0, 0, 0, 0, 0, 0
cs.FillSolid cm, 0, 0, 0, 0
cs.EndEditFill
```
(Maske entfernen)
```
cs.MaskRemove
```
(Dateiname und Pfad lesen)
```
filen = ActiveDocument.FileName
filep = ActiveDocument.FilePath
```
(neuen Dateinamen erstellen)
```
filen1 = filep + Left(filen, Len(filen) - 4) + "_changed_1_d.cpt"
```

```
(Datei speichern)
Set ef = ActiveDocument.SaveAs(filen1, 1808)
ef.Finish
(Datei schließen)
Application.ActiveDocument.Close
(datei öffnen)
Application.OpenDocument (filen1)
(Corelskriptobjekt an Datei binden)
cs.BindToActiveDocument
fileimage = filemask
(Dateinummer auf 1 setzen)
fno = 1
(weitere Bilder in Schleife bearbeiten)
Do While Not EOF(1)
 (weiteren Dateinamen lesen)
 Line Input #1, filemask
 (Dateinummer erhöhen)
 fno = fno + 1
 (Berechnung des aktuellen Farbbits für diese Datei)
 If fno < 9 Then
  rgbr = 0
  rgbg = 0
  rgbb = 2 ^ (fno - 1)
 Else
  If fno < 17 Then
   rgbr = 0
   rgbg = 2 ^ (fno - 9)
   rgbb = 0
  Else
   If fno < 25 Then
    rgbr = 2 ^ (fno - 17)
    rgbg = 0
    rgbb = 0
   Else
    rgbr = 0
    rgbg = 0
    rgbb = 0
   End If
  End If
 End If
 (Maske  laden)
 cs.MaskLoad fpath + filemask, 0, 0, dw - 1, dh - 1, 0
 (Maske invertieren)
 cs.MaskInvert
 (Maske füllen mit der Aktuellen Farbe)
 cs.EditFill 15, 0, 0, 0, 1, 0, 0, 0, 0, 0, 0
 cs.FillSolid cm, rgbr, rgbg, rgbb, 0
 cs.EndEditFill
 (Maske entfernen)
 cs.MaskRemove
 (neuen dateinamen erstellen)
 filen1 = filep + Left(filen, Len(filen) - 4) + "_changed_" + Trim(Str$(fno)) + "_d.cpt"
 (Datei speichern)
 Set ef = ActiveDocument.SaveAs(filen1, 1808)
 ef.Finish
 (Datei schließen)
 ActiveDocument.Close
 (Datei öffnen)
 Application.OpenDocument (filen1)
 (Corelskriptobjekt an Datei binden)
```

```
  cs.BindToActiveDocument
(Ende der Schleife)
Loop
Close #1
(Gangunterschiedsdatei öffnen und Werte einlesen)
Open fpath + "imagescript7.txt" For Input As #1
For i = 1 To 22
  Input #1, delta(i)
Next i
(Datei schließen)
Close #1
value = 0#
(letzte Maske entfernen)
cs.MaskRemove
(Ausgabedateien für Matlab öffnen)
Open fpath + "daten_d.out" For Output As #3
Open fpath + "matrix_d.out" For Output As #4
Open fpath + "mdaten_d.out" For Output As #5
(Alle Bildpunkte durchlaufen)
For i2 = 0 To dh - 1
  For i1 = 0 To dw - 1
    dotvalue = 0#
    dc = 0
    (Bildpunktfarbe auslesen)
    res = cs.GetPixelColor(i1, i2, cm, r, g, b, k)
    (Integerwert der Farbebestimmen)
    pixco = r * 256 * 256 + g * 256 + b
    (Farbe in der bisherigen Liste suchen, falls nicht vorhanden einfügen
    (Anzahl der Punkte dieser Farbe um eins erhöhen)
    ub = UBound(colors)
    If ub > 0 Then
      ic = 1
      leave = False
      Do While (ic <= ub) And Not leave
        If colors(ic) = pixco Then
          leave = True
        End If
        ic = ic + 1
      Loop
      If leave Then
        colorsdot(ic - 1) = colorsdot(ic - 1) + 1
      Else
        ReDim Preserve colors(UBound(colors) + 1)
        ReDim Preserve colorsdot(UBound(colorsdot) + 1)
        ReDim Preserve deltalist(UBound(deltalist) + 1)
        ReDim Preserve deltalistsum(UBound(deltalist) + 1)
        ReDim Preserve deltadots(UBound(deltadots) + 1)
        colors(ic - 1) = pixco
        colorsdot(ic - 1) = 1
      End If
    Else
      ReDim Preserve colors(1)
      ReDim Preserve colorsdot(1)
      ReDim Preserve deltalist(1)
      ReDim Preserve deltalistsum(1)
      ReDim Preserve deltadots(1)
      colors(1) = pixco
      colorsdot(1) = 1
    End If
    For i = 0 To 7
```

```
    If (r And (2 ^ i)) > 0 Then
      dc = dc + 1
      dotvalue = dotvalue + delta(17 + i)
    End If
    If (g And (2 ^ i)) > 0 Then
      dc = dc + 1
      dotvalue = dotvalue + delta(9 + i)
    End If
    If (b And (2 ^ i)) > 0 Then
      dc = dc + 1
      dotvalue = dotvalue + delta(1 + i)
    End If
  Next i
  (Ausgabe der Werte in die Matlabdateien)
  If dotvalue <> 0 Then
    valstr1 = CStr(dotvalue / dc)
    valstr = CStr(dotvalue / dc)
  Else
    valstr1 = "NaN"
    valstr = CStr(dotvalue)
  End If
  valstr = Replace(valstr, ",", ".")
  valstr1 = Replace(valstr1, ",", ".")
  Print #5, i1; ";"; i2; ";"; valstr1
  If i1 <> (dw - 1) Then
    Print #4, valstr1; ";";
  Else
    Print #4, valstr1
  End If
  If (dotvalue > 0) And (((i1 - 1) Mod 4) = 0) And (((i2 - 1) Mod 4) = 0) Then
    valstr = CStr(dotvalue / dc)
    valstr = Replace(valstr, ",", ".")
    Print #3, i1; ";"; i2; ";"; valstr
  End If
  (Farbwerte in Listen eintragen oder Zähler erhöhen)
  ub = UBound(colors)
  If (ub > 0) And (dc > 0) Then
    ic = 1
    leave = False
    Do While (ic <= ub) And Not leave
      If colors(ic) = pixco Then
        leave = True
      End If
      ic = ic + 1
    Loop
    If leave Then
      deltalist(ic - 1) = dotvalue / dc
      deltalistsum(ic - 1) = dotvalue
      deltadots(ic - 1) = dc
    End If
  End If
  (Integralsumme berechnen)
  If dc > 0 Then
    value = value + dotvalue / dc
  End If
  Next i1
  (Ende der Doppelschleife
  Next i2
  (Matlabausgabedateien schließen)
  Close #3
```

```
Close #4
Close #5
(Ergebnisse ausgeben)
(Unsortierte Liste der Farben und der Gangunterschiede ausgeben)
Open fpath + "imagescript_d.out" For Output As #1
Print #1, "Wert ", value, "  Punkte ", dw * dh
Print #1, ""
Print #1, ""
Print #1, "unsortiert"
Print #1, "Farben ", UBound(colors)
For i = 1 To UBound(colors)
  If colors(i) > ko Then
    r = Int(colors(i) / ko)
  Else
    r = 0
  End If
  If (colors(i) - ko * r) > 256 Then
    g = Int((colors(i) - ko * r) / 256)
  Else
    g = 0
  End If
  b = (colors(i) - ko * r - 256 * g)
  Print #1, "Farbe  r: ", r, "  g: ", g, "  b: ", b, "  Punkte ", colorsdot(i), "  DeltaSum ", deltalistsum(i), "
Farbenanzahl ", deltadots(i), "  Delta ", deltalist(i)
Next i
(Liste sortieren)
ReDim colors1(UBound(colors))
ReDim colorsdot1(UBound(colors))
ReDim deltalist1(UBound(colors))
ReDim deltalistsum1(UBound(colors))
ReDim deltadots1(UBound(colors))
For i = 1 To UBound(colors)
  maxp = 0
  max = -1
  maxd = 0
  maxdeltalist = 0
  maxdeltalistsum = 0
  maxdeltadots = 0
  For i1 = 1 To UBound(colors)
    If colors(i1) > max Then
      maxp = i1
      max = colors(i1)
      maxd = colorsdot(i1)
      maxdeltalist = deltalist(i1)
      maxdeltalistsum = deltalistsum(i1)
      maxdeltadots = deltadots(i1)
    End If
  Next i1
  colors(maxp) = -1
  colors1(i) = max
  colorsdot1(i) = maxd
  deltalist1(i) = maxdeltalist
  deltalistsum1(i) = maxdeltalistsum
  deltadots1(i) = maxdeltadots
Next i
(Sortierte Liste der Farben und der Gangunterschiede ausgeben)
Print #1, ""
Print #1, ""
Print #1, "sortiert"
Print #1, "Farben ", UBound(colors1)
```

```
For i = 1 To UBound(colors1)
  If colors1(i) > ko Then
    r = Int(colors1(i) / ko)
  Else
    r = 0
  End If
  If (colors1(i) - ko * r) > 256 Then
    g = Int((colors1(i) - ko * r) / 256)
  Else
    g = 0
  End If
  b = (colors1(i) - ko * r - 256 * g)
  Print #1, "Farbe  r: ", r, "  g: ", g, "  b: ", b, "  Punkte ", colorsdot1(i), "  DeltaSum ", deltalistsum1(i), "
Farbenanzahl ", deltadots1(i), "  Delta ", deltalist1(i)
Next i
Close #1
```
(Falschfarbenbild errechnen)
(Farbendatei öffnen)
```
Open fpath + "imagescript4.txt" For Input As #1
Input #1, anzahl
ReDim rr(anzahl + 1)
ReDim gg(anzahl + 1)
ReDim bb(anzahl + 1)
For i = 1 To anzahl
  Input #1, rr(i), gg(i), bb(i)
Next i
```
(die Farben aller Bildpunkte entsprechend ändern.)
```
For i = 1 To UBound(colors1)
  If colors1(i) > ko Then
    r = Int(colors1(i) / ko)
  Else
    r = 0
  End If
  If (colors1(i) - ko * r) > 256 Then
    g = Int((colors1(i) - ko * r) / 256)
  Else
    g = 0
  End If
  b = (colors1(i) - ko * r - 256 * g)
  cs.ColorMaskCreateMask 0, 1, 0, 0, 0, 0, 0
  cs.ColorMaskReset
  cs.ColorMaskColor 1, 5, r, g, b, 0, 0, 0, 0, 0
  cs.EndColorMask
  cs.EditFill 0, 0, 0, 0, 1, 0, 0, 0, 0, 0, 0
  cs.FillSolid 5, rr(i), gg(i), bb(i), 0
  cs.EndEditFill
Next i
```
(Neuer Dateiname)
```
filen1 = filep + Left(filen, Len(filen) - 4) + "_image_" + Trim(Str$(fno + 1)) + "_d.cpt"
```
(Bild abspeichern)
```
Set ef = ActiveDocument.SaveAs(filen1, 1808)
ef.Finish
```
(Farbendatei schließen)
```
Close #1
End Sub
```

Curriculum vitae

Juliane Groß

La-Roche-Str. 51
44629 Herne, Germany
Tel: +49 2323 9870599

Personal Information:

Nationality: German
Date of birth: April, 7th, 1979
Place of birth: Essen, Germany

Work experience:

2006-2009   Research assistant
                   Ruhr-University Bochum, Institute of Geology, Mineralogy and Geophysics

2000-2004   Student assistant
                   Ruhr-University Bochum, Department of Mineralogy

1993 - 1998   Tutor for children aged 3-7 years
                   Honorary supervising tutor of a children arts and crafts and play group ("die Schwimmis") of the church "Reformationskirche" in Essen-Rüttenscheid

Temporary employments abroad:

2005 Apr.-Dec.   Australia
                   Working Holiday Visa

1998-1999   USA, Boston
                   AuPair for 13 months, family with 3 children

Education:

2006-2009   PhD Student at the Institute of Geology, Mineralogy and Geophysics
                   Ruhr-University Bochum,
                   Thesis: "Mineral solubility measurements at highpressures: Redesigning the hydrothermal diamond anvil cell; Crystal volume computation and Birefringence mapping" supervised by Prof. Maresch

Mar. 2005	Diplom in mineralogy *Ruhr-University Bochum,* *Thesis: "Petrology of the contact zone between eclogite and* *host rocks at the Stümpelfelsen, Hammerunterwiesenthal,* *Westerzgebirge" supervised by Prof. Maresch*
1999-2005	Student of mineralogy and chemistry *Ruhr-University Bochum*
1998	Graduation *Maria-Wächtler-Gymnasium, Essen* *Grammar School*
1989-1998	Maria-Wächtler-Gymnasium, Essen *Grammar School*
1985-1989	Albert-Schweizer-Grundschule, Essen *Elementary School*

Experiences:

Languages	German: native language English: fluent Spanish: basic knowledge
Computer skills	Windows OS, MS Office (Word, Excel, PowerPoint), Corel Draw, Corel PhotoPaint, OriginPro 7.5
Analytical methods	Electron microprobe, Optical polarizing microscopy (transmitted light, reflected light) SEM (basics)
High pressure methods	Hydrothermal diamond anvil cell Piston-cylinder apparatuses (incl. preparation) Hydrothermal cold seal pressure vessels
Additional	High-energy implantation

Workshops:

2008   Participant (competitive) at Marie Curie EURISPET seminar on "State-of-the-Art Analytical and Imaging Techniques in Petrology", Paris, France (10 days)

2007   Participant at the seminar on "High pressure experimental techniques and application to Earth's interior", Bayrisches Geoinstitut, Bayreuth, Germany

Awards and prizes:

2009   Travel Grant Award
Goldschmidt 2009, Davos, Schwitzerland

2006   Paul Ramdohr Prize
1.000 Euro prize for best oral presentation of a young scientist at the annual meeting conference of the "Deutsche Mineralogische Gesellschaft".

Invited talks

2009   *New in-situ methods for determining mineral solubilities: Mineral geometry and birefringence approaches.*
Institut de Minéralogie et de Physique des Milieux Condensés, Paris, France

2008   *Determining mineral solubilities at high pressures: New methods combining weight-loss and in situ approaches.*
Lunar and Planetary Institute, Houston, TX, USA

Affiliation: Deutsche Mineralogische Gesellschaft
(German Mineralogical Society)

Mineralogical Society of America

Publications:

Abstracts:

Fockenberg, T. & Gross, J., (2002): The solubility of natural wollastonite in pure water up to 5 GPa and 800 °C. *J. Conf. Abstracts,* **7**, No. 1, p.34

Gross, J., Schertl, H.-P., Maresch, W.V., Burchard, M., (2006): Petrology of the contact zone between eclogite and marble, Stümplefelsen, Hammerunterwiesenthal, Westerzgebirge. Beiheft *zum European Journal of Mineralogy,* 18, p.50

Gross J., Maresch, W.V., Fockenberg, T., (2007): A new method of determining mineral solubilities and material diffusivities at high pressures: Combining weight-loss and in situ approaches. In: *Subduction Dynamics: Bridging the scales, Abstract Volume,* p.125

Gross, J.; Maresch, W. V.; Fockenberg, T., (2007): Determining mineral solubilities at high pressures: A new method combining weight-loss and in situ approaches. *Geochimica Cosmochimica Acta,* 15S, A357

Paper:

Gross, J., Burchard, M., Schertl, H.-P., Maresch, W.V., (2008): Common high-pressure metamorphic history of eclogite lenses and surrounding metasediments: a case study of calc-silicate reaction zones (Erzgebirge, Germany). *European Journal of Mineralogy, 20, 757-775.*

Hiermit erkläre ich, Frau Juliane Groß, dass die vorliegende Arbeit selbstständig und ohne unerlaubte Hilfen ausgeführt und verfasst wurde und dass die Arbeit in dieser oder ähnlicher Form noch bei keiner Fakultät oder einer anderen Hochschule eingereicht wurde.

Bochum, 11.05.09